Contribution to the study of structural and ferroelectric properties of HZO thin films

Mohammed Bilal Hachemi

▶ **To cite this version:**

Mohammed Bilal Hachemi. Contribution to the study of structural and ferroelectric properties of HZO thin films. Micro and nanotechnologies/Microelectronics. Université Grenoble Alpes [2020-..], 2022. English. NNT : 2022GRALT071 . tel-03946210

HAL Id: tel-03946210

https://theses.hal.science/tel-03946210

Submitted on 19 Jan 2023

HAL is a multi-disciplinary open access archive for the deposit and dissemination of scientific research documents, whether they are published or not. The documents may come from teaching and research institutions in France or abroad, or from public or private research centers.

L'archive ouverte pluridisciplinaire **HAL**, est destinée au dépôt et à la diffusion de documents scientifiques de niveau recherche, publiés ou non, émanant des établissements d'enseignement et de recherche français ou étrangers, des laboratoires publics ou privés.

THÈSE

Pour obtenir le grade de

DOCTEUR DE L'UNIVERSITÉ GRENOBLE ALPES

École doctorale : EEATS - Electronique, Electrotechnique, Automatique, Traitement du Signal (EEATS)
Spécialité : Nano électronique et Nano technologies
Unité de recherche : Techniques de l'Informatique et de la Microélectronique pour l'Architecture des systèmes intégrés

Contribution à l'étude des propriétés structurales et ferroélectriques des couches minces HZO

Contribution to the study of structural and ferroelectric properties of HZO thin films

Présentée par :

Mohammed Bilal HACHEMI

Direction de thèse :

Skandar BASROUR PROFESSEUR DES UNIVERSITES, Université Grenoble Alpes	Directeur de thèse
Ahmad BSIESY PROFESSEUR DES UNIVERSITES, Université Grenoble Alpes	Co-directeur de thèse
Bassem SALEM Directeur de recherche au CNRS, CNRS	Co-directeur de thèse

Rapporteurs :

Bertrand VILQUIN
MAITRE DE CONFERENCE, Ecole centrale de Lyon
Ausrine BARTASYTE
PROFESSEUR DES UNIVERSITES, université de Franche-Comté

Thèse soutenue publiquement le **29 septembre 2022**, devant le jury composé de :

Skandar BASROUR PROFESSEUR DES UNIVERSITES, Université Grenoble Alpes	Directeur de thèse
Bertrand VILQUIN MAITRE DE CONFERENCE, Ecole centrale de Lyon	Rapporteur
Ausrine BARTASYTE PROFESSEUR DES UNIVERSITES, université de Franche-Comté	Rapporteure
Alain SYLVESTRE PROFESSEUR DES UNIVERSITES, Université Grenoble Alpes	Président

Invités :

Ahmad BSIESY
PROFESSEUR DES UNIVERSITES, Université Grenoble Alpes
Bassem SALEM
CHARGE DE RECHERCHE HDR, Laboratoire des technologies de la microélectronique

Acknowledgments

In fact, it took me a long time to write this acknowledgment, after a deep look back on the Ph.D. journey. I was looking for the right words to thank properly who helped and supported me whereas I did not have words to thank others.

First of all, I want to thank Dr.Vilquin and Pr. Bartasyte for accepting to review this thesis and the valuable discussions. You initiated my learning phase after the defence presentation.

Pr. Sylvestre, as a president of the jury and a very kind and knowledgeable professor, helped a lot to push this thesis forward, with the famous TF Analyzer and welcoming each time at the G2E Lab. Thank you sincerely.

To Pr. Skandar Basrour, I looked for all the expressions to express my gratitude for him, but I didn't find anyone sufficient. I am forever grateful to you. You were more than a supervisor. I would like to thank my esteemed supervisor –for his invaluable supervision, continuous support, and patience during my Ph.D. journey. His immense knowledge and plentiful experience have encouraged me in all the time of my academic research and daily life. Additionally, my appreciation, for you, for giving me the chance for teach at Polytech Grenoble.

Dr. Salem, I enjoyed working with you through the daily reporting, advice, and beneficial discussions. I took many lessons about research, career, and life during the hard and good moments of my journey at LTM.

Pr. Bsiesy, thanks for all corrections and your words at the final CSI, which pushed me forward.

Despite he was not officially one of my supervisors, but I could not imagine finishing my research without his valuable contribution, with deeper characterizations and sincere recommendations. To Dr. Consonni, I am deeply thankful to you and H. Roussel.

I would like to thank all the Need for IoT direction members for the fund and the interesting meetings. Special thanks to Audrey.

I am also grateful for all the technical and administrative support from the people at TIMA and LTM/CEA Leti: Victor, Thierry, Gauthier, Seb, Sébastien, Sylvain, Mika, Mazel, Thibault, and Si Mohammed for the equipment trainings, processes, and technical support, Malou and Sylvain, Anne-Laure, Laurence for all the administrative help organizing my administrative papers/accesses, conferences, and summer schools.

I can't pass without thanking CIME Nanotech and PTA technical staff: Deborah, Nicolas, Christophe, Valentine, Delphine, Thomas, and Marlène. Special thanks to Guillaume and Christelle for the continuous support and discussion about the sputtering details.

I am very grateful to the researchers I shared an office with throughout the years: Youssouf, Maxime, Clément, Sarah, Manual, and Liliane, for showing me the way, scientific and non-scientific discussions, feedback sessions, and moral support. Thanks.

Thanks to the TIMA team: Martial, Thibault, Gaetan, Marwa, Thomas, Orphée, Adrien, and Pierre, for the precious support which was influential in shaping my experiment methods and critiquing my results.

I am also grateful to my friends, especially who impacted and inspired me; Dhiya, Khaled, Abdou, Youcef, Calix, Dr. Imene Z, Houda, Mahmoud Chakaroun, Mohammed, Baha, Aissa, Hakim, Ernesto, Alvaro, Enzo, Zakaria, Ahmed, Oleh, Abdelkader, Mohammed Seddouk and all the others.

Lastly, my deep appreciation also goes out to my big and small family, especially my parents, for their encouragement and support all through my studies. Loubna, Fouad, Imene and Abderezak thank you for your belief in me. I kept my motivation present during this journey.

Table of contents

LIST OF FIGURES.....I

LIST OF TABLES.....X

ACRONYMS..... XI

INTRODUCTION.....1

1 CHAPTER I SUSTAINABILITY IN MICROELECTRONICS MATERIALS AND DEVICES: THE CASE OF HZO 7

1.1 Introduction 8

1.2 Main definitions 9
1.2.1 Sustainability in microelectronics:.....9
1.2.2 Definition of critical materials:.....11

1.3 Hafnium and Zirconium materials: History and discovery, mineralogy, production, and applications 12
1.3.1 Zirconium 12
1.3.2 Hafnium.....13
1.3.3 Mineralogy of zirconium and Hafnium.....14
1.3.4 The Hf-Zr coproduction 17
1.3.5 Worldwide production, reserves, and markets 18
1.3.6 Applications 20

1.4 Sustainability in the sputtering method: The thin films deposition technique, does it include sustainability?.....21
1.4.1 Sustainable approach for deposition technique selection.....21
1.4.2 Sputtering target manufacturing.....25
1.4.3 Comparison between HZO and PZT 28

1.5 Conclusion.....30

2 CHAPTER II FUNDAMENTALS OF FERROELECTRICITY AND THE LITERATURE REVIEW.....32

2.1 Introduction 33

2.2 Fundamentals of ferroelectricity, pyroelectricity and piezoelectricity: 33
2.2.1 Crystal structure:.....35

2.3 Phenomenology of ferroelectricity: 37

2.4 The main effects affecting ferroelectricity: 45
2.4.1 Retention 45
2.4.2 Wake-up effect 45
2.4.3 Ageing 46
2.4.4 Fatigue 47
2.4.5 Imprint 48

2.5 HZO review: the state-of-the-art 49
2.5.1 From 2005 to 2011 49
2.5.2 From 2011 to now 55

3 CHAPTER III FABRICATION METHODS AND CHARACTERIZATION TECHNIQUES 74

3.1 Fabrication process 75
3.1.1 Sputtering deposition of HZO thin films and TiN electrodes 75
3.1.1.1 HZO Sputtering chamber 77
3.1.1.2 TiN electrodes: 79
3.1.2 Fabrication of the capacitors 80
3.1.3 Rapid thermal annealing 81
3.1.4 Photolithography 84
3.1.5 Etching 85
3.1.6 Summary 85

3.2 Physical and structural characterizations: 86
3.2.1 X-rays 87
3.2.1.1 X-ray Diffraction: 87
3.2.1.2 X-ray reflectivity 89
3.2.1.3 X-ray photoelectron spectroscopy 91
3.2.2 SEM and TEM 94
3.2.2.1.1 Scanning electron microscopy (SEM) 94
3.2.2.1.2 Transmission electron microscopy (TEM) 95
3.2.3 AFM 96

3.3 Electrical characterizations 97
3.3.1 Impedance spectroscopy 98
3.3.2 Leakage current measurements 99
3.3.3 Capacitance voltage measurements 100
3.3.4 Polarization Field measurements 100

3.4 Conclusion 102

4 CHAPTER 4 OPTIMIZATION AND CHARACTERIZATION OF HZO AND TIN ELECTRODES. 105

4.1 TiN electrodes 107
4.1.1 Introduction 107
4.1.2 TiN deposition by reactive sputtering 108
4.1.2.1 Optimized parameters of TiN electrodes deposition 110
4.1.3 Characterization of TiN electrodes 110
4.1.3.1 Structural and elemental composition properties 111
4.1.3.2 Electrical properties of TiN electrodes 118
4.1.4 Titanium nitride electrodes' etching 119
4.1.5 Discussion 124
4.1.6 Conclusion 127

4.2 HZO: Ternary transition metal oxide deposited by sputtering 127
4.2.1 Deposition of HZO 128
4.2.1.1 RF magnetron sputtering 128
4.2.2 Impact of RF magnetron parameters 129
4.2.2.1 Reactive sputtering 129
4.2.2.2 Pressure 139
4.2.2.3 Power target 141
4.2.2.4 Ar Flow 146
4.2.2.5 Deposition time 147
4.2.3 Characterization of HZO thin films 148
4.2.3.1 Optimized parameters 148
4.2.3.2 Thickness effect 152
4.2.4 Discussion 153
4.2.5 Conclusion 158

4.3 Thermal annealing 158
4.3.1 Rapid thermal annealing 159
4.3.1.1 Annealing atmosphere 160
4.3.1.2 Annealing temperature 162
4.3.1.3 Annealing time 166
4.3.1.4 Other parameters: 167
4.3.1.4.1 Heat ramp rate 167
4.3.1.4.2 TiN electrodes' thicknesses 168
4.3.1.4.3 Thickness dependence 169
4.3.2 In-situ thermal annealing 171
4.3.2.1 Thermal annealing of top-electrode free HZO stacks 174
4.3.3 Discussion 176
4.3.4 Conclusion 177

4.4 TEM-ASTAR: Crystallographic phase and orientation mapping of ferroelectric HZO 178
4.4.1 Introduction 178

4.4.2 ASTAR phase mapping 184
4.4.3 Discussion 189
4.4.4 Conclusion 191

5 CHAPTER 5 ELECTRICAL CHARACTERIZATIONS OF HZO-BASED MIM CAPACITORS 194

5.1 Copper impurities in HZO sputtering 195
5.1.1 Introduction 195
5.1.2 Discussion 196
5.1.3 Conclusion 197

5.2 Electrical characterizations of HZO-based MIM capacitors 198
5.2.1 Introduction 198
5.2.2 With capping layer during RTA 199
5.2.3 Without capping layer during RTA 203
5.2.4 Conclusion 208

5.3 Temperature-dependent dielectric properties of HZO in top electrode-free annealing configuration 208
5.3.1 Introduction 208
5.3.2 Discussion 216
5.3.3 Conclusion 217

DISSERTATION CONCLUSION 219

PERSPECTIVES 222

ABSTRACT 241

RESUME 242

List of figures

Figure 1 pillars of sustainability Summit 2005 [3] 8
Figure 2 The four focus areas of ST's sustainability approach 11
Figure 3 The periodic table of elements highlighting Hf and Zr (modified from (17)) 13
Figure 4 Biggest supplier countries of CRMs to the EU (11) 14
Figure 5 Schematic structure of the zircon industry, from TZMI (14) 17
Figure 6 Zr concentrate production 1990-2016 19
Figure 7 different thin films deposition techniques 22
Figure 8 PVD vs CVD coating process (small and big insert) 24
Figure 9 chip manufacturing flow chart and unit processes involved in wafer fabrication 25
Figure 10 Examples of sputtering targets of various shapes and sizes 26
Figure 11 a generic flow chart for the manufacturing of a sputtering target 28
Figure 12 The Heckmann diagram describing direct and cross-coupling phenomena between thermal, electrical, and mechanical state variables. For the sake of clarity, the magnetic properties are omitted [66] 35
Figure 13 Dielectric, piezoelectric, pyroelectric, and ferroelectric crystal classes 37
Figure 14 The characteristic hysteresis loop of ferroelectrics: Polarization as a function of electric field (Blue) and linear response for non-ferroelectric dielectrics (grey) 39
Figure 15 The Landau-Devonshire-Gibbs energy G as a function of polarization for a ferroelectric (left) and a paraelectric (right) 39
Figure 16 The Landau-Devonshire Gibbs energy showing the two spontaneous polarization states 40
Figure 17 Scheme of hysteresis loop with Gibbs energy variation according to LGD for an ideal ferroelectric [74] 40
Figure 18 First-order phase transition (a) Remanent polarization as a function of temperature (b) dielectric constant 43
Figure 19 Second-order phase transition (a) Remanent polarization as a function of temperature (b) dielectric constant 44
Figure 20 (Right) the variation of the polarization as a function of the applied cycles showing the wake-up effect (grey area) and the fatigue (Blue area) (left) the evolution of the hysteresis loop from pristine to cycled material. 46

Figure 21 (Right) a generic retention curve showing the ageing for retention and imprint effects (Left) degraded hysteresis loop by ageing. 46
Figure 22 (Right) a generic fatigue curve to the breakdown of a ferroelectric (red) with the contribution of the leakage current (dashed grey) (Left) the effect of fatigue over the hysteresis loop..... 48
Figure 23 Ferroelectric hysteresis loop degradation by the imprint effect: degraded (red) and original loop (dashed grey). 49
Figure 24 HZO monoclinic and tetragonal phases produced by VESTA software 51
Figure 25 Number of HZO papers (2005-2021) 52
Figure 26 Number of papers of HZO with dielectric properties 52
Figure 27 HZO orthorhombic phases produced by VESTA software 55
Figure 28 P.V. hysteresis at 1 kHz and small-signal CV hysteresis at 10 kHz (50 mV level) of 9 nm thin HfO_2—ZrO_2 based metal—insulator—metal (reproduced with permission)..... 57
Figure 29 (P-E) curves of $Hf_{1-x}Zr_xO_2$ films with various compositions and thicknesses (reproduced with permission) 57
Figure 30 The dielectric constant – electric field curves of HZO films with various (reproduced with permission) 58
Figure 31 (Color online) Room-temperature strain—electric field (S—E) and..... 60
Figure 32 Different reported annealing temperature ranges of ferroelectric HZO (2011 -2021) 60
Figure 33 Different reported HZO deposition techniques (2011 -2021) 63
Figure 34 Ferroelectric HZO deposition techniques with detailed sputtering systems..... 64
Figure 35 S-shaped P–E.F. curve Black and blue correspond to the increasing and decreasing Vmax sweep direction. Red corresponds to LGD theory, and the blue shows the P–E.F. hysteresis measured on a TiN/HZO/TiN sample (reproduced with permission) 66
Figure 36 Experimental set-up for the pulsed Q–V measurements. V is applied by a pulse generator, and both V and V.R. are measured via an oscilloscope, where V.R. is the voltage drop across the resistance R (reproduced with permission) 67
Figure 37 Figures of merit voltage sensitivity vs current sensitivity (reproduced with permission)..... 69
Figure 38 SEM image of the $Hf_{0.5}Zr_{0.5}O_2$-transduced Si nanomechanical resonator operating in out-of-plane flexural mode (the cross-sectional schematic of the device along A.A. ′ is

shown in Supplementary Fig. 2). b, Magnified SEM of the resonator around the Pt/TiN top electrodes used to apply stroboscopic a.c. voltage (reproduced with permission) 69
Figure 39 The frequency response of the $Hf_{0.5}Zr_{0.5}O_2$-transduced Si resonator extracted from stroboscopic analysis, showing the flexural resonance at 339 kHz and a Q of 250 in the air (reproduced with permission) 70
Figure 40 The cross-sectional schematic of the HZO transduced Si nanomechanical resonator. 70
Figure 41 The fQ product figure of merit of the recently demonstrated state-of-the-art nanomechanical resonators (reproduced with permission) 71
Figure 42 Illustration of sputtering phenomena 77
Figure 43 The user interface of the DP 850 sputtering equipment 78
Figure 44 The fabrication process flow of the HZO-base MIM structures 80
Figure 45 typical profile of a rapid annealing cycle 82
Figure 46 Sketch of rapid thermal annealing furnace 83
Figure 47 The photolithography mask of different diameters circular pads 84
Figure 48 SEM images of the circular pads after etching (left) the smallest circular pad of 100 µm 86
Figure 49 Schematic of X-ray diffraction principle 88
Figure 50 Sketch of the GIXRD configuration 89
Figure 51 Sketch of the features in an XRR plot for a single layer of HZO 90
Figure 52 Principle of X-ray photoelectron spectroscopy (XPS) 91
Figure 53 Survey spectrum from of HZO films 93
Figure 54 Example of Hf 4f doublets. 93
Figure 55 Angle XPS Zr 94
Figure 56 sketch of SEM working principle and main parts 95
Figure 57 Sketch of TEM working principle 95
Figure 58 Equivalent circuit of MIM structure 99
Figure 59 Schematic circuits comparison of Sawyer tower (left) and virtual ground (right). 101
Figure 60 Schematic of PUND measurement 102
Figure 61 Thickness versus deposition time of TiN layers by DC reactive sputtering 109
Figure 62 Diffractogram of TiN films (50 nm) compared to ICDD reference pattern of cubic TiN 111

Figure 63 graphical representation of cubic phase of TiN 111
Figure 64 X-ray reflectivity patterns of TiN with different thicknesses 112
Figure 65 variation of TiN density with thickness 112
Figure 66 Fitted X-ray reflectivity pattern of TiN 113
Figure 67 AFM scan of 50 nm TiN surface with a roughness of $R_q = 0.28$ nm for a surface of 5×5 µm 113
Figure 68 (Left) EDX results of Ti and N in TiN top and bottom electrodes (Right) cross-section TEM images in Bright Field Imaging mode 114
Figure 69 TEM cross section of TEM in Dark Field imaging mode 115
Figure 70 core-level XPS spectra and peak-fitting analysis of C1s 115
Figure 71 core-level XPS spectra and peak-fitting analysis of O1s 115
Figure 72 core-level XPS spectra and peak-fitting analysis of Ti2p 116
Figure 73 core-level XPS spectra and peak-fitting analysis of N1s 116
Figure 74 Angle resolved atomic % of TiN, TiO_2, and TiO_xN_y 117
Figure 75 XPS depth profile of TiN/Si 117
Figure 76 Sheet resistance of TiN as function of thickness 118
Figure 77 Ion Beam Etching (IBE) of TiN 50 nm 120
Figure 78 SIMS signals of Ti and Hf during IBE etching of 50 nm TiN an d15 nm HZO 121
Figure 79 Inductively coupled plasma etching of TiN 122
Figure 80 Chemical (wet) etching of TiN 123
Figure 81 Pictures of TiN samples before and after wet etching (left) SEM images (right) photos 123
Figure 82 EDX profile picture before and after etching by wet etching. 124
Figure 83 Variation of deposition rate and HZO density as function of oxygen partial pressure 130
Figure 84 XPS depth profile survey of HZO/Si 131
Figure 85 High resolution XPS spectra of samples deposited with different PO_2 values: C 1s (left) and O 1s (right) regions 132
Figure 86 Variation of oxygen vacancies as a function of PO_2 % (0-20%) 133
Figure 87 High resolution XPS spectra of samples deposited with different PO_2 values: Hf 4f (left) and Zr 3d (right) regions 134
Figure 88 Zoom on additional peaks appeared in XPS spectra of Hf 4f at 10% PO_2 (left) and Zr 3d at 20 % PO_2 (right) samples 135

Figure 89 The variation of the Zr:Hf and O/(Zr+Hf) ratios as the oxygen % increases from 0 to 20% PO_2. 135
Figure 90 High resolution XPS spectra of samples deposited with different oxygen partial pressure values: C 1s (left) and O 1s (right) regions 137
Figure 91 The variation of oxygen vacancies as a function of 0-2% PO_2 137
Figure 92 High resolution XPS spectra of samples deposited with different PO_2 values: Hf 3d (left) and O 1s (right) regions 138
Figure 93 The variation of the Zr:Hf and O/(Zr+Hf) ratios as c increases from 0 to 2%. 138
Figure 94 Diffractogram of TiN/HZO/TiN structures as deposited and annealed, as function of PO_2 139
Figure 95 Variation of deposition rate as a function of the deposition pressure 140
Figure 96 Variation of deposition rate as a function of the power density applied to the target. 142
Figure 97 High resolution XPS spectra of samples deposited with different power values: C 1s (left) and O 1s (right) regions 142
Figure 98 The variation of oxygen vacancies as a function of sputtering power 143
Figure 99 High resolution XPS spectra of samples deposited with different power values: Zr 3d (left) and Hf 4f (right) regions 144
Figure 100 Zoom on additional peaks appeared in Hf 4f XPS spectra for 500W (left) and 600W (right) samples 145
Figure 101 variation of Zr:Hf (blue) and O/(Zr+Hf) (red) as function of the sputtering power. 146
Figure 102 X-ray reflectivity patterns of HZO deposited at different Ar flow rates 147
Figure 103 The thickness of HZO deposited films as a function of the deposition time 148
Figure 104 XPS spectra of HZO deposited on Si with the optimized parameters for (a) Hf 4f region (b) Zr 3d region 149
Figure 105 Angle-Resolved XPS spectra for sputtered HZO (a) Hafnium 4f (b) Zr 3d 149
Figure 106 Atomic percent plotted versus emission angle ARXPS of HZO 150
Figure 107 TEM cross section of (left) full TiN/HZO/TiN stack (middle) focus of HZO/TiN top electrode, and (right) focus on TiN bottom electrode/HZO evidencing the thickness uniformity of both HZO and TiN and the interfaces besides the crystallization of HZO after annealing. 151

Figure 108 TEM image of annealed TiN/HZO/TiN stack can be seen in bottom; b) EDX along the structure indicated in a), where Gd signal is amplified by a factor 10 for better visualization; c) HRTEM detail in which a stronger crystallization of the N2 annealed film can be seen with respect to the d) as-deposited sample. 151
Figure 109 XRD patterns of as-deposited HZO films of various thicknesses..... 153
Figure 110 GIXRD patterns of TiN/HZO/TiN stack before and after RTA 159
Figure 111 X-ray reflectivity patterns of TiN/HZO/TiN before and after annealing 160
Figure 112 XRD patterns of HZO before and after annealing under N_2 and O_2. 161
Figure 113 XPS spectra of O 1s region of samples annealed at different RTA atmosphere 162
Figure 114 core-level XPS spectra and peak-fitting analysis of O1s..... 163
Figure 115 core-level XPS spectra and peak-fitting analysis of (left)Hf 4f and (right) Zr 3d 163
Figure 116 XRD pattern of HZO stack annealed at 400 and 650°C..... 164
Figure 117 XRD patterns of annealed HZO stacks at different temperatures, from 500 to 650°C 165
Figure 118 XRD patterns of annealed HZO stacks at different annealing times..... 166
Figure 119 XRD patterns of annealed samples at different heat ramps..... 168
Figure 120 XRD patterns of annealed HZO stacks with different TiN thicknesses..... 169
Figure 121 XRD patterns of annealed HZO stacks of different HZO thicknesses 170
Figure 122 XRD patterns of the TiN/HZO/TiN stack at different *in situ* thermal annealing temperatures in the range of 30–900 °C under N_2 atmosphere during heating. 171
Figure 123 XRD pattern extracted from the in-situ thermal annealing results. 172
Figure 124 XRD patterns of the TiN/ HZO/TiN stack at different in situ thermal annealing temperatures in the range of 30–900 °C under N_2 atmosphere during cooling down. 173
Figure 125 XRD patterns of HZO stacks annealed with different TiN thicknesses..... 174
Figure 126 XRD patterns of the TiN/ HZO stack at different in situ thermal annealing temperatures in the range of 30–900 °C under N_2 atmosphere during heating up 175
Figure 127 XRD patterns of the TiN/ HZO stack at different in situ thermal annealing temperatures in the range of 900–30 °C under N_2 atmosphere during cooling down 175
Figure 131 GIXRD pattern of TiN/HZO/TiN stack used for the ASTAR characterization, after annealing at 650 °C under N_2..... 180
Figure 132 Cross sectional TEM image of TiN/HZO/TiN stack with 100/15/100 nm..... 181

Figure 133 (left) cross sectional TEM and (right) HRTEM images of TiN/HZO/TiN stack with 25/15/25 nm thicknesses. 181
Figure 134 (left) Cross sectional TEM image of the first zone of investigation, in the white square (right) The Fast Fourier Transform (FFT) of the stack TEM image. the growth of the planes (111) along the direction of HZO is indicated. 182
Figure 135 (left) Cross sectional TEM image of the second zone of investigation, in the white square (right) The Fast Fourier Transform (FFT) of the stack TEM image. the growth of the planes (111) along the direction of HZO is indicated. 183
Figure 136 (left) Cross sectional TEM image of the first zone of investigation, in the white square (right) The Fast Fourier Transform (FFT) of the stack TEM image. The growth of the planes (111) along the direction of HZO is indicated. 183
Figure 137 ASTAR map representing the crystalline phases of a HZO and TiN. The colors of TiN, HZO and Pt are shown in Table 2. The inset is a typical electron diffraction pattern of HZO recorded on the corresponding map, as indicated by the blue arrow. The templates that correspond to the most probable solution (i.e., the best match) are represented by blue open circles. 185
Figure 138 ASTAR map representing the crystalline phases of a HZO and TN. The colors of TiN, HZO and Pt are shown in Table 2. The inset is a typical electron diffraction pattern of HZO recorded on the corresponding map, as indicated by the blue arrow. The templates that correspond to the most probable solution (i.e., the best match) are represented by blue open circles 185
Figure 139 Reconstructed correlation index map 186
Figure 140 ASTAR crystallographic orientation phase maps of TiN/HZO/TiN/Pt along the three different orientations (a) X orientation 187
Figure 141 The triangular color code depicts the crystalline directions exhibited for the corresponding plane for both HZO and TiN. The color codes for HZO and TiN. 188
Figure 142 Virtual BF image, Reconstructed correlation index map 188
Figure 143 Virtual BF image, Reconstructed correlation index map 189
Figure 128 XPS of copper in HZO sputtered films 195
Figure 129 XPS depth profile of Hf, Zr, and Cu in HZO sputtered films. 196
Figure 130 (left) Schematic cross section of facing target sputtering system used for HZO sputtering (right) picture of HZO sputtering. 197
Figure 144 Impedance and phase angle versus frequency of TiN/HZO/TiN stack 198

Figure 145 The equivalent circuit of TiN/HZO/TiN 199
Figure 146 Leakage current density versus electric field for 15 nm HZO 199
Figure 147 Dielectric constant versus electric field of HZO 15 nm 200
Figure 148 Dielectric constant of HZO phases reported in literature [13], [247], [254]–[259] 201
Figure 149 Polarization versus electric field hysteresis loop of the 15 nm HZO after different number of cycles. 202
Figure 150 (left) Leakage current density versus electric field (right) Dielectric constant versus electric field of HZO 22 nm. The inset: XRD pattern of the sample 203
Figure 151 GIXRD patterns of HZO stacks of different thicknesses annealed at 650°C. 204
Figure 152 The impedance and phase versus frequency of HZO 205
Figure 153 The capacitance and loss factor versus frequency of HZO stack without capping layer during RTA 205
Figure 154 The capacitance and dielectric constant versus pad's diameter 206
Figure 155 The capacitance-voltage curve for HZO stack without capping layer during RTA. 206
Figure 156 The I-V of HZO stack W/O capping 207
Figure 157 P-E loops of HZO stack W/O capping 208
Figure 158 The CV and loss factor versus voltage 209
Figure 159 Dielectric constant versus temperature – heating and cooling phases 210
Figure 160 loss factor versus temperature - cooling 210
Figure 161 Variation of dielectric constant – heating and cooling 211
Figure 162 Hysteresis loop at 250 and 350°C 211
Figure 163 Cycling of the device at 350°C 212
Figure 164 J-V measurement of the 35 nm device 212
Figure 165 capacitance versus voltage measured at room temperature 213
Figure 166 Dielectric constant and loss factor versus frequency 213
Figure 167 impedance versus frequency 214
Figure 168 dielectric constant and loss factor versus temperature 214
Figure 169 conductance and impedance versus temperature 215
Figure 170 dielectric constant and loss factor versus temperature 215
Figure 171 loss factor and capacitance variation versus temperature 216

Glossary

c The light speed

ε The dielectric permittivity

E The electrical field

P the electrical polarization

χ The dielectric susceptibility

X The stress

List of tables

Table 1 Critical raw materials for 2020 published by EU [30] 12

Table 2 Worldwide Zr production 2010-2016 and its reserves 20

Table 3 Comparison of hafnia and PZT based ferroelectrics for future non-volatile FRAM applications 29

Table 4 Comparison of electric polarization response to external influences between polar and non-polar dielectrics 34

Table 5 crystallographic classification of crystal materials 36

Table 6 The reference patterns for HZO crystal phases 89

Table 7 Reference peaks used for XPS spectra calibration 92

Table 8 Surface area ratios between the two peaks of a doublet belonging to a certain angular quantum number 93

Table 9 The optimized parameters of TiN sputtering 110

Table 10 Comparison of resistivity of TiN layers deposited on Si substrate for different thicknesses. 119

Table 11 The studied power values and the corresponding power density 141

Table 12 XRD reference patterns of TiN, HZO, and Pt phases 179

Table 13 the color code for the mapping 185

List of abbreviations

AFM Atomic Force Microscopy

ASTAR Automatic Crystal Orientation and phase mapping

BE Bottom electrode

EBSD Electron backscatter diffraction

HZO Hafnium Zirconium Oxide

IoT Internet of things

MIM Metal-Insulator-Metal

NV Non-volatile

PFM Piezoresponse force microscopy

TE Top electrode

XPS X-ray Photoelectron Spectroscopy

XRD X-ray diffraction

Introduction

The information and communication technology (ICT) industry worldwide is still growing fast. For example, the number of IoT (Internet of things) devices reached 35.82 billion devices in 2021 and forecasts suggest that there will be more than 75.44 billion devices in 2030 [1]. The consequences of this growth can be directly seen in two main branches: Firstly, the increase of energy consumption (use of electricity), by ICT products such as data centres, IoT devices, and networks, with a higher rate compared to the total worldwide consumption of electricity. Secondly, the environmental impacts of the ICT industry during its entire life cycle, from the raw materials to the final product used by the consumer, require energy and need environmental burdens over natural resources (water, soil, and air) [2], for example, greenhouse gas (GHG) emissions [3], use of hazardous materials and chemicals [4] and reduction of critical material resources [5]. Despite such consequences, the positive effects of this ICT trend can be bigger than the negative impacts if the environmental sustainability criterion is well integrated within the entire life cycle of any ICT product, at both macro and micro levels. This can be done by enforcing "the enabling effects" [6] such as optimization and supporting of the sustainable alternatives of the existing hazardous devices and taking into consideration the rebound effects[] to reduce them. Sustainable IoT devices are attracting more interest as IoT technology producers are competing to fulfil the consumers' requirements such as high-quality, low-cost products, and yet requesting green label 'eco-friendly' products that expend the minimum of energy and are free of any hazardous materials to health, water, or environment. This 'green' trend is well expanding and becoming more and more popular among consumers at the same time while companies are adopting a consumer-driven approach for the design and marketing of their products, which gives this trend more importance that pushed governments in Europe and Japan, first, to legislate obligatory agreement with a diversity of limitations and bans over the used materials,

based on the hazardousness and criticality of these materials mainly in the microelectronics industry. On a worldwide scale, Europe and Japan took the lead with this initiative due to dense populations and limited access to natural resources, starting in 2003 with the RoHS (Restriction of Hazardous Substances) directive, by the European Union (EU), as a revolutionary decision to order the prohibition of some toxic and dangerous materials taking effect on 1st July 2006 [7]. This decision was mandatorily applied to all products to be sold in the EU. The main motivation of RoHS directive was due to lead (Pb), a toxic material widely.

Used in the microelectronics industry in two main applications: interconnect soldering and MEMS (microelectromechanical systems) devices such as pMUT for fingerprint sensors, microphones, and loudspeakers, inkjet nozzle, energy harvesting, acoustic resonators, BioMEMS, etc. After the joining of countries, industries, and researchers, the first impacts led researchers to pave new research fields such as lead-free piezoelectrics and lead-free soldering. The latter is out of the scope of this thesis. Piezoelectric materials shape the backbone of numerous devices used in telecommunications, ultrasonic medical imaging, ultrasonic non-destructive testing, energy harvesting, and ICT. Due to their excellent piezoelectric and ferroelectric properties, $PbZr_xTi_{1-x}O_3$ (PZT) and other lead-based materials such as $Pb(Mg_{1/3}Nb_{2/3})O_3$ (PMN), $Pb(Mg_{1/3}Nb_{2/3})O_3$–$PbTiO_3$ (PMNPT) and $Pb(Zn_{1/3}Nb_{2/3})O_3$–$PbTiO_3$ (PZN-PT) have been the base for high-performance piezoelectric applications. Elimination of lead in applications such as actuators remains a challenge but in some other applications such as high-frequency electronic components it has been possible to utilize lead-free materials. In the framework of the NEED for IoT project devoted to sustainable IoT, our interest is focused on sustainable nanoelectronics devices, mainly, replacing PZT layers with a lead-free material while maintaining the same level of performance. PZT is one the most efficient materials in terms of electromechanical coupling factors for transducers and sensors, but unfortunately, it contains 60 % of lead which is toxic and prohibited in different countries as mentioned

above. Besides its incomplete compatibility with CMOS process growth. In this context, we focus on the elaboration of $Hf_{0.5}Zr_{0.5}O_2$ (HZO) films by CMOS compatible techniques to bring a contribution to a better understanding of this fluorite-structure type material. The ferroelectricity, recently discovered by a coincidence [8], within hafnia-based, including HZO, thin films is considered as a gamechanger in this field due to their promising properties at very low thicknesses. Currently, the core orientation of the scientific community, interested in this material, is about reaching a better understanding of the factors inducing ferroelectricity, its stabilization, and its mechanisms which is quite challenging at a few nanometres or a hundred nanometres thicknesses. Despite that the discovery of ferroelectricity in hafnium oxide is recent, some existing challenges are already known for the perovskites structure materials, such as interface engineering and phase stabilization [9]–[11]. Simultaneously, the potential of this new class of lead-free materials makes the efforts to resolve the challenges worthy. First, as can be seen in the tremendous increase of papers, HZO is considered as a leading lead-free candidate with excellent ferroelectric properties next to the good pyroelectric and piezoelectric properties. These exciting properties pave the way for HZO to be the sustainable key-enabler for the next generation of ferroelectric memories and lead-free piezoelectric applications. Additionally, HZO well-satisfies the criteria of device scaling and low energy consumption requested by nowadays innovations, such as IoT or industry 4.0.

This new class of materials with its promising properties renewed the attention to the non-volatile ferroelectric memories which are reflected by the growing interest in ferroelectric hafnia shown in scientific papers. The effect of this class of materials did not impact only the NV ferroelectric memories field only, but also other low power nanoelectronics like neuromorphic devices and sensors. The next expected interest to be renovated is mostly the piezoelectric applications at higher thicknesses. Finally, the commercialization of hafnia-based devices has also Its own challenges depending on the application of the field beside the challenges of full understanding of the material

properties. The choice of the deposition technique of any material depends on many criteria; the thickness of the layers, the field of application, the thermal processing, and the desired characteristics...etc. In contrary to the state-of-the-art, where ALD (atomic layer deposition) is the common technique given the desired thickness for NV memories, for HZO synthesis in this work, the sputtering technique is chosen, widely used in the microelectronics industry offering a large parameter space for tuning film properties.

Nevertheless, until today, the deposition of HZO by sputtering is little studied despite the multiple sputtering systems (single target sputtering of a compound, co-sputtering ...etc). Only three research groups have published papers on sputtered HZO [12]–[14].The potentials offered by this technique hence still lack a systematic investigation. This thesis identifies the related physical mechanism for the deposition of HZO by a single target sputtering system. Furthermore, using that knowledge, the deposition parameters are optimized to get high-quality thin films. However, this thesis is subsequently undertaking a complementary approach in tackling the challenges above. On one hand by studying the sustainability of HZO and its feasibility as a lead-free alternative and on the other hand by suggesting a systematic study of the sputtered HZO properties, the effect of rapid thermal annealing at different thicknesses considering the CMOS compatibility of the obtained films and investigating the dielectric and electric properties of HZO.

This manuscript is organized as follows:

Part I is dedicated to the study of the sustainability of HZO material and the sputtering.

Chapter 1 will present an overview of the hafnium and zirconium materials, their properties, life cycle from mines to sputtering targets, their markets producers and the main applications besides referring to the main factors influencing these materials and the feasibility of replacing PZT from a critical material and economic point of view. Finally, it will present a brief comparison between devices based on HZO and PZT.

Part II is dedicated to the literature review and experimental studies of HZO thin films properties.

Chapter 2 provides some needed fundamentals to understand the arguments debated in this thesis. The chapter is divided into two small sections. The first will be dedicated to general ferroelectric concepts, the second part will be committed to the understanding of the state-of-the-art challenges that lead ferroelectric hafnia field. The idea for this chapter is to uniform the concepts and to provide a general background for the readers.

Chapter 3 will describe the main experimental techniques utilized to elaborate, fabricate, and characterize the samples measured within this thesis. The theoretical working principles of each experimental technique will be provided. Interest will be dedicated to describing the single target sputtering parameters. The role of the rapid thermal annealing will be investigated and discussed.

Chapter 4 will focus on the investigation of structural properties of TiN electrodes and HZO thin films. Afterwards, we will focus the influence of sputtering parameters on the structural properties and their characterization. Then, we will investigate the structural properties of MIM capacitor by ASTAR-TEM technique.

Chapter 5 is dedicated to the investigation of the correlation between the structural and different electrical properties, from dielectric to ferroelectric characteristics. Afterwards, we will analyse and discuss the electrical measurements while comparing our work with the state-of-the -art.

To conclude with the perspective and ideas for future studies. Finally, in the general conclusion, a summary of the most relevant results and some perspective on the analysed structure and phenomena concludes the dissertation.

1 Chapter I Sustainability in microelectronics materials and devices: the case of HZO

1.1 Introduction 8

1.2 Main definitions 9
1.2.1 Sustainability in microelectronics: 9
1.2.2 Definition of critical materials: 11

1.3 Hafnium and Zirconium materials: History and discovery, mineralogy, production, and applications 12
1.3.1 Zirconium 12
1.3.2 Hafnium 13
1.3.3 Mineralogy of zirconium and Hafnium 14
1.3.4 The Hf-Zr coproduction 17
1.3.5 Worldwide production, reserves, and markets 18
1.3.6 Applications 20

1.4 Sustainability in the sputtering method: The thin films deposition technique, does it include sustainability? 21
1.4.1 Sustainable approach for deposition technique selection 21
1.4.2 Sputtering target manufacturing 25
1.4.3 Comparison between HZO and PZT 28

1.5 Conclusion 30

1.1 Introduction

As part of the NEED for IoT project, we devote this chapter to the sustainable aspect of HZO in order to have a complete sustainable and technical study of HZO. In this chapter, we answer it by introducing the terms of sustainability in a general manner and microelectronics specifically and the criticality of materials. Then, we focus on the materials used in this thesis, mainly zirconium and Hafnium, their properties, and markets. Finally, we compare the ecological evaluation of thin films' deposition techniques and explain the choice of the sputtering technique.

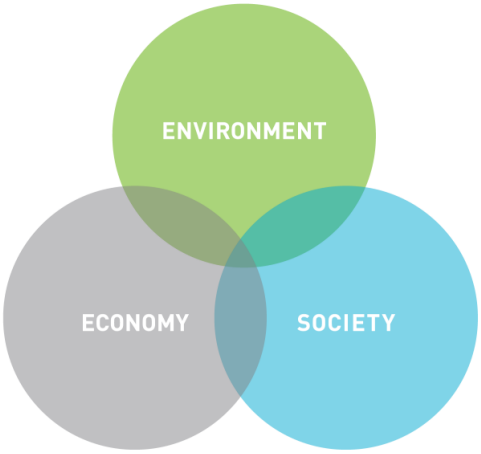

Figure 1 pillars of sustainability Summit 2005 [3]

Nowadays, the term: sustainability is one of the most-used buzzwords, from newspapers, media and scientific reports to political speeches and programs. Sustainability is applied to practically every field, including industry, strategy and even business management. The main idea of sustainability is a concern for the future of humanity's resources [15]. The meaning of 'sustainability' evolved, with time, to fit the required specifications of each period. It passed from: "never harvesting more than the forest can regenerate" from a forest handbook in 1713 [16] to an official definition adopted by the Brundtland Commission of the United Nations in 1987: "sustainable development is a development that meets the needs of the present without compromising the ability of future generations to meet their own needs" [15]. This definition represents the growing awareness about the overuse of resources and dependence on fossil energies since the 80s of the last century.

For many decades, the UN adopted the sustainability approach in many summits, especially the 2005 Word Summit on social development [17], in which Sustainable Development was set forth with three main aims, as shown in **Figure 1** [18]: economic growth, social development, and environmental protection, and the UN general assembly, in 2015, where all the members agreed on a collective plan until 2030 "SDGs" (the Sustainable Development Goals) [19]. This agenda gathers the efforts of the governments and the private sector to reach the outlined goals.
In this chapter, we refer to two linked industries: Mining, which is the backbone for many sectors and the microelectronics industry, which represents the continuous progress of humanity.

1.2 Main definitions

1.2.1 Sustainability in microelectronics:

Generally, the word 'sustainability' refers to the ability of something to maintain or "sustain" itself over time [20]. In industrial and governmental frameworks, sustainability goals are linked with natural resources, environment preservation, and social resources. Therefore, sustainable strategies give more importance to the future human, economic and ecological impacts of any given ecosystem or industry. The philosophy behind sustainability, unexclusively, corresponds to the idea that: "without major changes to the way the planet is run, it will suffer irreparable degradation"[21].

The microelectronics industry, especially ICT, is a significant part of the possible convergences between technological and environmental instances. It can play a crucial role in enabling systemic solutions that consider the ecological outwardness of economic progress. Microelectronic devices are more and more embedded in human societies and organizations. These technological innovations are increasingly known as the best way to promote sustainable development. In addition, considering the microelectronics industry's significant impact on the economy, the integration of sustainability strategies within this industry is particularly important. Since 2000, many prominent actors within the microelectronics industry joined the "United Nations Global Compact", the world's largest corporate sustainability initiative, aiming to mobilize a global movement of sustainable companies and stakeholders. It supports companies to do business responsibly and take strategic actions to advance broader societal goals, such as the UN Sustainable Development Goals (17 goals for

2030 [19, p. 17]), emphasizing collaboration and innovation. Since that, many companies from different sectors, such as STMicroelectronics[22], Volkswagen [23], and Apple [24], have published annual sustainability reports that highlight the sustainability performance and activities that reflect their commitments and awareness about the global sustainability concerns.

Many actors in the semiconductors industry, such as the equipment providers like Applied Materials, Tokyo Electron, and others, announced that they are making efforts to apply the UN sustainable development goals to reach future sustainability. They are taking their responsibilities towards sustainability and the societal goals also. Their main contributions can be seen in adopting the reduction of energy consumption' approach and the reduction of greenhouse gas (GHG) emissions. Other companies like TSMC, Intel, and ST microelectronics published their targets for 2030 and internal programs to reach the set objectives. In the case of TSMC, one of its goals is to supply 25% of the power consumed by its fabrication plants from renewable energy and 100% for other facilities' power consumption [25]. Intel introduced the SPARC program (Supplier Program To Accelerate Responsibility & Commitment) [26]. Intel aims to have 90 % of suppliers meeting the eight sides of its program of sustainability and transparency. As one of the key players in the microelectronics industry, ST microelectronics promotes its approach to sustainability and green electronics. It defined four focus areas and 24 sustainable goals to reach in the next few years. **Figure 2** shows the four areas: its clients' priority, assuring the progress, responsibility towards the environment and the collective action [27].

Such initiatives and programs represent the shift towards sustainability of the significant actor in this industry, which indirectly means a shift in academic research. Besides taking their responsibilities, the companies in this sector promote a good brand image in front of end consumers [28].

Figure 2 The four focus areas of ST's sustainability approach

1.2.2 Definition of critical materials:

Another term gained currency and is now broadly applied: “critical material”. However, it is possibly misleading because “critical” has many meanings, some of which can be dedicated to materials.

A critical material must be of decisive or crucial importance to something or an industry's success, failure, or existence. This material must be an essential one, but it may or may not be at a crisis point. However, although necessary, essentiality is not sufficient to assign the label ‘critical material’. This term is reserved for essential materials and has significant supply-chain uncertainties [29].

The statement that material is critical means considerable supply risks, which might have significant consequences on the current and future supply chain of any industry related to materials. Saying that material is critical represents a warning about the possible scenarios in which shortages and disruptions can happen, rather than an immediate alarm. It identifies a need for eventuality planning regarding supplies, resources, and strategies to avoid a crisis.

In annual reports of organizations or governments about the criticality of materials, it is common to refer to materials criticality in a binary sense—materials are either considered to be or not to be critical—but in reality, there is a spectrum of criticality: some materials are more or less critical than others, and it is essential to quantify their criticality, even if it can only be done approximately.

The definition of critical materials varies depending on the countries’ policies. Since 2011 and every three years, the EU has published an updated critical raw materials report [30]. Materials can be more or less necessary depending on the economic growth and the application field. Table 1 presents the critical raw materials in 2020 for the EU. United States (US) also releases an evaluation and a survey of critical materials every year (United States Geological Survey).

Table 1 Critical raw materials for 2020 published by EU [30]
2020 Critical Raw Materials (new as compared to 2017 in bold)

Antimony	Hafnium	Phosphorus
Baryte	Heavy Rare Earth Elements	Scandium
Beryllium	Light Rare Earth Elements	Silicon metal
Bismuth	Indium	Tantalum
Borate	Magnesium	Tungsten
Cobalt	Natural Graphite	Vanadium
Coking Coal	Natural Rubber	**B**auxite
Fluorspar	Niobium	**L**ithium
Gallium	Platinum Group Metals	**T**itanium
Germanium	Phosphate rock	**S**trontium

The information about the materials' criticality worldwide can be of geopolitical concern and business importance. This can explain the difficulty of having permanent access to a piece of updated, precise information about the materials markets, reserves, and resources.

1.3 Hafnium and Zirconium materials: History and discovery, mineralogy, production, and applications

1.3.1 Zirconium

Zirconium is a remarkable greyish-white metal of Group 4 (IVb) of the periodic table, **Figure 3** [31], with the symbol Zr and atomic number 40. It has exceptional properties that make it vastly significant for numerous applications for both industry and scientific research communities. In 2020, Zr appeared as the 18th most abundant material in the Earth's crust [32]. Zr cannot be found in its pure form alone in the latter. Still, it can often be found in two minerals: in silicate form ($ZrSiO_4$) is a mineral zircon, and in the baddeleyite mineral (known as the natural zirconia), in oxide form (ZrO_2) [33].

For the first time, Zr was discovered in Germany in 1789 by Martin H. Klaproth while analyzing zircon mineral samples. Then, J.J. Berzelius isolated Zr as a metal in 1824. One century later, the crystal bar process for highly pure zirconium was developed by A. E. Van Arkel and J. Hedrik de Boer, which led to Zr's commercialization in 1930 [34]. Finally, in the early 1940s, W. J. Kroll of Luxembourg developed his cheaper process of making the metal based on reducing zirconium tetrachloride, $ZrCl_4$, by magnesium [35].

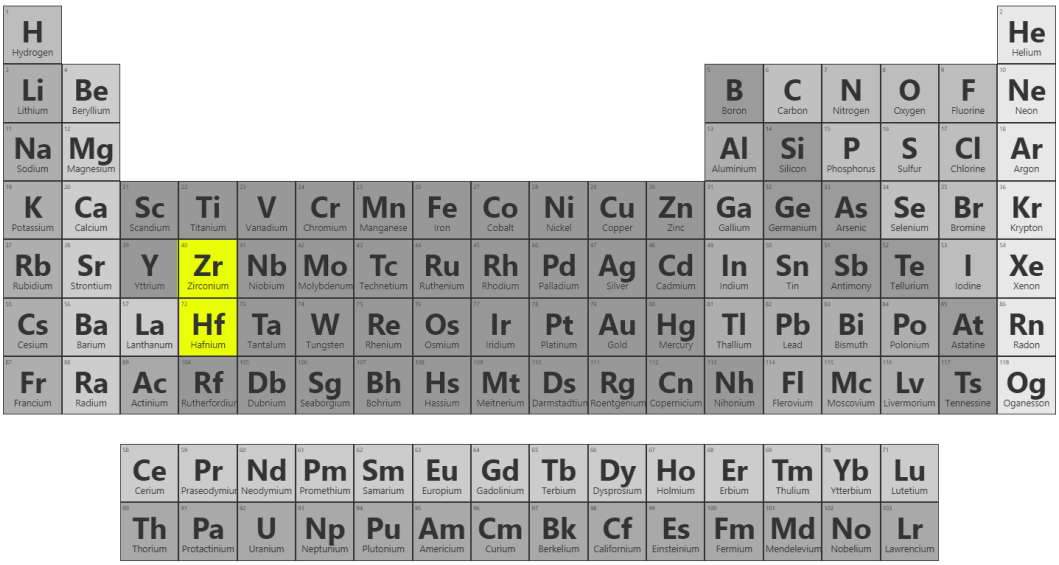

Figure 3 The periodic table of elements highlighting Hf and Zr (modified from [17])

1.3.2 Hafnium

Hafnium is a chemical element with the symbol " Hf " and atomic number 72 metal of Group 4 (IVb) of the periodic table, **Figure 3** [31]. Before its discovery, Hafnium was predicted by D. Mendeleev as a heavier element similar to Zr and Ti [36]. A silver-grey transition metal, Hafnium, and zirconium are chemically similar. For Mendeleev, there were several indications of the presence of one or more unknown elements in zirconium, but none had been found. Due to its extraordinarily similarity with Zr, no qualitative differences in chemical nature between the two elements were detected. A similar element (Hf) had been following zirconium in all the processing of its ores, despite being a colossal isotope of zirconium. Hafnium appears as the 43rd most abundant material. It is dispersed in Earth's crust to the extent of three parts per million and is invariably found in zirconium minerals up to a few per cent compared with zirconium [37]. It was discovered in 1923 by D. Coster and G. De Hevesy [36] ,which made Hf the second-last stable element discovered (the last was rhenium). They named the new element for Copenhagen (in New Latin, Hafnia). As shown in **Figure 4**, the EU, especially France, is a net producer of Hafnium despite being considered a critical material. Table 2 presents the worldwide Hf producers.

The similarities between the two materials are numerous. Among them, the atomic radii of Zr and Hf are 1.45 and 1.44 Å, respectively, while the radii of the ions are Zr^{4+}, 0.74 Å, and Hf^{4+}, 0.75 Å. The virtual identity of atomic and ionic sizes,

resulting from the lanthanoid contraction, makes the chemical behaviour of these two elements more similar than for any other pair of elements known. Although the chemistry of Hafnium has been studied less than that of zirconium, the two are so identical that only minimal quantitative differences—for example, in solubilities and volatilities of compounds—would be expected in cases that have not been investigated.

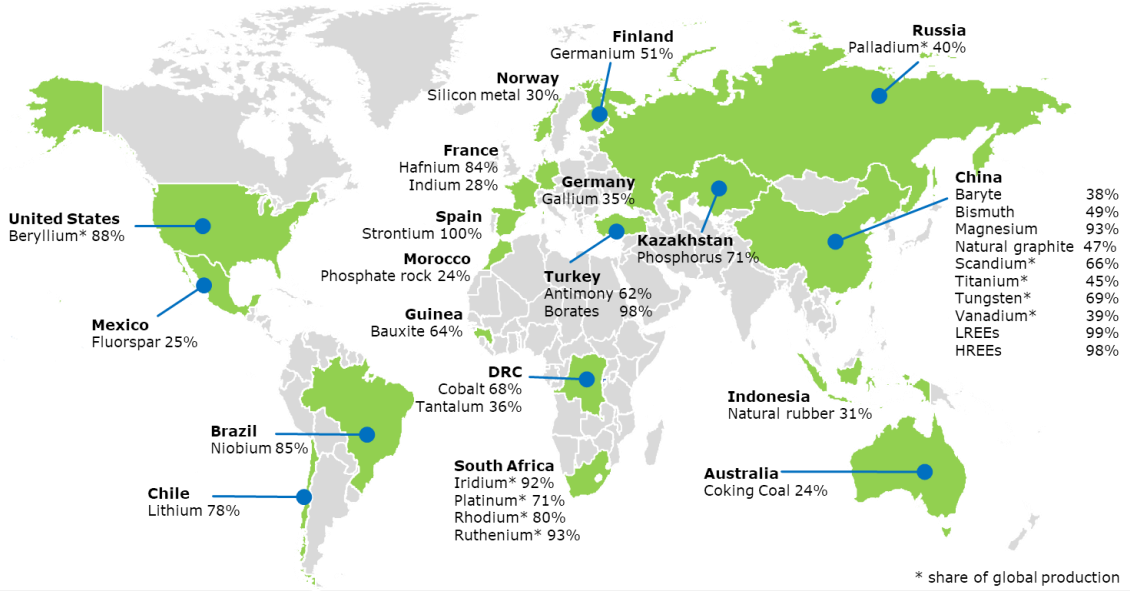

Figure 4 Biggest supplier countries of CRMs to the EU (11)

1.3.3 Mineralogy of zirconium and Hafnium

For a better understanding of the life cycles of both materials: Hf and Zr, we detail in this part the mineralogy of zirconium, mainly because they have the same process and coexist in the minerals with 0.5 – 4% Hf and since there is more available information about zirconium compared to Hf.

The heavy-minerals sand deposits are the primary source of ~ 97% of zircon (metal or compounds) worldwide. In contrast, the rest is recovered from direct igneous deposits like baddeleyite mining (Russia has the only commercially significant baddeleyite mining operation) [39].

Theoretically, zircon ($ZrSiO_4$) is composed of 67.22% zirconia and 32.78% silica, and it might contain Hafnium as a small percentage of 0.5 to 4%. Zircon with increased contents of up to 24 % Hf is called **Alvites** in mineralogical terms. After mining the heavy mineral deposit, zircon is separated and commercialized as zircon sand, which is used directly in applications such as foundry sands (zirconia) or retreated again to obtain Zr chemical compounds or metallic zirconium.

Zirconia exists in two forms: the natural form extracted from **Baddeleyite**, and the synthetic form obtained from zircon sand through fusion or chemical derivation process from zirconium oxychloride. Despite the low availability of natural zirconia, the demand from different sectors is significantly growing.

In the heavy mineral sands, zircon coexists with inclusions of other valuable minerals (e.g., titanium minerals; ilmenite and rutile, alumina-silicates, magnetite, iron, and tin) along with rare presences of elements such as uranium (U) and thorium (Th) in small quantities. Of course, the existing inclusions vary from one deposit to another; sometimes, zircon can be found as a by-product and sometimes as a co-product of titanium minerals production, or zircon is the main product and titanium minerals as co-products[33], [34], [39]. However, the production process of Zr and Ti is the same.

Several chemical decomposition-based process methods can extract zirconia from zircon sands. The concept of all methods is based on the isolation of zirconium compounds from residual impurities. All methods share the involvement of thermal, mechanical, or chemical treatments to decompose zircon. The results of zircon decomposition are afterwards treated by solubility differentiation. The apparent differences between all these methods are out of the scope of this study. Nevertheless, a reference list, studied by A.Manhique, of the essential methods is provided as follows [40]:

- Thermal dissociation
- Decomposition by fusion:
  - with sodium hydroxide
  - with sodium carbonate
  - with calcium oxide and magnesium oxide
  - with potassium fluorosilicate
  - with calcium carbonate (or lime)
- Chlorination
- Carbiding process

Other zirconia recovery methods:

a) Fusion with calcium sulphate
b) Mechanical zirconia processing
c) Hydrothermal decomposition
d) Anion-exchange process

As mentioned above, zirconia can be separated from **baddeleyite** mineral by:

a) Sulphate method
b) Oxychloride crystallization
c) Precipitation with Sulphur dioxide or sodium thiosulphate
d) Precipitation as phosphate
e) Purification as hydrated sulphate
f) Double fluorides procedure
g) Thermal decomposition of alkali chloro-zirconate
h) Sublimation of zirconium tetrafluoride
i) Mechanical processing
j) Sodium metaphosphate method

The main point in this part is to understand how the Hafnium is separated from zirconium to have both separately. Their separation passes through complex process methods. A liquid-liquid countercurrent-extraction procedure accomplishes it. Crude zirconium tetrachloride is dissolved in an aqueous solution of ammonium thiocyanate, and methyl isobutyl ketone is passed countercurrent to the aqueous mixture, with the result that the hafnium tetrachloride is preferentially extracted. The metal is prepared by magnesium reduction of hafnium tetrachloride (Kroll process, the same used for Ti) and by the thermal decomposition of tetraiodide known as the De Boer–van Arkel process.

So, zirconium and Hafnium are separated by one of the methods:

- Fluoride salt crystallization
- Methyl isobutyl ketone extraction
- Tributyl phosphate extraction
- Extractive distillation

The following procedures can achieve the metal reduction:

- Kroll process
- Sodium reduction zirconium tetrachloride
- Potassium hexafluoro-zirconate reduction with calcium metal
- Calcium or magnesium reduction
- Electrolysis

A summary of the mineralogy methods mentioned above is presented in **Figure 5**.

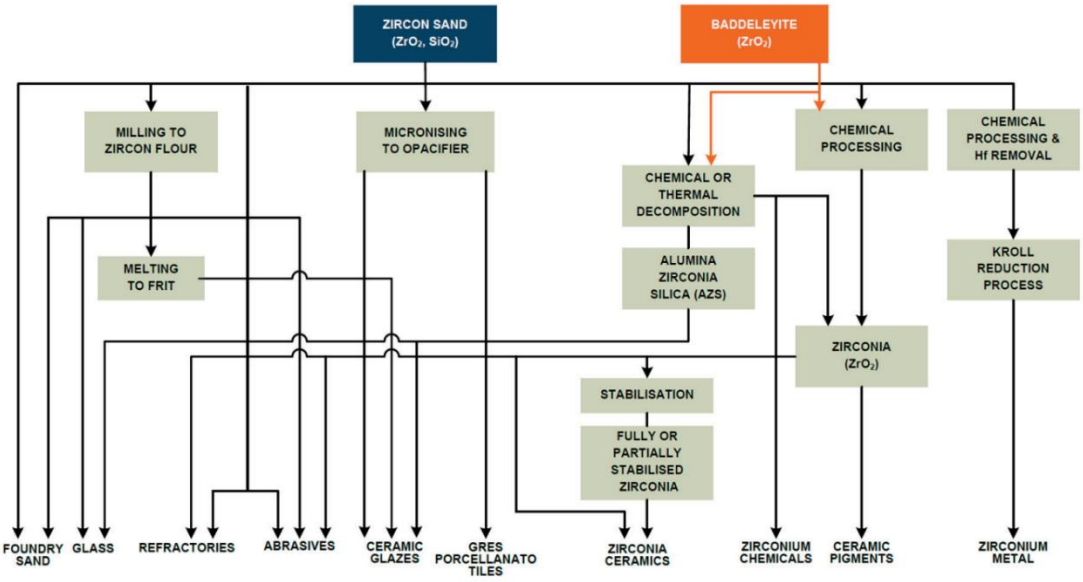

Figure 5 Schematic structure of the zircon industry, from TZMI (14)

1.3.4 The Hf-Zr coproduction

We do not need individual mines for every element in the periodic table. As many critical materials are jointly produced with other materials [41], Hafnium and zirconium are co-produced together. For example, having 1 ton of Hafnium is accompanied by the production (or disposal) of 50 tons of zirconium. The coproduction of different materials from a single resource provides environmental and economic benefits. To present, no one has ever dug a mine of Hafnium only. However, as a by-product, a possible alternative global source of Hafnium is being explored, such as Dubbo Project in Australia [42]. Coproduction is somewhat related to market size: large-market materials such as iron tend to be obtained from dedicated mines; in contrast, small-market materials may not justify the capital expenditure associated with establishing a dedicated facility (the case of Zr-Hf).

While the production ratios of different elements in a resource are more or less fixed, the proportions of their market demand are variable. A significant use for Hafnium, for example, is for neutron absorbers in nuclear reactors, which also use zirconium (purified to remove the Hafnium) in fuel cladding materials, which must be both corrosion resistant and neutron transparent. The demand for the two materials rises and falls in parallel, along with the fortunes of the nuclear industry. In 2008, A new use for Hafnium emerged when the length scales of individual devices in integrated circuits shrank below 45 nm. The design of these circuits called for a new gate oxide material with a higher dielectric constant than the existing industry standard, SiO_2,

and a variety of hafnia and hafnia-silica compositions emerged to meet the need generating new rise for the hafnium market and shifting balance of order toward Hafnium. Besides the recent discovery of ferroelectricity within doped hafnia, a further rise is predicted due to their integration in ferroelectric memories, lead-free piezoelectrics for IoT devices, in-computing memory, and artificial intelligence applications. Again, Hafnium and zirconium mixture is the most promising materials for the latter applications.

Soon after the microelectronics industry adopted Hafnium in its products, the nuclear industry was impacted by public reaction to the Fukushima power plant disaster of 2011 [43]. Many countries moved sharply away from relying on atomic energy, resulting in a slump in demand for zirconium, which impacted the production of Hafnium because the balance of production could not change to accommodate the shifting balance of an order. As a result, the price of Hafnium doubled between 2014 and 2015 (500 to 1000 $/kg) [44]. Hf and Zr are pretty related in the similarity of properties and the international markets. However, compared to PZT, the market of Hf-Zr presents a weak point due to the dependence on the two materials, while the PZT market is a result of three independent markets.

1.3.5 Worldwide production, reserves, and markets

As Zr is produced with a higher ratio than Hf, more information is available since both markets are strongly related. However, analyzing the market of Zr leads to the same conclusions about Hafnium, so we are focusing mainly on Zr as it is part of both HZO and PZT. Here is the current production and reserves by Zr producing country. Based on data collected from USGS (US geological survey) for years from 2010 to 2016 [45] as shown in **Figure 6**. **Table 2** presents a breakdown of zirconium mine production (in thousand metric tons of zirconium concentrate) and reserves by the producing countries.

Worldwide production of zirconium concentrates in 2014 was estimated to be accounted for 1.54 million metric tons, lower than 2011 production of 1.62 million metric tons but higher than 2010 and 2012 production. Therefore, in addition to the production and reserve figures shown in **Table 2**, the discovered zirconium world resources in 2014 (i.e. material that is potentially valuable and has reasonable prospects for eventual economic extraction) have been estimated to be around 78 million metric tons [33], distributed mainly among Australia (65%), South Africa (18%) and India (4%).

An important economic indicator to focus on is the market dynamics and behaviour. For the Zr case, zircon sand production has historically experienced different periods of shortage and over-supply accompanied by price volatility (1950 and 1981). This is a normal phenomenon if we consider that zircon is typically extracted as a by-product or co-product of mineral sands mining, as explained above, which indicates that its production tends to be impacted not only by its direct demand but also by the demand for other minerals contained in heavy mineral sands such as rutile or ilmenite [33]. An illustrative example of this occurred in 1981, when an economic recession and cutbacks in rutile and ilmenite production caused a shortage of zircon, or when strong demand for those minerals in the late 1950s generated an oversupply of zircon [34]. A future disruption can be estimated since there is an increasing interest in integrating these materials in ferroelectric memories and IoT applications. With the actual crisis of the Covid-19 epidemy, penury touched the semiconductors sector severely [46]. Unfortunately, we could not have access to in-real time information about the Hf-Zr to evaluate the impact of Covid-19.

The economics of mineral mining projects are typically evaluated through a unit cash cost measure, which considers the valuable mineral's grade, the project's scale, mining method, and associated costs [47]. Mineral sand mines exploit more than one mineral (ilmenite, rutile, zircon). Therefore the assemblage of the deposit needs to be considered when evaluating the revenue per ton characteristics [47]. This is performed by a revenue/cash cost ratio curve to assess the economic feasibility of deposits.

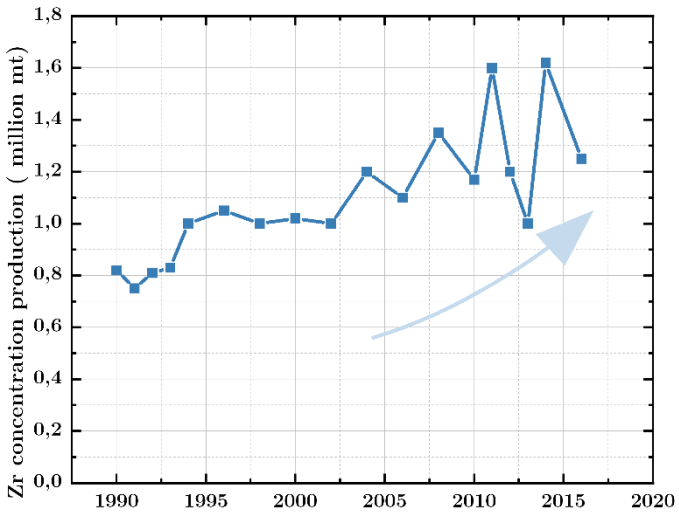

Figure 6 Zr concentrate production 1990-2016

In addition to the mixed production of minerals, geopolitical factors impact the production and consumption patterns. For example, the zircon production increase

observed after 2000 coincided with the considerable growth of Chinese demand for zircon sand.

Table 2 Worldwide Zr production 2010-2016 and its reserves

	Zr mine production ($*10^6$ kg)							Zr reserves ($*10^6$ kg of ZrO_2)
	2010	2011	2012	2013	2014	2015	2016	
Australia	540	762	610	850	900	601	450	51000
South Africa	381	383	400	170	170	330	360	14000
China	140	150	150	150	140	140	140	500
Indonesia	50	130	60	110	120	110	110	/
Mozambique	37	44	47	47	56	64	68	1100
India	38	39	40	41	40	40	40	3400
US	/	/	/	/	/	80	/	500
Other	84	110	109	140	110	150	157	7200
Total	1270	1620	1420	1510	1540	1520	1330	780000

1.3.6 Applications

Zirconium and Hafnium are metals used in various applications in chemical and nuclear reactors due to their properties of corrosion resistance, structural stability at high temperatures, specific alloying properties and specific neutron-absorption characteristics. In addition, their oxide form is used for microelectronics, especially in-memory applications, due to their excellent dielectric and ferroelectric properties.

As their chemical similarity, the applications of Hafnium and zirconium are almost similar, with some specific applications for each material.

The main applications of zirconium, in its all-different forms (metal, ceramics and oxide), can be summarized in the following points:

- The aerospace sector represents a significant part of Zr applications. For example, Zr ceramics offer diamond-like coating protection for jet turbines with high thermal resistivity and corrosion resistivity [48].
- Even for biomedical applications, Zr can be inserted in implants, replacing metals [49].
- For microelectronics, mobile phones and signal towers incorporate signal amplifiers containing zirconium to boost signal strength and clarity [50].
- In nuclear applications, hafnium-free zirconium metal has a low thermal neutron absorption. Therefore, it is used for structural materials in nuclear reactors and cladding for nuclear fuel rods [51].

- For renewable energies, hydrogen fuel cells are the application of Zr. It is used to produce green energy and can also be a part of hydrogen generation [52].

The main applications of Hafnium are pretty similar to zirconium, with few specific applications to Hf. However, here are some critical applications of Hafnium:

- In high-temperature turbines where Hf-based superalloys are used in jet engines and gas turbines for energy generation, they have high strength and stability when operating at very high temperatures. This accounts for nearly 60% of current world hafnium demand [53].
- In the aerospace sector, as Zr, due to the thermal resistivity properties of Hf and its alloys. Also, Hf is found in the rocket engine nozzles for thermal shielding [54].
- In plastics, Hf is used as a catalyst for thermoplastics like polyethene (PE) and polypropylene (PP) [55].
- HfO_2 is used as a high-k dielectric within microchips for miniaturization and higher efficiency as a gate oxide in microelectronics. Besides, memory applications are the new trend for HfO_2 applications [56].
- Hafnium also exists in thermoelectric applications such as cooling [57].
- In nuclear, Hafnium has a relatively high thermal neutron absorption and thus is used in nuclear control rods [58].

The application of hafnium-zirconium mixture is, to this moment, used for its dielectric and ferroelectric properties only in academic research with published proof of concepts. In the next chapter, we detail the advent of this oxide mixture for new applications. Before the current trend, we could not find any direct application of hafnium zirconium oxide, but some papers studied its properties as a dielectric [59].

1.4 Sustainability in the sputtering method: The thin films deposition technique, does it include sustainability?

1.4.1 Sustainable approach for deposition technique selection

The involvement of the technological manufacturing sector is crucial for sustainable development since much energy and resources are consumed for

production in direct and indirect manners. Moreover, this sector is the backbone of modern economies since it represents an innovative and high employed sector. As a result of the continuing demand for sustainability vis-à-vis industrial manufacturing processes, this part focuses on a simple comparison between the deposition techniques used to obtain HZO thin films on both research and industrial scales. As a central part of the device fabrication, even the deposition of thin films step can include sustainable-approach integration regarding the energy consumption, the waste, the environmental impact of chemical precursors processing for CVD techniques or the targets manufacturing for PVD techniques. Figure 9 presents the thin film deposition step within the device manufacturing process.

Figure 7 shows the principal deposition techniques of thin films [60]. There are three major deposition principles: Physical Vapor deposition (PVD), Chemical Vapor Deposition (CVD), and Solution-based Deposition (SBD). Each of the three principles has various techniques with slight differences between them. Generally, the choice of the deposition technique depends on the application and the desired properties of the films besides their quality. Nowadays, the sustainability criterion has been added by industrial manufacturers to promote their environment-friendly image to their consumers and also answer the legal limitations (in the framework of RoHS and REACH [61]) besides the current trend of the carbon neutrality of companies.

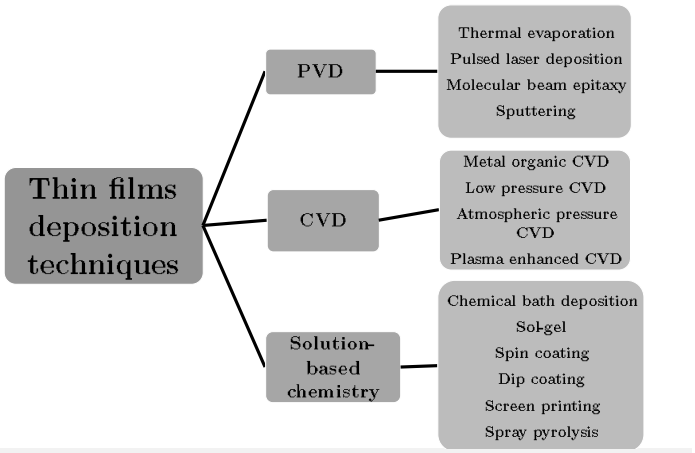

Figure 7 different thin films deposition techniques

Since 2009, The EU has recognized the equipment as an energy-consuming product [29] with a high improvement potential regarding energy efficiency. For the deposition of HZO thin films, most scientific research groups focus on the ALD (Atomic Layer Deposition) for many reasons, as explained in chapter II.

Briefly, ALD is a sub-set of CVD. ALD covers all deposition techniques in which the deposition depends on some chemical reaction by layer by alternatively pulsing the source gases. Most ALD reactions use two chemicals called precursors or reactants. ALD has many advents, such as high conformal quality deposited films, but it also has several disadvantages. Three major disadvantages, among others, are presented in the following points:

1. Before finding the favorable conditions for films' growth, various pre-deposition essays are required. This can lead to increasing the costs of the process. Besides, there may be a requirement to remove excess precursors at the end of the deposition.
2. The precursors must be volatile, which increases the complexity and costs of precursors manufacturing.
3. Despite the high uniformity and low roughness of the obtained films, the low deposition rate causes relatively higher energy consumption than the other techniques.

In this work, the sputtering deposition technique has been chosen over ALD for technical and sustainable reasons. The technical differences between the two methods are discussed in **Chapters II and III**.

We preferred the sputtering technique in sustainable terms, but it does not have any chemical processing during the target manufacturing or the film's deposition. At the lab scale, the difference can be neglected; nevertheless, at an industrial level, the economies of scale principle are inversed; the higher number of fabricated devices, the higher the demand for ALD precursors, which leads to more considerable chemical waste and higher impact on the environment.

Despite the importance of an ecological or sustainable evaluation of the deposition techniques, we could not find enough literature studies about it. Only F. Klocke et al.[62] compared PVD and CVD systems for coating applications (coatings are considered thin films). PVD and CVD are regarded as general deposition principles. From our point of view, it is challenging to compare two complex deposition systems, for example, sputtering and atomic layer deposition, due to the multiple existing systems for both techniques; each piece of equipment has its geometry and energy requirements. This makes the sustainable comparison impossible as the conclusions cannot be generalized. Though, comparing PVD and CVD systems can be sufficient.

The Life Cycle Assessment (LCA) is one of the most used methodologies to study both methods and have resilient conclusions about sustainable performance. In the narrow sense, Life Cycle Assessments cover the entire Life Cycle of a device, including raw materials production, manufacturing, use, and recycling. The LCA concept is also called the cradle-to-gate point of view, which considers mineralogy, processing, and manufacturing of raw materials. Its results can be merged with results obtained for the use and disposal phases to achieve a full Life Cycle Assessment. For his study, F. Klocke concluded that PVD systems are less consume gases and less electrical energy than CVD, as shown in **Figure.11**. The same conclusions cannot be extended to technical performance. **Figure.11** shows that the investigated PVD process generally requires less electrical power and effort for the gases during the deposition. Especially for the smaller systems, this conclusion can be observed as the impact of the substrate material is not as dominant as in the manufacturing of the oversized insert.

Additionally, their results confirm that the influence of the process gases is neglectable mainly, especially for the PVD process. Precursors have the most critical impact during the high-temperature CVD process. Besides, CVD can be preferred in the case of complex geometries. Otherwise, PVD is chosen.

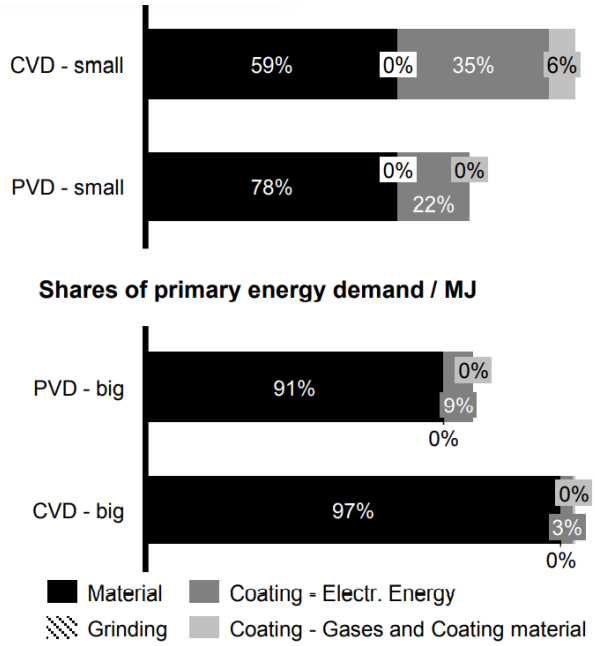

Figure 8 PVD vs CVD coating process (small and big insert)

1.4.2 Sputtering target manufacturing

Sputtering is one of the techniques for depositing such thin films in which atoms are ejected from a source material, sputtering target, using energetic particles inside a chamber. Most solid materials can be sputtered under suitable conditions to form thin films. A sputtering target can be a conductor, semiconductor, or insulator. Conductivity is one of the critical parameters that contrast these three solids.

With the development in microelectronics, sputtering found a crucial place in solid-state device manufacturing. Slowly sputtering started to replace evaporation because of the coming of DC magnetron. Unlike evaporation, a single alloy target was used for sputtering. Besides, these sputtered films retained stoichiometry. Moreover, other aspects such as purity, microstructure, resistivity, and surface roughness of the films were satisfactory.

Also, it was possible to scale up magnetron size and sputtering target size with technological growth requirements.

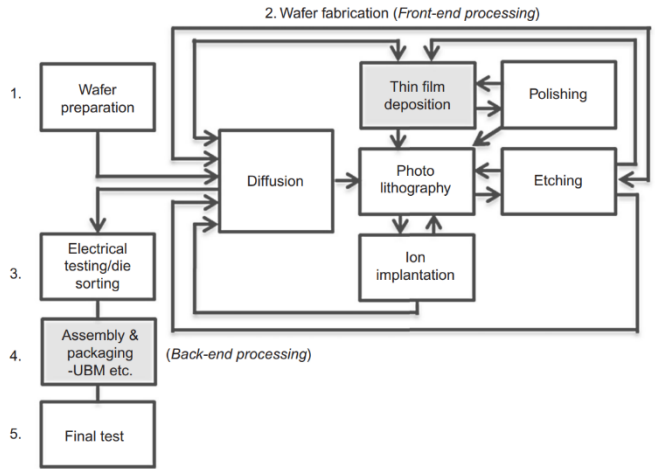

Figure 9 chip manufacturing flow chart and unit processes involved in wafer fabrication

Figure 9 shows a chip manufacturing flow chart and unit processes involved in wafer fabrication [63].

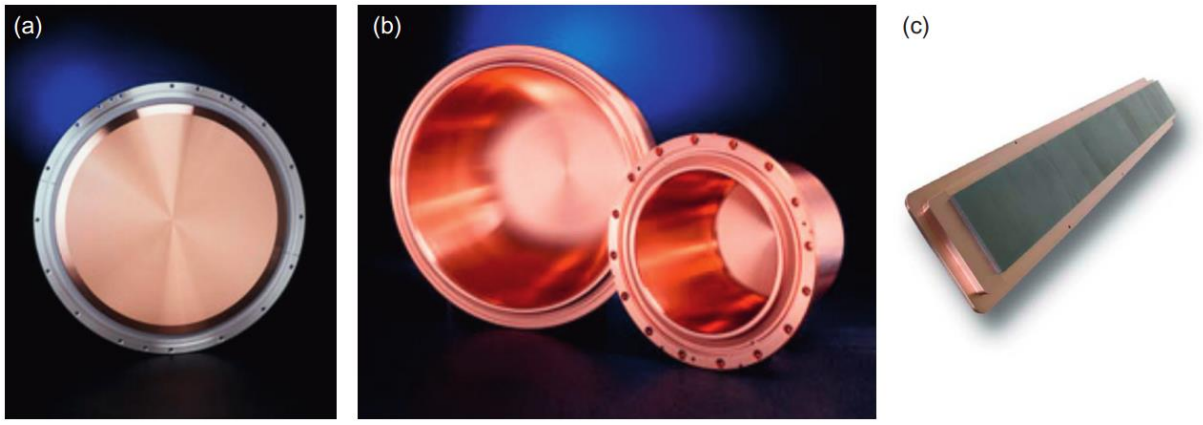

Figure 10 Examples of sputtering targets of various shapes and sizes

Figure 10 shows examples of sputtering targets of various shapes and sizes used for different applications. These are a disc-shaped bonded sputter target, a dome-shaped hollow cathode magnetron target, and a rectangular target [64].

There is a whole industry of sputtering targets. Leading manufacturers of sputtering materials and evaporation sources are based in the United States, Germany, Japan, Korea, and China. Examples: Praxair, Nikko, Materion. Various data indicate that the physical vapor deposition market was at $871 million in 2001, $1.8 billion in 2006, and $2.8 billion in 2007. Furthermore, it was projected that the value of the market would increase to $5.9 billion in 2012. These numbers included materials, equipment, and services [64].
In recent years, Asian countries such as Taiwan, S. Korea, and China have seen tremendous growth in the semiconductor, display, and photovoltaic industries. As a result, target manufacturers who originally served the semiconductor industry have also been trying to get market shares in these industries. It is believed that target material consumption will rise slower than sputtered films because of the efficient use of target and thinner films for specific devices [65].

It is expected that the demand for materials such as copper, titanium, tantalum, aluminum, tungsten-titanium, nickel-vanadium, and hafnium/zirconium will increase. Target manufacturers with access to inexpensive raw materials, efficient supply chains, low manufacturing costs, and satisfactory quality control will dominate these new markets. Other factors that would determine profitability are the affordable recycling capability of spent targets and bonding technology for large cylindrical targets. In addition, material innovation for technologies such as barriers

for 15 nm or smaller technology nodes in semiconductors, light-emitting diodes (LED), micro-electromechanical systems (MEMs), and various sensors will also drive the growth of the sputtering industry market.

For a sputtering target, two factors are essential: The performance of a sputtering target, which is the ability of a sputtering target to deposit film with desired properties in a consistent manner under a given set of process parameters, and secondly, the productivity, which refers to the number of processed wafers with selected film properties.

The performance of sputtering targets usually depends on the following factors when sputtering chamber operation and maintenance schedules pose no problems:

- Chemical characteristics of the sputtering material (purity and composition)
- Metallurgical characteristics of the sputtered material (e.g., grain size, second phases, defects such as porosity and inclusion, crystallographic texture and their distribution in the plane and along with the thickness of the target) and the interfaces with the backing plate [64].

Most sputtering materials for semiconductor applications are high purity metals or alloys. Some of these materials are sputtered in reactive mode in the presence of a specific gas to form nitride or oxide. For most semiconductor applications, the purity of sputtering materials varies between 99.99% and 99.9999%. Starting from raw materials, special attention is paid to controlling the limits of those impurity elements that strongly influence sputtering performance and film properties. In addition, most sputtering target manufacturers conduct their chemical analyses of incoming materials to check the chemistry of the procured materials.

The same approach applies to alloys, i.e., controlling composition is essential, and control limits are set for alloying and impurity elements.
In most cases, metallurgy processes are vulnerable to contamination, and often sources of contamination are unclean containers and grinding media used in powder metallurgy. The composition of a powder metallurgy product may also vary locally because of the inadequate mixing of powders and consequently incomplete chemical reactions between the elements.

The thickness of the sputtering target varies widely depending on the application and sputtering chamber. The thickness of non-magnetic targets can reach a maximum of 25 mm, while their life can be up to several thousand kWh. For semiconductor applications, the use of the non-magnetic sputtering target materials typically varies between 30% and 45%. In the case of large rectangular and cylindrical targets, service can be significantly high (up to 80%) [64].

Figure.9 shows a generic flow chart for manufacturing a sputtering target [64]. These unit steps can be placed in different orders or repeated to produce the desired target. The entire review process and target manufacturing can take several months for an advanced application. Because of the globalization of the supply chain for raw materials and services, to control cost structure, a sputtering target supplier may produce such targets in one part of the world and supply to customers in another part of the world. In addition to low-cost manufacturing, there are scopes for target suppliers to diversify their product portfolio and gain alarger market share for greater profitability.

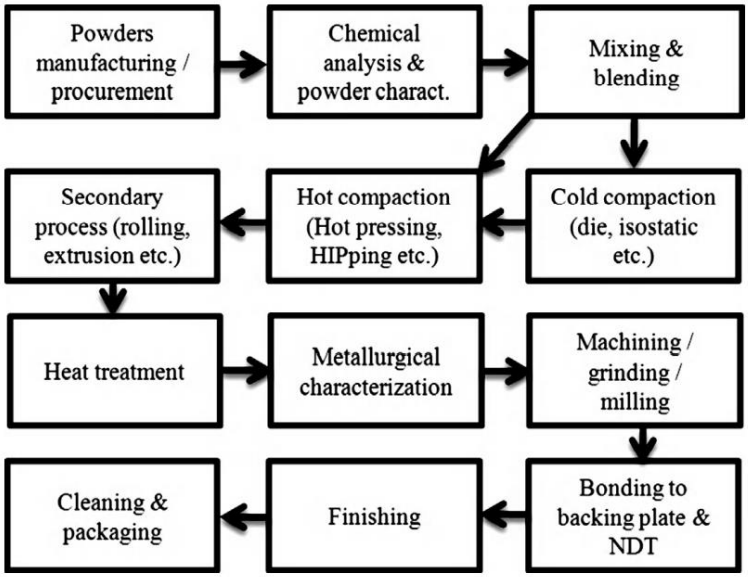

Figure 11 a generic flow chart for the manufacturing of a sputtering target

1.4.3 Comparison between HZO and PZT

To replace any material, the most crucial criterion is technical performance. Then, the adequation with the legal regulations and sustainably criteria. For PZT, many lead-free alternatives have been studied, but still, PZT is technically better

for piezoelectric applications. Despite that, PZT has a scaling limit and incompatibility with the CMOS process beyond the 130-nm-node (51). This scaling limit allowed hafnia-based ferroelectrics for next-generation technology beyond the 130 nm node. To our knowledge, neither HZO nor HfO_2 ferroelectrics have been elaborated at 130 nm, which makes the comparison quite difficult with PZT. This can be explained by the fact that the research aims not to find a lead-free alternative of PZT for the same technology node but to keep the progress rate for enhanced technology nodes while respecting the sustainability goals, which is the case for hafnia ferroelectrics, fortunately.

Unfortunately, due to the unavailability of the sputter equipment and Covid-19 during this thesis, we could not conduct a comparative study of HZO and PZT deposited at the same sputter chamber to compare the energy consumption, the sputtering target evaluation, the suitable electrodes, the functional thickness, and the technical performance and costs of the final devices.
Two studies could compare HZO and PZT for the same application in the literature: (52,53). The comparative studies were mainly technical. The main conclusion of both studies is that hafnia ferroelectrics represent the future generation of technology with its ad-equation with the sustainability goals. PZT is still an excellent performant material but inadequate with the future technology nodes and sustainability criteria. **Table 3** summarizes the main points of comparison for ferroelectric memory applications.

Table 3 Comparison of hafnia and PZT-based ferroelectrics for future non-volatile FRAM applications

	Characteristics	PZT	Ferroelectric HfO_2 (HZO)
Process	Deposition technique	Sol-gel	ALD/PVD
	Film thickness	Thicker than 70 nm	1 – 40 nm
	Doping	/	Less than 20 % (50%)
	Annealing temperature	Above 600 °C	400 – 1000°C
	CMOS compatibility	Pb and O_2 diffusion	Full and stable
	BEOL compatibility	H_2 damage	Full and stable
Electrical properties	Remanent polarization ($\mu C.cm^{-2}$)	20-40	1 – 52 (64)
	Coercive field	Around 50 kV/cm	1 – 2 MV/cm
	Breakdown field	0.5 – 2 MV/cm	4 – 8 MV/cm
	Dielectric constant	Around 1300	Around 37
	E for wake-up (eV)	0.6-0.9	0.32
	Endurance	10^4	10^7
Sustainability	Electrodes	Pt	TiN
	Toxicity	X	✓
	Costs	Low	High but reducing
	Prohibition regulations	✓	X

1.5 Conclusion

As sustainability in microelectronics is emerging. The fundamentals of comparison tools for materials selection based on sustainability are not yet created since the definitions of sustainability and criticality are broad, especially for the microelectronics industry.

For this work, sustainability was integrated within the material's selection and the deposition technique, despite it being quite complex to evaluate the sustainability degree for the deposition technique and especially at the materials' level. The latter contains a whole life cycle, including different steps of mining, waste generation, and manufacturing to the expired end device. Access to information about the life cycle of materials is not available. For HZO material, it has excellent properties for ultrathin films. It is a crucial enabler for the next generation of memories. However, the future focus must consider the criticality of Zr and Hf and the possible rebound effects of both markets due to the increasing demand for the two materials.

We cannot classify the deposition techniques or machines as sustainable, but preferring methods with less waste during the process or even at fabrication of precursors or targets besides the energy consumption level can be a good approach. Future studies are expected to provide a more detailed comparison highlighting the sustainable advantages of HZO as a lead-free alternative to PZT.

2 Chapter II Fundamentals of ferroelectricity and the literature review

2.1 Introduction 33

2.2 Fundamentals of ferroelectricity, pyroelectricity and piezoelectricity: 33
2.2.1 Crystal structure: 35

2.3 Phenomenology of ferroelectricity: 37

2.4 The main effects affecting ferroelectricity: 45
2.4.1 Retention 45
2.4.2 Wake-up effect 45
2.4.3 Ageing 46
2.4.4 Fatigue 47
2.4.5 Imprint 48

2.5 HZO review: the state-of-the-art 49
2.5.1 From 2005 to 2011 49
2.5.2 From 2011 to now 55

2.1 Introduction

This chapter indicates the main definitions of some smart dielectrics, such as ferroelectrics, pyroelectrics, and piezoelectrics. We start with the general descriptions of the physical phenomena behind these properties. Then, we focus on the phenomenology of ferroelectricity and the main theories that explain it for bulk and thin films ferroelectric materials. This chapter also introduces the main mechanisms to understand the must-have criteria within HZO films better.

The final part concerns the HZO-based ferroelectrics in the state-of-the-art, including the deposition techniques, electrodes, thermal annealing, the main breakthroughs, and the HZO-based possible applications.

2.2 Fundamentals of ferroelectricity, pyroelectricity, and piezoelectricity:

In present-day microelectronics devices, dielectrics attracted particular interest, especially by having good insulating properties, including very low electrical conductivity and high electrical strength that allow energy conversion or information conversion. The dielectrics with these properties can be named or considered smart or active dielectric materials. These materials dynamically respond to external factors such as mechanical stress, temperature, electrical field, and light. Smart dielectrics are categorized as piezoelectrics, pyroelectrics, ferroelectrics, electrets, microwave dielectrics with tunable permittivity, etc.

2.2.1 Dielectrics

In a dielectric, the atoms are considered ionized to a certain degree and charged positively or negatively. When an external electric field is applied, cations and anions are attracted to the cathode and the anode, respectively, due to the electrostatic interaction. The electron clouds also deform, causing the appearance of induced electric dipoles. This phenomenon is defined as **the electric polarization P**. For all dielectrics, this electrical polarization is their key characteristic. There are three primary contributions: related electronic, ionic, and dipole reorientation. The degree to which each mechanism contributes to the overall polarization of the material depends on the frequency of the applied field.

Table 4 Comparison of electric polarization response to external influences between polar and non-polar dielectrics

External factors	Type	Non-polar dielectrics	Polar dielectrics
Temperature	Scalar	/	$\partial P = \gamma \partial T (\text{pyro})$ $\partial P = \xi \partial T (\text{piezo})$
Electric field	Vector – 1st order tensor	$P = \varepsilon_0 \varepsilon_r E$	$P = \varepsilon \chi E + \left(\frac{e^2}{c}\right) E + \frac{(\gamma^2 T) E}{\varepsilon C}$ $(pyro)$ $P = \varepsilon \chi E + \left(\frac{e^2}{c}\right) E$ $(piezo)$
Mechanical stress	2nd order tensor	/	$P = d' X$ $(pyro)$ $P = dX$ $(piezo)$

One unique, uncommon feature of smart dielectrics is that their electrical polarization can be induced by external factors of different types, such as the temperature (scalar), the electric field (vector), or the mechanical stress (2nd order tensor). **Table 4** compares the nature of the external factors between polar and non-polar dielectrics.

The smart dielectrics execute different functions. **Piezoelectrics** convert mechanical energy into electrical energy, this is the direct piezoelectric effect and conversely, the indirect piezoelectric effect converts electrical energy into mechanical energy. **Pyroelectrics** convert heat into electricity. Ferroelectrics exhibit spontaneous polarization that an external field can reverse. These smart dielectrics can be multifunctional and allow the development of new solutions for microelectronics devices for sensing, actuating, or memory applications. The Heckmann diagram, in **Figure 12**, illustrates the most known effects observed and integrated into devices that are externally impacted.

The crystalline geometry and the symmetry determine whether the dielectric is polar or non-polar. In this work, we are interested in dielectrics with polar properties, i.e., ferroelectrics, which can be summarized in the asymmetry of the structure and that the centers of mass of positive and negative charges do not coincide. This interest is motivated by the desire to integrate HZO films into several devices due to their dielectric, ferroelectric, and piezoelectric properties. **Table 4** mentions an example of P response

as a function of the different external factors between polar and non-polar dielectrics. Smart dielectrics can be easily distinguished from non-polar dielectrics.

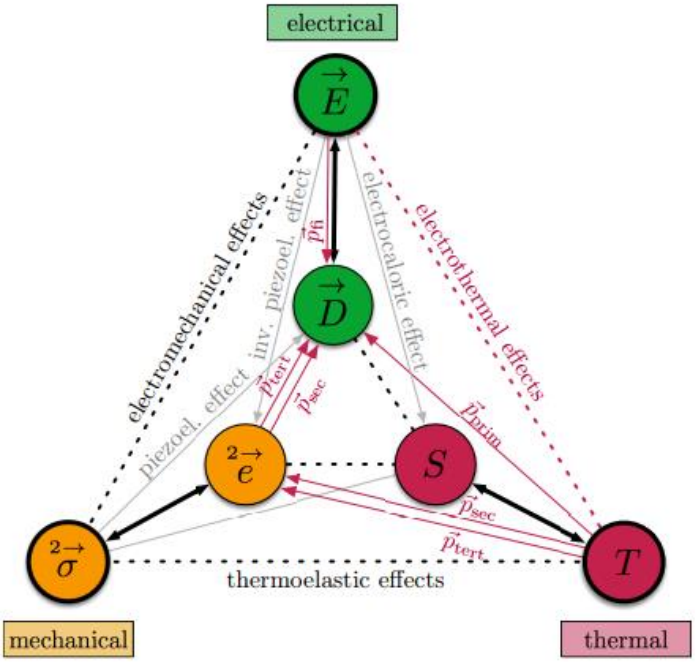

Figure 12 The Heckmann diagram describing direct and cross-coupling phenomena between thermal, electrical, and mechanical state variables. For the sake of clarity, the magnetic properties are omitted [66].

2.2.2 Crystal structure

All materials undertake a slight change in dimension when an external electric field is applied or any external mechanical or thermal forces. Any change in the dimension of these materials might cause a change in the electric polarization. This depends on the material structure. Henceforth, it can be one of the following properties: ferroelectric, pyroelectric, or piezoelectric. These three categories rely on the material's structure, so they must be polar materials of a particular order: crystals or polycrystalline. The position of the constituent atoms of a crystal structure lattice determines if the crystalline material belongs to ferroelectrics, pyroelectrics or piezoelectrics.

The crystalline materials can be categorized as a function of their symmetry and based on their elements of translational position and orientation, 230 space groups are found. If the translational repetition is ignored, the 230-space group is reduced to only 32 classes based on orientation [67]. Any class or point group can be distinguished by its coordinates

(x, y, z) regarding the origin of symmetry. Two major categories are identified: centrosymmetric and non-centrosymmetric.

A centrosymmetric crystal or class represents a crystal with a center of symmetry, for which any movement of any point (x, y, z) to a new one (-x, -y, -z) does not cause a recognizable change. This means that all centrosymmetric crystals or classes are non-polar as the existing symmetry transformation may invert any polar vector, so there is no finite polarization or dipole moment. On the other side, non-centrosymmetric crystals possess no center of symmetry.

Among the reduced 32 classes, 11 classes possess a center of symmetry (centrosymmetric), and the rest are non-centrosymmetric, possessing no center of symmetry (21 classes). The 32 classes are represented in **Table 5**, categorized by symmetry and piezoelectric properties. The piezoelectric properties were chosen as a criterion in this table as they include pyroelectrics and ferroelectrics within.

Among the 21 classes, 20 classes have positive and negative charges generated on the crystal surfaces when appropriate stress is applied. These materials are known as **piezoelectrics**. The exception group is 432, which does not possess piezoelectric properties.

Table 5 crystallographic classification of crystal materials

Crystals (32) with a symmetry system		Symmetric with a center of symmetry (11 groups)		Asymmetric with no center of symmetry (21 groups)				
Crystalline structure (point groups)	Cubic	$m3m$	$m3$	432	$\bar{4}3m$		23	
	Hexagonal	$6/mmm$	$6/m$	622	$\bar{6}m2$	$\bar{6}$	$6mm$	6
	Tetragonal	$4/mmm$	$4/m$	422	$\bar{4}2m$	$\bar{4}$	4	$4mm$
	Rhombohedral	$\bar{3}m$	$\bar{3}$	32	$3m$		3	
	Orthorhombic	mmm		222	$mm2$			
	Monoclinic	$2/m$		2	m			
	Triclinic	$\bar{1}$		1				

Ferroelectrics and pyroelectrics have the additional property that they involve the presence of spontaneous electric polarization. There are ten polar groups with a unique polar axis among the 21-point groups without an inversion center. This class of crystals may show a spontaneous polarization parallel to the polar axis. In pyroelectrics, a change in temperature of the crystal generates electric charges on the crystal surfaces,

corresponding to the change of spontaneous polarization due to its temperature dependence. Theoretically, if an electric field reverses the spontaneous polarization of any crystal among the ten pyroelectric crystals, it is ferroelectric (without exceeding the breakdown limit of the crystal). Experimentally, there is somehow an ambiguity in this definition. Applying an electric field on a pyroelectric material is necessary to ascertain the polarization reversal, i.e., the ferroelectricity. By definition, each ferroelectric material can be pyroelectric and piezoelectric, as illustrated in **Figure 13**.

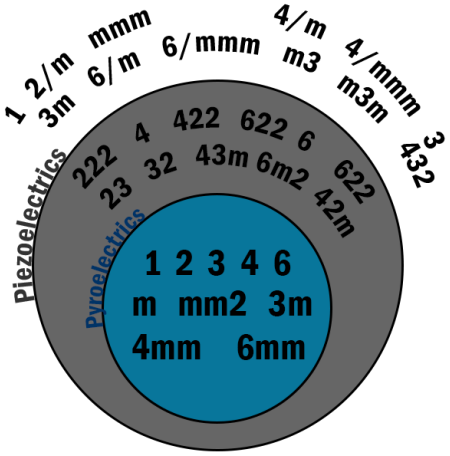

Figure 13 Dielectric, piezoelectric, pyroelectric, and ferroelectric crystal classes

2.3 Phenomenology of ferroelectricity

Thermodynamics is a branch of physics that deals with equilibrium, work, and temperature and their relation to energy, entropy, and the physical properties of matter. Its fundamentals and principles have been used to understand the many different phenomena, including ferroelectricity [68], [69].

One of the theories that explain ferroelectricity is the Landau theory. It describes the equilibrium of a system around a phase transition as the ferroelectricity can be defined by the non-polar to polar transition phase (paraelectric-ferroelectric). Its phenomenological approach shows the relationship between measurable quantities using a minimum set of input parameters that can be determined either, by comparison, to experiments or ab-initio calculations. The Landau theory can be a bridge between microscopic models and observed macroscopic phenomena. It has been successfully used to describe different properties or systems such as superconductors, ferromagnetic materials, or ferroelectrics. Linking several branches of physics is its central advent.

In the case of ferroelectrics, the Landau theory was enlarged and developed by Devonshire and Ginzburg [70], [71]. For example, $BaTiO_3$, the most known ferroelectric material, was discovered to be ferroelectric in 1945. During this period of time, because of the increasing interest in ferroelectrics inside the scientific community, Ginzburg developed and extended the Landau theory (ferroelectric mean-field theory) from a thermodynamics point of view to better understand the bulk and thin films ferroelectrics.

The Landau-Devonshire phenomenology theory is used, mostly, as a mean-field theory of the thermodynamic properties of bulk ferroelectrics. It is a case of the Landau theory with the Gibbs free energy representing the state function of the ferroelectric and the temperature, stress, and polarization as independent variables. In contrast, the Landau-Devonshire-Ginzburg (LGD) theory is dedicated mainly to thin films ferroelectrics by considering the size-finite effects and the spatial nonuniformity of polarization [72]. It represents a generalization of the Landau-Devonshire, in which the polarization is considered uniform.

The ferroelectric mean-field theory can be defined as the formation of two energetic minima because of a paraelectric-ferroelectric phase transition which means passing from a high temperature paraelectric non-polar phase to a polar phase at a lower temperature. This phase transition mainly depends on temperature.

For the sake of clarity, the Gibbs free energy G is defined as the maximum amount of work a system can do at a constant temperature and pressure [73], one of its forms is the following:

$$\mathbf{G = U + pV - TS} \qquad \mathbf{(2.1)}$$

U is the internal energy (J), p is the pressure (Pa), V is the volume, T is the temperature (K), and S is the entropy (J/K).

As mentioned above, the LGD is a function of the Gibbs energy. It directly shows the relationship between the Gibbs energy G and the displacement field D, which depends on the polarization P. The latter matters for ferroelectricity.

One of the main characteristics of ferroelectrics is the hysteresis loop, **Figure 14**, in which the polarization is a double-valued and nonlinear function of the applied electric field. This hysteretic nature of the polarization response differs from that of many dielectrics that exhibit a linear polarization-electric field relation, which is single-valued, as shown in **Figure 14**.

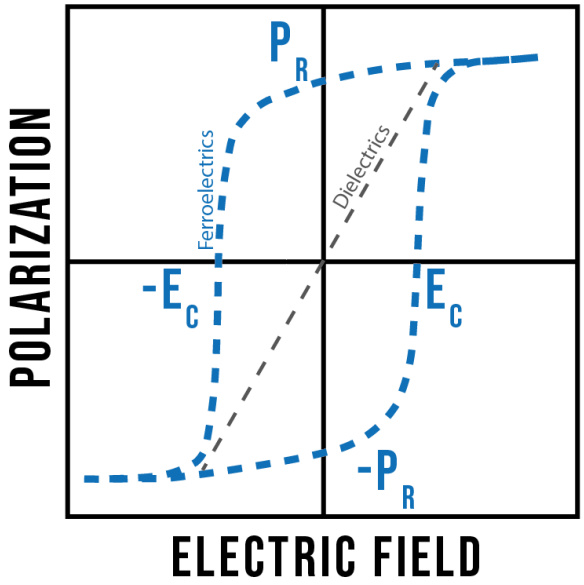

Figure 14 The characteristic hysteresis loop of ferroelectrics: Polarization as a function of electric field and linear response for non-ferroelectric dielectrics.

Also, ferroelectrics possess a spontaneous polarization without an external electric field, by definition, and an applied electric field can reorient its direction. The hysteresis loop of polarization indicates two states of polarization of opposite signs ($+P_r$ *and* $-P_r$). Both states are stable when $E_{ext} = 0$. Crystallographically, these two states of polarization represent two positions of ions inside the crystal lattice cell. Thermodynamically, both states are two energetic minima separated by an energy barrier. Consequently, a bi-directional movement is generated from a double-well curve of G as a function of the ion position, as is shown in **Figure 15** and **Figure 16**. This curve is often called the double-well potential curve.

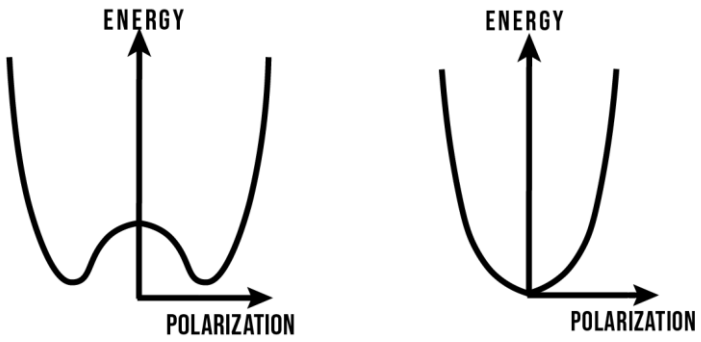

Figure 15 The Landau-Devonshire-Gibbs energy G as a function of polarization for a ferroelectric (left) and a paraelectric (right)

Figure 15 illustrates the Gibbs free energy as a function of the polarization P for two states of polarization of a ferroelectric (left) and a paraelectric effect (right).

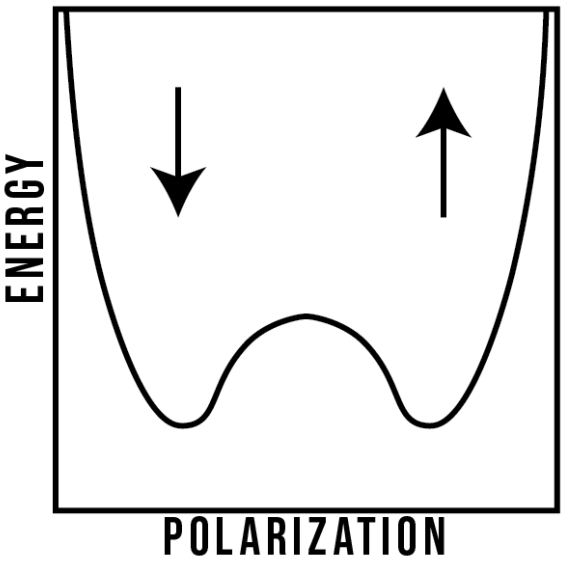

Figure 16 The Landau-Devonshire Gibbs energy showing the two spontaneous polarization states

For an ideal ferroelectric, the variation of the Gibbs free energy and the bi-directional movement between the two polarization states ($+P_r$ *and* $-P_r$) above the energy barrier, with the hysteresis loop under the applied electric field, is shown in **Figure 17**.

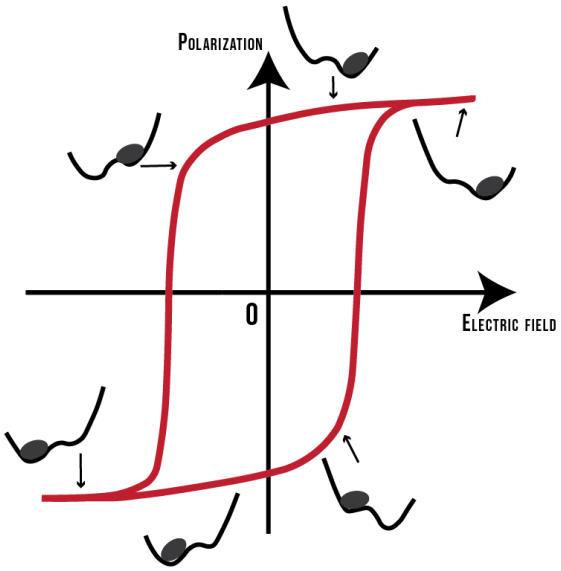

Figure 17 Scheme of hysteresis loop with Gibbs energy variation according to LGD for an ideal ferroelectric [74]

The value of the spontaneous polarization depends on temperature. It disappears above a specific temperature, called the Curie temperature, as shown in **Figure 18** and

Figure 19, depending on the transition phase order. Phenomena such as the Curie temperature and reduction in the spontaneous polarization are observed experimentally for thin ferroelectric films.

The G energy can be expanded in the Taylor series as a function of polarization (the order parameter) [70]:

$$\mathbf{G}=\frac{1}{2}\mathbf{c}_2\ \mathbf{P}^2+\frac{1}{4}\mathbf{c}_4\ \mathbf{P}^4+\frac{1}{6}\mathbf{c}_6\ \mathbf{P}^6\text{-}\mathbf{E.D} \qquad (2.2)$$

In this expression, the power series have been truncated at the sixth term due to symmetries between the two polarization states. The "-E.D" represents the contribution of the externally applied field (-E.P for a ferroelectric). The coefficients c_2, c_4 and c_6. For paraelectric, the coefficients c_4 and c_6 equal zero ($c_4 = c_6 = 0$). Both c_4 and c_6 are temperature-independent coefficients. This power series expression also represents the shape of the atomic potential for the switching ion(s). Instead of a harmonic oscillator, a sixth-order polynomial is applied to model the dielectric behavior. A positive E reduces G for a positive P, whereas a negative E favors negative P.

$$\boldsymbol{G = \frac{1}{2}c_2\ P^2 + \frac{1}{4}c_4\ P^4 + \frac{1}{6}c_6\ P^6 - E.P} \qquad (2.3)$$

The G energy is considered without the volume. In many references, $\mathcal{F}_G$ is called the total free energy considering the volume V; integrating G with volume would give the total free energy:

$$\boldsymbol{\mathcal{F}_G = \iiint \mathbf{G}\ \mathbf{dV}} \qquad (2.4)$$

For **(2.3)**, a stable state equals a minimum in G. It can be obtained by finding solutions for $\frac{dG}{dP} = 0$:

$$\frac{\partial \mathbf{G}}{\partial \mathbf{P}} = \mathbf{c_2\ P + c_4\ P^3 + c_6\ P^5 - E = 0} \qquad (2.5)$$

$$\mathbf{E = c_2\ P + c_4\ P^3 + c_6\ P^5} \qquad (2.6)$$

The condition that fulfills making this extremum the susceptibility and permittivity represent a minimum:

$$\frac{\partial^2 \mathbf{G}}{\partial \mathbf{P}^2} = (\boldsymbol{\varepsilon\chi})^{-1} \qquad (2.7)$$

$$\frac{\partial^2 \mathbf{G}}{\partial \mathbf{P}^2} = \boldsymbol{c_2\ + 3c_4\ P^2 + 5c_6\ P^4 > 0} \qquad (2.8)$$

At phase transition, $P = 0$ and the susceptibility are the inverses of the c_2 coefficient that depends on temperature.

$$\varepsilon\chi = \frac{1}{c_2} \quad (2.9)$$

$$c_2 = \frac{(T-T_0)}{C} \quad (2.10)$$

It is the Curie-Weiss law, reflecting the linear relationship of dependence of c_2 on T. C is the Curie-Weiss constant.

$$c_2(T) = c_2'.(T - T_0) \quad (2.11)$$

We replace c_2 with (2.11) in the equation (2.3):

$$G = \frac{1}{2}c_2'.(T - T_0).P^2 + \frac{1}{4}c_4 P^4 + \frac{1}{6}c_6 P^6 - E.P \quad (2.12)$$

This equation determines the transition phase order depending on the three coefficients. The c_6 is the coefficient of the highest order term in the equation, which must always be positive; otherwise, the Gibbs energy would be negative for positive polarization. The c_2 the coefficient is the inverse of the susceptibility. The two possibilities of c_4 define two orders of the transition phase paraelectric-ferroelectric.

$$\begin{cases} c_4 < 0\,, c_6 > 0 & \text{first-order phase transition} \\ c_4 > 0\,, c_6 \approx 0 & \text{second-order phase transition} \end{cases}$$

2.3.1 First-order phase transition

In this case, we assume that: $c_4 < 0\,, c_6 > 0$

A first-order phase transition is characterized by the existence of a sixth-order term in the Gibbs energy and the fact that T_C and T_0 do not coincide $(T_0 < T_C)$. **Figure 18** illustrates the curves of (a) dielectric constant and (b) polarization as a function of temperature for a first-order phase transition. The dielectric constant of a ferroelectric, with first-order phase transition, increases with temperature to its maximum at T_C. The phase transition occurs, and the dielectric constant drops abruptly. For the same increasing temperature, the polarization decreases until reaching T_C, at which P disappears: $P = 0$.

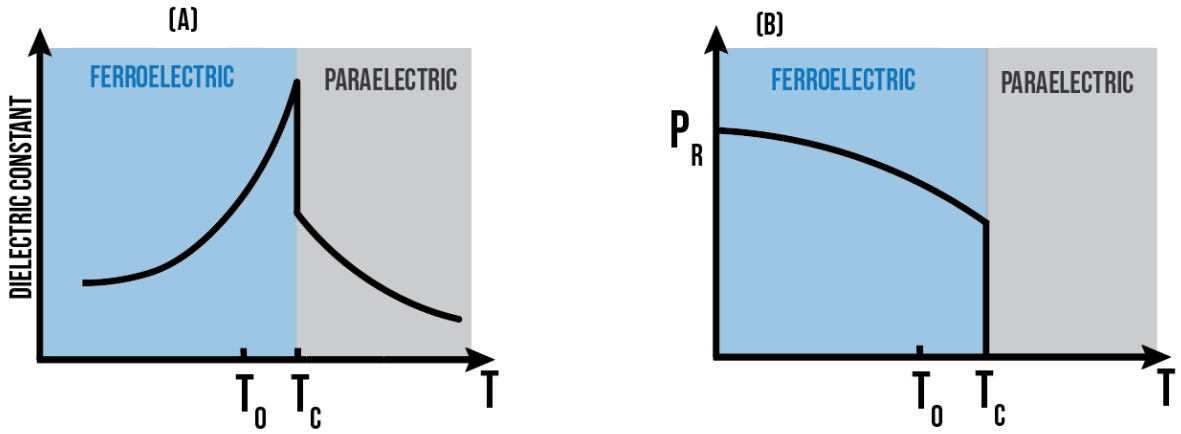

Figure 18 First-order phase transition (a) Remanent polarization as a function of temperature (b) dielectric constant

At zero field applied and with the first-order conditions of coefficients ($c_4 < 0, c_6 > 0$), the derivation of the equation is:

$$c_2 P + c_4 P^3 + c_6 P^5 = 0 \qquad (2.13)$$

The solutions are the following:

$$\begin{cases} P = 0 \ldots\ldots\ldots\ldots\ldots \text{for the paraelectric phase} \\ c_2 + c_4 P^2 + c_6 P^4 = 0 \ldots\ldots \text{for the ferroelectric phase} \end{cases}$$

The solution is

$$P^2 = \frac{-c_4 + \sqrt{c_4^2 - 4c_2c_6}}{2c_6} \qquad (2.14)$$

2.3.2 Second order phase transition

In this case, we assume that $c_4 > 0\,, c_6 \approx 0$

A second-order phase transition is known by the absence of the sixth order term and $T_0 = T_C$. **Figure 19** shows the evolution of (a) dielectric constant and (b) polarization as a function of temperature for a second-order phase transition. The dielectric constant of a ferroelectric, with second-order phase transition, increases with temperature, and it converges to infinity at T_0, at which the phase transition occurs. For the same increasing temperature, the polarization decreases to zero until reaching T_C or T_0, which are coincided, at which P reaches zero. Compared to a first-order phase transition, the dielectric constant and the polarization of a second-order phase transition ferroelectric are more reactive with temperature than those of a first-order phase transition ferroelectric.

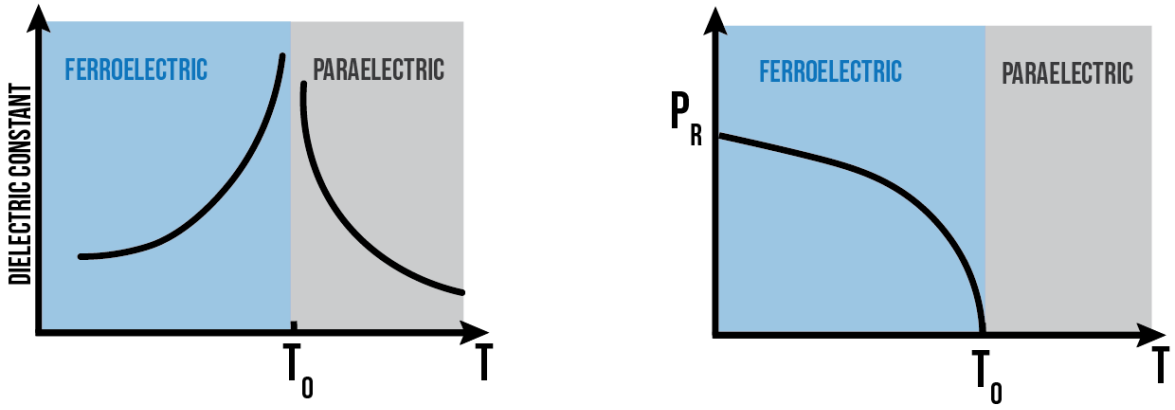

Figure 19 Second-order phase transition (a) Remanent polarization as a function of temperature (b) dielectric constant

With zero-field applied, and using the second-order conditions of coefficients ($c_4 > 0\,, c_6 \approx 0$) in the equation (2.13) the derivation is:

$$c_2 + c_4\,P^2 = 0 \qquad (2.15)$$

$$c_2'(T - T_0) + c_4\,P^2 = 0 \qquad (2.16)$$

It has two solutions.

$$\begin{cases} P = 0 \text{ for the paraelectric phase} \\ \text{and} \quad c_2'(T - T_0) + c_4\,P^2 = 0 \text{ for the ferroelectric phase} \end{cases}$$

For the second solution, the expression of P is the following:

$$P = \sqrt{\frac{c_2'}{c_4} T_0} \qquad (2.17)$$

The found solution is the decay equation for P as a function of T in **Figure 19**

This thermodynamic approach is an essay on the idealization of the complicated phase transition. It is based on ideal ferroelectric and simplified expressions. Despite that, the expression of energy in the polynomial Taylor series does fit with a real ferroelectric; it helps to understand the experimental observations. The nonlinear differential equations make the total understanding of the LGD. Some analytical solutions are represented in some reported models, such as Tilley and Zeks, who studied the phase transition of thin films and reported that the P could be expressed in terms of Jacobi elliptic functions [75], Ishibashi et al., who focused on thickness-dependent transition phase [76], and others.

For a deeper understanding, recently Ishibashi et al. proposed to recast the Landau-Ginzburg free energy in the same form as the Landau-Devonshire expression with a

redefined order parameter [77]. This new suggestion was called the effective Landau-Devonshire theory. This new theory can be used only to understand spontaneous polarization but not ferroelectric hysteresis.

2.4 The main effects affecting ferroelectricity:

In this part, we report the most investigated effects in ferroelectric thin films for a better understanding of the integration and commercialization challenges within ferroelectric memories mainly and other applications.

2.4.1 Retention

One important criterion of ferroelectrics for ferroelectric memories is retention. It describes the ability to retain the stored information over a long period of time without any power supply. A current commercial/industrial requirement is 10 years of data retention before the first readout failure.

This criterion is tested by an electrical test (Figure 21). The initial pulse is applied to write ON or OFF memory state; the readout is, afterward, achieved with an increasing logarithmic number of cycles. This test emulates a similar case of unpowered storage for real ferroelectric memory devices. The possibility of 10 years of storage can be verified either by extrapolating the experimental data or by temperature or bias acceleration tests [78].

2.4.2 Wake-up effect

One of the challenges to overcome in hafnia ferroelectric thin films is the wake-up effect. It represents the initial stage known as the de-aging stage for conventional ferroelectrics. It is described by the increase of remnant polarization against external field cycling forming a pinched hysteresis of the material at its pristine state. It can be explained by the depinning of ferroelectric domains by oxygen vacancies redistribution under field cycling [79], [80].

The pristine material often exhibits two or more distinct peaks in the transient current feature, which causes the pinched shape of $P - E$ curve.

During an increasing number of switching cycles at saturating field, these maxima move towards each other ending up merged into one single peak as Figure 20 illustrates.

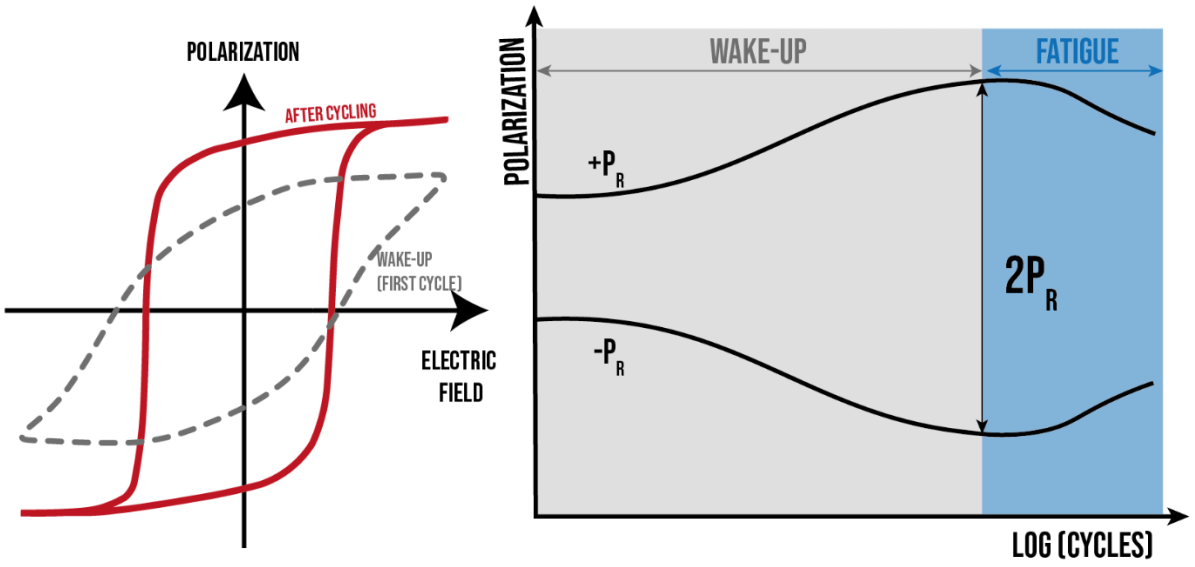

Figure 20 (Right) the variation of the polarization as a function of the applied cycles showing the wake-up effect (grey area) and the fatigue (Blue area) (left) the evolution of the hysteresis loop from pristine to cycled material.

2.4.3 Ageing

As the wake-up effect is termed "the de-ageing effect". Ageing occurs after. It is defined as the loss of polarizability of a ferroelectric because of being left in a polarized state. Consequently, the loss of switchable polarization with time in a poled ferroelectric thin film is called: ageing.

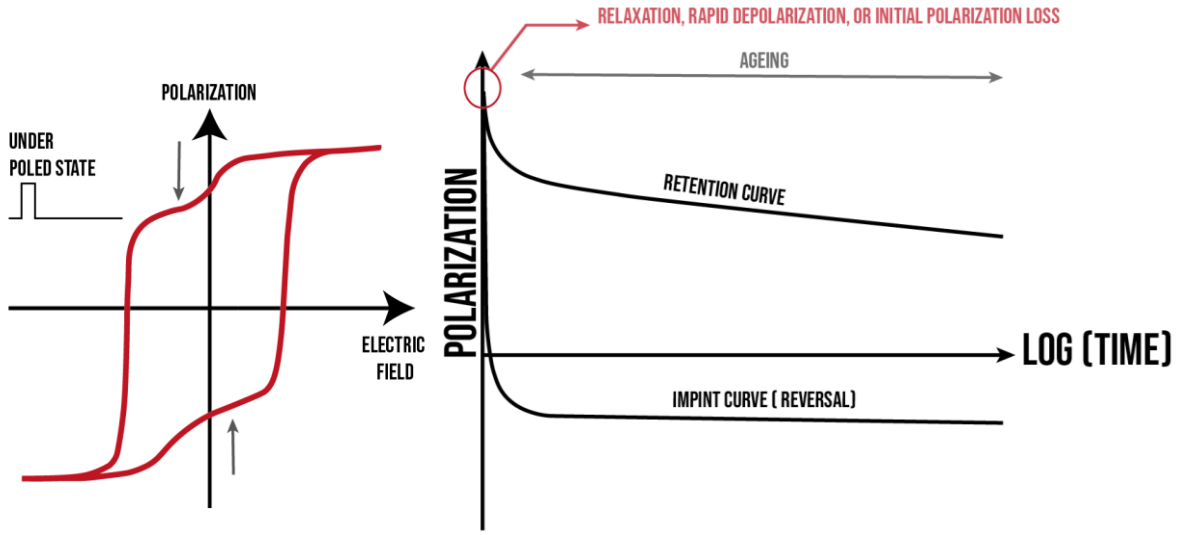

Figure 21 (Right) a generic retention curve showing the ageing for retention and imprint effects (Left) degraded hysteresis loop by ageing.

Figure 21 illustrates the trend of polarization during ageing with the contribution of leakage current. The remanent polarization of ferroelectrics decreases rapidly in the initial stages. This may be attributed to space charge migration or polarization reversal caused by an internal field formed due to remanent polarization. After this period, remanent polarization decays linearly with the logarithm of time [81]

Stabilization of ferroelectric domains has been proposed as the main feature of ageing [81].
Domains can be stabilized due to defect accumulation at the domain walls: known as the domain effect. When neutralization of internal stresses or compensation of electrical charges occurs, defects diffuse into the domain walls and fix their position. For polycrystalline ferroelectrics, second phases can appear due to the high concentration the dopant or alloy.

2.4.4 Fatigue

It is observed during continued field cycling (alternating pulses), Pr starts to decrease. This occurs due to the reducing number of domains able to be part of the switching dynamics. Fatigue is defined as the decrease in switchable polarization with the increasing number of cycles. As illustrated in the figure, it shows an induction period that depends on the applied voltage and the thickness of the films [82]–[84].

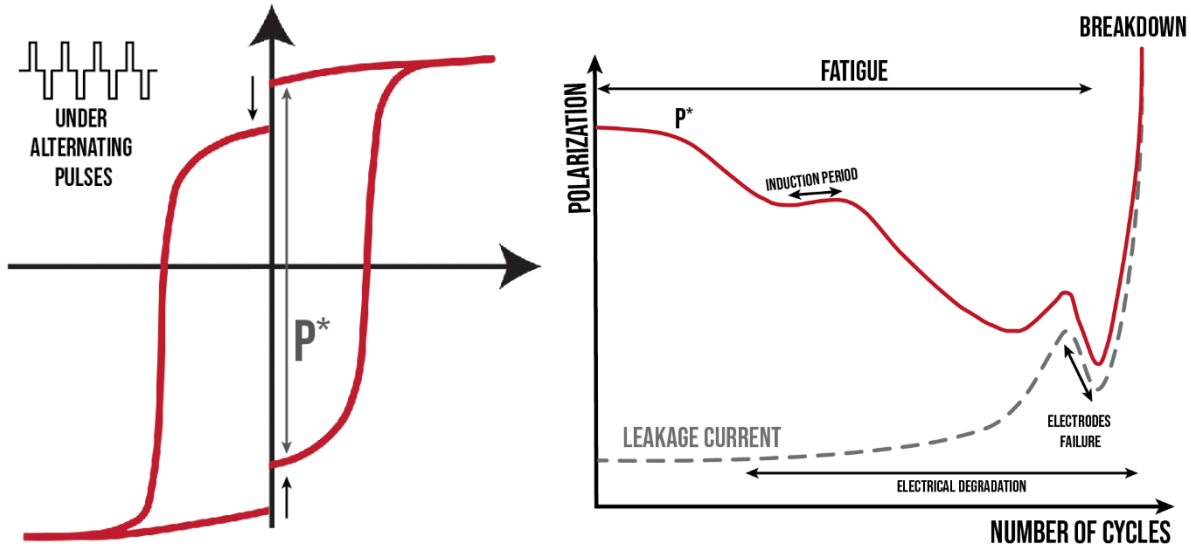

Figure 22 (Right) a generic fatigue curve to the breakdown of a ferroelectric (red) with the contribution of the leakage current (dashed grey) (Left) the effect of fatigue over the hysteresis loop

The Figure 22 shows the polarization-dependence on the number of applied cycles until reaching the breakdown. The leakage current reaches it maximum with the degradation of polarization at the breakdown.

Many models for fatigue have been reported for both bulk and thin-film ferroelectrics [83]–[86]. Detailed models of fatigue in ferroelectric can be found in the book [87].

2.4.5 Imprint

Imprint is defined as the shift of the hysteresis loop along the voltage axis and the loss of the remanent polarization state opposite to the built one. The imprint effect indicates the preference of one polarization state over the other or the lack of ability to distinguish between the two different polarization states $+Pr$ and $-Pr$

It is known to be the reason for the readout failure in ferroelectric memories due to the drastic reduction of polarization.

A typical imprint curve is shown in Figure 21. It is seen that rapid depolarization in a short period of time is followed by ageing occurring in a long period of time. The imprint also shows quick relaxation with either low polarization or polarization reversal.

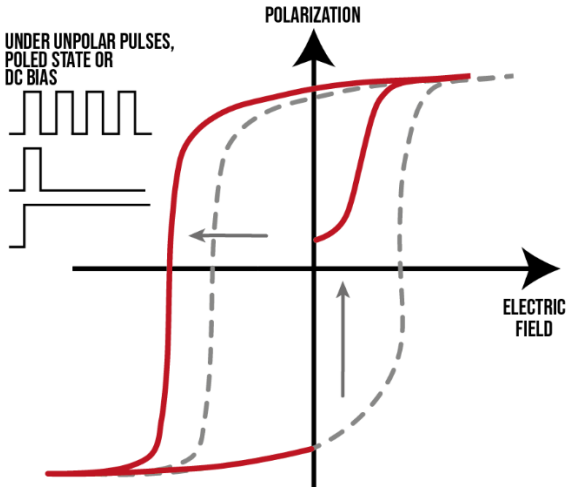

Figure 23 Ferroelectric hysteresis loop degradation by the imprint effect: degraded (red) and original loop (dashed grey).

Some mechanisms have been reported to understand the imprint of ferroelectrics such as the redistribution of the oxygen vacancies generates a defect dipole alignment that builds an internal bias in the ferroelectric film, which shifts the hysteresis and reduces the polarization, and the formation of a thin interface over the ferroelectric films [88]

2.5 HZO review: the state-of-the-art

Ferroelectric properties are the reason for the increasing interest in HZO thin films, besides hafnia-based materials. The multiple applications of HZO indicate that this interest in HZO will last for a long time, especially if it is seen from a sustainable point of view. As shown in **Figure 25**, the number of HZO scientific papers, after the discovery of ferroelectricity within HfO_2-based materials in 2011, passed from one paper per year in 2011 to more than 344 papers per year in 2021, with a total of approximately 1000 papers (based on the collected papers from different databases). Another essential matter we could observe is the increase in the number of patents concerning HZO, but we did not quantify their number as it is out of the scope pf this work.

2.5.1 From 2005 to 2011

Before the current ferroelectric era, HZO had never been reported as a ferroelectric material. Only a few papers reported the dielectric properties of Zr-doped HfO_2 as a high-k for DRAM applications. At the same time, HfO_2 was preferred due to its high thermal stability over ZrO_2 despite the same permittivity of both materials. While studying HfO_2

or ZrO_2 as high-k dielectrics, they were reported to have a leakage current density smaller by four orders than SiO_2 for the same equivalent oxide thickness.

The interest in ferroelectric memories has been renewed in recent years. HfO_2-based ferroelectrics, including HZO, are the promising candidate materials for the next-generation FRAM to replace PZT in capacitor FRAM cells. Compared with PZT, HZO is compatible with CMOS process flow [even back-end of the line (BEOL) thermal budget] and can exhibit ferroelectricity even for ultrathin films.

PZT has been facing many issues, for a few years now. Technically, the integration of 70 nm PZT capacitors is limited to the 130-nm node. Passing to the next generation means scaling down. Hence, a transition from planar to three-dimensional capacitors is difficult to realize with PZT (higher leakage current, its ternary nature is complicated to conserve while deposition and the high volatility of Pb in CVD processes). Legally, many countries announced the prohibition of Pb in the microelectronics industry due to its environmental issues, as mentioned in **Chapter 1**.

In this part, we review the different properties of HZO thoroughly, starting from dielectric to piezoelectric, passing by the ferroelectric and pyroelectric properties. The different deposition techniques of HZO thin films are reported with the primary studies. Finally, the integration of HZO films with devices is mentioned for the different properties and applications.

HZO can be found under numerous names: the most used one is Hafnium Zirconium oxide. Zr-doped Hafnium oxide, Hafnia-Zirconia and Hafnium Zirconate are the other names of HZO. The abbreviations used include HZO, $HfZrO_x$, $HfZrO_2$, $HfZrO_4$, $Hf_xZr_{1-x}O_2$, HfO_2-ZrO_2 and Zr-HfO_2. For the sake of clarity in this thesis, we are using HZO as an abbreviation for hafnium zirconium oxide with a Hf: Zr of 1 :1 ($Hf_{0.5}Zr_{0.5}O_2$).

HZO is a ternary metal oxide. It is composed of two oxides of HfO_2 and ZrO_2. Both oxides are known as high-k dielectrics. As mentioned in chapter 1, Hf and Zr have similar properties due to their similar atomic structure. This similarity is also found in their oxides HfO_2 and ZrO_2 that are transition metal oxides of a fluorite-type structure. The Hf^{4+} (or Zr^{4+}) cations are positioned in the corners and faces of a parallelepiped while the O^{2-} anions take the tetrahedral interstitial sites. HfO_2 has a bandgap between 5.3-5.7 eV, while the bandgap of ZrO_2 is around 5.8 eV.

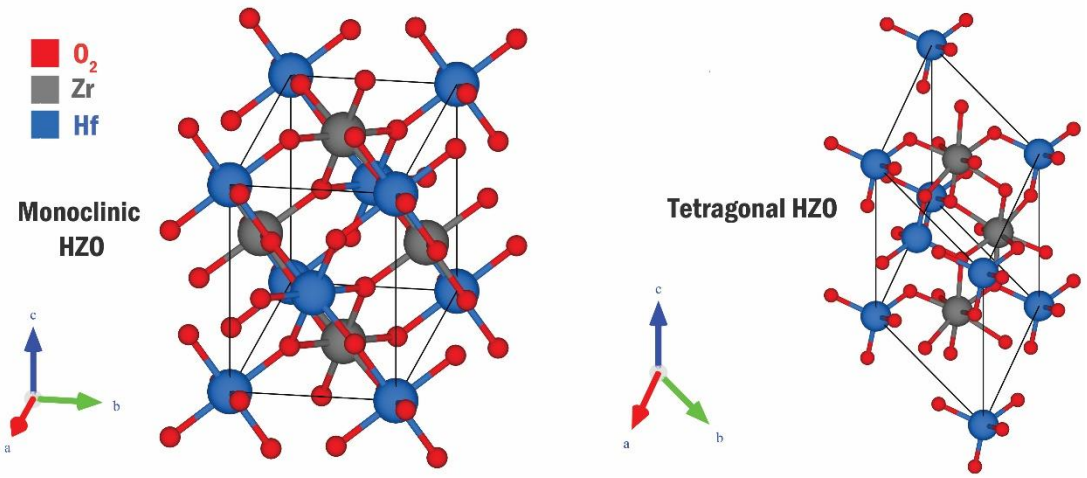

Figure 24 HZO monoclinic and tetragonal phases produced by VESTA software

Reviewing the state of the art of HZO can be divided into two periods: Before 2011 and from 2011 to-up-date. During the first period, from 2005 to 2011, the dielectric properties were the most investigated, whereas the general challenge was to enhance HfO_2 dielectric properties, by doping, for dielectric gate applications. The year 2011 represents a pivotal year for the history of HZO properties because ferroelectricity has been discovered within Si-doped HfO_2 for 10 nm thickness by Boscke et al.[8]. Months after, HZO was reported to be ferroelectric too. As a dielectric, the total number of HZO papers did not exceed 70 for 16 years (from 2005 to 2021), as shown in **Figure 26**. However, the discovery of ferroelectricity in doped HfO_2, including HZO, changed the game and attracted more attention, which is reflected by the growing number of HZO papers after 2011. the average rate of HZO papers passed from 6 papers per year to more than 344 papers per year in 2021, as shown in **Figure 25**.

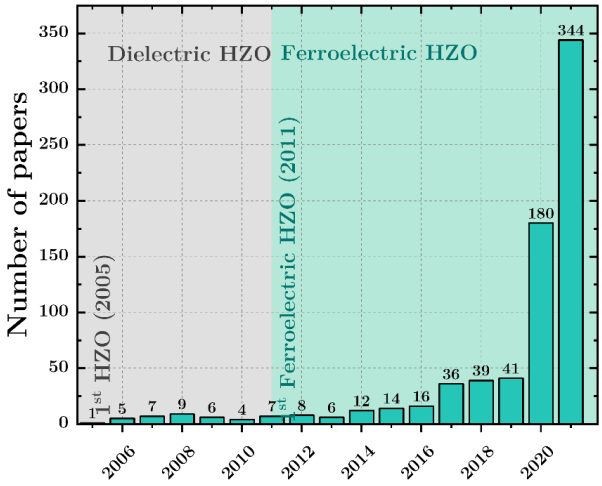

Figure 25 Number of HZO papers (2005-2021)

Before 2011 and to our knowledge, the first to report the Hf-Zr-O system was R.I. Hedge et al. [89] in 2005. In this paper, the aim was to bypass the dielectric properties of HfO_2 as a dielectric gate. By studying the dielectric properties of zirconium doped hafnium oxide, the goal was to enhance the dielectric properties of hafnium oxide. HfO_2-based materials have been intensively studied to overcome the limitations associated with the low dielectric constant of SiO_2 for many years. ALD has deposited HfZrOx, and it showed higher transconductance, less charge trapping, and lower interface state density than HfO_2.

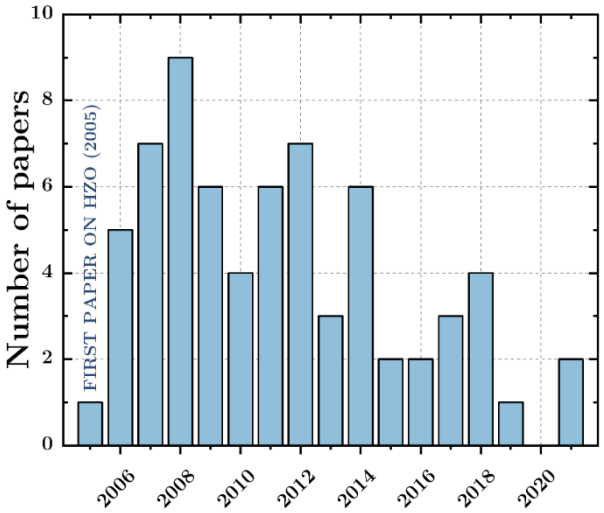

Figure 26 Number of papers of HZO with dielectric properties

In 2005, D.H. Tryioso et al.[90] studied the impact of Zr addition to HfO_2. The ZrO_2 content varied from 25 to 75 %. It has been found that 50% of ZrO_2 allows a higher stabilization of the tetragonal phase of the $Hf_xZr_{1-x}O_2$ alloy. The electrical properties of HZO have been studied using a metal-oxide-semiconductor (MOS). The Zr addition was

reported to reduce the charge trapping compared to HfO_2. After that, R.I. Hedge [91] confirmed the effect of Zr addition on stabilising the tetragonal phase and showed its correlation with increasing the dielectric constant of HfO_2 from 20 to 30. **Figure 24** illustrates the tetragonal phase of HZO. In both studies, the HZO was deposited by ALD to obtain a thickness of around 4 nm. The HZO-based devices have been annealed under N_2 for 5 seconds at 1000 °C.

Sub-2 nm sputtered HZO films were obtained in the same year (2006) by Kuo et al. [92] using Hf and Zr targets. The electrical investigations reported excellent insulation properties of sputtered HZO after a 700 °C annealing under N_2. It was reported to be a promising dielectric for MOSFET applications.

At this first stage of studying HZO properties, ALD and PVD were the used deposition techniques to deposit HZO films. D.H. Triyoso reported the impact of the deposition techniques, among other factors such as the capping layer, annealing and the precursor used, that impact the dielectric properties of HfO_2-based high-k dielectrics [93], [94].

The dielectric properties of HZO reached their maximum in terms of investigation and manufacturability in 2007. M. Muller et al. reported an industrial view of the manufacturability and the integration of HZO within the CMOS process for low-power applications. A buried channel enabled perfectly symmetric threshold voltages down to 30 nm gate length and very competitive device results. Device dispersion has been well controlled, leading to excellent, at the time (2007), 0.499 μm^2 static random-access memory (SRAM) results with mean values of 203 mV (358mV) and Static Noise Margin (SNM) and Write Margins (W.M.) at $V_{dd} = 1.1$ V [95]. HZO dielectric films have shown smaller band gaps, smaller and more uniform grains, and fewer charge traps than HfO_2. HZO/Ta_xC MOSFET was fabricated and showed improved device performance and reliability compared to HfO_2 [96].

Another application that witnessed the integration is the non-volatile memories (NVM). MOS capacitors based on HZO high-k dielectric have been used with different embedded nanocrystalline materials such as ITO, ZnO, Mo and RuO_x [97]–[100]. The memory function was reported to be based on hole trapping during the forward sweep and electron trapping during the backward sweep when the starting voltage is high. The trapped holes could not be wholly eliminated except when a large positive voltage is applied in the backward sweep. Holes are efficiently trapped at the nanocrystal position and loosely

trapped at its interface with the high-k dielectric material, while most electrons are trapped at the nanocrystal site. [101]

For example, MOS capacitors with a single and dual-layer ZnO embedded in amorphous HZO gate dielectric were reported. Electrons instead of holes were trapped by the embedded nanocrystalline of ZnO dots, which is responsible for the large memory window of the device. The dual layer of ZnO was reported to have several advantages, such as the charge trapping density and writing speed. Charge trapping in the dual-layer sample can be accomplished in a concise amount of time. The embedded nanocrystallites within the gate dielectric structure are promising for high-density non-volatile memories.[98]

After 2011, HZO, as a ternary metal oxide, was used for its electroluminescence properties [102]. Without any embedded nanocrystalline, a 10-nm HZO based-device of solid-state light (SSL) emitting was fabricated and proved [103]. Y. Kuo and CC. Lin reported the first HZO-based light-emitting device. The emission spectrum, extended from visible light to infrared, has been broadened, and the intensity has been improved with the embedding of a ZnO nanocrystalline. They explained the light emission by the defect generation mechanism in the film. The device can be easily fabricated. In another paper, Y. Kuo reported light emission from sputtered amorphous HZO. The light was emitted from tiny conductive paths formed after the dielectric breakdown. The light emission was explained to be generated from thermal excitation. The power density within the conductive path, with the thickness of HZO, directly affects the intensity of electroluminescence and peak location. The light emission happened after the breakdown of the HZO dielectric layer.
A nano-resistor device, which emits the white light and shows the diode-like behaviour, has been reported [104], [105]. In addition, several embedded nanocrystalline materials have been reported to enhance electroluminescence, such as CdSe, ZnO, and WO_x [103], [106], [107]. There are many possible applications of this HZO-based device, such as lighting, on-chip interconnects, NVM, nano-heaters, etc.

Hafnium zirconium oxide can be possibly a multiferroic material (exhibit more than one of the primary ferroic properties in the same phase: ferromagnetic, ferroelectric, ferroelastic, etc.). We are discussing the ferroelectric properties in the next section. The main interest of the research community was the ferroelectric properties to speed up the integration of HZO in the next generation of ferroelectric memories. Unfortunately, the other properties have not been thoroughly investigated, such as the magnetic properties. In our bibliographical research, we found only Kalam et al. who reported the investigation

of magnetic properties of HZO as a function of the Hf: Zr ratio [108]. On the other hand, ZrO_2 has known ferromagnetic properties, and while studying HZO, the highest saturated magnetization was obtained for $Hf_{0.5}Zr_{0.5}O_2$. Further studies can confirm these results and explore the multiferroicity of hafnium zirconium oxide films.

2.5.2 From 2011 to now

In 2011, ferroelectricity was reported in 10 nm Si-doped HfO_2-based films by Böscke et al. [8], but it had not been discovered in the same but five years before. As a result of our bibliographical study, we can see that it has been discovered simultaneously as different additives to HfO_2 have been tested to enhance its dielectric properties. The central hypothesis on the origin of ferroelectricity within HfO_2 films was proposed by Böscke, saying that the ferroelectric nature of doped HfO_2 originated from the non-centrosymmetric orthorhombic phase ($Pca2_1$), which has not been reported in the HfO_2 equilibrium phase diagram. This phase is hard to determine experimentally from the XRD data, and it is difficult to separate it from the tetragonal phase peaks. The metastable orthorhombic phase has been obtained for 10 nm film capped by a top electrode layer of TiN and processed by an annealing step after the electrode deposition. These fabrication steps have been suggested to build an in-plane strain within the film, causing the stabilization of the orthorhombic phase, as illustrated in **Figure 27**.

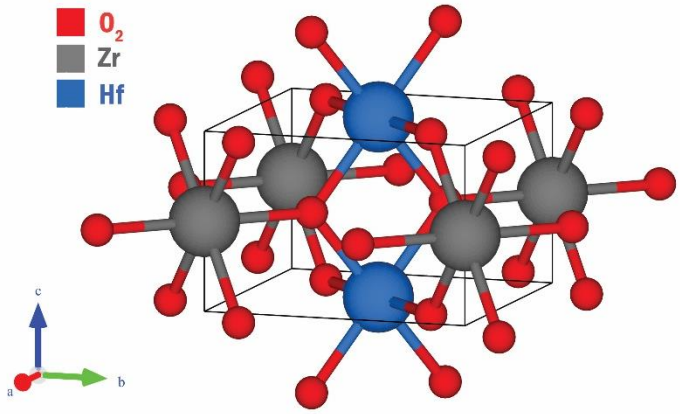

Figure 27 HZO orthorhombic phases produced by VESTA software

As this ferroelectric property at small thickness represented a solution for the next generation of ferroelectric memories, several experimental and simulation studies on the ferroelectric behaviour of HfO_2-based films have been published in order to build a collective understanding of the mechanism of ferroelectricity induction and its influencing

factors. The first investigated factors were doping, the top electrode material and the annealing parameters.

In addition to Si, other dopants of HfO_2 such as Zr, Al, Gd and La have been studied. The motivation behind these studies was to distort the HfO_2 lattice structure by a larger or smaller radius. All of them induced ferroelectricity, but no trend has been reported as a function of the valence's radius of the dopant element. Besides, for every dopant proved to induce ferroelectricity, the optimal concentration was different compared to the others. This has not been understood yet.

The dopant or the additive that gained the most interest is Zr. Forming HZO has the highest reported concentration to induce ferroelectricity, and the orthorhombic phase was the most stable. Higher P_r, endurance and the lowest annealing temperature during the process are the most advent of HZO, making it the most exciting material among the HfO_2-based ferroelectrics.

For all HfO_2 ferroelectrics, including HZO, the same explanations are generalized. However, until now, a specific understanding of each one is not achieved yet. As these ferroelectric materials are all the fluorite-type structure, Perovskite-structure ferroelectrics, especially PZT, are often the model used to compare and understand the phenomena within fluorite-type ferroelectrics.

One of the physical properties that define the research direction is the thickness of ferroelectric films. It is strongly related to the amount of the orthorhombic phase and the remnant polarization.

Each dopant or additive has an optimal concentration to induce the orthorhombic phase, so a specific window for the best ferroelectric properties (P_r, endurance, thickness, etc.). HZO represents the highest tolerance for Zr concentration. M.H. Park et. Al studied theoretically and experimentally the thermodynamic energy of an extensive range of HZO films with Hf: Zr ratio varied from 0 to 1 and varied thicknesses from 9.2 to 29.2 nm [109]. In **Figure 29**, P-E plotted curves were a function of the Hf: Zr ratio and the thickness of the films. Briefly, the highest P_r (16.5 $\mu C.m^{-2}$) was reported for Hf: Zr=1 and thickness of 9.2 nm. This result confirmed the previous result of the first ferroelectric HZO of 9.5 nm by Muller [110]. More Zr content in HZO causes the apparition of an antiferroelectric behaviour of HZO. It has been previously reported that ZrO2 is antiferroelectric material. At the same time, as a function of thickness, P_r is almost

constant, and it decreases abruptly at 24.2 nm, which suggests that this thickness is the limit of ferroelectricity in HZO. The same behaviour of P_r as thickness increases can be observed for the different compositions.

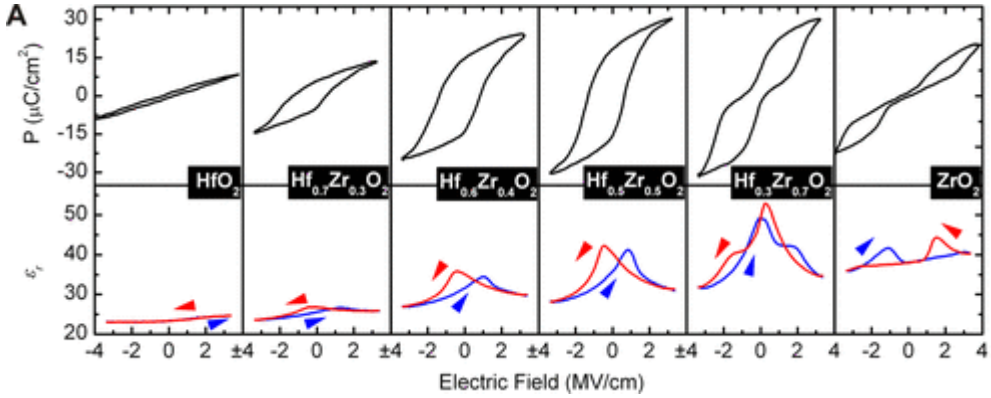

Figure 28 P.V. hysteresis at 1 kHz and small-signal CV hysteresis at 10 kHz (50 mV level) of 9 nm thin HfO_2–ZrO_2 based metal–insulator–metal (reproduced with permission) [110]

This study suggested that the phase transition within HZO is a first-order transition from the orthorhombic to the tetragonal phases.

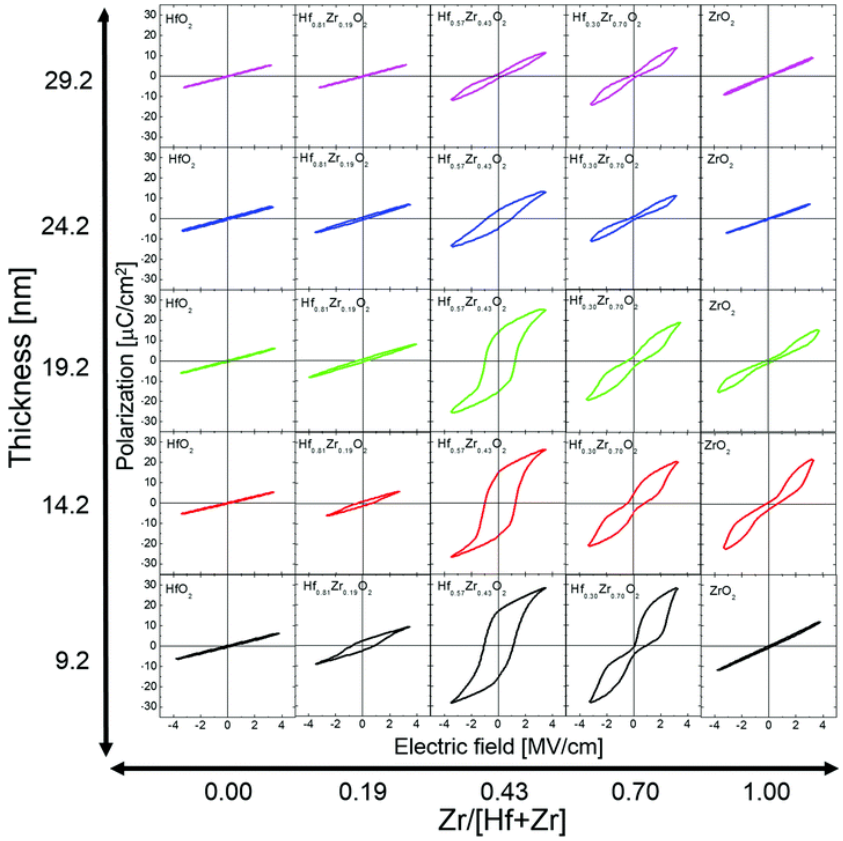

Figure 29 (P-E) curves of $Hf_{1-x}Zr_xO_2$ films with various compositions and thicknesses (reproduced with permission) [110]

The variation of the dielectric constant k as a function of the thickness and composition is shown in **Figure 30**. The Butterfly-shaped k-E curve is another signature of

ferroelectricity. It appeared for the same samples in which a ferroelectric hysteresis loop appeared in **Figure 29**. The dielectric constant of ferroelectric HZO varies between 30 and 38. It matches well with the previously reported values of the dielectric constant of the orthorhombic phase. In this study, the electrode material is TiN, and the capacitors were annealed at 500 °C under N_2 for 30 seconds.

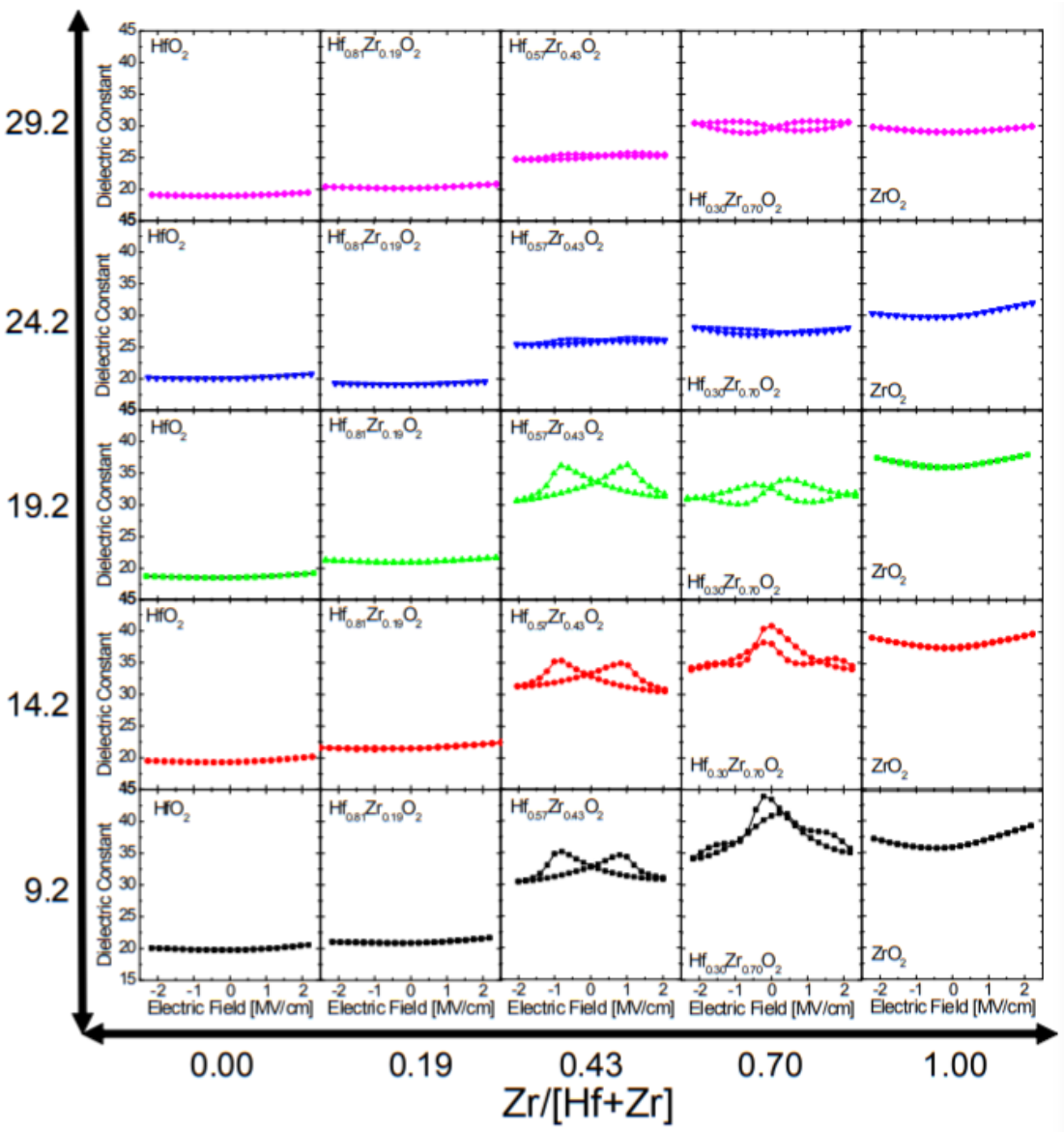

Figure 30 The dielectric constant – electric field curves of HZO films with various (reproduced with permission) [110]

Many studies reported the degradation of the ferroelectric properties of HZO for films thicker than 20 nm. It is explained by the formation of the non-polar monoclinic phase, represented in **Figure 24**. Some solutions have been proposed to overcome this limit, such as adding a 1-nm layer of Al_2O_3 between two HZO layers. Realizing this HZO/ Al_2O_3/HZO structure allowed to obtain ferroelectricity at 40 nm thickness, as reported

by Kim et al. [111]. Riedel et al. used the same idea to obtain a total thickness of laminated Al_2O_3/HZO of 50 nm. The thickness of Al_2O_3 was 5 nm.

After all, the current challenge of the scientific interest in ferroelectric HZO is not about reaching the highest ferroelectric thickness. This can be useful for piezoelectric applications for actuators and sensors. However, currently, the challenge is conserving the ferroelectric properties of ultrathin films in order to integrate them into the ferroelectric memories.

Ultrathin ferroelectric HZO of 1 nm has been reported by SS. Cheema [112] deposited by ALD on Si. This result indicates no critical thickness for ferroelectricity and enhanced polar distortions as the thickness is reduced, unlike perovskite ferroelectrics. 2.5 nm-thick HZO films were reported to be ferroelectric by Chouprik et al. [113]. This unlimited ferroelectricity opens the door for polarization-driven memories and advanced ferroelectric-based transistors. This nonexistent minor limit of ferroelectricity swings the search for the fundamental limits of ferroelectricity to simpler transition-metal oxide systems in which 'reverse' size effects counterintuitively stabilize polar symmetry at the ultrathin level.

To our knowledge, the thickest ferroelectric HfO_2-based material is Y-doped HfO_2 deposited with a sputtering technique [114]. The obtained remnant polarization and coercive field of Y-HfO_2 films were about 12 $\mu C.cm^{-2}$ and 1.2 $MV.cm^{-1}$, respectively. The measured d_{33} value was approximately 2.5 pm. V^{-1}. **Figure 31** shows the S—E and P—E curves of a butterfly shape and a hysteresis loop that clearly show the film's piezoelectricity and ferroelectricity. The d_{33} effective piezoelectric coefficient was calculated from the slope of the positive displacement curve in S—E near 0 $MV.cm^{-1}$. This value of d_{33} matches well with the reported values, such as 3.5 $pm.V^{-1}$ value reported for La-doped HfO_2 by Schenk using a double beam laser interferometer (DBLI) in the aixACCT tester [115].

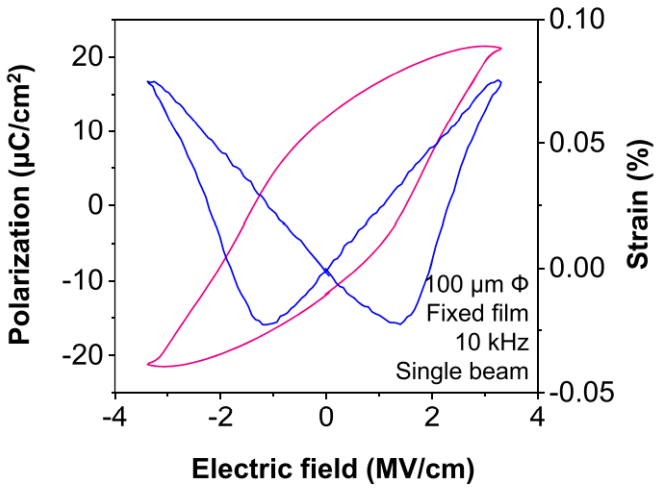

Figure 31 (Color online) Room-temperature strain–electric field (S–E) and

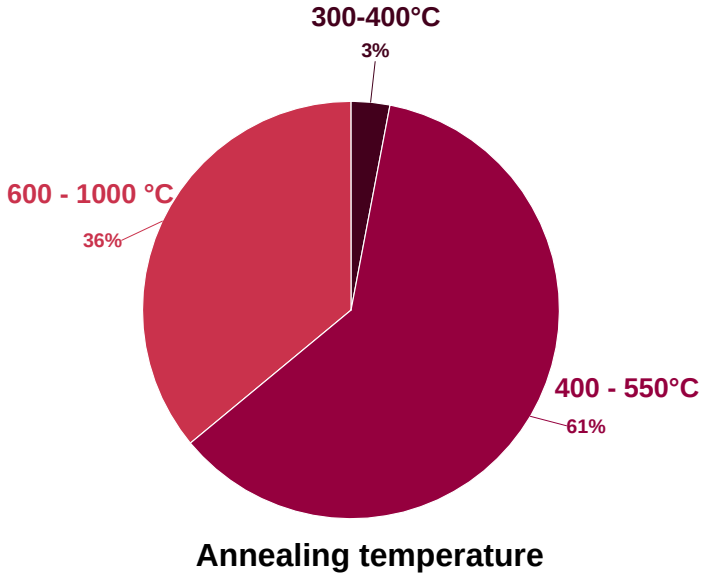

Figure 32 Different reported annealing temperature ranges of ferroelectric HZO (2011 -2021)

To induce ferroelectricity, a crucial step of annealing is required. Independently of the deposition technique, HZO films need rapid thermal annealing (RTA) in order to be crystallized into the orthorhombic phase. It was reported in the first ferroelectric doped HfO_2 [8]. RTA impact has been studied as a function of its parameters: temperature, annealing atmosphere, and annealing time. In literature, induced ferroelectricity in HfO_2-based materials has been reported to be annealed by different techniques: RTA, furnace annealing, laser annealing and microwave annealing [116]–[119]. In this part, we are focusing only on RTA as it is the most used technique.

Complete understanding and controlling the impact of RTA for each dopant of HfO_2 have not been fully achieved yet. **Figure 32** shows a pie chart of the reported annealing temperature ranges that induce ferroelectricity within HZO thin films. The first used annealing temperature by Böscke [8] was 1000 °C. One of the reasons to choose Zr as an additive was that it allows for reducing the annealing temperature or the thermal budget specifically. The first ferroelectric HZO studies reported a 500 °C annealing temperature to induce the ferroelectricity. The most used temperatures belong to the 400-550°C range, as shown in **Figure 32**. The aiming can explain the focus on this range to induce ferroelectricity in HZO or any HfO_2 material with a temperature compatible with the CMOS process. Generally, the limit is 500 °C. Considering the annealing temperature only, we found that it differs from one dopant to another, as proved by M.H Park et al. while investigating the lowest annealing temperature for Al, Gd and Sr by in situ XRD measurements [120]. The required temperatures to induce the o-phase for the three dopants were different (515 ± 5, 458 ± 5, and 524 ± 5 °C, respectively). For HZO, before conducting an in situ XRD characterization, the lowest temperature was 450°C. We realized an XRD in situ measurement on 22 nm-thick HZO films and found that the o-phase can be induced at 370 °C [121]. This result was confirmed later by Presson et al. [122]. The annealing temperature has been reduced to 300 °C by using high-pressure RTA as reported by Kim et al.; meanwhile, the o-phase was not induced at 300 °C high pressure [123]. To this day, 300°C is the lowest annealing temperature used to obtain the orthorhombic phase.

Another parameter of annealing is the atmosphere. It can affect the physical and ferroelectric properties of HZO films. The most used gazes are H_2, N_2, Ar and O_2. The hydrogen atmosphere degrades the electrical properties of the films. The nitrogen atmosphere is the most used one as TiN is the most chosen material for electrodes in order to avoid the oxidation of TiN. The oxidation atmosphere affects HZO and TiN, and it was used to control the oxygen vacancies. However, it can also deteriorate the quality of the films and the electrodes. Lee et al. reported better electrical properties for O_2-annealed sputtered HZO films [124]. It was explained by the fact that sputtering HZO in oxygen-deficient plasma leads to a higher number of oxygen vacancies, contrary to ALD deposited HZO that has an oxidizing agent O_3, so O_2-atmosphere during annealing reduces the oxygen vacancies in HZO. In other reports, the N_2 atmosphere was found to be the optimal atmosphere to induce the o-phase. Future studies are required to investigate the impact of annealing parameters [125] precisely.

The electrode material has its vital contribution to inducing the ferroelectricity in HfO_2 based materials. The relationship between capping materials and ferroelectric properties is essential to modulate ferroelectric device performance and improve the flexibility of the device design. The choice of the electrode material is strongly independent of the thickness of the ferroelectric layer, the deposition technique, and the annealing parameters. The top and bottom electrodes also have their thickness, material choice, and deposition technique parameters. These parameters react differently to the same annealing conditions or any other step of fabrication. No fully comprehensive the detailed impact of electrodes has been reported yet, but only some insights from studies. Besides the other factors, electrodes' different parameters and possibilities multiply the relationships and increase the complexity of a complete understanding of the ferroelectricity phenomena.

To date, TiN is commonly the choice since the discovery of ferroelectricity in Si-doped HfO_2 films by Böscke [8]. Statistically, TiN, and TaN electrodes are both used for research and industry, and both have been heavily studied. The impact of various capping materials was investigated [126]. Polakowski et al. reported a different behaviour for a ferroelectric TiN/HfO_2/TiN stack with a sputtered TiN top electrode. In contrast, a paraelectric behaviour appeared for TiN/HfO_2/TiN with a TiN deposited by CVD. Confirming the role of the TiN top electrode, HZO film was sandwiched between the TiN bottom electrode and one of the three (TiN, RuO_2, or Pt) as the top electrode. The highest P_r was reported for TiN with 17.1 $\mu C.cm^{-2}$ while 12 and 10.3 $\mu C.cm^{-2}$ for RuO_2 and Pt, respectively. Park explained this due to the different stress applied by the top electrode.

To summarize, different materials can be used as electrodes for ferroelectric HZO, but each one needs to be optimized as a function of the other fabrication steps. Besides, the current comparison is in terms of Pr only. Other electrical characteristics can be investigated to confirm these reports. The impact of electrodes is not entirely understood yet, and further studies are required.

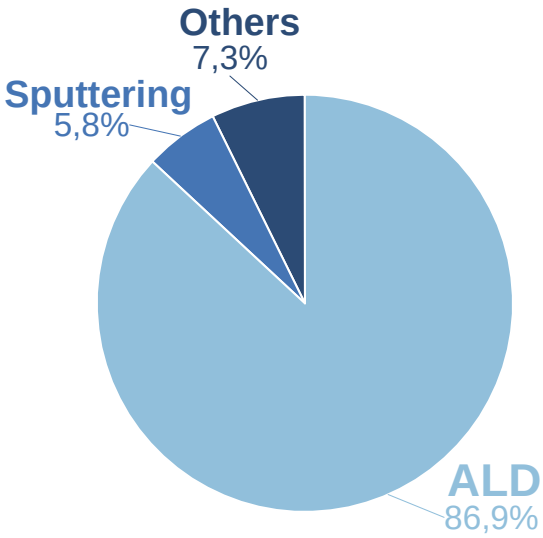

Figure 33 Different reported HZO deposition techniques (2011 -2021)

The reported HfO_2-based ferroelectrics were entirely CMOS compatible and reproducibly deposited by several deposition techniques such as ALD, CVD, CSD, PLD and sputtering as the PVD method. Compared to perovskite ferroelectrics, the multiplicity of ferroelectric HfO_2 deposition techniques represents a superiority for HfO_2 films. Furthermore, ALD is especially suitable, considering its precise atomic-level thickness control, high crystallinity, and good three-dimensional step coverage (3D ferroelectric memories). Therefore, already matured ALD technology in the semiconductor industry dramatically facilitates the development of HfO_2-based ferroelectrics.

To date, studies have been conducted primarily on doped HfO_2 layers grown by atomic layer deposition. **Figure 33** shows the repartition of the deposition techniques for HZO. the most intensively used deposition technique is ALD. It is based on a self-limiting mechanism with chemical reactions between a metal precursor, oxygen source, and substrate. However, there are few deposition parameters to be controlled, only the deposition temperature and precursor/ purge pulse times. Nevertheless, for sputtering, it has more factors such as target density power, reactive plasma, deposition pressure and deposition temperature. These factors are easily controlled. This suggests that sputtering offers different physical influences on the film and provides degrees of freedom to engineer the deposition condition of sputtering. Therefore, it is a more attractive option to understand the formation of the orthorhombic phase in HfO_2-based thin films. One inconvenience of sputtering is the presence of contaminants such as C, N or H within the film, but the target quality and purity can control it. Therefore, Sputtering is a timesaving and more cost-effective option.

As shown in **Figure 33**, sputtered doped HfO_2 is rarely undertaken. To date, only a few research teams have initiated studies on sputtered ferroelectric HfO_2-based thin films. Xu et al. reported the ferroelectric behaviour of HfO_2 film doped with various cations (Sc, Ge, Y, Zr, and Nb) [127]. Fan et al. [128] reported ferroelectric HZO thin film obtained by sputtering. In Lee's work [129], the physical and electrical properties of sputtered HZO were studied by investigating the role of target power and working pressure and the thermal annealing conditions of reactive co-sputtering. In the co-sputtering process, monitoring the chemical composition of HZO through the ratio of Hf: Zr is more challenging than the straightforward single target sputtering system, as shown in the results of the study by Woo et al. and Ryu et al. [13], [116].

To summarize, polarization switching has been reported in sputtered ferroelectric HfO_2 by investigating the electrode materials and oxygen vacancies, but the characteristics of P_r have rarely been discussed. However, the effects of sputtering systems or parameters have not been thoroughly investigated to date. One paper by Mittmann et al. [130] revealed the benefit of different deposition techniques by reporting ferroelectric properties within undoped HfO_2 deposited by sputtering.

As shown in **Figure 34**, there are two central systems to deposit the ternary HZO oxide: a single target of the HZO system and co-sputtering with two targets of Zr and Hf. the targets for the co-sputtering can be ceramic or metallic. However, the single-target sputtering of ferroelectric HZO has been reported by three research teams only: Woo et al., Ryu et al., Yu et al. and our group [13], [116], [121], [131].

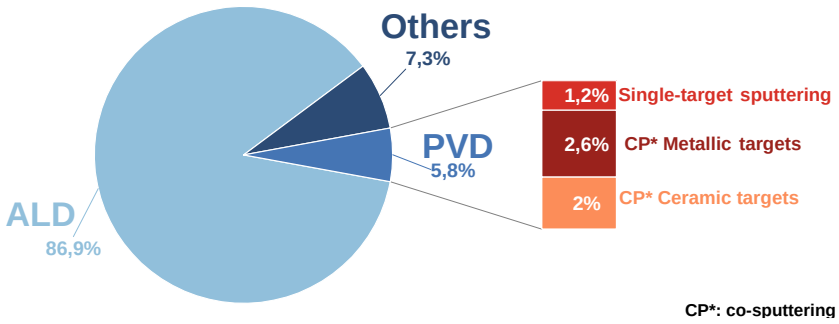

Figure 34 Ferroelectric HZO deposition techniques with detailed sputtering systems

The environmental and sustainability motivation to replace PZT has led us to consider the use and development of single target sputtering of HZO instead of ALD, the most widely used deposition technique of HZO. Indeed, the single target sputtering technique, being cheaper than ALD and exhibiting higher throughputs, is more suitable for industrial processes. Moreover, the fabrication of HZO targets has a more negligible

environmental impact than the metalorganic precursors used in ALD in terms of cost, energy consumption, and process complexity.

The reported results for ferroelectric HZO by single-target sputtering reveal a high potential for this technique concerning ferroelectric HZO. Furthermore, the record of 1 µm ferroelectric Y-doped HfO_2 can be realized with this technique for HZO. Consequently, it initiates the interest in sensors and actuators based on piezoelectric HZO with its lead-free label.

Further studies are required better to understand the deposition of this ternary oxide of HZO and explore its properties for varied thicknesses and applications.

The discovery of ferroelectric properties in HfO_2 did renew the interest in ferroelectric memories or lead-free ferroelectrics and started the challenge of characterizing this phenomenon at the nanoscale level. Piezoresponse force microscopy (PFM) is often the best option for piezo-, ferroelectricity, and piezoelectricity at the nanoscale. However, using this technique to characterize ultrathin HfO_2-ferroelectrics is the subject of a current scientific debate due to artefacts of PFM that complicate the interpretation of results and can be misleading in identifying ferroelectric materials. For the case of HfO_2 ferroelectrics, PFM is used to detect the local response in order to understand the polarization reversal mechanism. Using direct and alternative voltages within the probing tip in contact mode can characterize an nm-level region of domain structure and the switching polarization inside it. PFM is based on the strong coupling between polarization and mechanical displacement. The coupling can be measured by applying a highly localized electric field to the material and probing the resultant surface displacements within picometer precision. The PFM technique can be of particular importance for the case of HfO_2 ferroelectrics because there is a wake-up phenomenon of the polarization, and the PFM helps understand the different mechanisms of passing from weak P_r to a higher one.

Another attractive property of HZO ferroelectric films is the negative capacitance. It occurs in some conditions, and it causes a local voltage drop opposing the applied bias. Its response can enhance the voltage in the circuit. However, this phenomenon is not fully understood or explained definitively. Even ferroelectric materials can exhibit a negative capacitance effect. R. Landauer was the first to report a negative capacitance effect within ferroelectrics. The spontaneous polarization is like the spontaneous charging of a capacitor with a negative capacitance. For the Field-Effect Transistors (FET) with a negative capacitance condition, the ferroelectric can be totally depolarized and shows

a hysteresis loop of P. This would allow amplification of the semiconductor surface potential concerning the gate voltage. Consequently, the subthreshold swing can be lower than the Boltzmann limit $\frac{ln(10)k_BT}{q}$ (where k_B is the Boltzmann constant, T is the temperature, and q is the charge). This would lead to better power consumption devices, so further miniaturization.

The signature of a negative capacitance is the S-shaped curve, as shown in **Figure 35**, but it cannot be observed in the circuits of polarization measurements. **Figure 36** shows the experimental set for the first demonstration of the S-shape curve in ferroelectric HZO, with a Ta_2O_5 dielectric, reported by Hoffmann et al.[132] by applying nanosecond pulses to avoid charge compensation and the stabilization of the domains at the HZO/Ta_2O_5 interface (**Figure 35**).

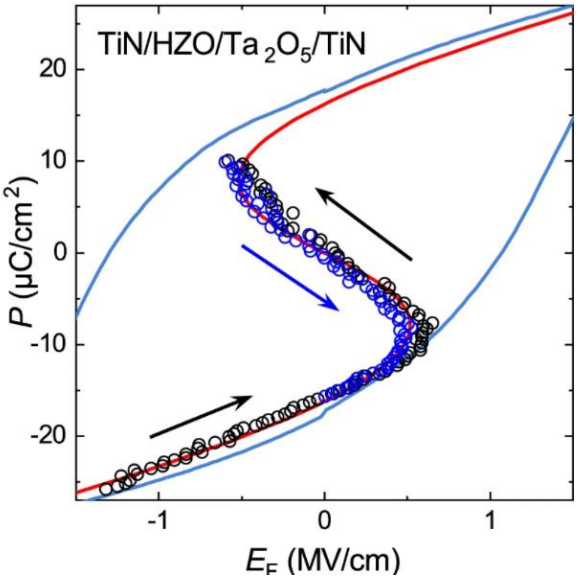

Figure 35 S-shaped P–E.F. curve Black and blue correspond to the increasing and decreasing Vmax sweep direction. Red corresponds to LGD theory, and the blue shows the P–E.F. hysteresis measured on a TiN/HZO/TiN sample (reproduced with permission) [132]

Through high-speed pulsed charge voltage measurements, Hoffmann et al. [133] also reported the experimental observation of hysteresis-free negative capacitance in thin ferroelectric HZO films. In addition, hysteretic switching was suppressed by adding dielectric Al_2O_3 layers on top of the HZO to prevent the screening of the polarization.

To better understand the negative capacitance within ferroelectrics, these reports are handy [134]–[137].

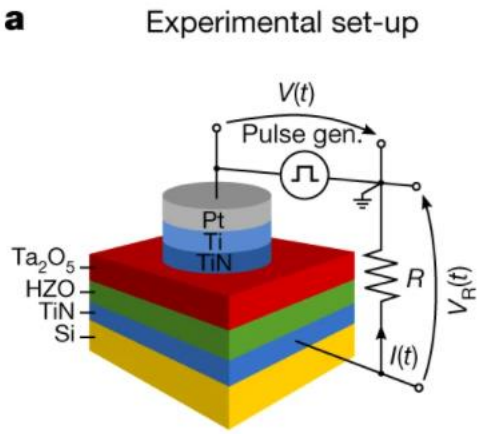

Figure 36 Experimental set-up for the pulsed Q–V measurements. V is applied by a pulse generator, and both V and V.R. are measured via an oscilloscope, where V.R. is the voltage drop across the resistance R (reproduced with permission) [132]

As the current global challenges and the technological shift toward the IoT ecosystem, HZO, by its multiple applications, is one of the essential materials. For low-power consumption, HZO-based negative capacitance FET shows improved device performance. Stabilized negative capacitance has been reported for ferroelectric/dielectric perovskite heterostructures and fluorite-type ferroelectrics like HZO and doped HfO_2. The impact of HZO on FDSOI NCFET was reported to increase the improvement of sub-threshold slope and reduce I_{OFF} [138]. The impact of HZO thickness on the performance of NCFET has been investigated by S. Semwal et al.[139]. The interest in the negative capacitance of HZO is growing; however, investigating the temperature impact is of urgent importance to pass to practical applications. Wang et al. studied the influence of temperature on NCFET based on HZO [140]. It was found that the temperature increases the negative capacitance in the NCFET, which is degraded due to the temperature increase. Further studies are required to improve the integration of HZO in NCFET.

Ferroelectric HZO allows overcoming the current CMOS compatibility issues and the high cost of the different memory types (SRAM, DRAM and Flash memories). This opportunity opens the way for improving IoT devices. For memory applications, data storing is made with the polarization state of the ferroelectric film, while the writing process is made by applying an appropriate electrical field. This makes a power-efficient writing process. Three main structures of memories are based on ferroelectric HfO_2: 1T1C FeRAM (One Transistor One capacitor), 1T FeFET, and the FTJ (ferroelectric tunnel junction).

HZO has been successfully integrated within FeRAM with a 130 nm CMOS process for NVM applications [141]

Ghatge and co-workers were the first to report the integration of HZO into a transducer [142]. They have shown a fabricated 10-nm HZO-integrated nanoelectromechanical transducers, as shown in **Figure 38**. It was reported that the electromechanical properties of HZO were based on the electrostrictive effect. The transducers were integrated on silicon and aluminium nitride membranes. They yielded resonators with a 340 kHz - 13 GHz frequency range and a figure of merit of frequency quality-factor ($f \times Q$) of around 3.97×10^{12}, as shown in **Figure 39**. This figure of merit is the best-reported value for nanomechanical resonators operating in the centimetre-wave regime (**Figure 41**). The 340 kHz -13 GHz frequency range of the HZO transducer makes it operational for super high-frequency resonators (3-30 GHz) for wideband spectral processors and high-resolution resonant sensors. However, such application requires the reduction of resonator dimensions to tens of nanometres, and current devices typically rely on transducers, for which miniaturization and chip-scale integration are challenging.

As mentioned above, each ferroelectric material is pyroelectric and piezoelectric. The main interest of research was focused on the ferroelectric properties. The pyroelectric and piezoelectric properties of HfO_2 ferroelectrics, including HZO, were rarely studied. Some reports reported the pyroelectric coefficient of ferroelectric doped HfO_2 to be between 40 and 84 $\mu C.m^{-2}K^{-1}$, which is considered reasonable compared to the conventional $LiNbO_3$.

Despite that, 3D integrated HfO_2 pyroelectric deep trench capacitors were demonstrated. It allowed improving the high-performance integrated I.R. arrays [143] as ferroelectric hafnia has its own effects, such as the wake-up effect of the polarization. Such effects are expected to affect and delay the profound understanding of the pyroelectricity within hafnia. This suggests a longer interest in ferroelectric hafnia. For HZO, D. Lomenzo et al. studied the impact of thickness and annealing temperature on the pyroelectric coefficient. HZO thickness varied from 1 to 30 nm, and the annealing temperature varied from 450 to 600 °C. The reported optimum for the pyroelectric coefficient was 56 $\mu C.m^{-2}K^{-1}$ for 15 nm thickness and 450°C.

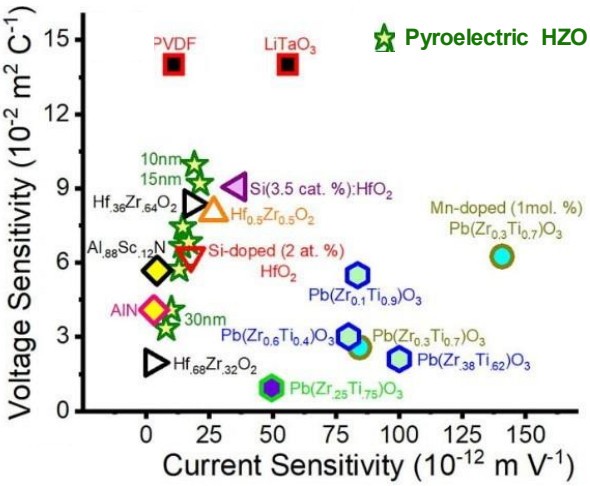

Figure 37 Figures of merit voltage sensitivity vs current sensitivity (reproduced with permission)[142]

Compared to the other HfO_2-based pyroelectric materials, HZO exhibits the highest voltage sensitivities for the 10-15 nm range annealed at 450 °C due to HZO's lower permittivity as shown in **Figure 37**. Compared to PZT, HfO_2-based ferroelectrics exhibit lower zero-field pyroelectric coefficients and, thus, have lower current sensitivity.

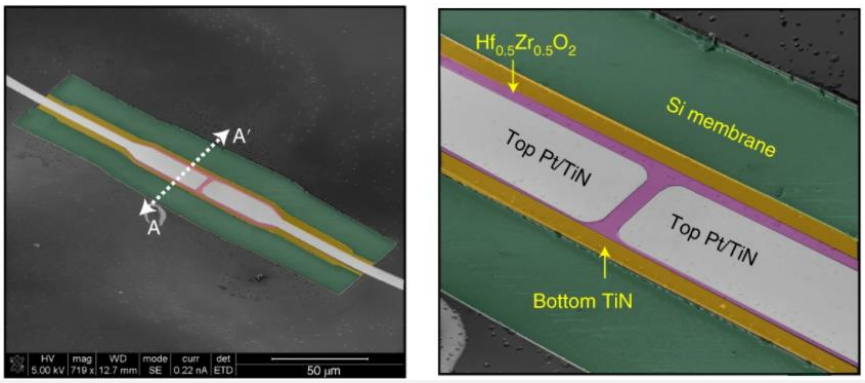

Figure 38 SEM image of the $Hf_{0.5}Zr_{0.5}O_2$-transduced Si nanomechanical resonator operating in out-of-plane flexural mode. b, Magnified SEM of the resonator (reproduced with permission) [142]

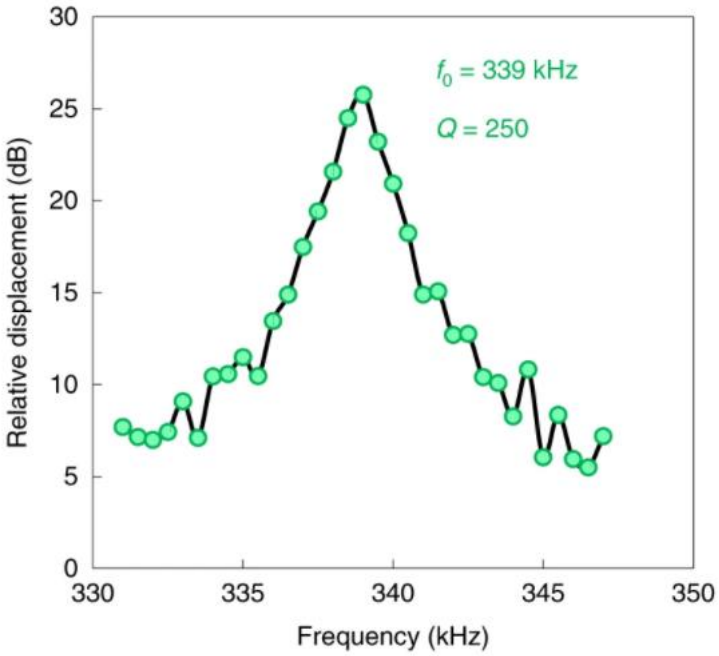

Figure 39 The frequency response of the $Hf_{0.5}Zr_{0.5}O_2$-transduced Si resonator extracted from stroboscopic analysis, showing the flexural resonance at 339 kHz and a Q of 250 in the air (reproduced with permission) [142]

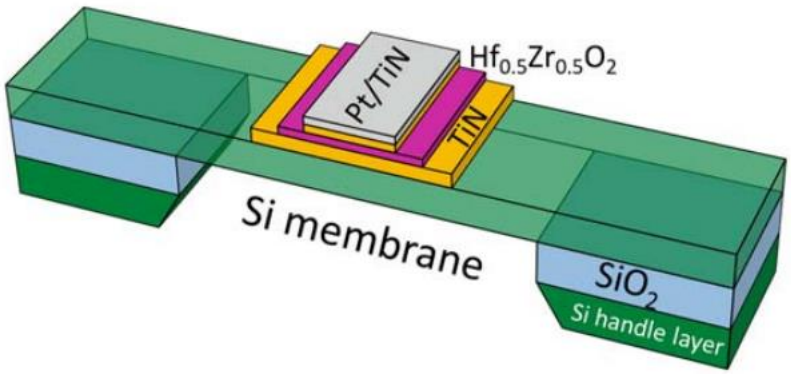

Figure 40 The cross-sectional schematic of the HZO transduced Si nanomechanical resonator.

All these exciting properties of ferroelectric HZO allow the shift toward the next generation of ferroelectric memories and low-power devices. In addition, further investigations on the pyroelectric and piezoelectric of HZO will undoubtfully lead to more HZO-based applications.

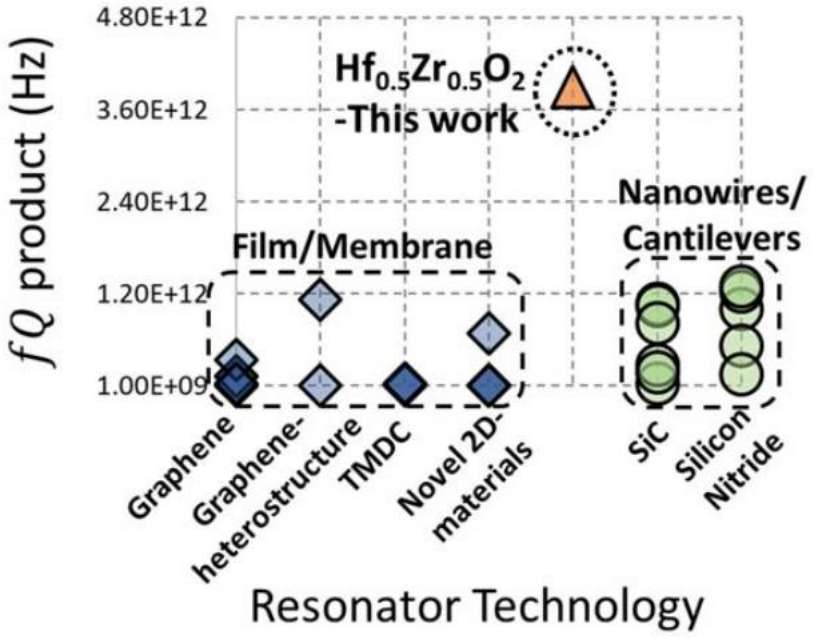

Figure 41 The fQ product figure of merit of the recently demonstrated state-of-the-art nanomechanical resonators (reproduced with permission) [142].

HZO is also in the middle of emerging technology: neuromorphic computing which enables the next generation of A.I. (artificial intelligence) and autonomous devices. Neuromorphic computing is based on biological neural computation by emulating the human brain's neural system. This approach allows overcoming the limits of the Neumann architecture by using spiking neural networks (SNN) to decide on response to machine learning over time.

Due to the ferroelectric switching, HZO-based non-volatile memories provided a new platform for both synaptic and neuronal applications such as synaptic learning due to the gradual tuning of their conductivity, low power consumption, and various structures (2-terminal or 3-terminals structures). Furthermore, the non-volatility with a multi-domain nature reveals high potential for synaptic applications in compute-in-memory architecture.

Two categories can be defined for the used structures based on HZO ferroelectric films, or HfO_2 in general: two-terminal structures such as FTJ or MIM heterostructures, and three-terminal structures such as FeFET. The figure shown earlier presents examples of synaptic devices. In two-terminal HfO_2-based synaptic devices, ferroelectric FTJ attracted more attention due to its non-destructive read mechanism and ultra-low power consumption [144], [145]. An HZO FTJ-based deep binary neural network has been

reported [41, 42]. Shim and Yu realized 3D NAND architecture for an on-chip accelerator for energy efficiency applications using HfO_2-based FeFET [146]

For the three-terminal structures, Yu et al. reported successful manufacturing of HZO-based memristor for multilevel storage and artificial synaptic plasticity [147]. The fabricated memristor shows excellent properties in the modulation of the bidirectional gradual resistance. At the same time, D.H. Min et al. investigated the role of oxygen pressure during single target sputtering on the synaptic operations of FEFET based on HZO [131]. Controlling the oxygen vacancies was found to delay the polarization switching, which is interesting for FEFET synaptic devices. biological activity, such as paired-pulse facilitation and spike-timing-dependent plasticity, was emulated using HZO-based FTJs [144], [148]

Even antiferroelectric HZO has been integrated into devices due to its promising characteristic: its endurance strength is higher by orders than HZO ferroelectrics.

3 Chapter III Fabrication methods and characterization techniques

3.1 Fabrication process 75
3.1.1 Sputtering deposition of HZO thin films and TiN electrodes 75
3.1.1.1 HZO Sputtering chamber 77
3.1.1.2 TiN electrodes: 79
3.1.2 Fabrication of the capacitors 80
3.1.3 Rapid thermal annealing 81
3.1.4 Photolithography 84
3.1.5 Etching 85
3.1.6 Summary 85

3.2 Physical and structural characterizations: 86
3.2.1 X-rays 87
3.2.1.1 X-ray Diffraction: 87
3.2.1.2 X-ray reflectivity 89
3.2.1.3 X-ray photoelectron spectroscopy 91
3.2.2 SEM and TEM 94
3.2.2.1.1 Scanning electron microscopy (SEM) 94
3.2.2.1.2 Transmission electron microscopy (TEM) 95
3.2.3 AFM 96

3.3 Electrical characterizations 97
3.3.1 Impedance spectroscopy 98
3.3.2 Leakage current measurements 99
3.3.3 Capacitance voltage measurements 100
3.3.4 Polarization Field measurements 100

3.4 Conclusion 102

In this chapter, we introduce three main sections: the first one is dedicated to the fabrication process of the metal-insulator-metal structures used during the thesis, from the deposition of the electrodes and the HZO films to the photolithography and etching process steps, while the second section describes the techniques used for the characterization of the physical and structural properties of HZO thin films. Finally, the third section focuses on the electrical characterization of HZO-based MIM structures, including impedance spectroscopy, leakage current, capacitance, and polarization measurements.

3.1 Fabrication process

As mentioned in the previous chapter, the ferroelectricity of HZO films has been observed at the nanoscale level, so to characterize their properties, a suitable structure is required to be fabricated to allow structural and electrical characterization. Therefore, we used a MIM-structure capacitor in which the HZO film is sandwiched between two similar metallic electrodes.

The HZO-based MIM structures have been realized in the CEA Leti, PTA, and BCAi cleanrooms. The fabrication process starts with cleaning 4 inches of Si wafers inside the cleanroom. The wafer is often cut into small samples of 2*2 cm^2. Then, the TiN bottom electrodes were DC-sputtered, followed by the RF sputtering of HZO film inside another chamber before being returned to the first chamber for TiN top electrodes deposition. A crucial step to have the desired properties is the post-metallization annealing to crystallize the amorphous HZO sandwiched between the TiN electrodes. Next, the patterning of circular pads with different diameters to have capacitors at the end is performed by successive steps of photolithography, metal evaporation, lift-off, and etching awarded by obtaining the desired capacitors on top of the Si substrates.

Among the different steps, the annealing step is the most important one because it directly affects the properties of the HZO thin films [8], [121], [149]. The process flow is presented in the following section.

3.1.1 Sputtering deposition of HZO thin films and TiN electrodes

In the state-of-the-art, the deposition of HZO thin films or TiN electrodes has been achieved by different techniques, as reported in the previous chapter:

Atomic layer deposition (and Plasma Enhanced ALD) [150], [151]

Sputtering (with a single target, co-sputtering from metallic targets or ceramic targets)[12], [121], [152]

Chemical solution deposition [153]

In this work, the metal-insulator-metal structure has been chosen to study the different properties of the hafnium zirconium oxide (HZO) layer and the related influencing conditions such as TiN electrodes' thickness, the interfaces TiN/HZO, and the annealing parameters ...etc.

We only used the sputtering deposition technique for HZO and TiN thin films. The choice of sputtering as adeposition technique was based on sustainable criteria, as mentioned in chapter 1, and technical criteria (high deposition rate, high-quality films, and thicker films above 100 nm.) for both the HZO layer and TiN electrodes. Besides, sputtering offers the possibility also to deposit the full MIM structure without breaking the vacuum, as reported by Lee et al. using ALD [154]. Unfortunately, the latter possibility was not investigated during this work due to some technical issues related to the sputter equipment Alliance-Concept DP 850 and its long unavailability (mainly due to the COVID crisis).

Sputtering belongs to the physical vapour deposition (PVD) deposition family. Its working principle is based on the creation of plasma to guide the gas ionized molecules towards the target (by applying a voltage between the anode and cathode, which are, in this case, the substrate and the target, respectively). As a result, the molecules of the target's material are ejected and transported to the substrate, where they stick to form the thin film [155].

For the HZO thin films, we used a radiofrequency (RF) sputtering system, which is usually used for dielectrics deposition. While a Direct Current (DC) system, in other equipment, has been used to deposit TiN electrodes. The DC sputtering system is the basic model of sputtering. The other systems are upgrades of DC sputtering [156]. The DC sputtering system comprises a couple of planar electrodes (cathode and anode). The glow discharge is created after applying several kilovolts of a DC voltage with a series resistance between 1 and 10 kΩ at a proper argon (Ar) pressure. As a result, Ar ions are accelerated and sputter the target's material. For an RF system, the main difference with a DC system is substituting the target's material with a dielectric one because the plasma cannot be sustained with a dielectric due to the immediate buildup of a positive surface charge on the surface target (dielectric) [157].

3.1.1.1 HZO Sputtering chamber

All HZO thin film samples are prepared inside a sputtering chamber schematically shown in Figure 42. First, samples are inserted via a load lock with a separate pumping system like the one used for the deposition chamber. Next, HZO Samples are clamped onto a substrate holder. During the deposition process, it is suspended from the chamber ceiling. An electrical connection to the substrate holder allows the application of a radiofrequency (RF) bias. Finally, the substrate can be rotated around the chamber axis. This allows to get a homogeneous film and, at the same time, keeps the substrate temperatures low.

The deposition equipment is a commercial Alliance Concept DP850 device. It is composed of the main enclosure, maintained under ultra-vacuum (lower base pressure at 10^{-8} mbar), and a transfer airlock. The substrates are introduced into the enclosure through this airlock, in which a high vacuum (10^{-7} mbar) is established to minimize contamination in the deposition chamber during the introduction of the sample and, therefore, reduce the pumping time.

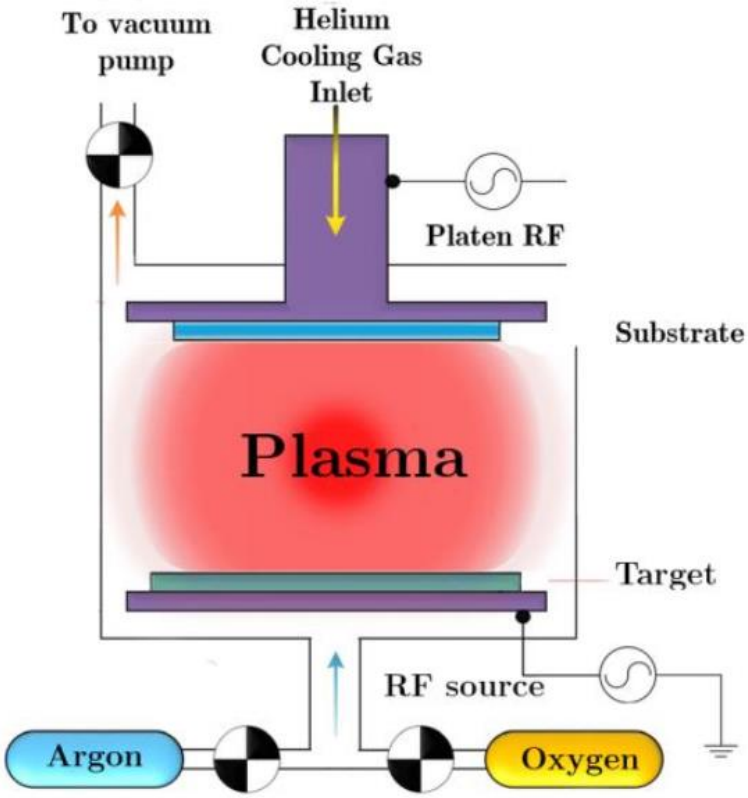

Figure 42 Illustration of sputtering phenomena

The main sputtering chamber has: 4 rectangular targets of the same surface and two sputtering systems: radiofrequency (RF) and direct current (DC) sputtering. The HZO thin films used within the framework of this thesis are deposited by RF sputtering. Figure 43 shows the user interface of the sputter with HZO targets located in position 3. The targets of HZO are installed to be convergent. The deposits were carried out with an argon gas plasma, introduced at a working pressure of 5.10^{-3} mbar.

Under normal operating conditions, the flow of atoms is constant; the thickness of the deposited material, therefore, depends only on the exposure time of the substrate. Knowing the thickness of the deposited layers is based on a calibration of the material flow. It is carried out ex-situ by measuring the thickness of standard samples using a micro-profilometer, X-ray reflectometry, ellipsometry or TEM images.

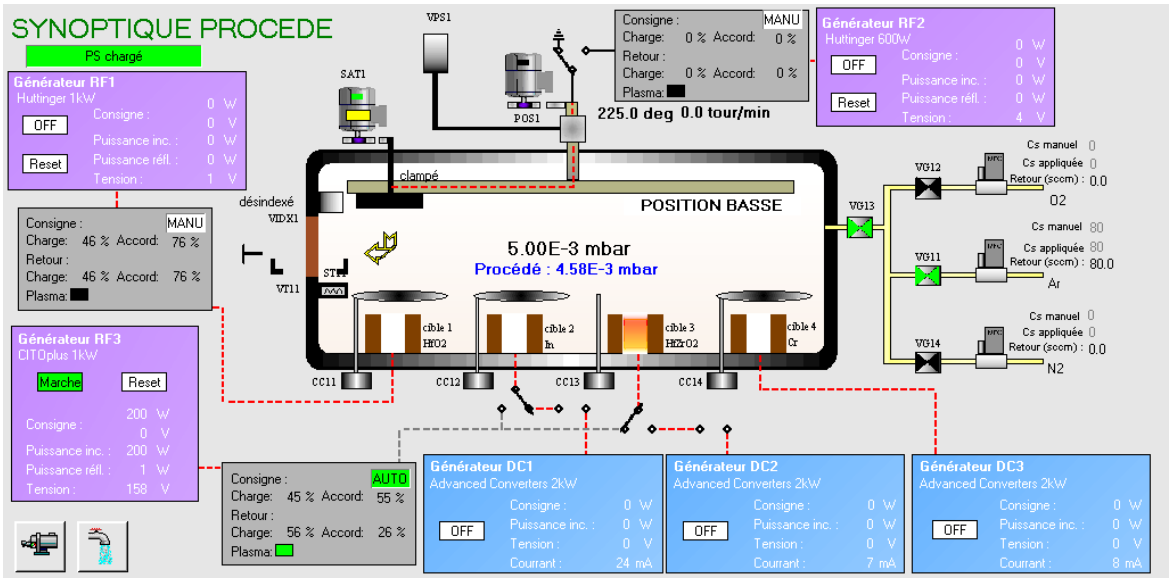

Figure 43 The user interface of the DP 850 sputtering equipment

There is no perfect deposition technique. Each deposition technique has its advents and drawbacks, and the choice of the deposition technique strongly depends on the desired application.

In general, the sputtering technique, with its different systems, has some advents such as:

- A large range of materials can be deposited with high purity.
- Both elements and compounds can be sputtered.
- The target assures a stable and reproducible deposit for a long time.

- The reactive sputtering adds more options compared to other techniques.
- The substrates can be very small or very large, discrete, or continuous.
- The dimensions of a sputter chamber can be small due to the close target-substrate distance.

And each sputtering equipment can additional advents. The used DP 850 equipment presents some advents such as:

- Single-target deposition of compounds (HZO in our case)
- The multiplicity of the sputtering parameters to be optimized to get excellent quality films.
- The substrate dimension can vary from 1*1 cm^2 to 200 mm Si wafer.
- The control of substrate rotation during the deposition
- RF power can reach 1 kW.
- The possibility of substrate biasing
- The possibility of different dielectrics deposition without breaking the vacuum (Metal-Ferroelectric-Insulator-Semiconductor, for example).

On the other side, some drawbacks can be found in the sputtering technique, such as:

- The optimization of some materials takes more time before reaching the producible phase, and the targets can be expensive.
- The non-uniform removal of particles from the target can lead to non-uniform deposited films in the long term.

Moreover, for our equipment, its main drawbacks can be summarized in the following points :(not necessarily related to the drawbacks of sputtering but mostly to technical issues):

- The short availability of the equipment due to
    - The multiple breakdowns
    - COVID-19 impact.
    - Target contamination with Cu.
- The substrate temperature cannot be controlled.

3.1.1.2 TiN electrodes:

For TiN electrodes, a commercial Alliance-Concept CT 100 deposition equipment has been used. It is a two-chamber sputtering system with manual loading; each chamber contains four targets. One chamber is dedicated to the metals, and the other is for

dielectrics. The plasma power can reach 1 kW, and the size sample can be from a small to 4 inches wafer. In this sputter, we can rotate the substrate holder during deposition. The deposition of TiN is a reactive sputtering deposition in which we used a Ti metallic target with Ar/N_2 gas flux to form the nitride of titanium.

3.1.2 Fabrication of the capacitors

As mentioned in the introduction of this chapter, the first part is device fabrication. It consists of film deposition and annealing, patterning of capacitors, metal evaporation, lift-off, and etching. This includes several cleanroom steps. The fabrication steps were performed in PTA and BCAi cleanrooms, contrary to the film deposition steps. **Figure 44** presents the scheme of the fabrication process steps.

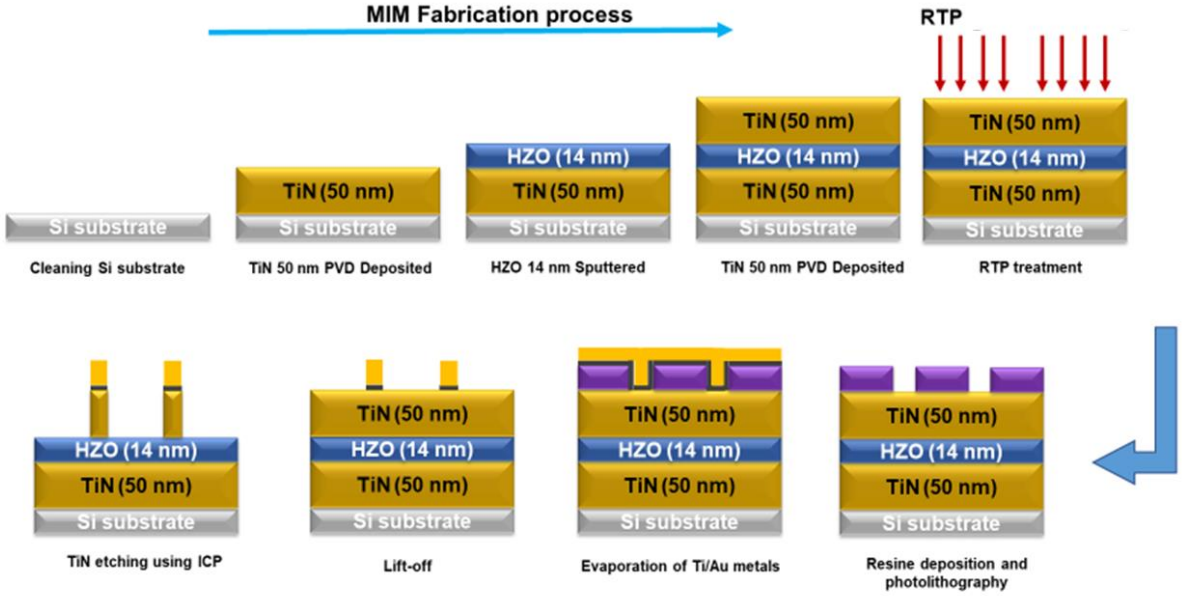

Figure 44 The fabrication process flow of the HZO-base MIM structures

As shown in Figure 44, we used p-type (100) silicon substrates covered with a native SiO_2 layer to deposit the TiN/HZO/TiN stack for a reference sample. Then, A 50 nm-thick TiN layer used as a bottom electrode was deposited by sputtering using a Ti target under an N_2 +Ar plasma at a pressure of 3.10^{-3} mbar and 100 W power. The Ar and N_2 gas flow rates were 40 and 5 sccm, respectively. Before the redeposition of the TiN top electrode, HZO films were deposited in another chamber from a single target of HZO in Ar plasma at a pressure varied from 0.8 to 10×10^{-3} mbar with an Ar flow rate of 60 sccm. The RF power was varied from 200 to 600 W (1.7 to 5 $W.cm^{-2}$).

Before post-deposition annealing (PDA) of the TiN/HZO/TiN stack, an XRD measurement is conducted to check the crystalline state of the HZO films. Once

confirmed to be amorphous, annealing is conducted to crystallize the amorphous film, and after that, an XRD measurement confirms the crystalline structure of the HZO films. At this level, different structural information is obtained. A patterning/etching step is required to obtain small capacitors for electrical measurements to correlate them with electrical properties.

Using a photoresist resin, spun at the surface of the stack, then the capacitor pads mask is patterned using a mask aligner. Next, the resin is removed using a developer solution. Finally, a 50 nm thick Ti layer and 200 nm-thick Au layer were evaporated on top of the stack. A final etching step is needed to obtain the structure of the final capacitor, whatever the etching technique is (chemical or dry).

At this level, electrical measurements are conducted on each capacitor in a specific order mentioned in the third section of this chapter.

3.1.3 Rapid thermal annealing

Inducing the orthorhombic phase via the crystallization of HZO films requires an annealing step to follow the deposition in a range of temperatures going from 300 to 650 °C. Therefore, different combinations of annealing parameters (Gas, temperature, time) were carried out to evaluate their effect. Most of the samples subsequently underwent annealing at low temperatures (450°C).

For the annealing step, we used two pieces of equipment: Jibelec and Unitemp RTP-100. We used the first one during the optimization phase before switching to the second one, as it showed a better performance and closer results to the desired thermal budget.

It has the following advent:

- It can anneal a 100 mm wafer at maximum.
- Ramp up rate up to 150 °C/sec
- Vacuum up to 10^{-3} mbar
- Process gas line with Mass Flow Controller for Nitrogen
- Max Temperature is 1200 °C
- Temperature uniformity ±1.5 % of the set temperature
- Cooling with N_2 with a rate of 200°C/min (from 1200 to 400°C) and 30°C/min (from 400 to 100 °C).

The Jibelec furnace increases the temperature in steps, stabilizing the temperature at each step. This method makes understanding the crystallization of HZO more complicated as the crystallization mechanism and temperature are not fully understood yet. The Unitemp furnace increases the annealing temperature directly to the set one with a 150°C/s ramp, eliminating any undesired effects. Figure 45 shows a typical profile of rapid annealing conducted by the Unitemp furnace. The temperature ascent ramp is well controlled and quickly achieves the annealing temperature. The cooling descent ramp is not controlled by it remains better than the other furnace.

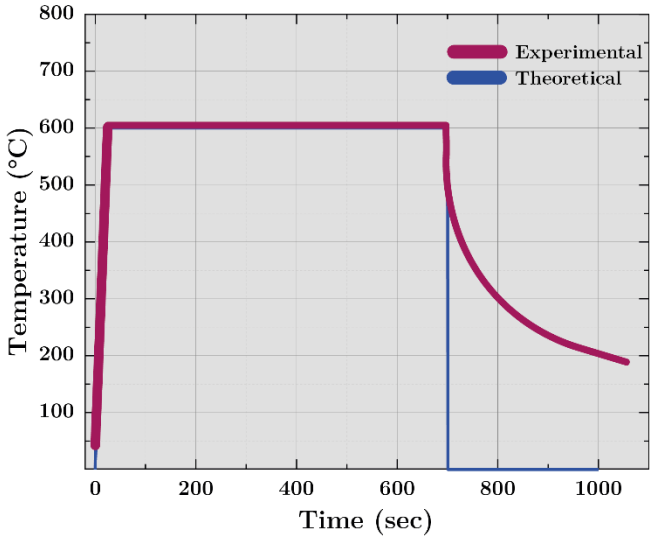

Figure 45 typical profile of a rapid annealing cycle

The annealing part in its theoretical part is quite different from the real one due to the incontrollable cooling process. Real annealing is considered when one counts the thermal budget applied to the sample considering the cooling part.

The particularity of rapid annealing consists of a fast rise from the room temperature to the annealing temperature and a very rapid fall to room temperature. This process is used in the microelectronics industry, and it is generally used to activate the dopants without redistributing them. In our case, it serves to crystallize the amorphous as-deposited HZO film into a metastable orthorhombic phase, as discussed in detail in **Chapter 4**.

The RTA furnace, a diagram shown in **Figure 46**, receives a single wafer at a time or several small samples of a few square centimeters, which are positioned below a set of incandescent lamps. The lamps illuminate the plate, therefore, causing rapid heating.

The temperature ascent ramp is of the order of 150°C/s. A typical annealing profile used for our samples is shown in **Figure 45**.

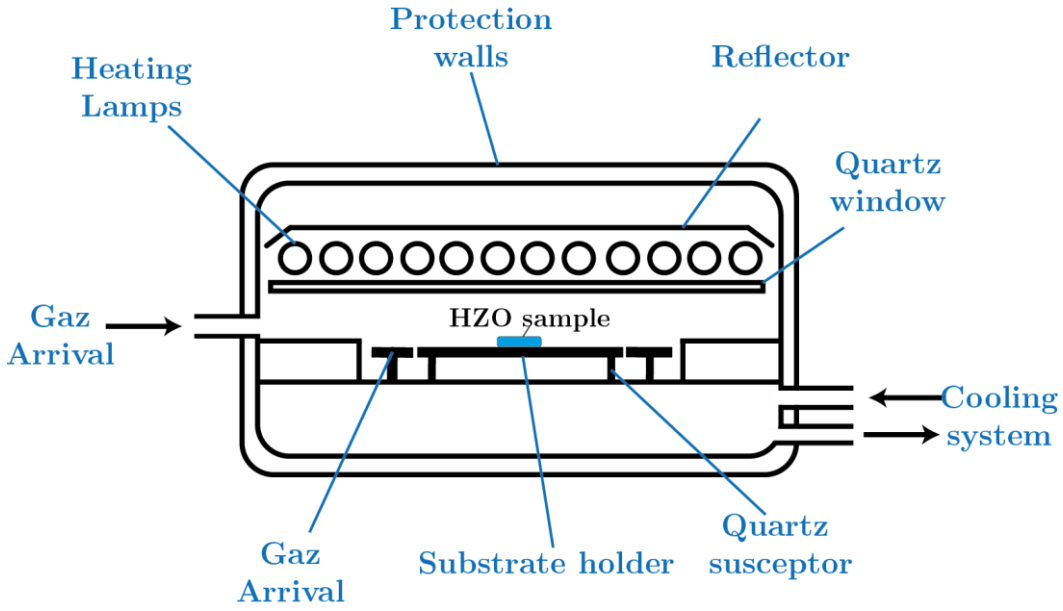

Figure 46 Sketch of rapid thermal annealing furnace

The annealing occurs under an N_2 atmosphere to reproduce the same conditions as the first reports about ferroelectric HZO films.

All the parameters of RTA (initial temperature, heating ramp, gas insertion time, cooling…etc.) were considered and adjusted to obtain reproducible temperature distributions. Figure 46 illustrates a sketch of the rapid thermal annealing furnace.

For the sake of reproducibility, the temperature distribution on the surface of the sample holder was confirmed to be uniform, which allows the annealing of several samples at the same time.

To obtain ferroelectric HZO films, they must be crystallized into the metastable orthorhombic Pca21 phase [121], [158]. It should be noted that the as-deposited HZO films are amorphous, and the sputtering of the TiN top electrode does not change that. At this level, rapid annealing is required to crystallize the films into the orthorhombic phase, and the other phase can appear. To better understand the evolution of the induced phases during annealing, an in-situ XRD measurement has been conducted on amorphous HZO films. More details are mentioned in **Chapter 4**.

3.1.4 Photolithography

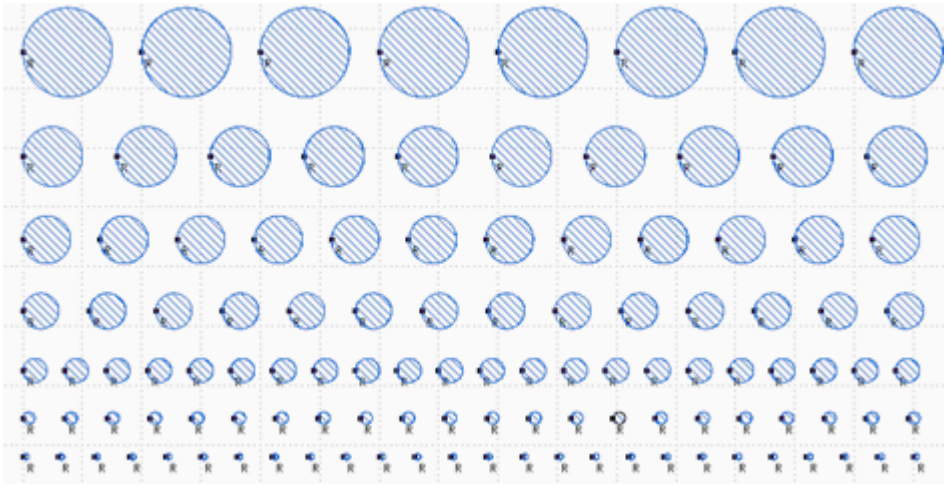

Figure 47 The photolithography mask of different diameters circular pads

After the TiN/HZO/TiN stack deposition and the annealing step, a photolithography/etching process is required. TiN/HZO/TiN was patterned into circular capacitors of different diameters using optical lithography. The desired mask is shown in Figure. UV lithography is adequately precise to achieve the desired dimensions (width of 100 -1500 µm).

The photolithography step requires the spin coating of a reversible photoresist AZ5214 from Microchemicals, a polymer sensible to UV light, on top of the deposited thin films. For a spinning at 4000 rpm, we obtain a thickness of about 1.4 µm. A subsequent hardbake is performed on a hotplate at 100 °C in order to prepare the resist for the exposure step. Finally, using MJB4 SUSS MicroTec Mask Aligner, the UV light is exposed through the mask, with a wavelength of 365 nm, in vacuum contact mode.

The sample is dipped into a developer solution for 40 seconds and then rinsed in double deionized water. The pattern is over the resin layer but not the TiN top electrode at this step. Next, the pattern transfer is accomplished through physical etching, which is stopped upon reaching the ferroelectric film: the desired structures are now obtained. Finally, the sample must be cleaned in order to remove the residual photoresist and be ready for analysis.

For Ti/Au metallic contacts, the sample was installed on a sample holder inside the evaporation chamber (PLASSYS MEB 400S). We deposit 10 nm Ti for better adherence to the Au layer (150 to 200 nm).

After that, the deposited Ti/Au bilayer on top of the sample is lifted off using an acetone bath for a few minutes. Finally, the sample is placed in isopropanol and dried with N_2. An optional step can be added to check the success of each step by the optical microscope.

3.1.5 Etching

A final etching step involves removing the TiN top electrode outside the patterned capacitors with metallic Ti/Au contacts for a proper electrical connection. Three etching techniques have been optimized to etch TiN: Inductively coupled plasma (ICP) etching, IBE Ion beam (IBE) etching and wet chemical etching.

Firstly, ICP-RIE has been used to etch TiN using chlorine-based chemistries. The etch process was performed on an Oxford Instruments Plasmalab 100 RIE-ICP tool with 100 W RIE power and 250 W ICP power. The plasma is generated with an RF powered magnetic field. By adding an inductively coupled plasma source to a standard RIE system, a high plasma density can be reached by adding a source of ICP to the standard RIE system. Other optimized fluorine-based chemistries showed better reproducibility with 10 nm/min etching speed.

After that, TiN etching was done by IBE etching on MU400 equipment from PLASSYS using Ar gas. It is realized by a beam of charged Ar ions directed to the sample suitably in a high vacuum chamber. Ar ions' directional beams control the etched sidewall profile and radial uniformity etching. Therefore, it is considered a non-selective physical etching. The etching speed was around 0.4 nm/min.

Finally, the chemical etching was performed using ammonia solution (NH_4OH), Hydrogen peroxide (H_2O_2) and deionized water with a ratio of 1:2:25 heated at 50°C. This etching solution is selective to oxides, i.e., the etching stops once the TiN is removed and the oxide layer is exposed. The resulting etching speed was around 5 nm/min. As a result, the chemical etching showed better reproducible results than the other techniques.

Now, the capacitor devices are ready for the electrical characterization

3.1.6 Summary

MIM structures' fabrication steps have been realized to conduct structural and electrical characterizations. Figure 48 illustrates the resulting circular pads obtained after the photolithography/etching process. Furthermore, each step of the fabrication flow has been optimized, from the TiN deposition, HZO sputtering, annealing, and etching, in order to assure reproducibility, and no step affects the properties of HZO films in a detrimental way.

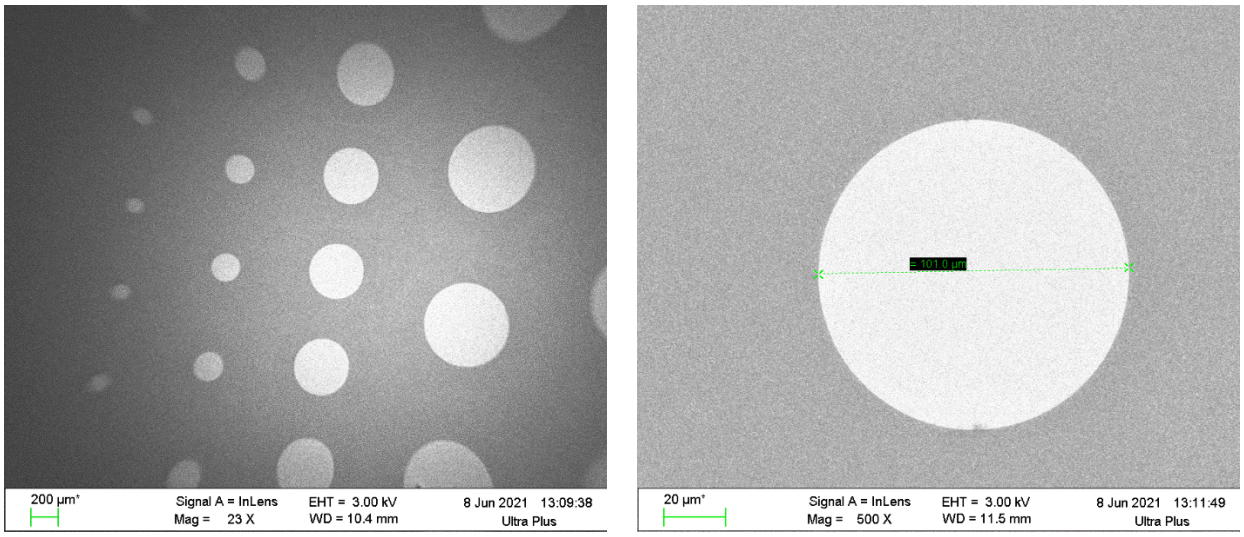

Figure 48 SEM images of the circular pads after etching (left) the smallest circular pad of 100 µm

3.2 Physical and structural characterizations:

As the MIM capacitors fabrication is described in the first section, we describe the characterization techniques used to determine the different properties of the films and the impact of the annealing step. The characterization tools' choice was made to completely understand the ferroelectricity induction within HZO thin films. The challenge was to find a correlation between the microstructural properties, mainly the stabilization of the orthorhombic phase at room temperature, and the electrical properties principally resumed in the hysteresis loop of the P-E measurements or the butterfly-shaped C-V measurements. As the literature review shows, there is a consequent lack of information about the microstructure of HZO and its dielectric properties, so another goal has been set to investigate the microstructural and dielectric properties.

Hereafter, the characterization of the microstructural properties provides a central part of information about the crystalline state, i.e., the orthorhombic phase, responsible for the ferroelectricity. It is presented first.

Physical information was first obtained using XRR (X-Ray Reflectivity) to determine the films' thickness, density, and roughness. Then, the roughness value is confirmed by AFM (Atomic Force Microscopy). Finally, XPS (X-Ray Photoelectron Spectroscopy) was employed to determine the composition of the films.

In the first round, structural hints about the crystallinity of the as deposited and annealed films were obtained through GIXRD (Grazing Incidence X-Ray Diffraction).

The TEM (Transmission Electron Microscopy) was also used to confirm the films' thickness, composition, and crystallization. Finally, GIXRD and TEM were reconducted to investigate the impact of the annealing parameters.

3.2.1 X-rays

The characterization of structural properties of HZO thin films is mandatory to determine the crystalline phase, which is responsible for the dielectric properties, including ferroelectricity. The basic characterization method to obtain such information is based on X-ray diffraction. Therefore, it is an essential tool for characterizing thin films of dielectric materials. XRD has several operation modes and measurement types that allow having different information such as the present phases, the degree of crystallinity, the grain size, crystal defects, and others. The choice of the measurement type also depends on the sample type (thin films, powder, epitaxial growth, polycrystalline materials, etc.). In addition, it is used in the microelectronics field to determine the amorphous-to-crystalline transition temperature of dielectric materials after annealing processing. In this work, the choice of operation mode and measurement type is made for the thin films only for the deposited HZO and TiN layers in the range of 10 to 400 nm at maximum, which remains thinner than the standard samples for conventional diffractometers.

3.2.1.1 X-ray Diffraction:

XRD's principle is based on an X-ray beam directed to the sample's surface, where the X-rays hit the atomic planes and then scatter, as shown in Figure 49. The wavelength of the X-ray beam is in the same order of magnitude as the distance between the crystal planes. This is a basic fact to understand the interference pattern caused by the scattered photons from adjacent planes. The detector collects the interference pattern, and it allows to distinguish the different crystals according to Bragg's law:

$$n\lambda = 2d\sin\theta$$

d: the distance between the parallel planes, θ: the angle formed between the incident beam and the diffracted beam, n: the diffraction order, and λ the wavelength of the X-ray beam.

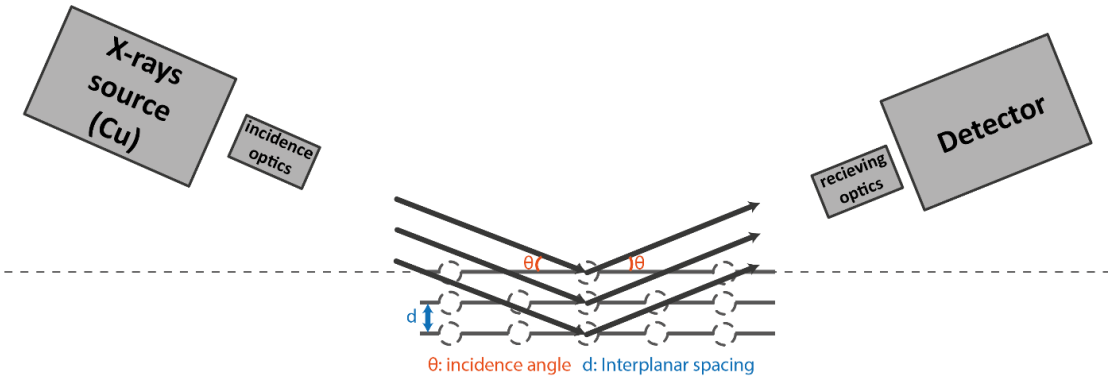

Figure 49 Schematic of X-ray diffraction principle

For the GIXRD configuration, the diffraction patterns are collected from the top layers of the sample, so a very low incident angle is chosen for the beam, between 0.5 and 1°, which limits the penetration depth of the X-rays to a few nm only. The polycrystalline nature of the films causes the diffraction of the incident X-rays at different angles. Scanning along 2θ allows capturing them all with different intensities. Based on the crystal symmetry, some combinations of diffraction peaks at certain angles of 2θ can be used to distinguish different phases in the polycrystalline layer, which is the case often for hafnia ferroelectrics with the ferroelectric orthorhombic and tetragonal phases, which have very close lattice parameters and very close 2θ peak positions.

All the XRD data reported in this work have been taken between LMGP Lab and CEA Leti diffractometers with GIXRD configuration (fixed incident angle and moving detecting angle), with a RIGAKU Smartlab diffractometer and X'Pert Pro by Panalytical, respectively, with the 1D detector of X'Celerator type and using a Cu (λ = 1.54 Å) X-ray beam. Both diffractometers are equipped with a 9-kW rotating anode Cu source (45 kV and 200 mA).

Since the main peak of the orthorhombic phase is 30.4°, so most measurements were scanned around the 30° with a scan length of 10° which is sufficient to cover the different phases of HZO, and some measurements were wider from 20 to 60°.

The number of counts represents the GIXRD result as a function of the 2θ angle. The plots are fitted with OriginLab software, and for the peak identification, the resulting patterns are compared to the different patterned HZO referenced in databases using DIFFRAC.EVA software from Bruker. The patterns are presented in the following table:

Table 6 The reference patterns for HZO crystal phases

HZO phase: crystal system	Space group	Behaviour	Reference in database
Orthorhombic	Pbcm	Paraelectric	040036960
	Pbca	Antiferroelectric	010830808
	$Pmn2_1$	Ferroelectric	/
	$Pca2_1$	Ferroelectric	040055597
Cubic	Fm3m	Paraelectric	040032612
Tetragonal	$P4_2/nmc$	Paraelectric	040118820
monoclinic	$P2_1/c$	Paraelectric	000340104

For TiN electrodes, we compared the obtained patterns with 00-038-1420 for the cubic phase of TiN from the ICDD database.

A last important note to be mentioned is that the GIXRD measurement was conducted on TiN/HZO/TiN stacks before and after annealing since the presence of the TiN top electrode is essential to induce the orthorhombic phase.

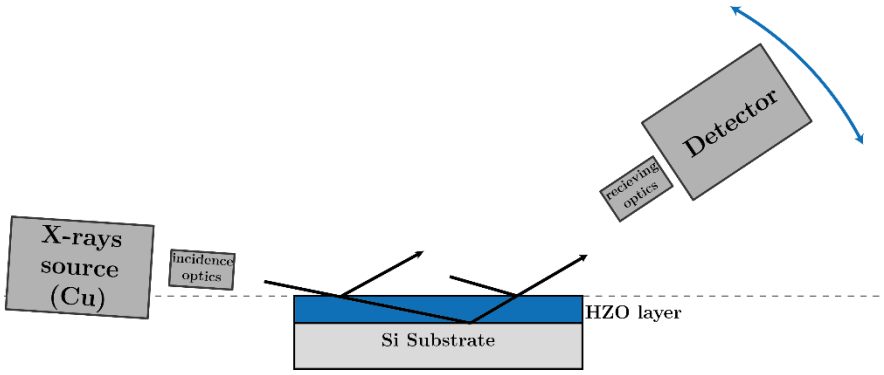

Figure 50 Sketch of the GIXRD configuration

3.2.1.2 X-ray reflectivity

Another technique based on X-rays has been used during this thesis; X-ray reflectivity (XRR).

It has been used to determine film thickness, density, and roughness. X-ray reflectivity is a non-destructive technique. Compared to XRD, the crystalline state of the films is not essential for XRR. Figure 51 shows the reflectivity plot of HZO film deposited on a Si substrate.

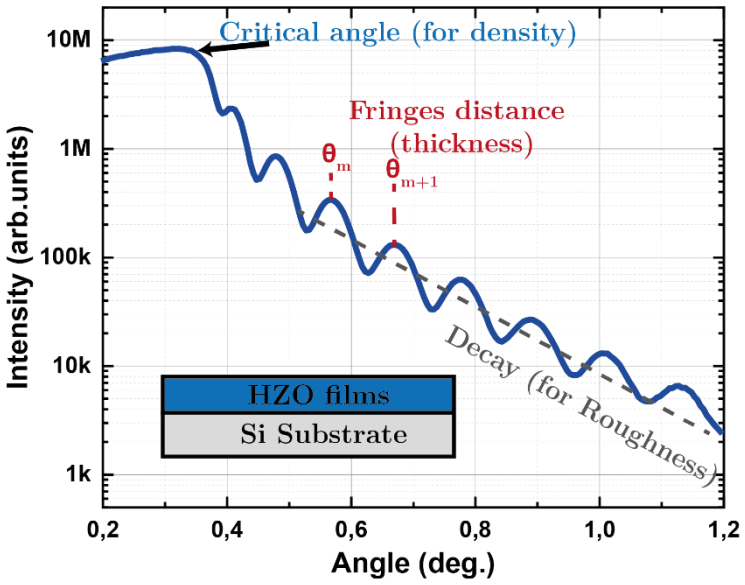

Figure 51 Sketch of the features in an XRR plot for a single layer of HZO

The XRR data collected have been in an X'Pert Pro by Panalytical with a 1D detector of X'Celerator type and a Cu (λ = 1.54 Å) X-ray beam. The operation setup is almost identical to the Bragg Brentano geometry of XRD. The difference remains in the optics, where we use an X-ray mirror for a parallel beam instead of the incident beam optic. The incidence angle is varied from 0.4 to 3°, depending on the critical angle of the material and the layers of the sample.

The determination of the incidence angle range is based on avoiding the critical angle which causes the total reflection. This critical angle is dependent on the film's density and composition. The density of the top layer ρ can be calculated from the critical angle θ_c as first proposed by Kiessig [159]

$$\rho \approx (\frac{\theta_c}{\lambda})^2 \frac{\pi}{r_e}$$

ρ: the density, λ is the wavelength and r_e the electronic radius

The incident angle is above the critical angle. The X-rays are reflected from each interface in a single-layer thin film. Oscillations have resulted from their interferences. These oscillations are called Kiessig fringes. They are formed by the phase difference between X-rays reflected from different surfaces, and their period is dependent on the film thickness (for thicker films, the oscillations are shorter). The following Fresnel equation determines the thickness

$$e = \frac{\lambda}{2} \frac{1}{\theta_{m+1} - \theta_m}$$

e: the thickness, λ: the wavelength, and θ_{m+1}-θ_m: the angular distance between two successive interference maxima.

Finally, the film's roughness is determined by the reflectivity intensity decay. It includes the film's roughness and interface.

The XRR resulting plots, reflectivity intensity versus the incident angle, are fitted with DIFFRAC.LEPTOS software from Bruker. More information about the fitting and extraction of parameters can be found in [160].

3.2.1.3 X-ray photoelectron spectroscopy

As HZO is a ternary oxide and the elements fraction determines the dielectric properties, we used another X-ray based technique to investigate the impact of sputtering parameters and annealing over the initial composition ($Hf_{0.5}Zr_{0.5}O_2$).

We used the X-ray photoelectron spectroscopy (XPS) technique for this aim. It was used to determine the stoichiometry and chemical state of the elements in the HZO films. XPS was performed on Si/HZO samples using a Thermo Fisher Scientific Theta 300 equipment with a monochromatic Al K_α source, a beam size of 400 µm, and a pass energy of 100 eV.

XPS measurements have been conducted inside an ultra-high vacuum chamber to eliminate any possible contamination, incident beam absorption, or any collisions of the ejected electrons before reaching the detector. The XPS principle is illustrated in Figure 52.

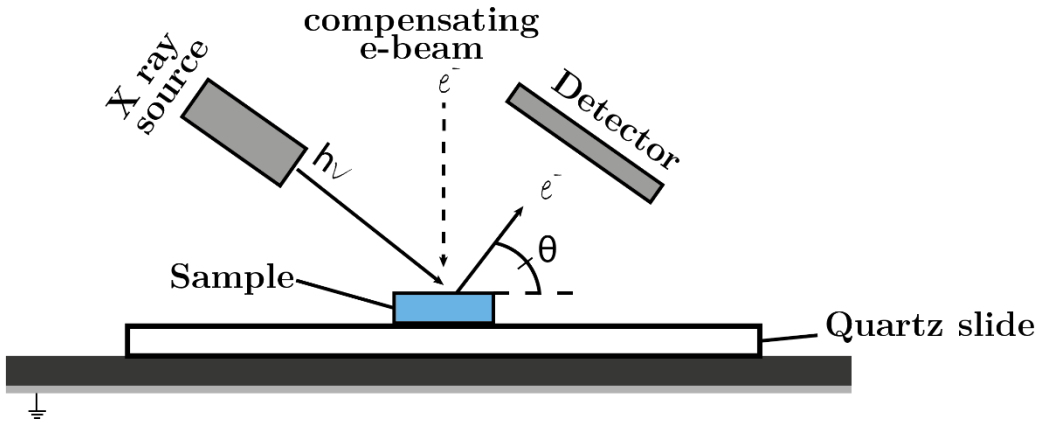

Figure 52 Principle of X-ray photoelectron spectroscopy (XPS)

It should be noted that an electron beam exists to continuously compensate for the positive charge left on the sample by the charges ejected. The sample is insulated from

the ground to avoid any compensation, causing in different results due to the different surface potentials.

Electrons lied to an atom are described by their principal, angular and spin quantum numbers **n (1, 2,....), l (s,p,d,....) and s = ±1/2**, respectively. The total angular quantum momentum **j** is the total of angular and spin quantum numbers **(j = l + s)**. For all electrons from orbitals of an **l > 0**, doublets are formed except ***s*** orbitals **(l = 0)** that form singlets in which no spin-orbit coupling exists.

The obtained binding energies were corrected using a standard. In this work, the carbon was the internal standard with a binding energy of C1s = 284.8 eV for the data processing of the peaks. The binding energies of carbon are mentioned in Table 7.

Table 7 Reference peaks used for XPS spectra calibration

Element	Orbital	Chemical	Peak (eV)	Reference
C	C1s	C-C	284.8	[161]
		C-O-C	~286	
		O-C=O	~288.5	

The position of a doublet is dependent on the binding partners of an atom. Thus, nitride bonds shift a metallic peak to higher binding energies, such as TiN, for example, and bonding to oxygen can shift it even more.

Generally, the obtained spectrum is the envelope of several doublets because of the averaging over many atoms, so more than bonding appears. Finally, the envelope is deconvoluted to see the different doublets. This has been done in this work using Avantage [162] and CasaXPS [163] for data processing.

For the deconvolution of the envelope, there are three essential a-priori limits we used:

1. The corresponding peak area of a doublet is fixed following the values mentioned in **Table 8**.
2. The values of full width at half maximum (FWHM) of two peaks from the same doublet are the same.
3. The difference between a doublet peak is the range of 1.6 to 2.1 eV.

Table 8 Surface area ratios between the two peaks of a doublet belonging to a certain angular quantum number

Angular quantum number l	j	Surface area ratios
s	½	singlet
p	½, 3/2	1:2
d	3/2, 5/2	2:3
f	5/2, 7/2	3:4

Among the resulting spectra, a survey spectrum appeared for the HZO sample. Figure 53 shows an example of the XPS survey spectrum. Hf, Zr, O, Si and C elements have been observed. No contamination/impurity is detected except for the surface contamination of carbon. Figure 54 illustrates a zoom on the Hf doublet in the envelope without processing yet.

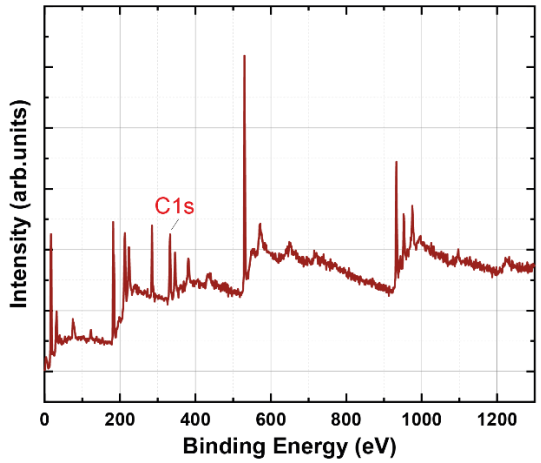

Figure 53 Survey spectrum from of HZO films.

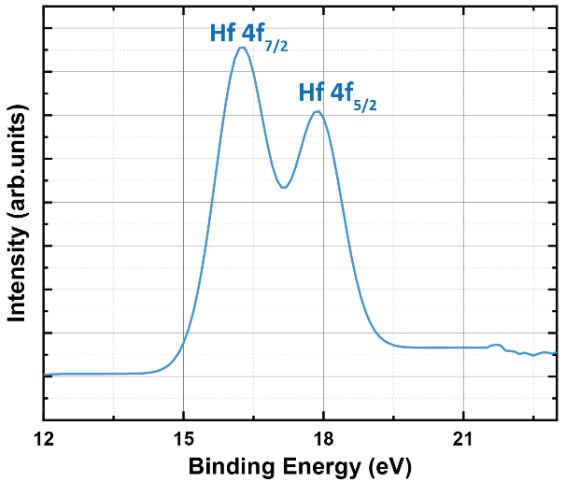

Figure 54 Example of Hf 4f doublets.

Angular analysis mode:

It is a non-destructive mode based on varying the angle between the detector and the normal to the sample's surface, often between 23° and 76°. This variation causes a change in the mean free path of the photoelectrons, so a change in the analysis depth. Measurement at 76° corresponds to analysis very close to the surface, while at 23°, the analysis is deeper, as shown in Figure 55 for Zr doublet.

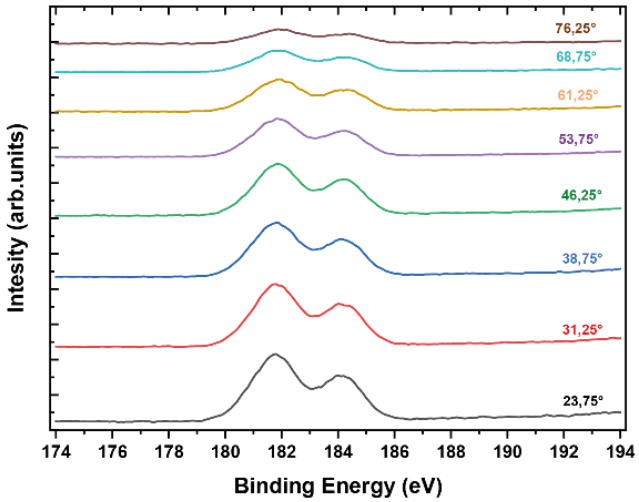

Figure 55 Angle XPS Zr

A concentration profile over a depth of the order of 3λ can be obtained from this mode. This resulting profile results from mathematical processing of the XPS data using the Avantage software, CasaXPS or OriginLab. Besides, the thickness of the films can also be obtained based on the ratio of the area of the peaks at different angles.

3.2.2 SEM and TEM

Electronic microscopy is another branch of structural characterization. It allows to check the crystallinity of the films and determine their thickness.

Its working principle is based on the acceleration of a focused beam of electrons in a vacuum in the direction of a sample. The interactions between the electron beam and the sample generate an image that allows obtaining the desired information.

3.2.2.1.1 Scanning electron microscopy (SEM)

SEM is based on a fine focused electrons beam directed to the sample. Using SEM, magnified images can be obtained in the order of $x10^6$, which helps obtain information about the surface of the sample and its elemental composition.

Its working principle is based on an electron gun that emits a stream of high-energy electrons towards a sample, as illustrated in Figure 56. First, the electronic beam is focalized using electromagnetic lenses. Then, it scans its surface in a rectangular raster. The SEM has a large depth of field, which allows a large area of the sample to be in focus at one time and produces an image that is a good representation of the three-dimensional sample. The SEM also produces high-resolution images, which means that closely features can be examined at high magnification.

The beam-sample interaction generates secondary electrons, backscattered electrons, and X-rays. These interactions are detected and treated to generate a magnified image.

In this work, ULTRA plus SEM equipment by Zeiss has been used and equipped with an EDS module (Energy Dispersive X-ray spectroscopy).

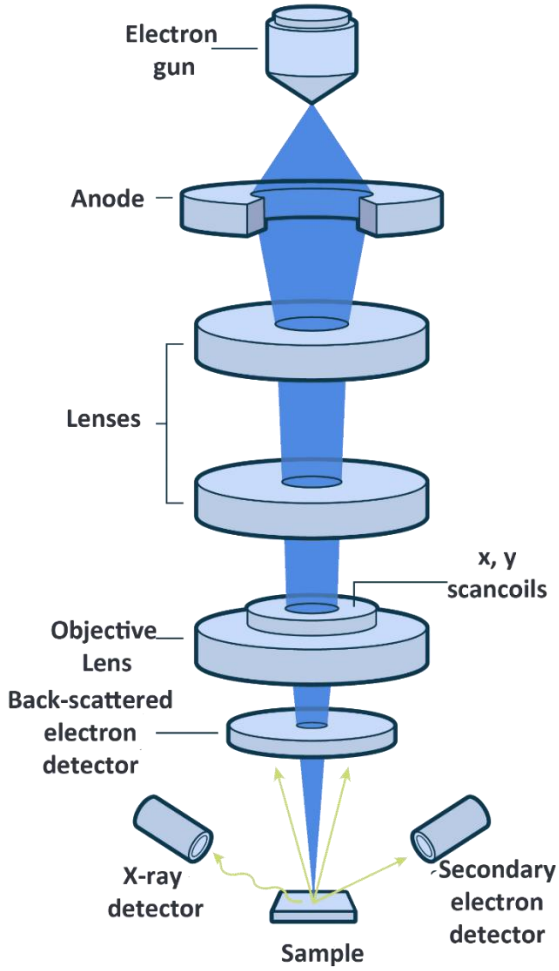

Figure 56 sketch of SEM working principle and main parts

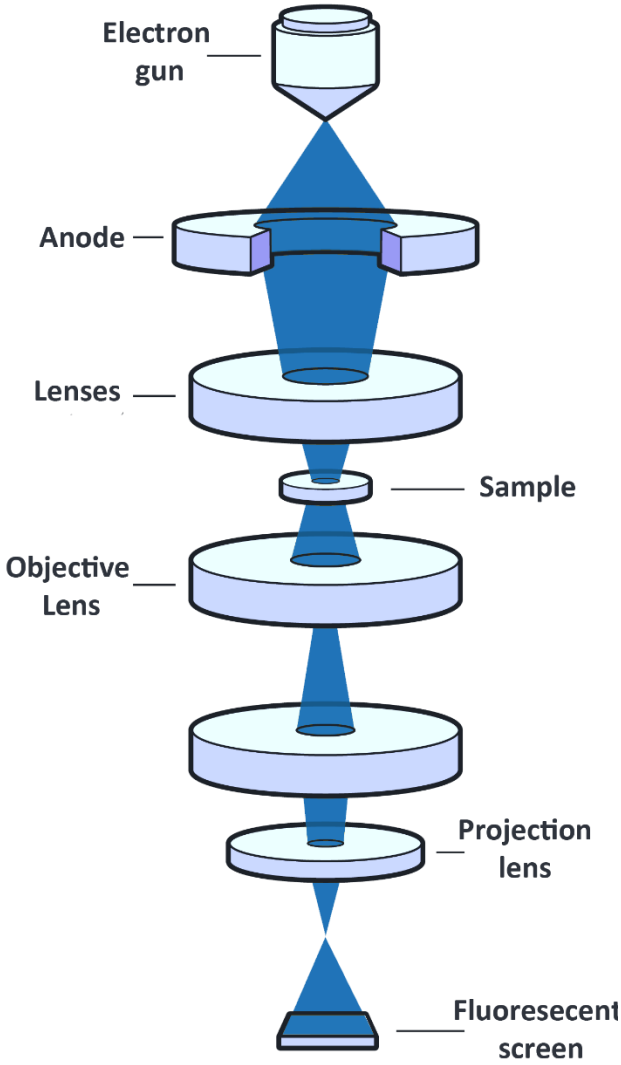

Figure 57 Sketch of TEM working principle

3.2.2.1.2 Transmission electron microscopy (TEM)

TEM is a structural technique using a broad electrons-beam to generate an image of a sample's internal structure by penetrating through the sample, allowing to have information about the morphology, composition, and crystal structure. Both images and diffraction patterns are obtained by TEM. It has a higher resolution compared to the SEM because it uses a smaller de Broglie wavelength ($\lambda < 0.05$ Å) instead of the visible light (3900 – 7000 Å). Since the wavelength of these electrons is orders of

magnitude smaller than visible light, much more detailed features can be resolved using TEM. However, it requires a specific preparation of the sample to conduct the measurement. Before starting, a thin lamella is cut using a focused ion beam. The conventional thickness of lamella is around 50 nm, but it can vary depending on the targeted information, impacted by the intensity, which becomes too low due to absorption and inelastic scattering [164].

As shown in Figure 57, the TEM's working principle is based on a parallel electron beam transmitted through the lamella, which interacts with it and makes a complex image. Its contrast depends on the thickness, atomic mass, and crystal structure of the sample. TEM's three main modes of contrast formation are mass-thickness contrast, diffraction contrast, and phase contrast[164].

In polycrystalline samples, grain overlap often occurs, generating interference patterns (Moiré fringes [164]) that hinder the structural results.

However, the lamella of different films was prepared for TEM employing the focused ion beam (FIB) technique. TEM measurements were performed by Gauthier Lefevre (LTM) using a double-aberration-corrected FEI Titan Ultimate TEM equipped with a high brightness electron source working at an acceleration voltage of 300 keV and with a Gatan Quantum energy filter.

3.2.3 AFM

The simplest form of AFM can be resumed in a tiny probe scanning the top surface of a sample. Important information such as topography can be extracted. The basic elements of an AFM are the following:

- A scanning probe made of a cantilever and tip.
- An XY scanner to move the sample.
- A Z piezo actuator.
- A laser and a photodetector.
- Feedback loop

Depending on the probe-material (sample) interaction type, the AFM mode is chosen (contact, non-contact, or tapping mode). Two main components define the probe: one is the cantilever, which is a beam having one end clamped to its holder and the other end loose and free to oscillate. The second one is a pyramidal-shaped tip located on the bottom side of the cantilever at its loose end. A typical tip is several µm high and has an end radius of as little as a few nm. On the top side of the cantilever, in

correspondence with the tip location, is shined a laser that is reflected against a photodetector.

The AFM's principle consists in sweeping the studied surface using a point fixed on a deformable beam. When the tip has approached the surface, interaction forces will be applied on the tip, for example, the Van der Walls force as a function of the sample-tip distance. The applied forces are sensed and analyzed via the deflection amplitude of the beam carrying the tip due to the laser beam focused on the end of the tip.

Consequently, the deflection of the cantilever corresponds to the position of the laser spot on the photodetector, which is divided into four quadrants to separate vertical and horizontal components. The laser position becomes an input of the feedback loop that ensures that cantilever deflection or oscillation, corresponding to the contact or non-contact modes, respectively, remain constant and equal to the value set by the user. The information recorded by the photodetector makes it possible to trace the topography of the surface. A surface scan is acquired by moving the sample on the horizontal plane thanks to an XY scanner while the probe always remains fixed in its position.

Depending on the components and desired information to extract, AFM can be expanded to more sophisticated techniques such as the PFM (Piezo Force Microscopy), which is a trending technique to characterize piezoelectric and ferroelectric materials, including HZO, at the nanoscale level (few nanometres of thickness) [165], [166]. In addition, the electromechanical nature of ferroelectric can be sensed by the AFM's tip, which detects the small displacement of the material subjected to an electric field.

In this thesis, AFM is used primarily to measure the surface roughness and grain size of HZO and TiN films. The roughness of the films was also analysed by atomic force microscopy on a Bruker Dimension ICON system using VTESPA-300 probes.

3.3 Electrical characterizations

Nevertheless, the most important side of ferroelectric HZO is its electrical properties, which are one of the main focuses of this work; they can be summarized in a hysteretic behaviour. The principles of impedance spectroscopy, leakage current (I-V), Capacitance-voltage (C-V), and Polarization-Electric field (P-E) measurements are described.

MIM capacitors have been fabricated in order to characterize the electrical properties of HZO layers. The desired quantities such as dielectric constant, coercive field, remanent polarization, and leakage current are measured via the capacitor. The measurements were carried out on a Ferroelectric Analyzer TF 3000 equipment produced by the equipment manufacturer Aixacct. It allows the different electrical measurements on the same bench and the possibility of heating the sample during the measurements.

On the bench, two micromanipulator probes are connected to the MIM capacitor's TiN bottom and top electrodes. A Thorlabs CMOS camera facilitates identifying the capacitors, their position and diameter, and moving the probes.

Once the probes are in their position, a first connection is established via the impedance analyser (Hioki IM3570) to assure having a capacitor behaviour by measuring the impedance as a function of frequency which is varied from 50 Hz to 5 MHz.

3.3.1 Impedance spectroscopy

Impedance Spectroscopy allows determining the existence of structural inhomogeneities within the samples via frequency-dependent (5 Hz to 5 MHz) measurements of the complex impedance.

$$Z=Z'+ jZ''$$ [167].

It is based on modelling the dielectric AC response of a system by an equivalent circuit. Information related to the sample can be extracted from the fit parameters of the selected equivalent circuit. The impedance measurements were performed on an IM3570 Impedance analyser, including an LCR meter by the Hioki manufacturer. It allows measuring the parallel capacitance, resistance, impedance, dielectric constant, loss coefficient, and other quantities.

A small-signal amplitude of 100 mV was used to have the same field as the small-signal capacitance-voltage measurements. The analysed frequency range was 50 Hz to 5 MHz.

Coaxial BNC cables connected the low and high current directly and voltage ports, of the IM3570 impedance analyser, to the micromanipulators in the bench of electrical measurements. The current response is sensed at the bottom electrode of the samples.

As we measure the impedance of a capacitor (MIM structure), Figure 58 presents the corresponding equivalent circuit for the MIM structure. This case is the basic one. An ideal case is to have a perfect capacitor without any losses. However, the existence of

interfaces between the dielectric layer and the electrodes can make the equivalent circuit more complex. This is discussed in detail in chapter 5.

The reactance of an ideal capacitor reactance is calculated by

$$X_c = \frac{1}{j\ 2\pi fC}\ [\Omega].$$

When X_c is small, the impedance is considered to be almost X_c if R_p is placed. A real capacitor relates to R_s and R_p in series and in parallel, respectively. However, R_p is frequently extremely large (MΩ order), and R_s are extremely small (several Ω or less). Therefore, Rs is not negligible when X_c is small; the setup is considered as a series equivalent circuit with X_c and R_s. By contrast, R_p cannot be negligible when Xc is large, but R_s can, so the setup can be treated as a parallel equivalent circuit.

For the impedance spectroscopy, a linear response of the system is assumed, i.e., the applied sinusoidal voltage excitation V (t) results only in a sinusoidal current response I (t) of the same angular frequency ω and shifted by a certain phase angle ϴ. The measurement method and the choice of equivalent circuit are detailed in chapter 5.

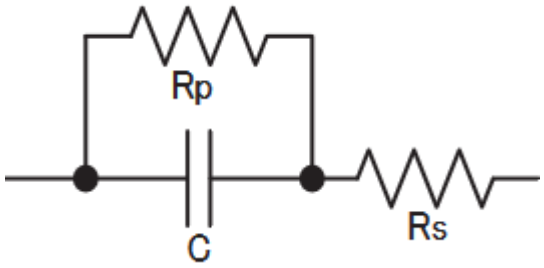

Figure 58 Equivalent circuit of MIM structure

3.3.2 Leakage current measurements

A basic characteristic to be measured for insulators is conductivity. An externally applied voltage generates a leakage current flow through the dielectrics. This current flow can be impacted by temperature. It depends on the mobility of free electronic or ionic charges in the dielectric properties [9–13].

For conductivity, the leakage current measurements or the Current-Voltage (I-V) is a basic and well-established electrical characterization technique of capacitors.

The measurements were carried out on a Ferroelectric Analyzer TF 3000 equipment produced by the equipment manufacturer Aixacct.

They are mainly used to measure the leakage current density and the conduction mechanism of the MIM capacitors. High leakage currents can affect the shape of the hysteresis loop, especially at high voltages or low frequencies. In addition, they can also be performed while heating the sample and fatigue measurements. The C-V measurements are also performed on the same Ferroelectric Analyzer.

A special step-shaped voltage waveform is applied to the sample during the measurements, and a virtual ground amplifier measures the current response at each voltage step.

HZO-based capacitors are considered as a model of parallel capacitors, RC-time constants, and a voltage-dependent resistor. Thus, the current response due to an applied staircase waveform must be analysed to extract the leakage current information because it results only from the voltage-dependent resistive part of the sample.

3.3.3 Capacitance voltage measurements

Another important measurement often characterized by dielectrics is capacitance. It is measured via a small-signal triangular continuous wave of 100Hz-10 kHz frequency modulated on top of a bias voltage. The measurement was performed on the ferroelectric Analyzer. The excitation signal is a changing triangular-shaped base waveform of low frequency with small-signal voltage to generate less stress over the sample. Many essential electrical properties of dielectrics, including dielectric constant, loss factor, and others, can be extracted from the C-V results.

The C-V measurements confirm the results of polarization-field measurements, whether the measured material is ferroelectric or just a dielectric. The shape of the C-V curve depends on the material's nature.

3.3.4 Polarization Field measurements

The main feature of a ferroelectric material is the hysteretic nature of polarization, which makes the polarization-electric field (P-E) measurements the most important among the electrical methods by revealing the remanent polarization and the coercive field. The I-V measurement gives information about the dielectric nature of the materials (Its leakage current) and contributes mainly to polarization measurement, while the capacitance-voltage measurement can present a signature of ferroelectricity if a butterfly-shaped curve is obtained. As presented in chapter II, a hysteresis loop is the signature of

ferroelectricity in the polarization-electric field measurements. It is the key to more advanced characterizations such as fatigue, imprints, etc.

Historically, Sawyer and Tower were the first to propose a circuit to measure the ferroelectricity of Rochelle salt [168]. Unfortunately, this very used circuit has a significant drawback: the capacitor under test is continuously cycled, so the number of measurement cycles is not defined. Besides, the parasitic capacitances of cables can contribute significantly [169]. For this reason, we used a ferroelectric analyzer (TF 3000) based on the virtual ground circuit. Polarization results from current integration versus the electric field swept as a triangular waveform in our setup. The current is measured indirectly via an operational amplifier and a feedback resistor. The negative voltage necessary to keep the node at the input of the operational amplifier at 0 V is proportional to the current flow through the feedback resistor [170]. The non-inverting input is connected to the ground. The signal from the capacitor is fed to the inverting input, which is simultaneously connected to the output via the feedback resistance. The output voltage adjusts automatically to achieve the equilibrium state with equal voltages at both inputs. The virtual ground circuit eliminates the parasitic effects of cabling capacitance and voltage losses on the reference capacitor. Figure 59 illustrates the two circuits for polarization-electric measurements. There is also a shunt method that is similar to the Sawyer-Tower circuit, but it is based on a reference resistor. Till today, the virtual ground remains the most accurate polarization measurement circuit.

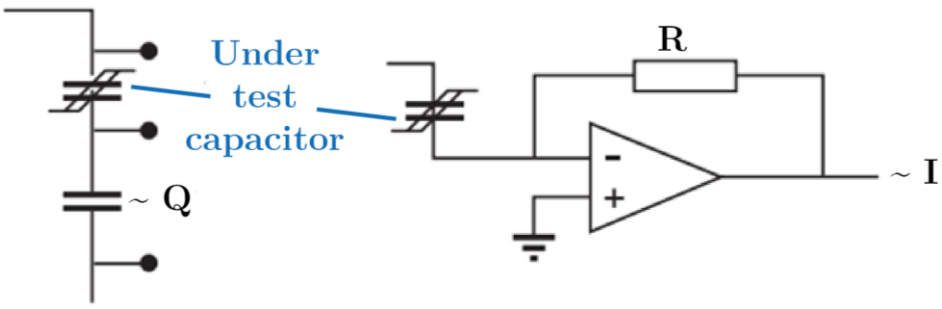

Figure 59 Schematic circuits comparison of Sawyer tower (left) and virtual ground (right).

During the characterizations of the samples, we used two modes of polarization measurement within the Aixacct Analyzer: Dynamic Hysteresis Measurement (DHM) and Pulse measurement (known as PUND for Positive Up Negative Down). The first mode records the hysteresis loop of a ferroelectric material and assists in examining the

influence of process parameters (amplitude and frequency of the signal). In addition, it results in the extracted parameters of the hysteresis such as P_r, Vc, etc.

A pre-polarisation pulse is followed by three bipolar excitation signals generated with a relaxation time of 1 second. The pre-polarization pulse and the second pulse of the excitation signal establish defined polarization states. The pre-polarization pulse has a negative state of relaxed remanent polarization. The second pulse ends in the positive state of relaxed remanent polarization [170].

The second mode: Pulse Measurement (PM), is the most used. It records the current response of the capacitor under test after applying a sequence of pulse excitation signals. The PUND pulse sequence is known for two positive and two consecutive negative pulses. Compared to DHM, in PUND, only unipolar pulses are used (rectangular in our case). The rise time is modified according to the measurement. The coercive voltage depends on the excitation signal frequency. A PUND sketch is illustrated in Figure 60.

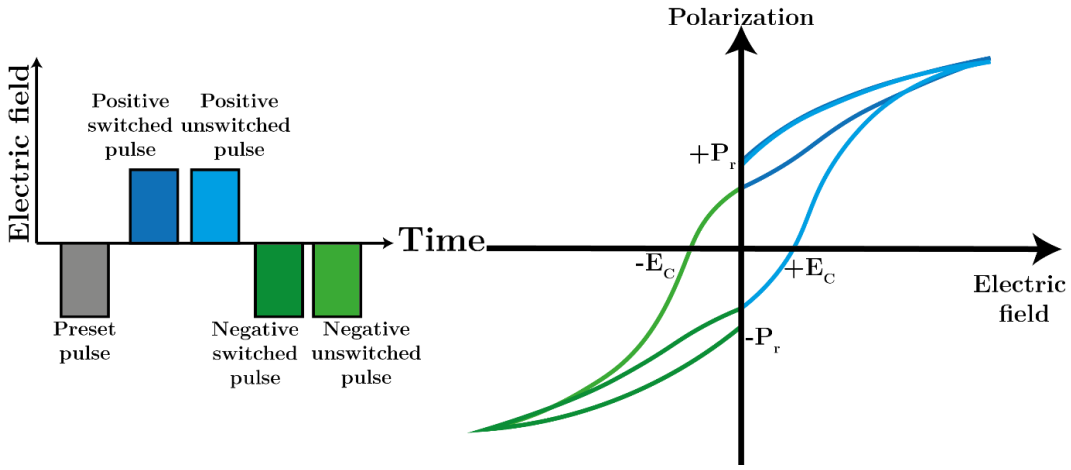

Figure 60 Schematic of PUND measurement

3.4 Conclusion

This chapter presents the methodology of fabrication and characterization techniques used throughout this work. In the first section, HZO-based MIM capacitors were made by sputtering. This technique ensures a good quality of the films, which is required for the fabrication of MIM capacitors. The sputtering of electrodes and dielectric films was highlighted. The capacitors fabrication was always performed as part of this work and is

described in the first section. Characterization techniques employed in this work for analysis of ferroelectric thin films are presented in the second section,

Several experimental techniques have been used to characterize thin layers of hafnium zirconium oxide. First, the crystalline structure of the layers is studied thanks to the diffraction of X-rays in grazing incidence. Second, x-ray reflectivity measurements are used to verify the thickness of the films. Third, the composition of the deposited films is quantified by X-ray photoelectron spectroscopy. Fourth, transmission electron microscope analysis studied the diffusion of the elements. Finally, electrical characterizations were performed to evaluate the properties of thin films.

The following chapters will present the results obtained using the structural and electrical characterization methods. Obviously, other characterization methods have not been performed but are not mentioned in this chapter.

4 Chapter IV Optimization and characterization of HZO films and TiN electrodes

4.1 TiN electrodes 107
4.1.1 Introduction 107
4.1.2 TiN deposition by reactive sputtering 108
4.1.2.1 Optimized parameters of TiN electrodes deposition 110
4.1.3 Characterization of TiN electrodes 110
4.1.3.1 Structural and elemental composition properties 111
4.1.3.2 Electrical properties of TiN electrodes 118
4.1.4 Titanium nitride electrodes' etching 119
4.1.5 Discussion 124
4.1.6 Conclusion 127
4.2 HZO: Ternary transition metal oxide deposited by sputtering 127
4.2.1 Deposition of HZO 128
4.2.1.1 RF magnetron sputtering 128
4.2.2 Impact of RF magnetron parameters 129
4.2.2.1 Reactive sputtering 129
4.2.2.2 Pressure 139
4.2.2.3 Power target 141
4.2.2.4 Ar Flow 146
4.2.2.5 Deposition time 147
4.2.3 Characterization of HZO thin films 148
4.2.3.1 Optimized parameters 148
4.2.3.2 Thickness effect 152
4.2.4 Discussion 153
4.2.5 Conclusion 158
4.3 Thermal annealing 158
4.3.1 Rapid thermal annealing 159
4.3.1.1 Annealing atmosphere 160
4.3.1.2 Annealing temperature 162
4.3.1.3 Annealing time 166
4.3.1.4 Other parameters: 167
4.3.1.4.1 Heat ramp rate 167
4.3.1.4.2 TiN electrodes' thicknesses 168
4.3.1.4.3 Thickness dependence 169
4.3.2 In-situ thermal annealing 171
4.3.2.1 Thermal annealing of top-electrode free HZO stacks 174
4.3.3 Discussion 176
4.3.4 Conclusion 177
4.4 TEM-ASTAR: Crystallographic phase and orientation mapping of ferroelectric HZO
4.4.1 Introduction 178
4.4.2 ASTAR phase mapping 184
4.4.3 Discussion 189
4.4.4 Conclusion 191

4.1 TiN electrodes

4.1.1 Introduction

In the journey of understanding HZO films' properties, several studies have investigated all the HZO-related parameters, susceptible to impact and improve the orthorhombic phase, such as doping, film's composition, and thickness. External parameters, such as the choice of electrodes' material, deposition technique, or rapid thermal annealing parameters, need to be studied thoroughly also, to have a global understanding of phase transition, crystallization, and the structural origin of ferroelectricity in HZO films.

The electrodes' material is important for better mechanical stress and high interfacial quality with HZO film. In this part, we introduce titanium nitride (TiN) as our choice for the electrode's material for the metal-insulator-metal structure with HZO as the insulator. The choice of TiN answers two main questions for us:

- Are its properties in adequation with HZO films? does it allow to have to induce ferroelectricity?
- Does TiN answer for the sustainability criteria (criticality of materials, toxicity, availability…etc)

The good adequation with HZO films and its role in inducing the ferroelectricity during the annealing. Understanding the growth mechanism of TiN and the impact of deposition parameters is out of the scope of this thesis. The elaboration of TiN was based on previous work within the lab (shared internally). We optimized the deposition of TiN electrodes in order to reach state-of-the-art properties.

Then, the aim behind the elaboration of titanium nitride electrodes is:

- The resistivity of TiN must be as small as possible.
- The surface smoothness is a must-have property to ensure the reproducibility of the deposition.
- Must know the crystallinity of TiN electrodes.
- Chemical compatibility.

In literature, TiN has been deposited by different techniques. For this work, TiN has been deposited by DC reactive sputtering inside CT-100 Alliance Concept equipment. Sputtering of TiN offers two main advents: the growth rate is high, compared to other techniques (around 10 nm/min), and the future possibility of TiN/HZO/TiN stack's realization without vacuum breaking since HZO is deposited by sputtering too. According

to Y .Lee et al., unexpected high P_r value was obtained in MIM capacitor fabricated without vacuum breaking [154].

TiN thin films are deposited by magnetron sputtering, on Si substrates, from a metallic titanium target (99.99% pure disc). While the N_2 element is introduced in the working gases with a convenient ratio with Ar which means the deposition of TiN electrodes is a result of reactive sputtering, between the sputtered titanium ions and the reactive plasma containing N_2.

Before Ti deposition, the vacuum chamber was set off to a pressure of $3 \cdot 10^{-7}$ mbar. The power applied to Ti target was increased to 250 W, with a step of 50 W, at the same time as the Ar insertion with a starting flow of 100 sccm that decreases to 40 sccm. The N_2 gas is introduced slowly until reaching 5 sccm flow. The working pressure has been set to 2.10^{-3} mbar.

To have optimal TiN growth, the N_2/Ar gas flow ratio needs to be less than 1. For our case, this ratio is in the order of 0.125 which is reasonable as if N_2 nitrogen flow is too small, the films are more Ti-like films the titanium will settle on substrate as nitrogen will not be sufficient for a reaction with titanium, otherwise, it also becomes a working gas and only titanium growth begins on a substrate.

The deposition rate of TiN increased linearly with deposition time, for the targeted thicknesses from 10 to 200 nm. This is explained by the optimal N_2/Ar chosen for TiN deposition of 0.125 which does not allow to reach a saturation state. The growth rate with the previously mentioned conditions is 12.4 nm/min, as presented in **Figure 61**.

4.1.2 TiN deposition by reactive sputtering

For TiN deposition, many deposition techniques have been used in order to obtain the best possible properties of TiN for several applications such as plasmonic, ferroelectric, and piezoelectric applications [171]–[173].

Diverse types of PVD techniques were reported for TiN deposition like magnetron sputtering, filtered cathodic arc, and ion implantation. The control of the deposition and heat parameters, available in PVD techniques, can directly influence the microstructure of thin TiN films hence the electrical properties consequently.

In magnetron sputtering, used in this work, the deposition parameters such as the substrate temperature, deposition pressure, and power applied to the target, affect the growth and crystallographic structure. The choice of the magnetron sputtering has been made also by taking into consideration the following elements:

- TiN electrodes are the most reported electrodes used for inducing ferroelectricity in hafnia thin films [174]. In addition, TiN was reported in the first paper about ferroelectric HfO_2 [8].
- An existing knowledge, at the level of the lab, about TiN deposition by sputtering.
- The possibility of having a high deposition, compared to other deposition techniques.
- The choice of sputtering is an additional sustainable advantage, as reported in Chapter 1.
- The successful deposition of TiN by sputtering represents an adequation with HZO deposition technique. It is a pre-step for realizing a TiN/HZO/TiN structure without vacuum breaking. The latter has been reported to optimize the ferroelectric properties of HZO [154].
- Sputtered TiN has been reported to be more advantageous, for ferroelectric HZO, compared to ALD-deposited TiN [175].

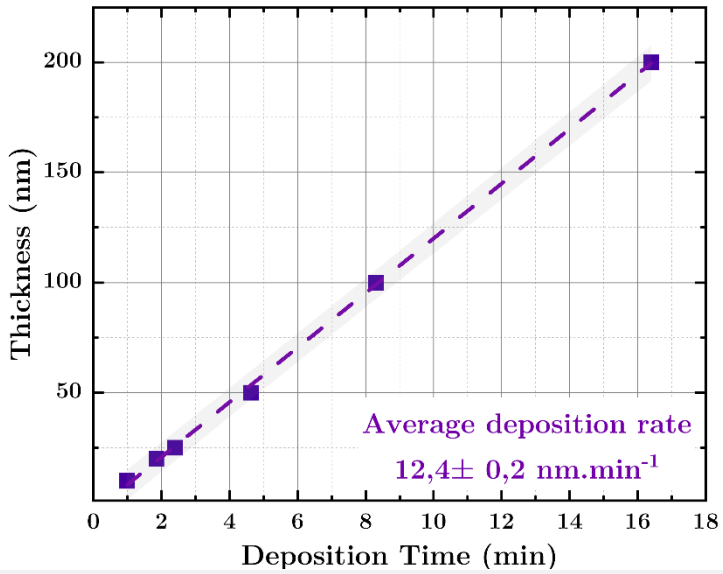

Figure 61 Thickness versus deposition time of TiN layers by DC reactive sputtering

For TiN sputtering, the reactive sputtered is preferred. It allows to control the film stoichiometry, structure, and properties (in our case the Ti/N ratio changes the properties). Despite the several advents of reactive sputtering, it has some major drawbacks that can affect the quality of deposited TiN related to the phenomenon of target poisoning and the fast oxidation of the TiN surface due to the oxygen inside the sputtering chamber (we did not measure it).

Once the reactive gas (N_2) is injected to the plasma, it reacts on both film surface and metal target surface. The reaction of the gas with the target results into a compound

formation that directly lowers the deposition rate by a factor of 5 to 30 due the re-sputtering effect [176]. This phenomenon is observed in the hysteresis shape of the deposition rate as function of the gas flow rate of the reactive gas. This hysteresis effect can be avoided by optimizing the Ar/N_2 ratio and the deposition pressure. During a previous study by our colleagues, it has been found that the best ratio for TiN deposition, for our deposition chamber, is 40/5 sccm at 2.10^{-3} mbar.

Another important characteristic for nitrides deposition, in our case the sputtered TiN, is the deposition temperature, which is in the used chamber: the room temperature. The substrate temperature was not controlled during the deposition. This low deposition temperature is another advent of the deposition technique because it facilitates its compatibility with CMOS process that requires low thermal budget techniques. Besides, the columnar growth of TiN with extended voids along the column boundaries is mainly due to the room temperature deposition. The columnar growth is a widely reported characteristic of TiN [177], [178]. SEM and TEM cross sectional images show the columnar growth of our sputtered TiN, as shown in **Figure 68**.

A final process parameter to check is the reproducibility of TiN deposition as function of sputtering time, i.e., constant deposition time within time. The deposition rate was found to be around 12.4 $nm.min^{-1}$ and it barely varies in the [0, 16 min] interval of deposition time, as illustrated in **Figure 61**.

4.1.2.1 Optimized parameters of TiN electrodes deposition

The optimized parameters of TiN deposition are presented in Table 9. These parameters allowed us to have stable deposition rate, reproducible and uniform thickness of TiN on Si substrates. The characterized TiN films, in this work, are deposited with these parameters.

Table 9 The optimized parameters of TiN sputtering

TiN deposition parameters	
Power	250 W
Pressure	2.10^{-3} mbar
N_2/Ar ratio	5/40
Deposition temperature	Room temperature
Substrate bias	Not used

4.1.3 Characterization of TiN electrodes

After assuring that the deposition of TiN electrodes is reproducible with the optimized parameters, the characterization of TiN properties is mandatory to be aware of these different characteristics and their possible impact on HZO films.

The characterization of TiN electrodes is based on two kinds:

- Physical and structure-related properties to understand the nitride.
- Electrical properties which are the most important for any electrode's material.

4.1.3.1 Structural and elemental composition properties

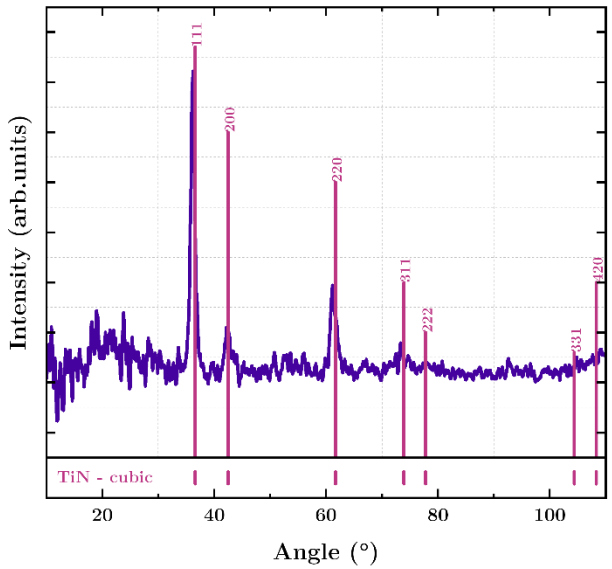

Figure 62 Diffractogram of TiN films (50 nm) compared to ICDD reference pattern of cubic TiN

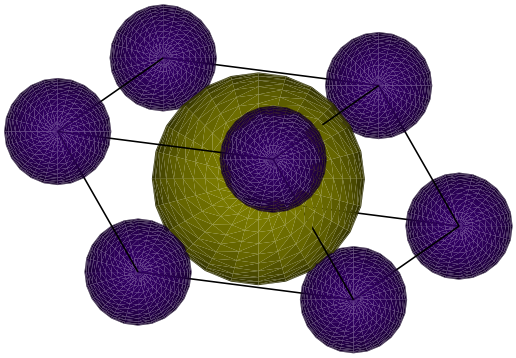

Figure 63 graphical representation of cubic phase of TiN

The crystalline nature of TiN electrodes was firstly targeted for characterization to have information about the crystalline structure of TiN, grain size…etc. The structural properties of TiN have been characterized using grazing incidence XRD. **Figure 62** illustrates the GIXRD results for 50 nm TiN (the most used thickness in this work), obtained with the following settings: grazing incidence of 1° with an angular resolution of 0.06°. In **Figure 62**, the pink sticks give the peak positions and intensities of the identified phases of titanium nitride TiN sample cubic fcc, $m\bar{3}m$, TiN (111) phase is textured. The cubic phase of TiN is shown in **Figure 63**, the cell parameters of $m\bar{3}m$ point group are the following: a=b=c= 3.008Å. Three intense peaks are observed: (111), (200), and (220) crystal orientation that correspond to the metallic-like TiN crystallization. It means that the set power (250 W) allows for having TiN films with a polycrystalline nature TiN film. The main peak (111) is at, $2\theta = 36.17°$ with a tiny shift from the reference (36.4°). This shift can be explained by the oxidation of the surface, by the air exposure, during the transfer to the characterization equipment, causing the formation of TiON on the surface. The XRD reference pattern of TiN peak positions is from the ICDD database [PDF Card No. 00-038-1420].

Starting from 50 nm thickness, TiN layers clearly show (111) (200), and (220) diffraction peaks with (111) as the preferred orientation. The intensity of diffraction peaks increases, from 50 to 200 nm samples, due to the material's quantity incorporated in the diffraction spot. However, for the samples thinner than 50 nm, the peaks intensity is rather weak and seemingly disappears.

Debye-Scherrer's formula [179] was used to estimate the average grain size TiN. The calculated crystallite size was found to be 10,9 nm using Lorentz fitting. The calculation of grain size of TiN is important while the investigation of the TiN/HZO interface and the existence of any possible misfit between TiN and HZO.

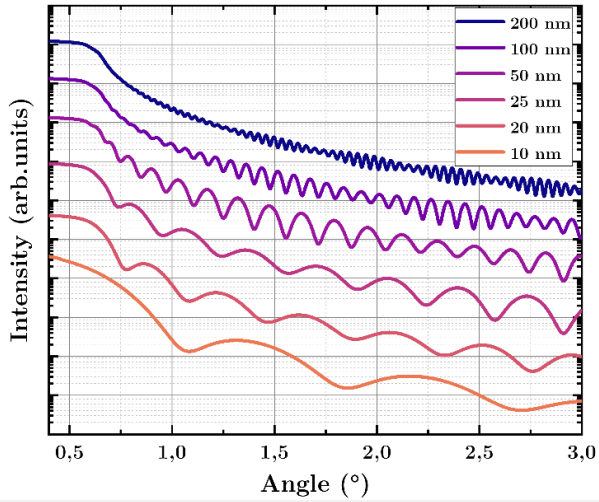

Figure 64 X-ray reflectivity patterns of TiN with different thicknesses

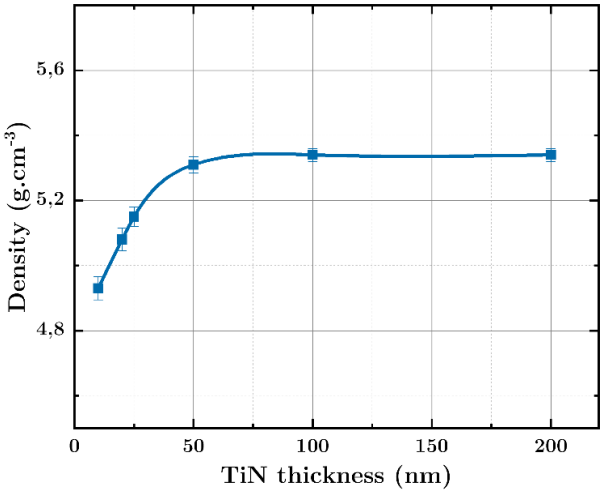

Figure 65 variation of TiN density with thickness

The most important physical characteristic to determine, about the sputtered TiN layers, is the thickness. Using several techniques have been used, in this work, such as XRR, TEM, and ellipsometry, helped confirm the obtained results. In addition to the thickness, XRR helped determine the density and roughness of TiN.

As observed in **Figure 64**, X-ray reflectivity patterns of TiN films with different thicknesses have been obtained after fitting the results with Leptos software **(Figure 66).** The deposition rate is constant as a function of time as shown in **Figure 61** (linear relationship between thickness and deposition time) with a deposition rate of 12.4 $nm.min^{-1}$. TiN film density (**Figure 65**) approaches the density of TiN (for the cubic phase by calculation), 5.34 $g.cm^{-3}$, as film thickness increases. The reported values of TiN density are 5.21 and 5.34 $g.cm^{-3}$ [180, p. 3], [181]

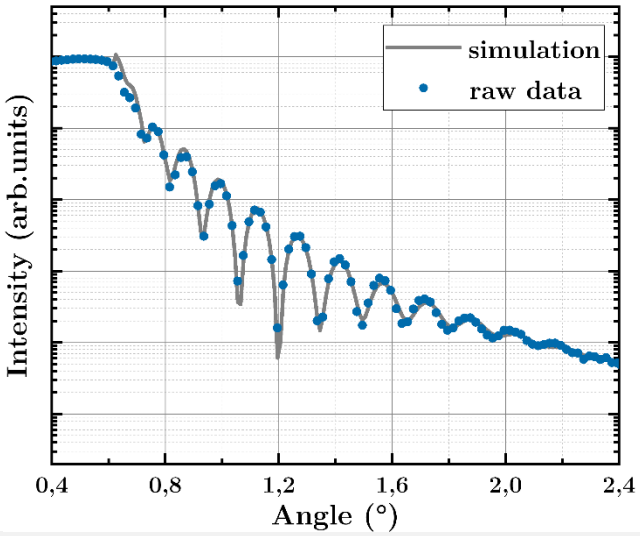

Figure 66 Fitted X-ray reflectivity pattern of TiN

The thin TiN film of 10 nm has an average density of 4.93 g.cm^{-3} while the TiN with higher thicknesses is denser and closer to 5.34 g.cm^{-3}. XRR results show that the TiN roughness does not vary significantly as a function of thickness. On average, thin TiN films on silicon have an average roughness of 0.28 nm, indicating that the films are smooth over the substrate surface as shown in **Figure 67**.

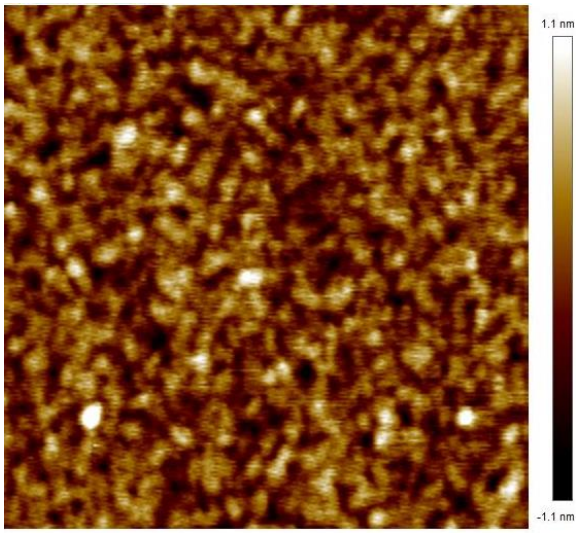

Figure 67 AFM scan of 50 nm TiN surface with a roughness of R_q = 0.28 nm for a surface of 5×5 µm

Since the roughness of TiN is one of key parameters that contribute to inducing the orthorhombic phase in ferroelectric HZO, AFM has been used to confirm the fitting results of XRR measurements related to roughness, using (Bruker AFM). The AFM scan was carried out with semi-contact mode on sputtered TiN on Si substrate with a scan

area of 5 µm × 5 µm. From AFM results, TiN surface topography shows a porous structure that consists of tapered crystallites with fewer hillocks. **Figure 67** shows an AFM image of a thin TiN film with the measured root mean square roughness (R_q) around 0.28 nm. These results show that the sputtered TiN films have a smooth surface. The uniformity and roughness of TiN deposition are confirmed by TEM images as illustrated in **Figure 68**.

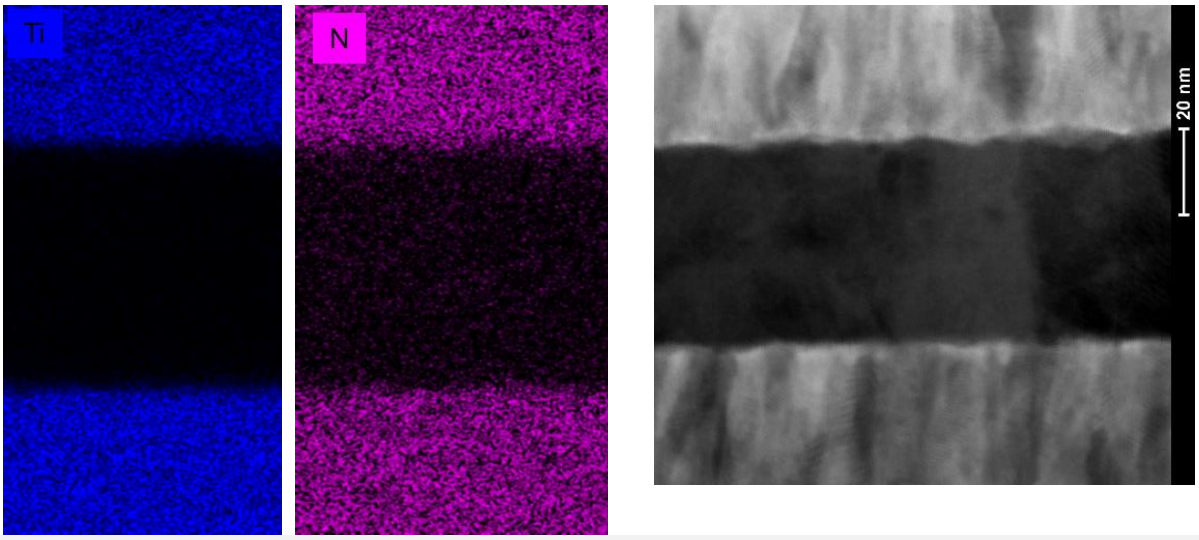

Figure 68 (Left) EDX results of Ti and N in TiN top and bottom electrodes (Right) cross-section TEM images in Bright Field Imaging mode

To gain a better understanding of the reactive sputtering of TiN on the morphology and the chemical composition of the films, a TiN (50nm)/HZO/TiN (50 nm) structure has been chosen for cross-sectional TEM analysis and also EDX.

For both bottom and top electrodes, the reactive sputtering parameters are the same as previously described. From the bright-field TEM analysis shown in **Figure 68**, it is clear that the samples have the same average thickness (50 nm). The thickness uniformity of deposited TiN electrodes is confirmed by the stable distribution of measured sheet resistance values, as illustrated in **Figure 76**.

The dark-field analysis shown in **Figure 69** shows a higher density of crystallites for thicker TiN layers, as evidenced by the XRD patterns observed. These patterns are consistent with electron transmission through a film where the axes of the crystallites in the beam path are rotated at different angles in the plane normal to the electron beam.

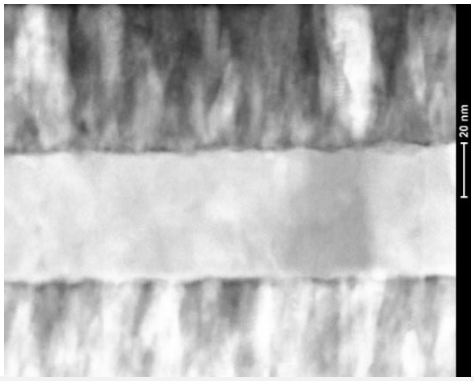

Figure 69 TEM cross section of TEM in Dark Field imaging mode

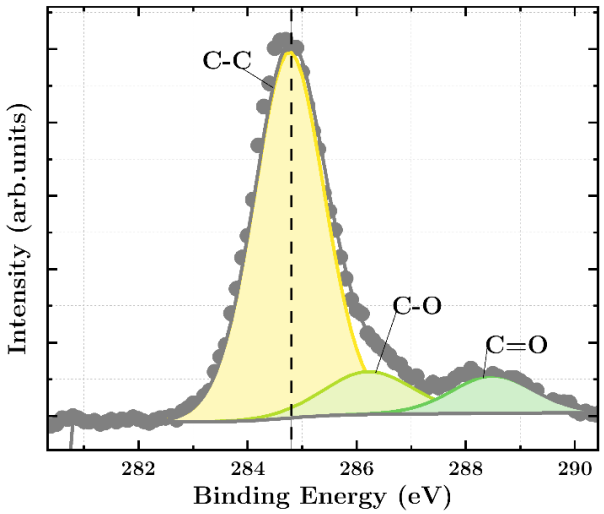

Figure 70 core-level XPS spectra and peak-fitting analysis of C1s

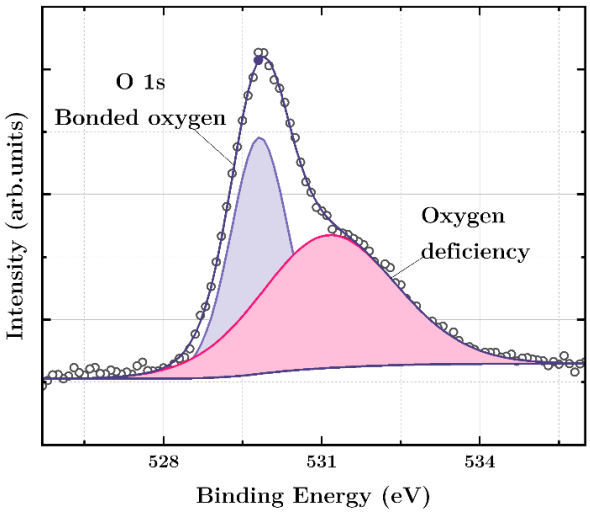

Figure 71 core-level XPS spectra and peak-fitting analysis of O1s

To confirm the successful deposition, XPS was employed for more quantitative characterization of TiN films grown on a silicon substrate.

Using XPS, we have measured high-resolution core-level XPS spectra corresponding to Ti 2p, N1s, and O 1s to measure the composition of the TiN sample precisely upon depth-profiling.

As illustrated in **Figure 70**, all spectra were shifted regarding the C–C binding energy that was set at 284.8 eV. Prior to XPS measurements, the surface contamination for the sample caused by exposure to air is taken into consideration. Carbon signal method is usually used to compensate for charging.

Additionally, the oxygen 1s peak region, as shown in **Figure 71**, has a peak that can be resolved into two peaks, one located at 529.8 eV indicative of TiON and another at 531.16 eV indicative of TiO_2. The presence of oxygen in a TiN has been reported to be better for the metallic properties of the film due to its good conductivity. The oxygen

origin is attributed to the air exposure of the sample after deposition and the oxygen impurity inside the sputtering chamber. The XPS measurements have been conducted days after the TiN deposition.

As shown in **Figure 71**, the core-level O 1s spectrum has been decomposed into two peaks at, 529.8 and 531.16 eV, corresponding to Ti–O bonding in the oxynitride and adsorbed oxygen, respectively.

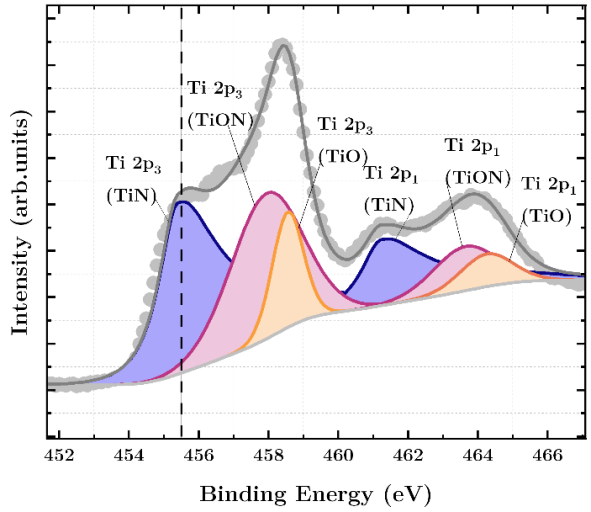

Figure 72 core-level XPS spectra and peak-fitting analysis of Ti2p

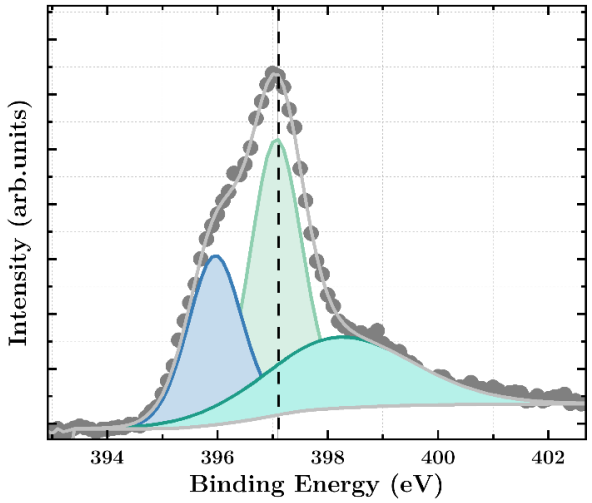

Figure 73 core-level XPS spectra and peak-fitting analysis of N1s

The Ti 2p peak region of TiN, illustrated in **Figure 72**, which has resolved spin-orbit components, $2p_{1/2,}$ and $2p_{3/2}$, in which the binding energy of the $2p_{3/2}$ peak is utilized to indicate the chemical state. Generally, the Ti 2p spectrum is of a complex nature and it consists of doublet peaks Ti $2p_{3/2}$ and Ti $2p_{1/2}$ due to spin-orbit splitting as shown in **Figure 72**. The Ti $2p_{3/2}$ peaks are deconvoluted into two peaks at 455.5 and 458 eV which is indicative of the Ti^{2+} States due to Ti–N bonding and Ti^{3+} states due to Ti-O or Ti–N–O bonding of the $TiO_{1-x}N_x$ phase, respectively, which is reliable with metallic TiN. The assigned peak positions of Ti^{2+} and Ti^{3+} states are in a similar range and are consistent with the earlier reported values for the corresponding binding states [182]. Similarly, Ti $2p_{1/2}$ peaks have been decomposed into two peaks corresponding to Ti^{2+} and Ti^{3+} binding states, respectively.

The nitrogen 1s peak region has a peak that can also be resolved into three peaks, In **Figure 73**, one located at 397 eV which is indicative of Ti–N bonding in the oxynitride and the other located at and 395.96 and 398.26 eV indicative of N–Ti–O as reported in previous studies [182], [183]. The O 1s peak at 531.16 eV and N 1s peak at 397 eV correspond to N–O bonding.

After excluding the minor contribution of XPS peaks corresponding to N–O, the composition of the TiO_xN_y film is determined to be $Ti_{48.3}O_{29.4}N_{22.2}$ with a Ti:N ratio of almost 1.2, calculated from the quantification of Ti2 p_3 and N1s peaks. This ratio Ti—to-N is stoichiometric despite the relatively high oxidation due to the incorporation of oxygen from the sputtering chamber and air exposure. The metallic behaviour of TiN is confirmed by the sheet resistance measurements and Ti-to-N ratio. The oxidation can be avoided by chamber cleaning and vacuum transport of samples for XPS measurements, besides, if a TiN/HZO/TiN structure is realized in the same chamber without vacuum interruption, the oxidation would be less quantified.

In **Figure 74,** the ratios of the TiN: TiON peaks both indicate the film is 69.2% TiN and 30.8% TiON which confirms the previous results of a non-negligible oxygen content in the TiN film, 29 at%. As the resolution angle is varied from bulk to surface the TiO_2 at% is increasing to a maximum of 22 at% compared to 12% in the bulk. This increase means that the oxidation of the surface, by air exposure, is more important. Besides, the oxygen contamination inside the chamber is not negligeable.

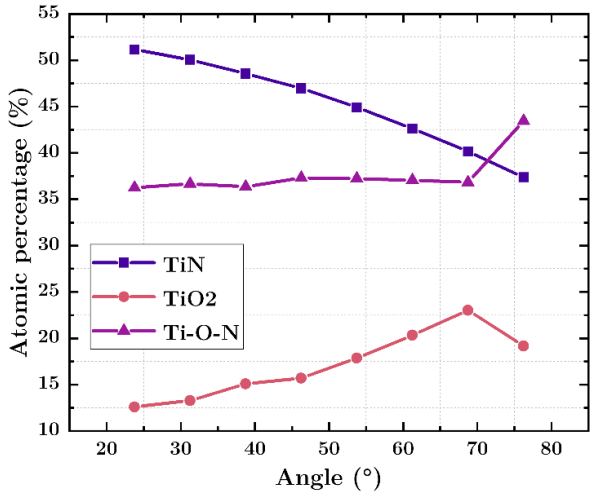

Figure 74 Angle resolved atomic % of TiN, TiO_2, and TiO_xN_y

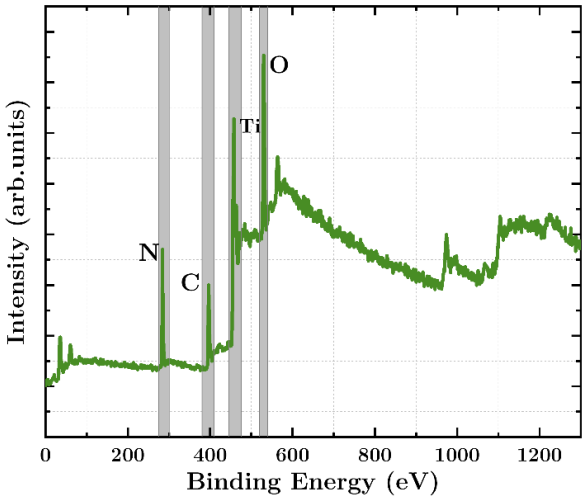

Figure 75 XPS depth profile of TiN/Si

The survey spectrum is presented in **Figure 75**. It has been acquired to determine the elements existed on the TiN layer (Ti, N, O, and C) without any contamination detected. The thickness of TiN layer was around 50 nm deposited on Si substrate. This chosen thickness allowed to conduct angle-resolved scan to follow the composition, the stoichiometry, and the oxidation from bulk to surface, in the 10 nm depth range, without any interference from the Si/TiN interface (which is out of the scope of this work).

4.1.3.2 Electrical properties of TiN electrodes

The structural and compositional properties of TiN are to be confirmed by the electrical resistivity as TiN has been elaborated for the role of top and bottom electrodes. The sheet resistivity can yield information about both the electrical properties of the TiN electrodes, also its impurity content and stoichiometry [184].

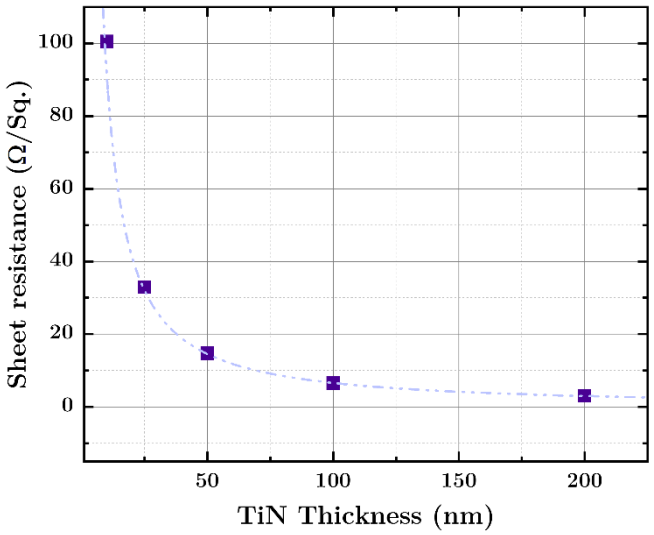

Figure 76 Sheet resistance of TiN as function of thickness

At room-temperature, the sheet resistivity was measured using a 4-point probe with a contact spacing of 1.2 mm on non-patterned films, deposited on 4-inch wafers. The resistivity was probed across the entire wafers, which resulted in 49 data points per wafer. Reproducibility of the resistivity was investigated using two samples grown at the same conditions with a time interval of 2 months. Resistivity was found to vary by less than 3 % within any single film, and within 2 % between different films deposited at the same conditions.

The dependence of the TiN sheet resistance and the thickness values sputtered at a pressure of 2.10^{-3} mbar is shown in **Figure 76**. The sheet resistance is lowered in an almost reciprocal way from 100.5 Ω/Sq at about 10 nm to 6.3 Ω/Sq at 100 nm. The measured resistivities of the deposited TiN films are shown in Table 10. It can be also observed that resistivity is lowest at higher TiN thicknesses. The resistivity of 50 nm thick TiN is less than the 10 nm film resistivity with a factor of 6.8.

At the structural level, the resistivity of TiN thin film is mainly influenced by phase orientations, i.e. (111) and (200) [185]. The resistivity of the (200) phase is lower as compared to the (111) phase hence with an increase in TiN thickness, the resistivity of the film decreases logarithmically. The electrical resistivity of TiN can be influenced by

phase orientation, Ti:N ratio, Ar/N_2 gas mix, the oxygen contamination, and the thickness.

Table 10 Comparison of resistivity of TiN layers deposited on Si substrate for different thicknesses.

TiN thickness (nm)	Sheet resistivity (Ω/Sq)
10	100.5
25	32.91
50	14.72
100	6.5
200	3

4.1.4 Titanium nitride electrodes' etching

After the evaporation of Ti/Au metal for electrical contacts, the Ti/Au contact pads serve as a hard mask for the final step of the fabrication process of TiN/HZO/TiN MIM structures which is the etching of TiN outside the patterned top electrodes.

For dry etching of metal, two techniques are generally employed, either IBE or RIE-ICP. Ion beam etching is often used for multiple thin layers, or alloys with no optimized chemical etch recipes. A dry etching by a RIE-ICP process is possible and it can have a higher etching rate than IBE.

To realize the electrical characterization tests, the choice of etching top TiN has been adopted over etching of both TiN and HZO due to the complexity of etching TiN/HZO multilayer by RIE-ICP with one recipe besides the slow etching rate by IBE. Keeping the HZO layer, while short-circuiting one capacitor to serve as a bottom electrode contact, protects the bottom TiN from more oxidation.

In this work, the etching of TiN, by IBE, RIE-ICP and chemical etching, has been conducted. The top TiN layer was etched, at once, and used for the electrical test capacitors included in the mask. The etching results have been checked by EDX and electrical resistivity. The multiplicity of etching techniques was due to the unsuccessful characterization tests of dielectric HZO that showed an unexpected conduction behaviour of HZO. So, the etching step has been doubted to be the reason behind this. After all, the conduction in HZO occurred due to other reasons as will be explained in chapter 5.

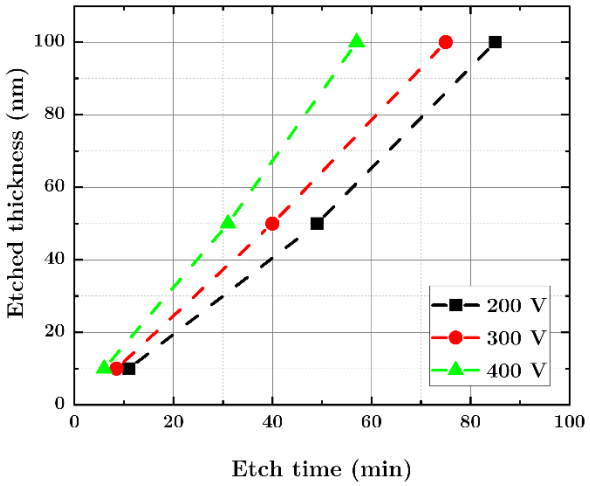

Figure 77 Ion Beam Etching (IBE) of TiN 50 nm

The IBE etching was performed using MU400, Plassys equipment, where Ar ions bombard the sample removing all materials indiscriminately, with a Secondary Ion Mass Spectrometer (SIMS) allows the etching end. The beam supply voltage was varied from 200 to 400 V. The incident angle of the Ar ion beam was controllable by tilting the rotating sample stage 35°.

The highest IBE etch rate was~1.6 nm.min^{-1} at 400V, as shown in **Figure 77**, for the total etching thickness of 50 nm. Two SIMS spectra are shown in **Figure 78** which, even though they look very alike, give valuable information about the process and samples. From a SIMS spectrum it is possible to determine which layer is currently being etched and to stop at a certain layer, in our case: etching of TiN and stopping at HZO. Reading a spectrum from left to right, the initiation of the etch which is the same as opening the sample shutter is seen as a spike in signal for almost every material When this spike disappears the two signals except titanium decrease to a lower value meaning that a titanium-based layer is at the top.

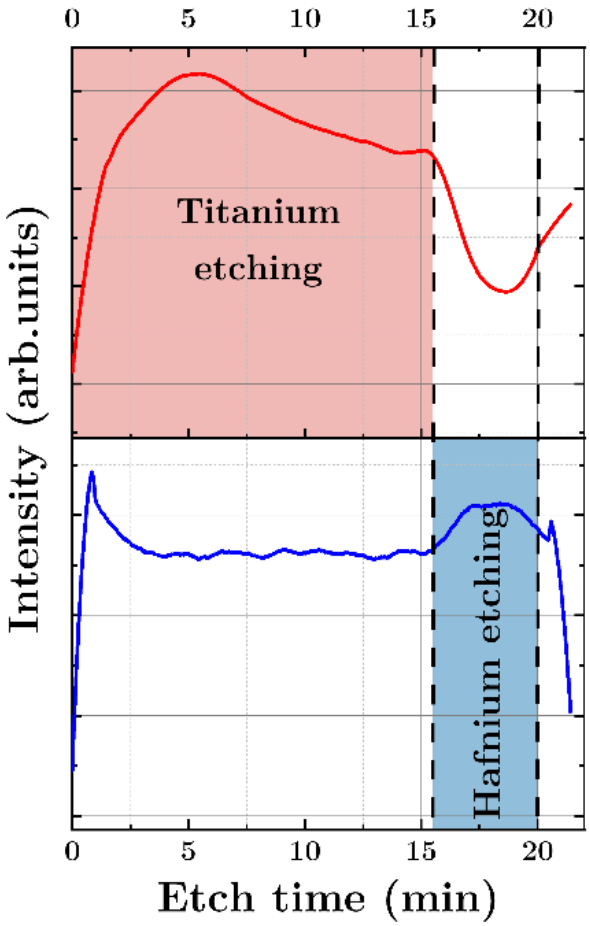

Figure 78 SIMS signals of Ti and Hf during IBE etching of 50 nm TiN an d15 nm HZO

The IBE worked well but we faced some leakage current issues, so we speculated that the IBE is the reason because of the left TiN very thin layer. So, we switched to ICP-RIE to have a full etching processing and shorter etching time.

An ICP-RIE (inductively coupled plasma reactive ion etching), using PlasmaLab100 from Oxford, of TiN electrodes was performed using a SF_6/O_2 gas mix with 100 RF Power at 1.33×10^{-2} mbar. The etch characteristics such as the etch rate were optimized by varying gas concentration mix and etch parameters including radio frequency (RF) power, the gas ratio, and gas pressure. TiN thin films with the thickness of 200 nm were deposited on thermally oxidized Si wafer by RF magnetron sputtering in N_2 ambient.

The profilometer (Dektak) and the XRR techniqes were used to measure the etch depth for the calculation of the etch rate. The full etching of TiN was checked by electrical test. **Figure 79** shows the etch rates of TiN films.

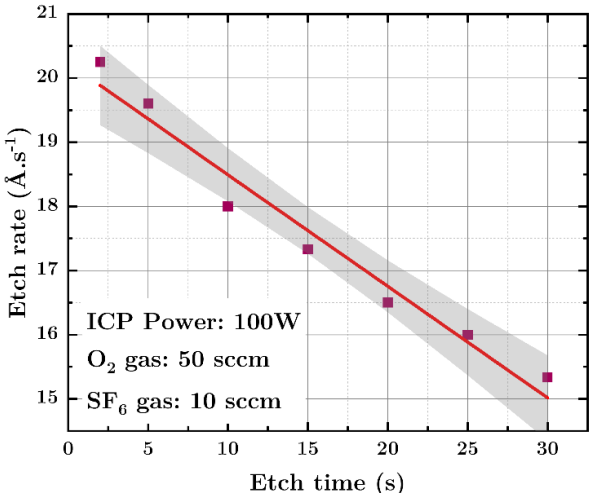

Figure 79 Inductively coupled plasma etching of TiN

As the etch time increased, the etch rate of TiN films decreased from 20.2 A.sec^{-1} decreased while the sidewall slope of etched films became slanted. While investigating the etching parameters effect on etching rate, we found that gas pressure has small impact on the etching rate. Optimizing the etching parameters of TiN etching is out of the scope of this work. We were only limited to a working etching process.

The TiN, using ICP-RIE, was reproducible and the etch rate was higher than the IBE. Unfortunately, the leakage current persisted and we suspected the etching step. Again, we tested a new etching technique: Chemical (wet) etching. We patterned the top electrode in a wet etch using a solution of H_2O, H_2O_2 and NH_4OH with a ratio of 25:2:1 (a diluted type of a Standard Clean 1) at 50 °C. The etch rate is strongly dependent on the dilution. We kept the ratio at 25:2:1 that looked stable and reproducible after several etching steps. The etch rate of the chemical etching is illustrated in **Figure 80**.

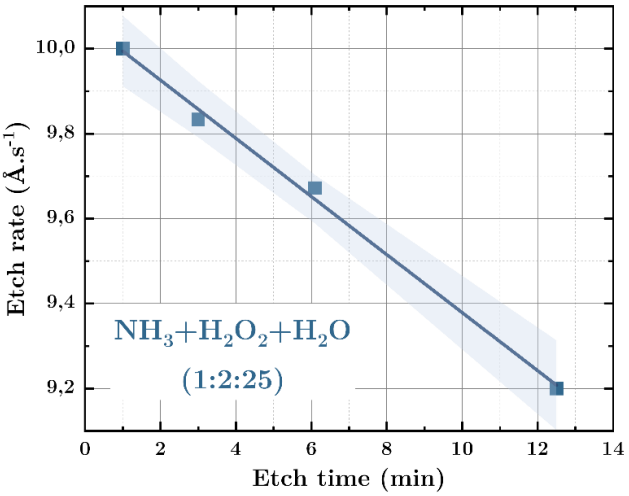

Figure 80 Chemical (wet) etching of TiN

The etch rate decreased as the etch time is longer. The decrease was very slight, from 10 to 9.2 A.sec^{-1}. We adopted this etching technique for the rest of the thesis. We checked the etching of TiN using EDX coupled with SEM, as the pictures present in **Figure 81**.

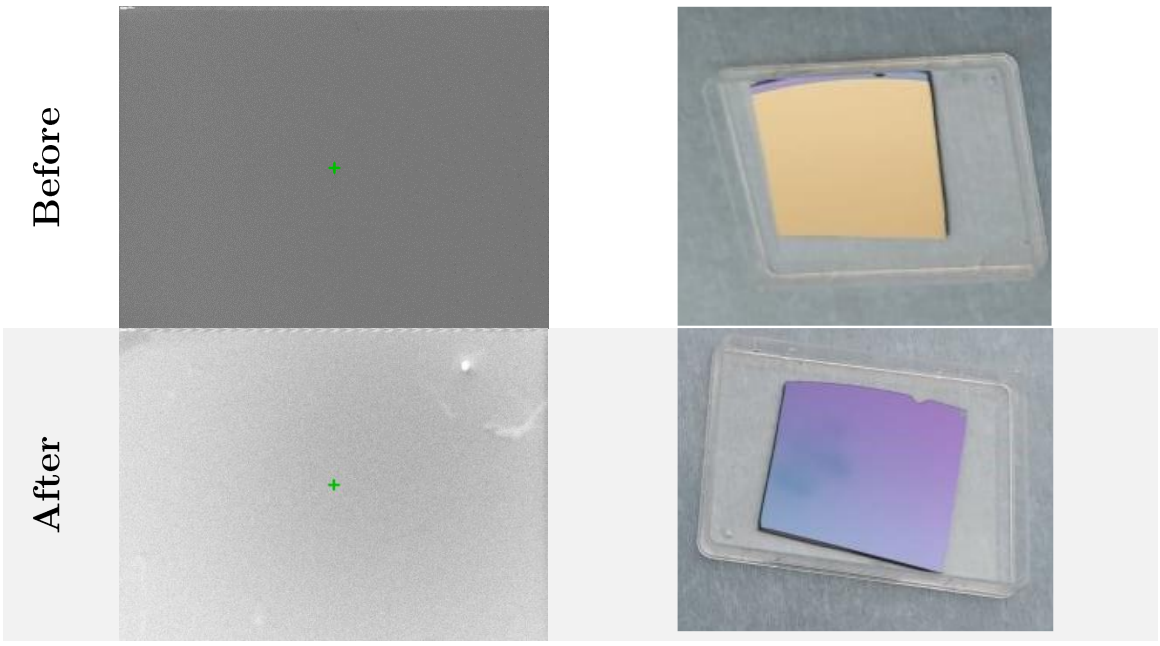

Figure 81 Pictures of TiN samples before and after wet etching (left) SEM images (right) photos

The pictures show a visual signature of the TiN etching by the change of color. Very thin TiN is almost transparent so the visual signature can be misleading. The EDX profiles, in **Figure 82**, shows ni Ti or N peaks after the TiN etching. This result confirms the visual signature and the electrical testing.

All the etching techniques, in this work, were able to etch TiN reproducibly and the change of etching techniques occurred due to a wrong susception to be an origin of the leakage current of the capacitors during electrical measurements. The reason behind that was the Cu contamination as will be illustrated in **Chapter 5.**

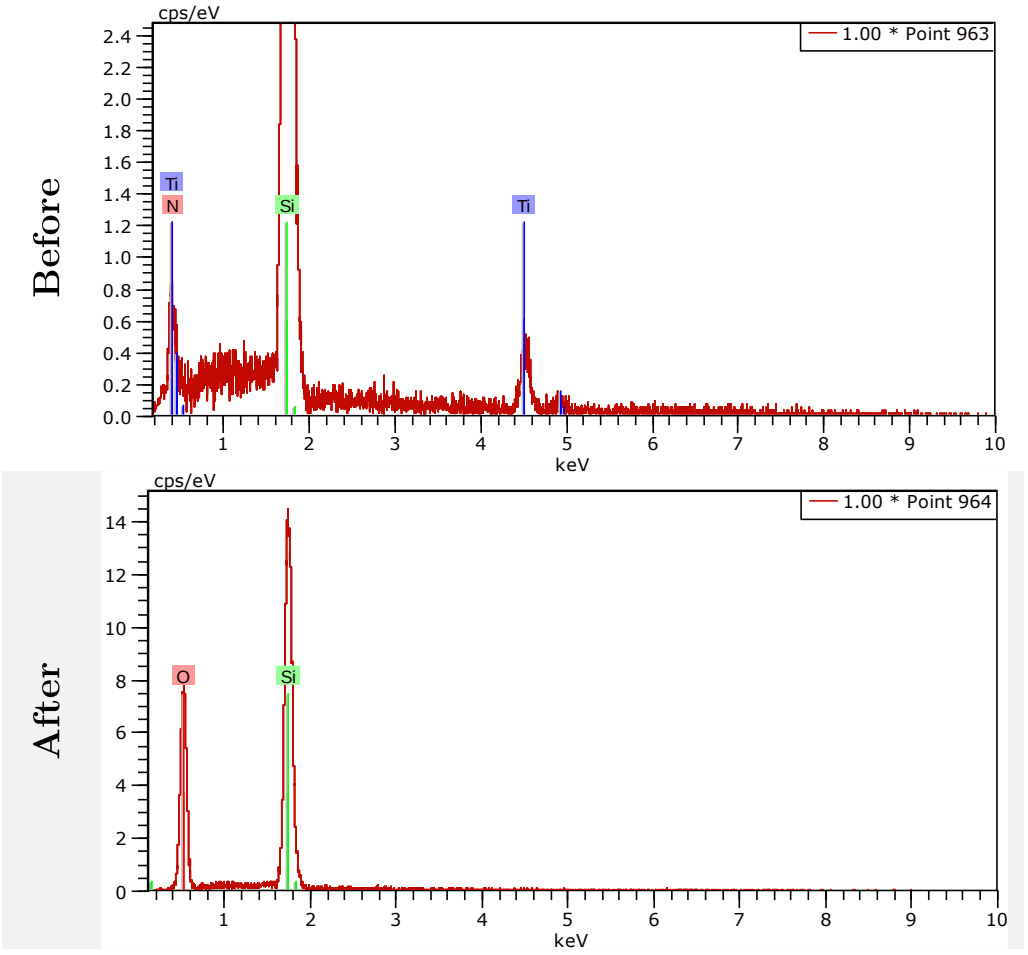

Figure 82 EDX profile picture before and after etching by wet etching.

4.1.5 Discussion

The deposition rate of the TiN electrodes is strongly influenced by the nitrogen/argon ratio, sputtering power, and deposition pressure (**Figure 61**). Mostly, the aim is to avoid the empoisoning of the target, a known phenomenon in reactive sputtering [186]. The thickness measurements data show a considerable deposition rate, of 12.4 nm.min^{-1}. It allowed us to investigate the effect of TiN thickness and study the variation of properties with thickness. It reveals that high deposition rates are always a characteristic of sputtering deposition for electrodes and dielectrics. S. Grosso et al.[187] reported higher deposition rates of TiN (60 nm.min^{-1}) at 1 kW power. Knowing that the power-deposition rate relationship is linear, our finding is in good agreement with this

reported value by taking into consideration that the applied power is 250 W (1/4 of power used by S. Grosso. The choice of deposition rate and power is explained by the desire to avoid the Ti target empoisoning. It is worth noting here that the density increases as the film is thicker in total agreement with the reported values in literature.

The roughness data resulted in 0.28 nm roughness. As function of the thickness, the roughness was steady. C.Charpin-Nicolle et al. [188] reported the same order of roughness of TiN electrodes. Its impact on the hafnium oxide forming voltage was studied experimentally and confirmed by TCAD simulations.

Based on the XPS and EDX data (**Figure 70 and 66**), the 5/40 ratio allowed having almost 50 at. % (stoichiometric Ti/N), as expected. The golden color of 50 nm, and thicker, TiN was obtained, which is a signature of TiN with the right ratio, and also the metallic mode of sputtering instead of the poisoned mode, according to literature [187], [189]. The golden colour appears, in **Figure 81**, due to high reflectance of TiN and the red end of the visible spectrum with low reflectance near the ultraviolet region [190].

The golden colour is an indication of the oxygen presence too. The golden colour corresponds to low oxygen at. % while high oxygen at. % indicates a brown colour. The oxygen at.% is linked to the nitrogen high flow [187]. The obtained golden colour is related to the right nitrogen flow (N_2/Ar ratio) and the oxidation of TiN. The apparition of oxygen in XPS data can be explained by the contamination inside the chamber and the contamination by the air (notably due to the process, the target purity (99.9%), the gas purity and the adsorbed water).

Due to the strong affinity of oxygen with titanium, oxygen content in the film is inevitable, over-stoichiometric TiN cannot be deposited and TiO_xN_y with oxygen incorporation were obtained instead. We suppose that when N composition reaches about 50 at. % in the TiN film, O substitution is favoured compared to N_2 incorporation which explains that residual oxygen is incorporated into thin films.

Even if the oxygen incorporation is an undesirable effect, these films do not exceed minor oxygen and interferometric colours have not been found in the studied films with different thicknesses. Above 50 nm, different thicknesses of the same composition led to the same colour.

To control the colour of the coating and the chemical composition, controlling the oxygen content in the film is key. To reduce the oxygen at%, a very practical process step is

using negative substrate bias before HZO deposition. Unfortunately, we could not perform this step inside the sputtering chamber of HZO.

The Ti 2p spectrum presents a significant Ti-O component as well as Ti-O-N component in the N 1s spectrum. We can observe that the Ti-N peak is less than TiON, because of the small XPS depth of analysis around 10 nm, TiN is shadowed by the oxidation surface layer. We speculate that by removing the oxidation surface layer, the intensity of the O 1s spectrum reduces.

Reported in the next chapter (**Figure 137**), TEM-ASTAR measurements can identify phases associated with their morphologies and crystalline orientation at a high resolution. the microstructure was also studied and differences in crystallography, and texture are observed between TiN top and bottom electrodes. Bottom TiN electrode is polycrystalline and composed of 40 nm columnar grains with (001) plane, whereas TiN top electrode is polycrystalline with more diverse plans, especially the (101). Despite the lower layer, both TiN layers tend to grow columnar with a NaCl structure.

In the 50 nm TiN films, orientation maps have indicated that the growth of TiN started in the first 5 to 10 nanometers of layer on Si substrate. Columnar grains are observed, favouring (001) plan for bottom TiN, whereas columnar grains in the top TiN present (101) preferred plane. These observations given by ASTAR-TEM orientation maps are in good agreement with previous works [187], [191] and allow to give a complete view of the layer compared to structural characterization of the electrodes mainly performed by our XRD and TEM data, Figure 62, and the literature reports [187], [192], [193]. The deposited TiN electrodes are crystallized into cubic phase (m3m) for thicknesses above 25 nm.

Our XRD, TEM, and ASTAR characterizations tend to present a typical columnar structure in total accordance with reported results [194]. We did not investigate the mechanisms behind this preferred orientation, but our results are consistent with the studies that reported the responsible mechanisms [178], [194], [195].

The change from (001) to (111) with increasing thicknesses is reported to be a kinetic-driven mechanism [192], [195]. Greene et al. [195] have clearly shown that the preferred orientation of polycrystalline TiN films can be modified by only controlling the incident N_2/Ti ratio. The influence of the substrate temperature modified by polarization of electrodes on the microstructure was also studied. It must be reminded that in this work the substrate temperature was not modified (room temperature) and substrate biasing.

The discussions of electrical properties of TiN using the four probes' measurements and etching of TiN are reported above. TiN etching was successful with three different techniques for practical fabrication reasons and understanding the etching mechanism is out of the scope of this work. The etch rate differs from a technique to another.

In addition to the obtained structural, chemical, and electrical properties of TiN, it is a good sustainable electrode' material for HZO. TiN is reported as a non-toxic used for biomedical applications [196], which joins the aims of this thesis.

4.1.6 Conclusion

The characterizations of TiN electrodes deposited using the optimized parameters are in good agreement with the reported properties of TiN in literature. TiN thin films were deposited on Si substrates using reactive sputtering. From XRD patterns, the films show (111) preferred orientation and the films with the thicknesses of below 25 nm are amorphous. When the film thickness increased from 10 to 200 nm, the sheet resistance of the films varied from 100 to 3 Ω/Sq. As shown in XPS results, there is an oxidation of TiN due to the air exposure. Despite that, the desired properties of TiN are still present. The XRD and TEM results confirmed the columnar growth of TiN films with the (111) preferred orientation. Measurements are in good agreement with previous studies for the electrodes colour with the sputtering mode in link with the chemical composition. The colour is related to the N/Ti ratio, being equal or close to 1 for a golden colour whereas a brown color is due to an increase of the oxygen content. Orientation maps have permitted to access to each grain orientation and morphology in the thin films locally. Sputtered TiN layer tend to present columnar microstructure.

In the next sections, HZO sputtering conditions are studied. Besides, the effects of TiN properties are discussed in part 3 of this chapter during the thermal annealing.

4.2 HZO: Ternary transition metal oxide deposited by sputtering

As detailed in the previous chapter, HZO can be deposited by different systems of sputtering (single target, co-sputtering, and reactive sputtering). In this thesis, we used a single target system with HZO target. As the XPS measurement was not possible on

the surface of the target or any other technique. we studied the impact of the different sputtering parameters on the deposition of HZO.

4.2.1 Deposition of HZO

4.2.1.1 RF magnetron sputtering

As explained previously, the deposition of HZO films was handled inside a sputtering chamber. Among the various sputtering systems, RF magnetron sputtering technique was selected due to its several advantages such as the easy handling, reduced consumption of source materials, the low thermal budget, nontoxic nature, and the possibility of multi-targets deposition. The RF sputtering is used for the deposition to the dielectrics and insulators from ceramic targets. If the DC sputtering is used like for the TiN deposition, the sputtering discharge cannot be sustained because of the immediate build-up of a surface charge of positive ions on the target's surface that leads to the formation of an oxide layer on the target.

For the investigation of sputtering parameters for the deposition of HZO films, we used an Alliance Concept DP 850 sputter equipment [197] with planar targets of HZO ($Hf_{0.5}Zr_{0.5}O_2$) provided by Neyco.

In the sputter chamber, the following parameters can be controlled:

- Sputtering with Ar gas plasma with the possibility of adding reactive gases like O_2. In this case, it is called "reactive sputtering".
- The deposition pressure.
- The sputtering power or the power density applied to the target.
- The gas flow rate.
- The deposition time.
- The target-substrate distance.
- The rotation of substrate holder.
- The substrate bias.

For the sputtering process, there are first order parameters that directly influence the deposition rate and the properties of the deposited films like the deposition pressure, the sputtering power, and the substrate temperature [198]. The other parameters can change from a sputter chamber to another and have less impact on the deposited films.

We investigated the impact of the reactive sputtering, the sputtering power, the deposition pressure on the deposition rate and the quality of the films. Then, we studied

the argon flow rate and the deposition time to assure the stability and the reproducibility of the depositions. Unfortunately, the investigation of the substrate temperature and bias was not possible.

4.2.2 Impact of RF magnetron parameters

4.2.2.1 Reactive sputtering

During a sputtering process, the sputtering gas is used for knocking out of target atoms, whereas reactive gases are used to form the final compound after the reaction with the sputtered species.

The first investigated element was the oxygen partial pressure (PO_2 %) to choose whether the HZO sputtering is better with an argon non-reactive plasma, or with an oxygen reactive plasma. If the latter is the case, which oxygen percentage or O_2/Ar flow rate ratio is the best? The total gas flow rate is 60 sccm ($Ar+O_2$). The investigation of this parameter passed by two steps.

In the first one, we investigated the oxygen role for 0, 5, 10 and 20 % with long steps while the second step concerned the variation of oxygen with smaller steps for 0, 1, 1.5, and 2%. The small variation of oxygen is under investigation for different oxides [199]–[201]. It has not been fully understood how the oxygen reacts for small % around 0. Even with oxide targets, the addition of oxygen in plasma can be preferred to compensate the possible oxygen vacancies within the deposited films.

We conducted XPS on HZO samples deposited with different PO_2 % to follow the stoichiometry ratios, the oxygen vacancies, and the existence of any contaminants. HZO films were deposited on Si substrate. Unfortunately, conducting XPS on the target's surface was impossible due to the thickness of the target with its support. It would de

assuring for the Zr: Hf stoichiometry. The 15 nm-thick samples have been deposited at 400 W, 4.5×10^{-3} mbar with 60 sccm total gas flow.

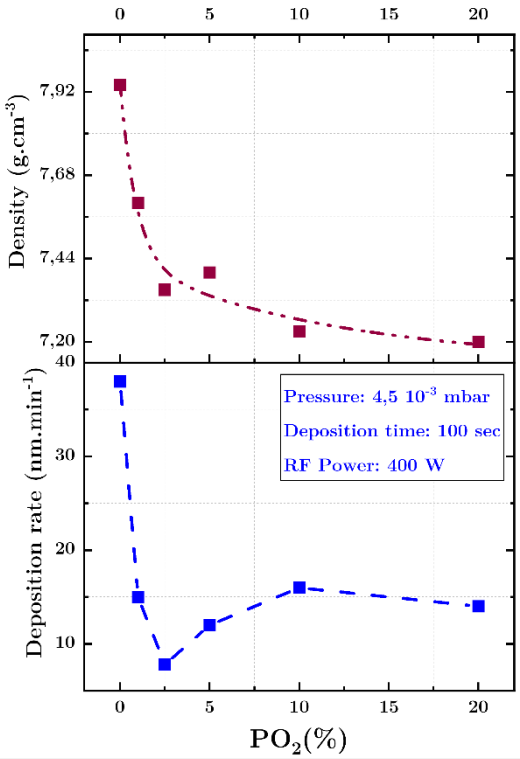

Figure 83 Variation of deposition rate and HZO density as function of oxygen partial pressure

The XRR technique was used for thickness and density measurements, as illustrated in **Figure 83.** It illustrates the variation of density and deposition rate as function of PO_2. As the latter increased, the deposition rate decreases relatively from 38 nm.min^{-1}, at 0%, to 14 nm.min^{-1} at 20%. The oxygen reduces the deposition rate due to its reactive nature in the plasma when collision with the sputtered atoms from the target's surface. This reduction in the deposition rate passed by two regions: the first one, from 0 to 5%, and the second one, from 5 to 20%. In the latter, the reduction of deposition rate is stable and linear contrary to the first one, where abrupt variations occurred despite the general reduction. The same trend of reduction occurred for the variation of density as function of PO_2. The density decreased from 7.94 to 7.2 g.cm^{-3}, at 0 and 20 % respectively. At high PO_2 values, the target's surface becomes oxidized to a larger extent and the deposition rate decreases, corresponding to the sputter yield of an oxide target. The aim behind these measurements is to determine the highest possible deposition rate with the closest density value to the theoretical one.

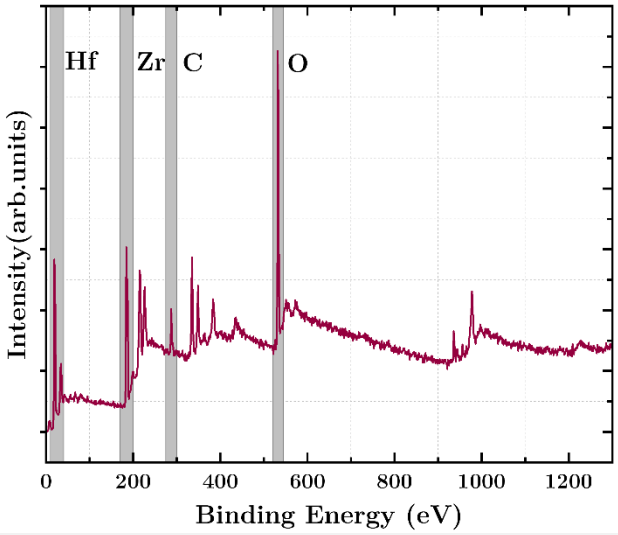

Figure 84 XPS depth profile survey of HZO/Si

The chemical composition of HZO film was studied by XPS, which can also yield the chemical bond nature through the analysis of the XPS peak chemical shift. By varying the x-ray beam incident angle between 23° and 76°, the HZO layer was probed to a depth of 10 nm. All XPS spectra in this part are the result of amorphous films.

The survey spectrum is presented in **Figure 84**. It has been acquired to determine the elements existed on the HZO layer (Hf, Zr, O, and C) without any contaminants detected. The thickness of HZO layer was around 14 nm deposited on Si substrate. This chosen thickness allowed to conduct angle-resolved scan to follow the composition and the stoichiometry from bulk to surface, in the 10 nm depth range, without any interference from the Si/HZO or TiN/HZO interfaces (which is out of the scope of this work).

The C 1s region is important to calibrate the data and compare the different samples. The XPS core level of C 1s peaks recorded is shown in **Figure 85 (left)** for the four samples with 0, 5, 10, and 20 % PO_2. The different XPS spectra were positioned, and the corresponding elements were identified by taking the adventitious C1s peak as a charge reference and shift it to **284.8 eV corresponding to C-C peak**. This adventitious carbon contamination is due to the air exposure of the samples. The small shift in binding energy, of C-O-C and O-C=O, between the four samples can be explained by the difference in the surface compositions of the samples in terms of carbon contamination and oxidation. For the 0, 10, 20% PO_2 samples, the C-O-C and O-C=O peaks are the same while for 5% PO_2 sample the O-C=O has a very low intensity.

One major information is extracted from the XPS results is the percentage of oxygen vacancies (V_O) extracted from the O 1s region. Here we compare the O 1s peak of the four samples with a special focus on V_O. The XPS core level of O 1s peaks is shown in **Figure 85 (right).** For the four samples, it consists of two very close peaks; the Hf–O and Zr–O bonds and the O–Hf–O and O–Zr–O bonds overlapped at 529.9–530 eV (for the 0% sample). The oxygen vacancies (V_O) peak is observed at 531.9 eV corresponds to interstitial oxygen or oxygen deficiency related to Hf and Zr sub-oxides.

As the PO_2 increased, the bonded oxygen peak is slightly shifted with -0.3 eV. At the same time, the V_O peak was shifted by -0.75 eV to 531.15 eV while the intensity of Vo peak increased to 25.8%. For the 10 and 20% PO_2 samples, the shift for the two peaks is no more than 0.2 eV while the intensity of V_O peak increased to 20.1% and 34.3% for 10 and 20 % PO_2 samples, respectively.

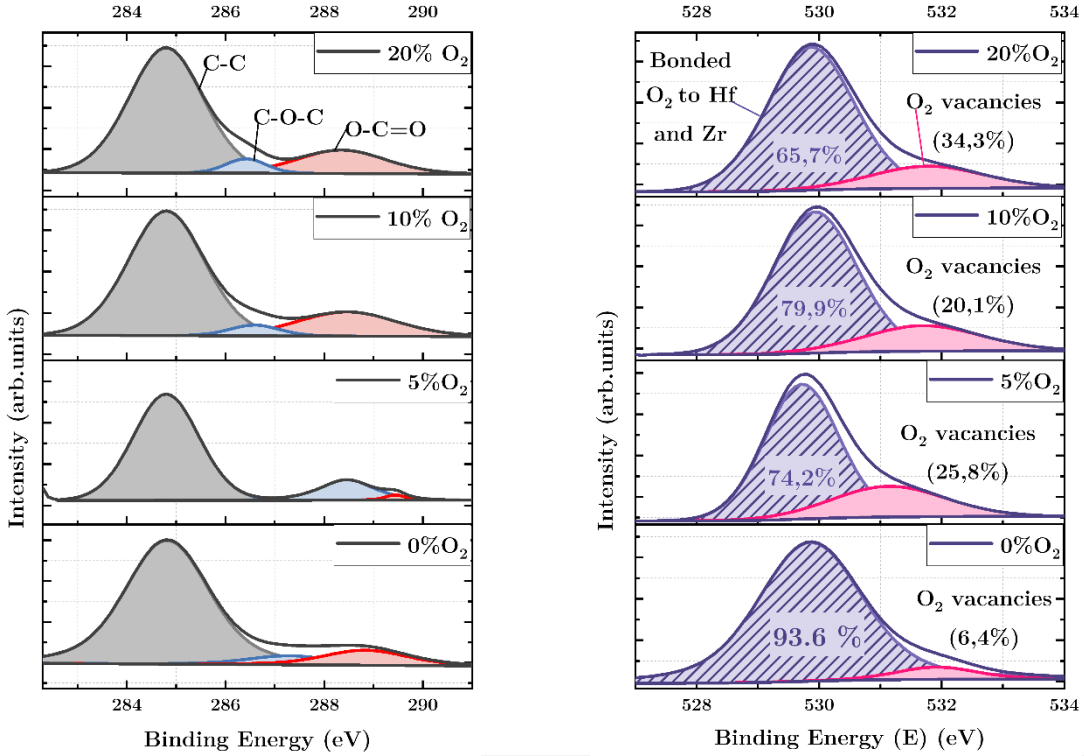

Figure 85 High resolution XPS spectra of samples deposited with different PO_2 values: C 1s (left) and O 1s (right) regions

The variation of V_O as a function of PO_2 is illustrated in **Figure 86**. V_O increased from its minimum (6.4%), at 0% PO_2, to its maximum (34.3%), at 20% PO_2, passing by an average value of 25 and 20% at 5 and 10% PO_2. The oxygen vacancies characteristic is important for the mechanism of inducing ferroelectricity in HZO [202]–[204]. Knowing that the oxygen vacancies increase after post-deposition annealing as reported in the next part.

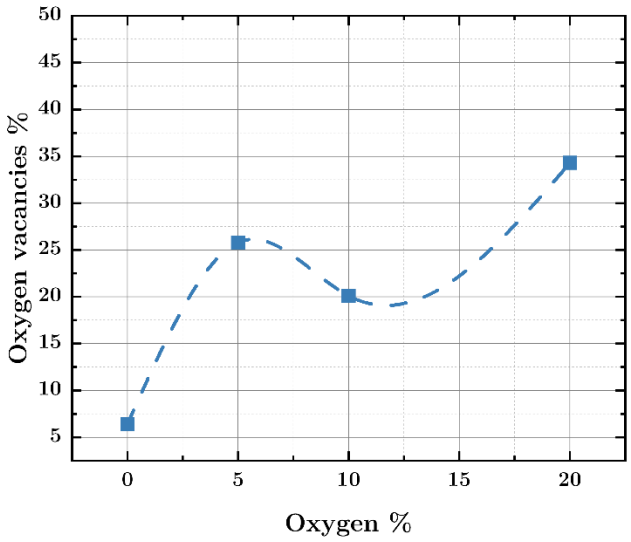

Figure 86 Variation of oxygen vacancies as a function of PO_2 % (0-20%)

For all samples, the Hf, Zr, and O elements are equally distant from the C1s peak. In **Figure 87** (left) two components are identified at 16.46 and 18.16 eV corresponding to hafnium oxide O–Hf–O bonds (for the 0% PO_2 sample). Moreover, the Hf $4f_{5/2}$ /Hf $4f_{7/2}$ doublet spin-orbit splitting, and the peak intensity ratio are 1.7 eV and ~3/4, respectively, in good agreement with reported values [205]. As PO_2 increased to 5%, both Hf $4f_{5/2}$ and Hf $4f_{7/2}$ were shifted by -0.32 eV while the same shift did not exceed 0.1 eV for both 10 and 20 % PO_2. The energy differences within the Hf 4f doublet are 1.7, 1.62, 1.72, and 1.69 eV for the 0, 5, 10, and 20% PO_2 samples. This energy difference is a characteristic of the hafnium oxide XPS spectrum as reported [205]. For the four samples, the energy difference is in a good correspondence with the reference HfO_2. The same conclusion was observed for the peak intensity ratio. All the ratios are close to ¾.

Similarly, the Zr 3d spectrum consists of two spin-orbit deconvoluted peaks at 181.95 and 184.35 eV as illustrated in **Figure 87** (right). The energy splitting of 2.4 eV and the Zr $3d_{3/2}$/Zr $3d_{5/2}$ intensity ratio of are consistent with ZrO_2 values found in the literature [206].

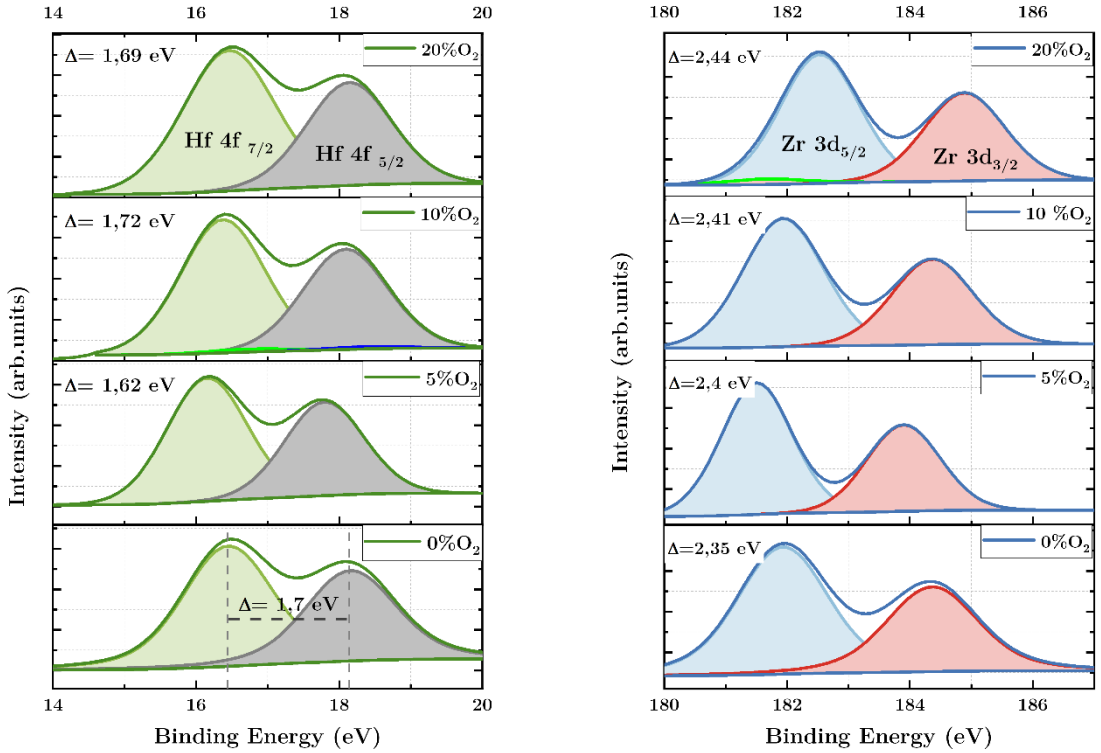

Figure 87 High resolution XPS spectra of samples deposited with different PO_2 values: Hf 4f (left) and Zr 3d (right) regions

Among the four samples, the 20% PO_2 sample shows two peaks corresponding to metallic Zr and the 10% PO_2 sample shows two peaks corresponding to metallic Hf. This is due to the saturation of plasma by oxygen and the sputtered Zr and Hf ions are deposited directly on the substrate surface of these two values of PO_2. These phenomena require a future detailed investigation.

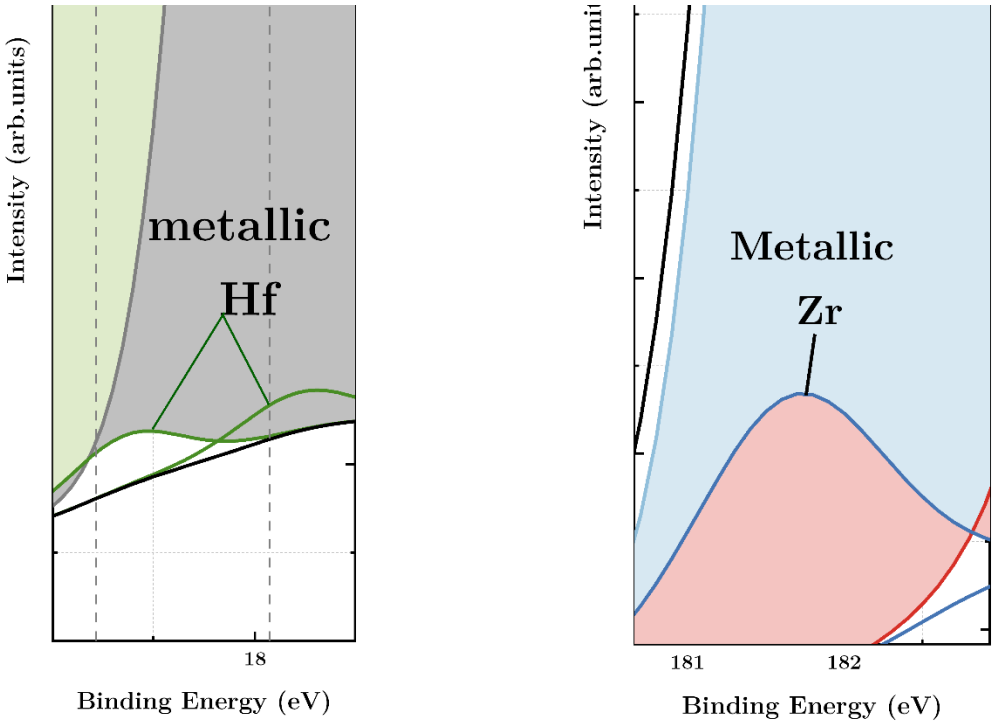

Figure 88 Zoom on additional peaks appeared in XPS spectra of Hf 4f at 10% $\mathbf{PO_2}$ (left) and Zr 3d at 20 % $\mathbf{PO_2}$ (right) samples

Moreover, two low-intensity XPS peaks are detected at 13.58 eV and 181.9 eV, for the 10 and 20 % PO_2 samples respectively, that can be attributed to the Hf $4f_{7/2}$ line in the metallic hafnium [207] and Zr $3d_{5/2}$ in the metallic zirconium. The additional peaks are illustrated in **Figure** 88.

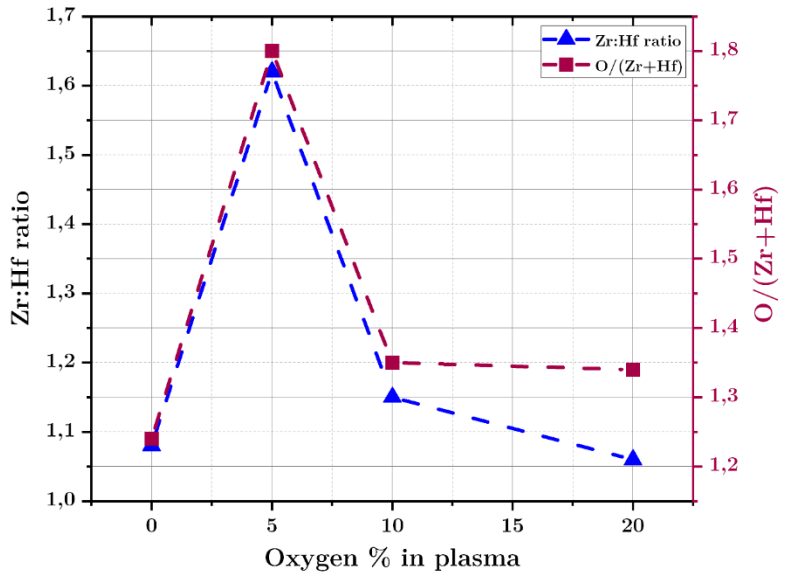

Figure 89 The variation of the Zr: Hf and O/(Zr+Hf) ratios as the oxygen % increases from 0 to 20% PO_2.

Figure 89 shows the variation of stoichiometry ratio, Zr: Hf and O/(Zr+Hf) extracted from the XPS results, as function of the PO_2 %. Both ratios varied with the same tendency.

The Zr:Hf ratio increased abruptly from 1.09, at 0% O_2, to its maximum 1.65, at 5% PO_2. Then, it decreased to 1.15 and 1.05, at 10 and 20% PO_2, respectively. While for the second ratio, it also abruptly increased from 1.23 to 1.8 then it decreased to 1.35 and 1.34 at 10 and 20% PO_2. Considering the two ratios, the closest stoichiometry to $Hf_{0.5}Zr_{0.5}O_2$ was found at 0% PO_2 ($Hf_{0.46}Zr_{0.54}O_2$). The rapid increase recorded at 5% PO_2, for both ratios, led us to redeposit a sample with the same conditions and reconduct an XPS measurement. The results were the same as the first one. So, the abrupt increase was confirmed.

The unexpected results found for the 5% PO_2 sample was the trigger to investigate the variation of PO_2, within the second part, with smaller steps in the range of [0, 2 %] to confirm the tendency for small percentages of oxygen compared to the relatively bigger percentages in the first part of this investigation.

In this second part of this investigation, we kept a reference sample of 0% PO_2 and deposited 3 more samples of 1, 1,5 and 2% PO_2. We conducted the same measurements on these samples to be in full adequation with the first part. The variation of deposition rate and the density has been already reported in **Figure 83**. The XPS results are reported in the following figures.

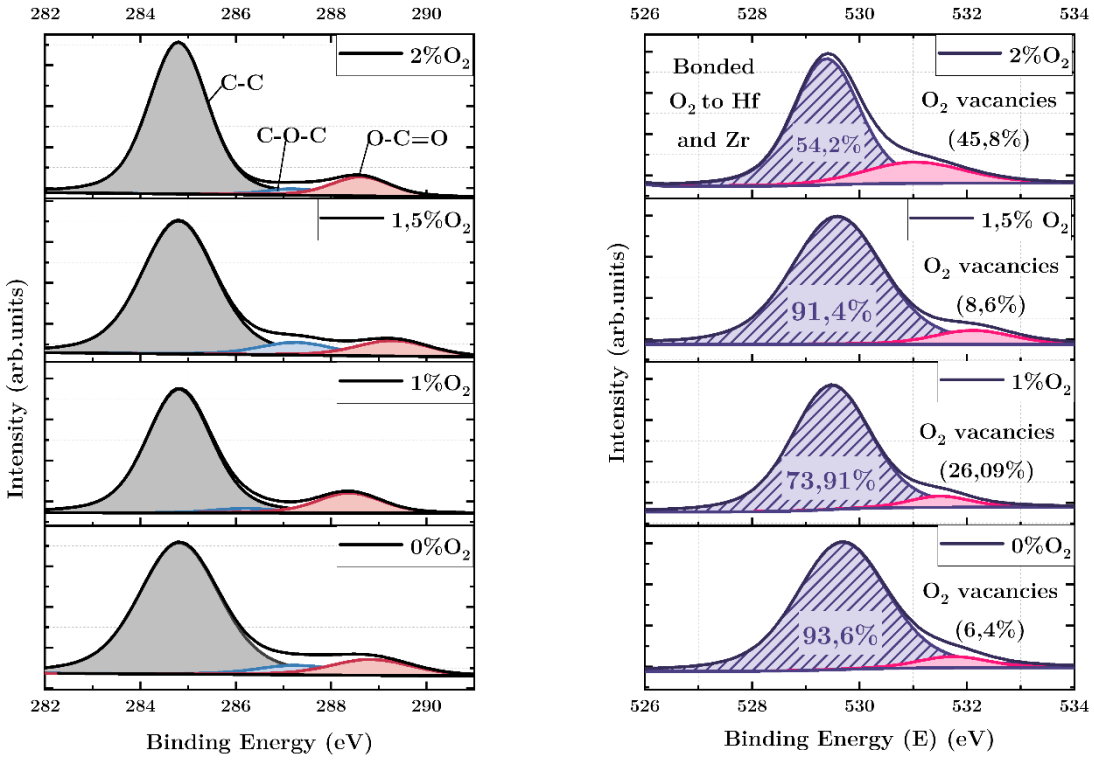

Figure 90 High resolution XPS spectra of samples deposited with different oxygen partial pressure values: C 1s (left) and O 1s (right) regions

The same methodology was applied to the XPS data**.** The different XPS spectra were positioned, and the corresponding elements were identified by taking the adventitious C1s peak as a charge reference and shift it to **284.8 eV corresponding to C-C peak. Figure 90** shows the high resolution XPS spectra of samples deposited with different PO_2 values: C 1s (left) and O 1s (right) regions.

The three peaks of C 1s region are very similar for the four samples (0, 1, 1.5, and 2% PO_2) with a small shift observed of the O-C=O peak compared to the other samples. The similarity between the four samples for the C 1s region can be explained by the quasi-similarity of the surface compositions of the samples in terms of carbon contamination and oxidation. The PO_2 effect on the C 1s region is more apparent in the first part.

The XPS core level of O 1s peaks is shown in **Figure 90(right).** For the four samples, it consists of two very close peaks; the Hf–O and Zr–O bonds and the O–Hf–O and O–Zr–O bonds overlapped at 529.9–530 eV (for the 0% sample). The oxygen vacancies (V_O) peak is observed at 531.9 eV corresponds to interstitial oxygen or oxygen deficiency related to Hf and Zr sub-oxides.

As the PO_2 increased, the bonded oxygen peak is slightly shifted with -0.3 eV, at 1% PO_2. At the same time, the V_O peak was shifted by -0.75 eV to 531.15 eV while the intensity of Vo peak increased to 26.09%. For the 1.5 and 2% PO_2 samples, the shift for the two peaks is no more than 0.2 eV while the intensity of V_O peak decreased to 8.6% then increased to 45.8% for 1.5 and 2 % PO_2 samples, respectively.

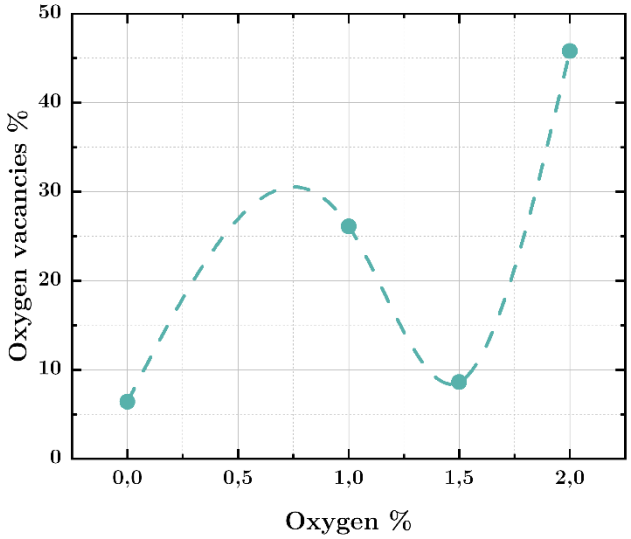

Figure 91 The variation of oxygen vacancies as a function of 0-2% PO_2

The variation of V_O as a function of PO_2 is illustrated in **Figure 86**. V_O increased from its minimum (6.4%), at 0% PO_2, to its maximum (45%), at 2% PO_2, passing by an average value of 25 and 1% at 9 and 1.5% PO_2. The oxygen vacancies increase after post-deposition annealing as reported in the part 3.

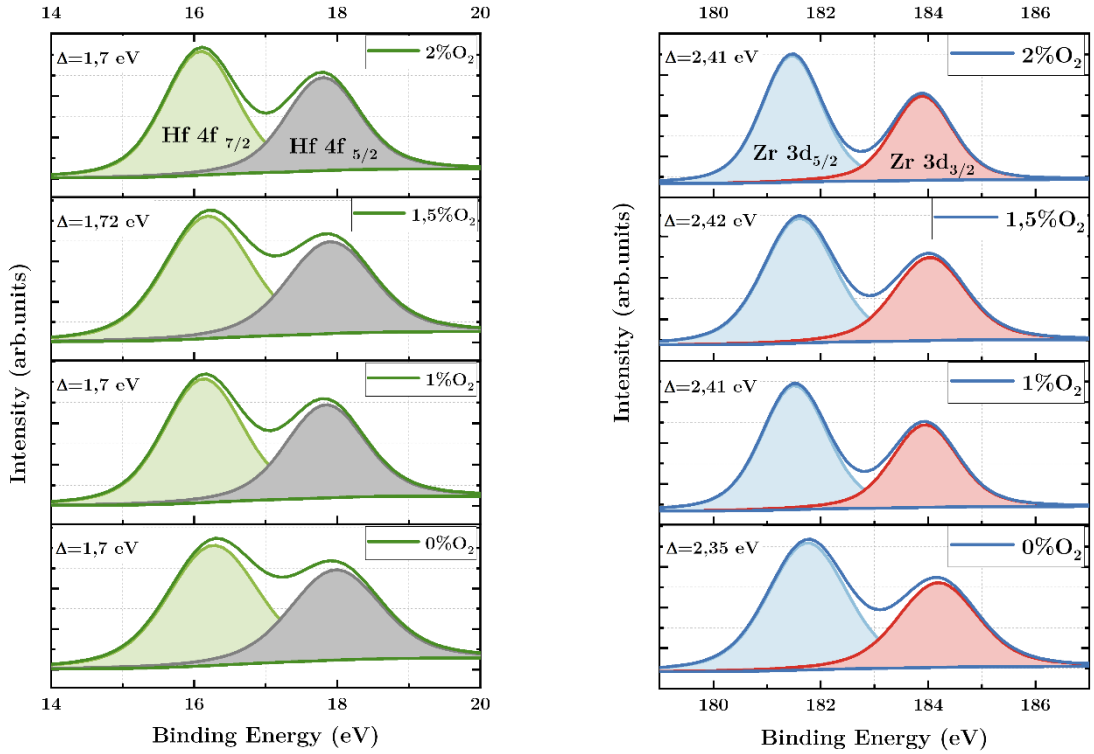

Figure 92 High resolution XPS spectra of samples deposited with different PO_2 values: Hf 3d (left) and O 1s (right) regions

Figure 92 shows High resolution XPS spectra of samples deposited with different PO_2 values: Hf 3d (left) and O 1s (right) regions.

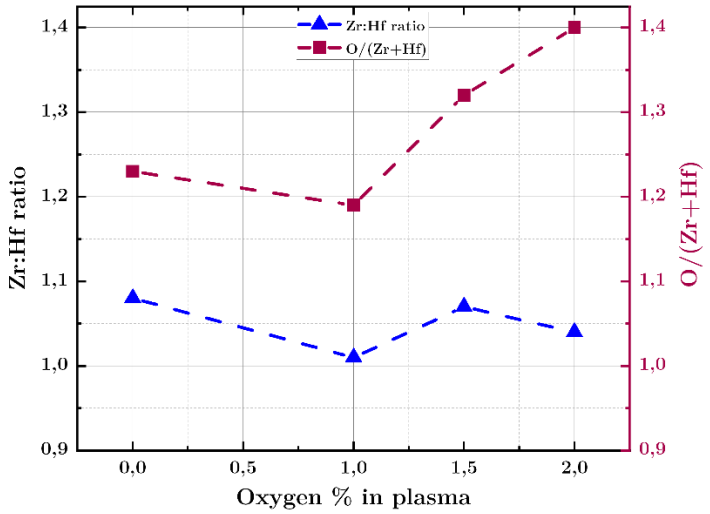

Figure 93 The variation of the Zr: Hf and O/(Zr+Hf) ratios as c increases from 0 to 2%.

Figure 93 shows the variation of stoichiometry ratios, Zr: Hf and O/(Zr+Hf) extracted from the XPS results, as function of the PO_2 % from 0 to 2. Both ratios varied with the same tendency from 0 to 1.5 % PO_2 then varied oppositely for the 2% PO_2 sample.

The Zr:Hf ratio (blue) decreased slightly from 1.1, at 0% O_2, to its minimum 1, at 1% PO_2. Then, it increased again to 1.1 and 1.05, at 1.5 and 2% PO_2, respectively. While for the second ratio (red), it also slightly decreased from 1.23 to 1.2 then it increased to 1.32 and 1.4 at 1.5 and 2% PO_2. Considering the two ratios, the closest stoichiometry to $Hf_{0.5}Zr_{0.5}O_2$ was found at 1% PO_2 ($Hf_{0.5}Zr_{0.5}O_2$).

The rapid increase recorded at 5% PO_2, for both ratios, led us to redeposit a sample with the same conditions and reconduct an XPS measurement. The results were the same as the first one. So, the abrupt increased was confirmed.

To confirm the amorphous characteristic of the deposited films as function of PO_2. XRD measurement was conducted on three samples (0, 2.5 and 5% PO_2) before and after rapid annealing at 650°C for 1 min under N_2.

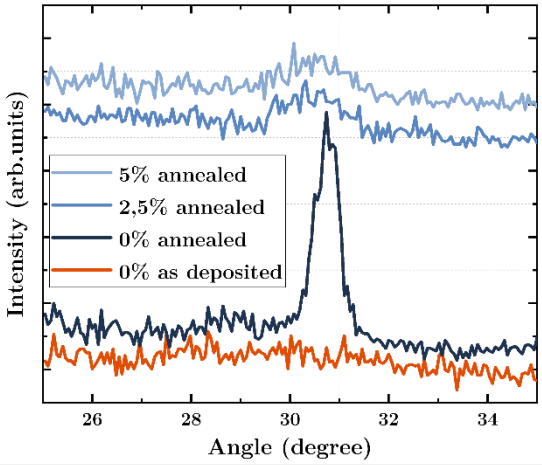

Figure 94 Diffractogram of TiN/HZO/TiN structures as deposited and annealed, as function of PO_2

Figure 94 illustrates the diffractogram of TiN/HZO/TiN structure as deposited and annealed, as function of PO_2. The three samples were amorphous, and no HZO-related peak has been detected except the TiN peaks. We limited the 2θ range to 25-35°. After annealing, the 0% PO_2 showed the most intense peak compared to the other samples with low intense peaks around 30.4°. the intense peak corresponds to the t/o phase. No monoclinic phase appeared for the three samples.

4.2.2.2 Pressure

We investigated the effect of sputtering deposition pressure on the deposition rate to determine the optimum deposition pressure. **Figure 95** shows the variation of deposition rate with the sputtering deposition pressure of HZO, deposited on Si substrate at 60 sccm Ar gas flow and 400 W. The measurement of thickness was conducted by

XRR technique. The aim, behind the investigation of deposition pressure, is to determine the optimal value of pressure for the highest deposition rate and keeping the amorphous nature of HZO with desired density. The deposition pressure affects the deposition rate and the nucleation of the films. Very high pressure can increase the porosity within the films.

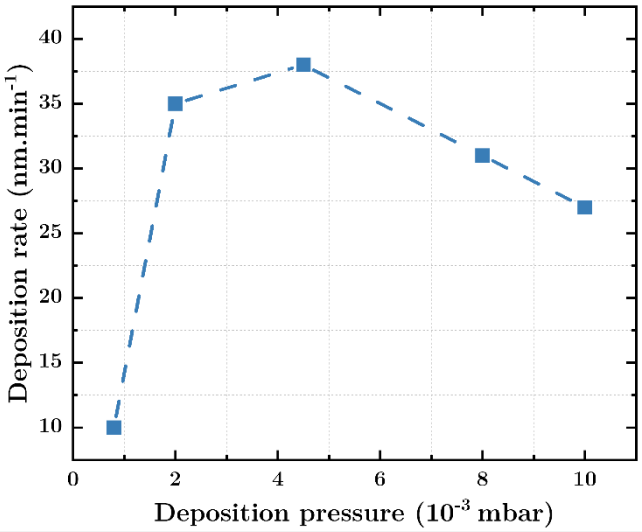

Figure 95 Variation of deposition rate as a function of the deposition pressure

For this investigation, we varied the deposition pressure from 0.8×10^{-3} mbar to 1×10^{-2} mbar. The determination of this range was based on preliminary experimental investigation. The lowest deposition rate was found at 0.8×10^{-3} mbar pressure while the highest deposition rate was found around 4.5×10^{-3} mbar. As function of the deposition pressure, the deposition rate varied differently in two regions: an increase from 10 nm.min-1 at 0.8 $\times10^{-3}$ mbar to 37.2 bm.min-1 at 4.5 $\times10^{-3}$ mbar, and a decrease from at 4.5 $\times10^{-3}$ mbar to 27.1 nm.min-1 at 1 $\times10^{-2}$ mbar.

The variation of HZO density was not the same as the deposition rate. It was stable around 7.94 g.cm-3 for the all the samples except for the sample deposited at 1 $\times10^{-2}$ mbar, it reduces to 6.9 g.cm-3 (the figure is not illustrated).

This investigation allowed us to determine a key sputtering parameter; the deposition pressure, at which the most samples were deposited at. The deposition rate remained relatively stable except for other technical issues. Determining the optimal deposition pressure revealed the highest possible deposition rate at have HZO films with the desired requirements.

4.2.2.3 Power target

Another key parameter for the sputtering of HZO films is the power applied to the target or the sputtering power. This parameter directly affects the deposition rate: the sputter yield. Films properties are basically controlled by the sputtering power. Studying its effect on the deposition rate allowed us to determine which power value is the suitable to obtain the highest possible deposition rate. Many criteria were respected to determine this key value of power such as avoiding any contamination generated by the target's support and conserving the stoichiometry of the films. For the sake of clearness, the power target is applied as function of the target dimensions and the power density is more precise term for this sputtering parameter. **Table 11** indicates the corresponding power density to each power value used in this work.

Table 11 The studied power values and the corresponding power density

Power target (W)	**200**	**300**	**400**	**500**	**600**
Corresponding power density (W.cm^{-2})	1.67	2.5	3.33	4.17	5

The sputtering power applied to the target was varied in the range of 200 -600. The maximum power can be applied to the target is 600W as mentioned in the technical datasheet provided by the manufacturer.

To get further insights on the sputtering power effect, two properties were targeted: the deposition rate and the stoichiometry of HZO. For that, the XRR technique allowed to determine the deposition rate while XPS revealed the variation of stoichiometry within the as deposited films. All sample were deposited on Si substrate and most of them were amorphous except the 600 W samples (crystallized into monoclinic phase).

Figure 96 indicates the variation of deposition rate as function of the increasing power applied to the target. Increasing the power from 200 to 600 W means increasing the

ionization energy of Ar^+ ions to sputter more ions for the target's surface. The deposition rate increased linearly from 21 to 57 nm.min^{-1}.

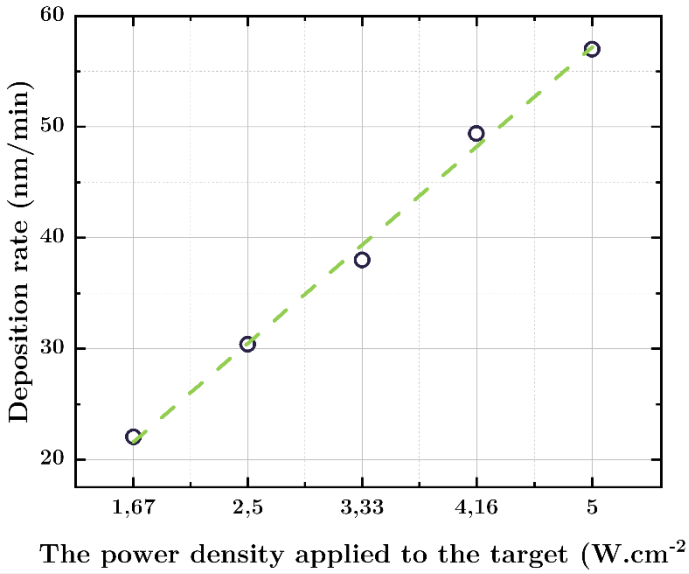

Figure 96 Variation of deposition rate as a function of the power density applied to the target.

Unfortunately, at this stage, the highest deposition rate is not enough to determine the optimal power value. So, XPS measurements were conducted on the different samples as shown in **Figure 97** and **Figure 99**.

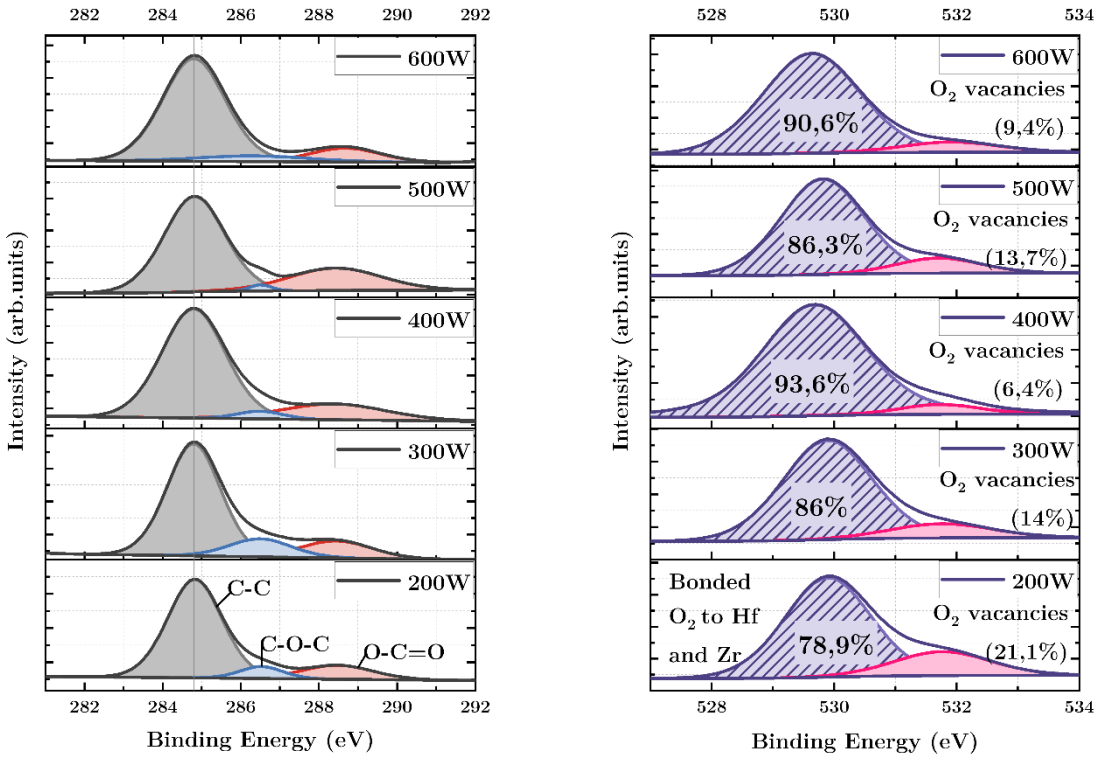

Figure 97 High resolution XPS spectra of samples deposited with different power values: C 1s (left) and O 1s (right) regions

The thickness of HZO layer was around 14 nm deposited with 60 sccm Ar on Si substrate. This chosen thickness allowed to conduct angle-resolved scan to follow the composition and the stoichiometry from bulk to surface, in the 10 nm depth range. As can be seen in **Figure 97,** XPS spectra of C1s (left) and O1s (right) regions are illustrated as function of the increasing sputtering power. The first one helps calibrating the other regions and the second one is important for V_O.

For the five samples, the recorded C 1s spectrum was decomposed into three contributions, namely, C–C, C–O, and C=O, arising from typical ambient carbon contamination. The different XPS spectra were positioned, and the corresponding elements were identified by taking the adventitious C1s peak as a charge reference and shift it to **284.8 eV** corresponding to C-C peak. This adventitious carbon contamination is due to air exposure of samples.

For the O 1s core level, it consists of two very close peaks for the five samples; the Hf–O and Zr–O bonds and the O–Hf–O and O–Zr–O bonds overlapped at 529.9–530 eV. The oxygen vacancies (V_O) peak is observed at 531.9 eV corresponds to interstitial oxygen or oxygen deficiency related to Hf and Zr sub-oxides. The oxygen vacancies decreased from 21.1% to 6.4% as the power increased from 200 to 400 W while it increased to 13.7% at 500 then decreased to 9.4% at 600 W. the lowest oxygen vacancies was recorded at 400 W and the highest at 200W. The information about oxygen vacancies is important as it plays an important role in the mechanism of ferroelectricity induction in HZO films. The selection criterion is to have oxygen vacancies as low as possible.

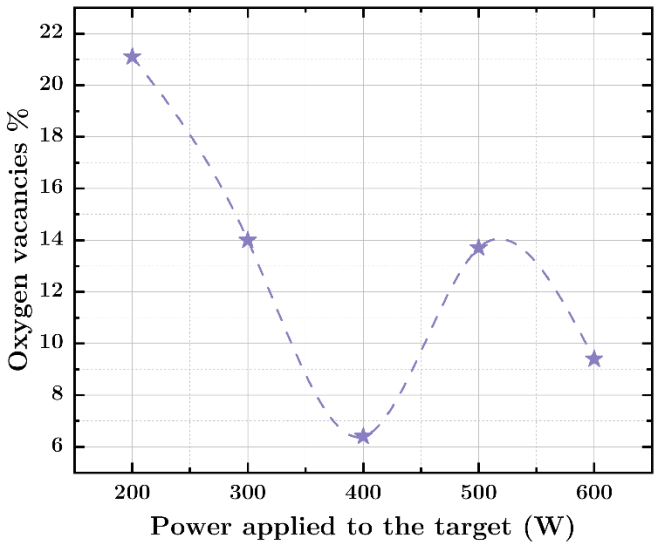

Figure 98 The variation of oxygen vacancies as a function of sputtering power

The variation of V_O as a function of sputtering power is illustrated in **Figure 98**. V_O decreased from its maximum (21.1%), at 200W, to its minimum (6.4%), at 400W. V_O increased, at 500W, to 13.7% then slightly decreased to 9.4% at 600W.

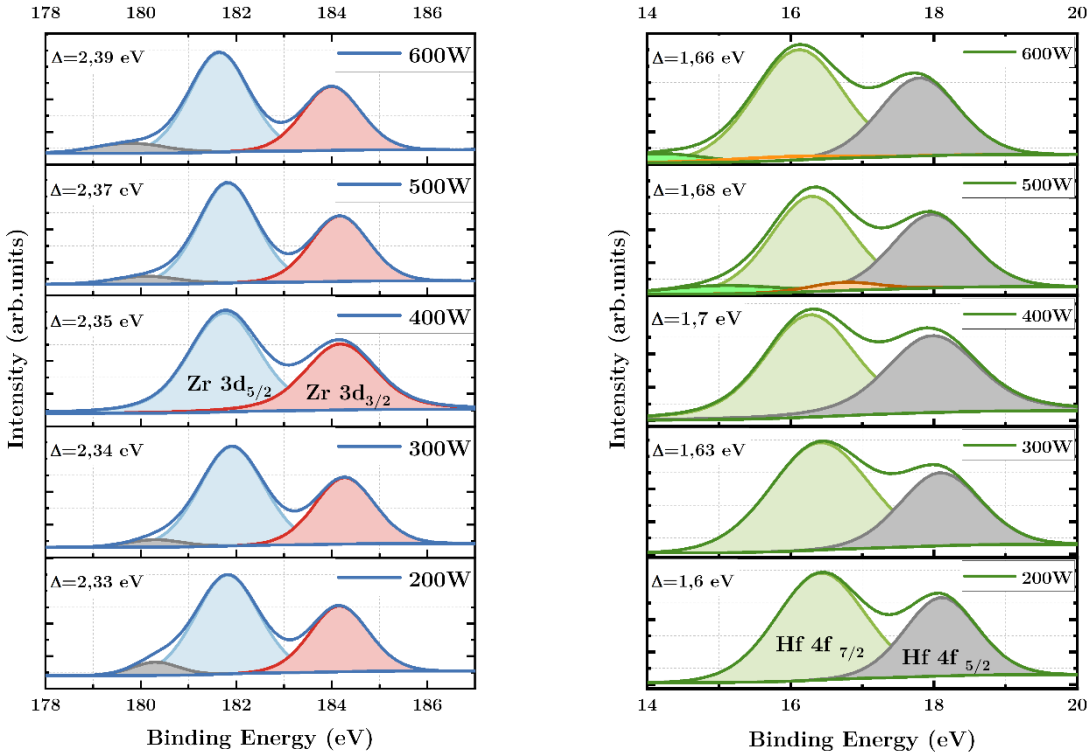

Figure 99 High resolution XPS spectra of samples deposited with different power values: Zr 3d (left) and Hf 4f (right) regions

For all samples, the Hf, Zr, and O elements are equally distant from the C1s peak. In **Figure 99** (left) two components are identified at 16.46 and 18.16 eV corresponding to hafnium oxide O–Hf–O bonds (for the 0% sample). Moreover, the Hf $4f_{5/2}$ /Hf $4f_{7/2}$ doublet spin-orbit splitting, and the peak intensity ratio are 1.7 eV and ~3/4, respectively, in good agreement with reported values []. As the oxygen % increased to 5%, both Hf $4f_{5/2}$ and Hf $4f_{7/2}$ were shifted by -0.32 eV while the same shift did not exceed 0.1 eV for both 10 and 20 %. The energy differences within the Hf 4f doublet are 1.7, 1.62, 1.72, and 1.69 eV for the 0, 5, 10, and 20% samples. This energy difference is a characteristic of the hafnium oxide XPS spectrum as reported in. for the four samples, the energy difference is in a good correspondence with the reference HfO_2. The same conclusion was observed for the peak intensity ratio. All the ratios are close to ¾.

Among the four samples, the 10% sample shows two peaks corresponding to metallic Hf. This is due to the saturation of plasma by oxygen and the sputtered Hf ions are deposited directly on the substrate surface.

For as-deposited film, the XPS spectra showed the Hf doublet: Hf 4f $_{5/2}$ and Hf 4f $_{7/2}$ peaked at 18.48 and 16.98 eV, respectively, which are typical for the Hf–O bonds in hafnium oxide.

The XPS peaks of the main Hf 4f doublet did not change their positions after the increase of sputtering power from 200 to 6o 600 W, whereas a small shift of these XPS peaks toward lower binding energies was found for the film deposited at 400 W.

Similarly, the Zr 3d spectrum consists of two spin-orbit deconvoluted peaks at 181.95 and 184.35 eV as illustrated in **Figure 99** (right). The energy splitting of 2.4 eV and the Zr $3d_{3/2}$/Zr $3d_{5/2}$ intensity ratio of are consistent with ZrO_2 values found in the literature.

Except the 400 W sample, the other samples had a low intensity peak appeared around 180 eV for the Zr 3d region. This peak is attributed to a sub-oxide of Zirconium.

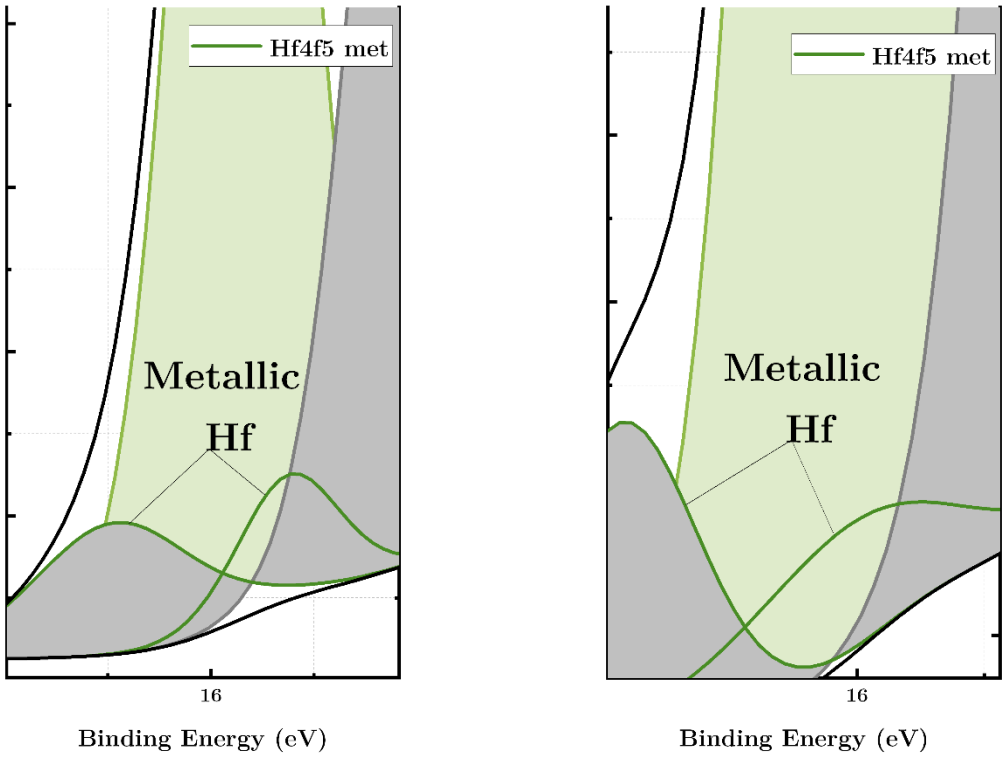

Figure 100 Zoom on additional peaks appeared in Hf 4f XPS spectra for 500W (left) and 600W (right) samples

Additionally, the small intensity XPS peak is detected at 13.58 eV, for 500 and 600W, that can be attributed to the Hf 4f 7/2 line in the metallic hafnium [207].

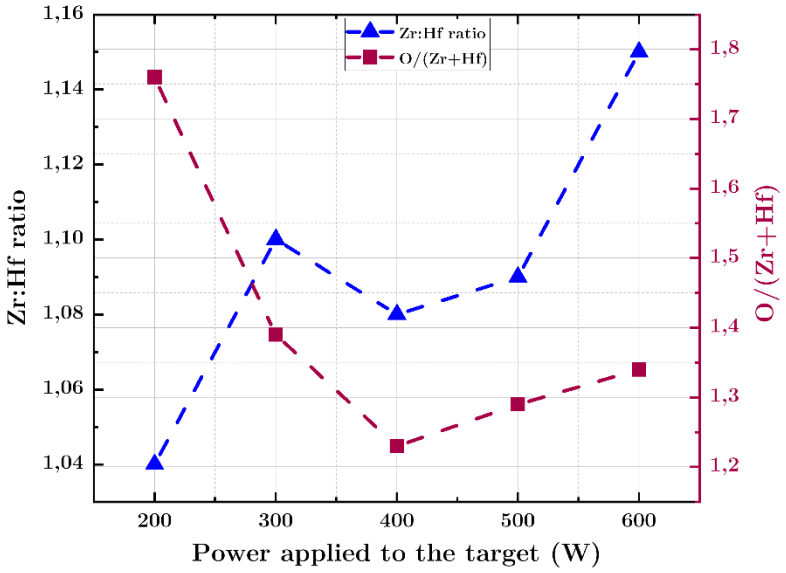

Figure 101 variation of Zr: Hf (blue) and O/(Zr+Hf) (red) as function of the sputtering power.

Extracted from the XPS spectra, the stoichiometry of HZO was investigated via two ratios: Zr: Hf and O/(Zr+Hf). **Figure 101** illustrates the variation of both ratios as function of the sputtering power. Their variations do not follow the same tendency. For the Zr:Hf ratio, the closest sample to 1:1 ratio was the 200 W sample. (1.04). Then, it increased to 1.1, for 300 W, before slightly decreased to 1.08 at 400W and increased again to 1.15 at 600 W. The second ratio varied differently, it decreased from 1.14 to 1.07, at 200 and 600 W respectively passing by the lowest value of 1.05 at 400W. For both ratios, the same tendency is observed in the 300-500 W range. Compared to the extremities (200 and 600W), both ratios varied slightly between 300 and 500 W. It is noteworthy that the best values, in this range, are found at 400 W.

4.2.2.4 Ar Flow

The choice of gas flow rate was not arbitrary. By investigation the impact of the gas flow rate on the deposition rate and the density of the films, we investigated the effect of increasing energy flux at the substrate. It can affect the deposition rate and the crystal growth. This parameter was reported to influence the properties of sputtered films [208], [209].

As explained in the reactive sputtering section, HZO films were deposited using Ar only. The Ar flow rate was varied from 20 to 80 sccm by a step of 20 sccm. We investigated the possible effect of this variation on the deposition rate, density, and roughness of HZO films.

As illustrated in **Figure 102**, XRR patterns are presented of HZO samples deposited with different Ar flow rates. No noticeable change in thickness of the HZO films deposited at Ar flow rate (20 to 80 sccm) was observed. In addition, there is no substantial difference in film roughness between samples except the 60 sccm sample that showed the lowest Rq value. The density was the only property that changed, from 7.4 to 7.94 g.cm^{-3} at 20 and 80 sccm, respectively. The XRR measurements were conducted on HZO deposited on Si substrates. All the as-deposited films were amorphous.

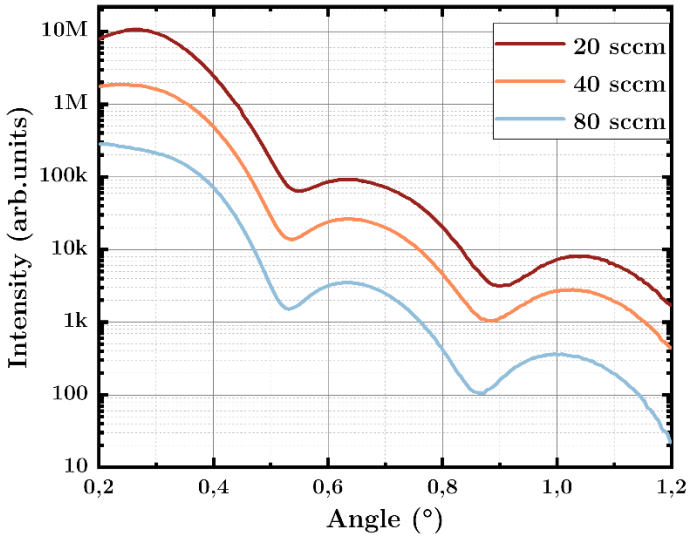

Figure 102 X-ray reflectivity patterns of HZO deposited at different Ar flow rates

4.2.2.5 Deposition time

As we targeted characterizing different thickness of HZO films, we studied the deposition time to assure having the same sputtering conditions of HZO films of different thicknesses. It is the last sputtering parameter that we investigated, related to the sputtering process. The aim of deposition time investigation is to check the linear relationship between the deposition time and the deposited thickness or in other words, the constant deposition rate as function of time.

The XRR technique was used to determine the deposition rate. The measurements were conducted on HZO samples, deposited on Si substrates at 400 W and 4.5 $\times 10^{-3}$ mbar.

Figure 103 illustrates the linearity between thickness and deposition time which means that the deposition rate, at these chosen parameters, is quite stable in time and reproducible. This stability allowed us to obtain the wanted thicknesses after a simple calculation of the deposition time.

The deposition time can be considered an illustration of the advent of sputtering of time saving deposition technique compared to other techniques.

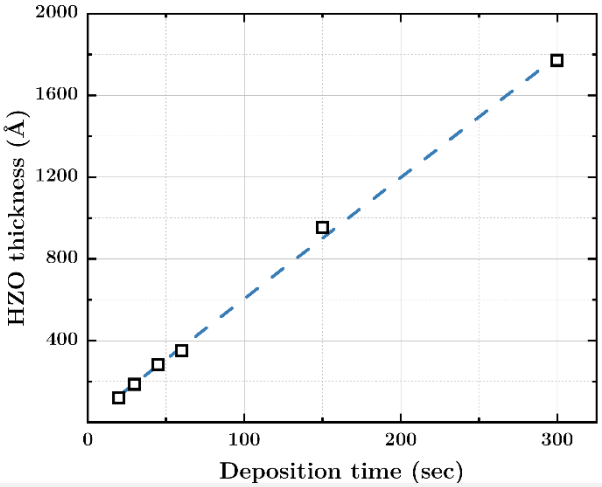

Figure 103 The thickness of HZO deposited films as a function of the deposition time

4.2.3 Characterization of HZO thin films

4.2.3.1 Optimized parameters

After studying each, possible, sputtering parameter for HZO deposition, here are the optimized parameters for HZO deposition while satisfying the criteria of keeping Zr: Hf as close as possible to 1:1, amorphous as-deposited films and having less oxygen vacancies, as will be explained in the discussion section.

The principal parameters that matter for HZO deposition are Deposition pressure, Power target, while the other parameters such as Total gas flow are neutral without significant impact on HZO films' quality.

The parameters	Values
Deposition pressure	4.5 10^{-3} mbar
Power target	400 W (3.33 W.cm^{-2})
Gas flow rate	60 sccm
Deposition time	38 nm.min^{-1}

As a reminder, the substrate temperature and bias are also considered as important parameters. Studying their effects would lead to better results of HZO sputtering. In addition, the rotation speed of the substrate holder can also on the uniformity of the films. We found 30 rpm speed as the suitable to have uniform thickness over the Si substrate. Also, we found that 7 cm as a target-substrate distance leads to higher deposition rate than the 12-cm distance. This is simply explained by the shorter free mean path. These parameters can vary for other sputter chambers, different target's geometry or stoichiometry, or different substrates.

The following **Figure 104** illustrates the XPS spectra for XPS of HZO films deposited with the optimized parameters while **Figure 105** shows the Angle-resolved XPS spectra for O1s, Zr 3d, and Hf 4f regions.

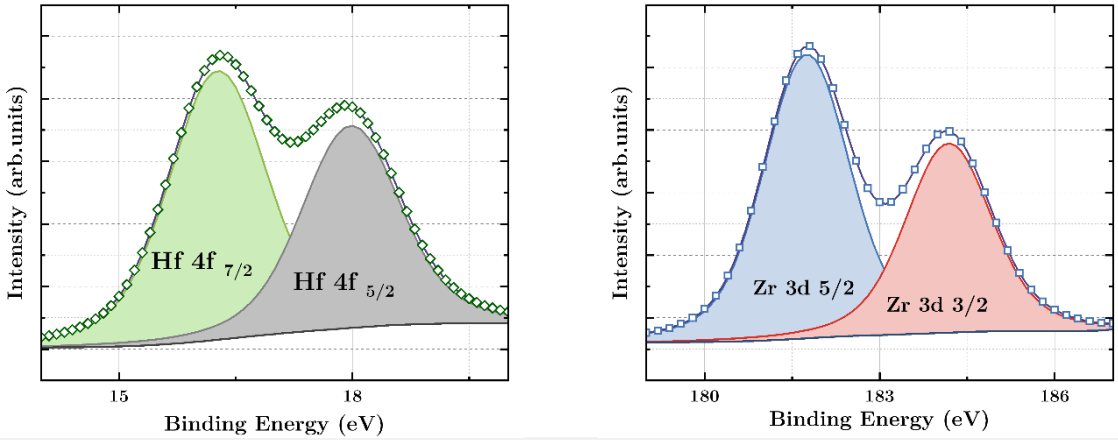

Figure 104 XPS spectra of HZO deposited on Si with the optimized parameters for (a) Hf 4f region (b) Zr 3d region

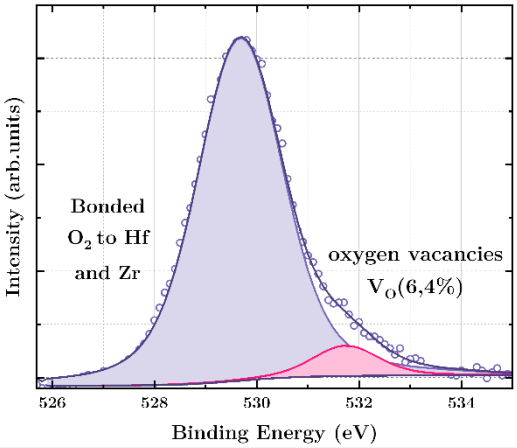

(c) O 1s region

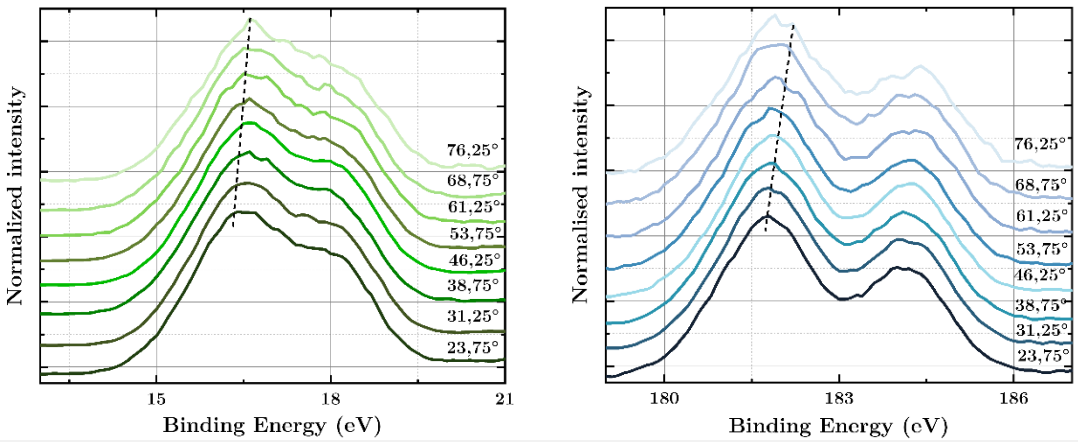

Figure 105 Angle-Resolved XPS spectra for sputtered HZO (a) Hafnium 4f (b) Zr 3d

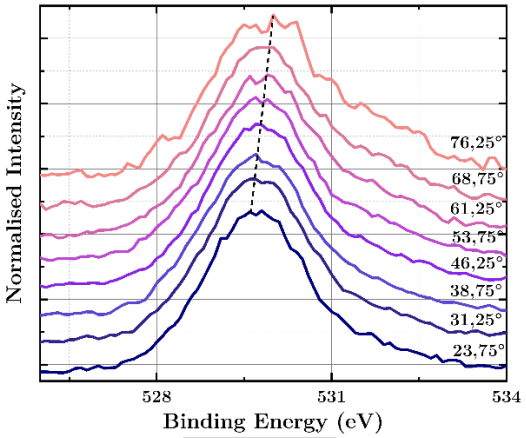

(c) oxygen 1s

To analyse the depth distribution of bonded hafnium, zirconium, and oxygen atoms, we performed ARXPS analyses on HZO sample using photoemission angles from 23 to 76° and stepped every 7.5°.

For the as-deposited HZO film, **Figure** 105 (a) and (b) indicate that the main content of Hf and Zr sub-oxides decreased slightly at a photoemission angle of 76°, possibly due to oxidation near the surface. Hence, the small shifts marked in the spectra from 23 to 76° at both the Hf 4f, Zr 3d, and O 1s regions, as illustrated in **Figure 105**, is due to the variation in coupling between the electric field and the components of the adsorbed molecules on the surface.

It is apparent that the major impurity at the layer surface is carbon, the concentration of which is even higher than that of oxygen. Although the carbon concentration decreases as the layer depth increases, it sustains its high value (45%) almost up to 4 nm, as illustrated in **Figure 106**.

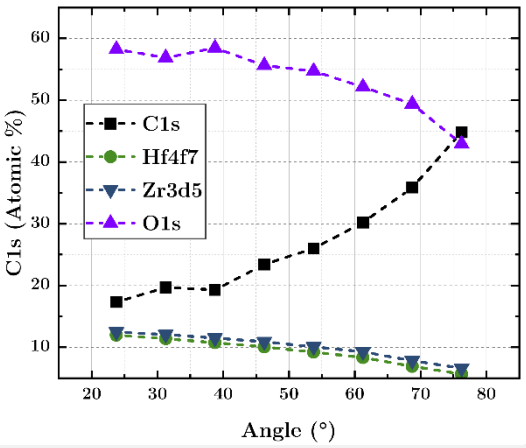

Figure 106 Atomic percent plotted versus emission angle ARXPS of HZO

The normalized intensities were determined by integrating the area under each core peak and divided it by the photoionization cross section for that element. The atomic concentration of each element was calculated by dividing the normalized intensity of the element by the sum of all normalized intensities. As the ARXPS emission angle is increased, the measurements become more surface sensitive. The effective mean free path is defined as $\lambda eff = \lambda \cos \theta$. At the largest emission angles, only the top couple of atomic layers are probed by ARXPS.

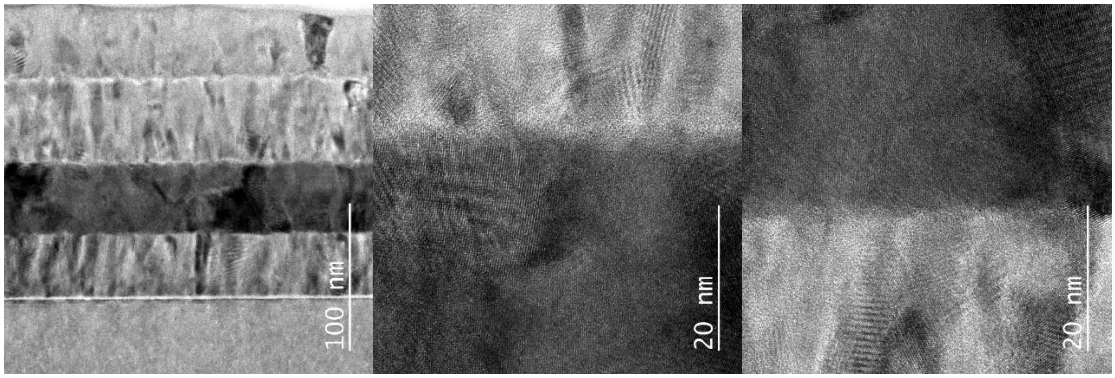

Figure 107 TEM cross section of (left) full TiN/HZO/TiN stack (middle) focus of HZO/TiN top electrode, and (right) focus on TiN bottom electrode/HZO evidencing the thickness uniformity of both HZO and TiN and the interfaces besides the crystallization of HZO after annealing.

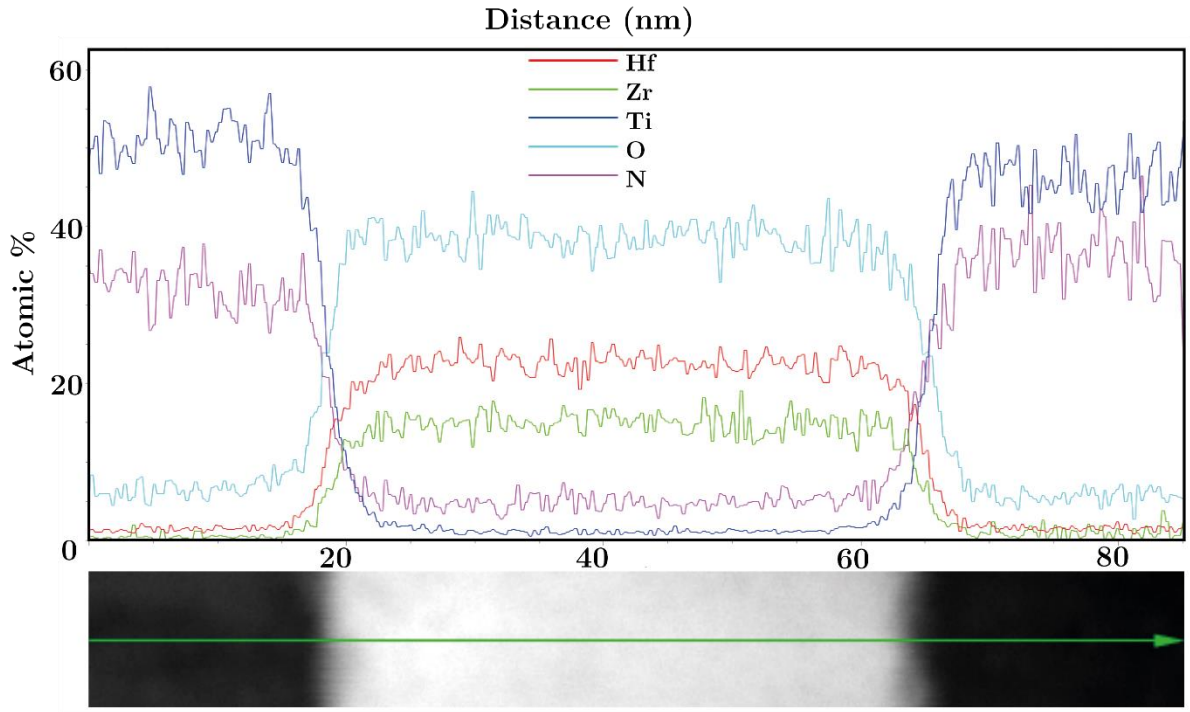

Figure 108 TEM image of annealed TiN/HZO/TiN stack can be seen in bottom; b) EDX along the structure indicated in a), where Gd signal is amplified by a factor 10 for better visualization; c) HRTEM detail in which a stronger crystallization of the N2 annealed film can be seen with respect to the d) as-deposited sample.

TEM analysis was performed on a TiN/HZO/TiN stack, after annealing, to get an insight checking, in once, the thickness uniformity for TiN and HZO, checking the TiN/HZO interfaces after annealing, and the crystallization of HZO layer. **Figure 107** shows a highly uniform HZO film with no inter-layers between the HZO and TiN electrodes. Moreover, the formation of crystallites with a typical diameter of about 10 nm is observed.

An EDX analysis was conducted on the same lamella for the elemental composition investigation.

The EDX elemental profiles in **Figure 108** , taken along the TiN/HZO/TiN structure highlighted in **Figure 108**, show some interdiffusion of species; most notably, oxygen migration towards the electrode layers is observed due to the known scavenging effect of TiN, as it will be discussed later. A good stoichiometric ratio is detected for the Zr: Hf film (the counts of Gd have been multiplied by a factor 10 for better comparison with other elements). EDX has a lower accuracy compared to XPS but it confirms the Zr: Hf, reported earlier by XPS, despite the emission spectra interference between Hf and Zr which makes the accurate determination requires a reference sample.

The total detected amount of Hf and Zr is around 45 % in the HZO layer, which is quite close to the XPs results and the target' stoichiometry. This result is acceptable given the resolution of the EDX. The HRTEM image in **Figure 108** further confirms that the annealing at 450 °C was sufficient to bring the thin films to a crystallized state, in contrast to what is observed on the as-deposited sample in **Figure 108**, which consists of a mostly amorphous film with some locally crystallized regions. It is in principle possible to distinguish between t- and o phase with this technique but the measurements required to accurately detect O ions position in the unit cell are beyond the scope of this work.

4.2.3.2 Thickness effect

The thickness of HZO films is another determinant characteristic that matters for ferroelectricity in HZO. As mentioned above, ferroelectricity in HZO was reported to be limited to 25 nm basically, except for some thicker films reported in **Chapter 2**. During the rapid thermal annealing, the amorphous nature of as-deposited HZO films is reported to facilitate the crystallization of the film into the orthorhombic phase.

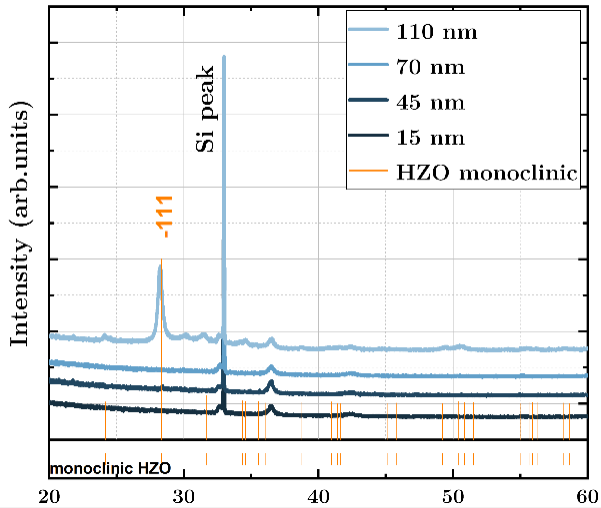

Figure 109 XRD patterns of as-deposited HZO films of various thicknesses

HZO films with several thicknesses have been deposited and characterized by XRD for crystallinity. As shown in Figure 109, three samples below 100 nm are amorphous as-deposited whereas the 110 nm-thick sample presents m-phase peak even before the thermal annealing step.

4.2.4 Discussion

During the sputtering deposition of HZO, the energy of Ar^+ ions varies from in the range of 5 eV to 5 keV, and it also depends on the RF power density (linear relationship). The collisions between the Ar ions and the target led to the ejection of the target atoms. The ejected atomic species travel through a distance randomly and get deposited on the substrate. More and more atoms condense and form a uniform film on the substrate. The surface atoms are ejected from the HZO target surface when the incident ion kinetic energy overcomes the binding energy. Mostly, the average surface binding energy and covalent bonding energy of solids are of the order of a few eV (~ 5 eV). The increase of deposition power induces more energy to the Ar ion and subsequently causes an increase in the deposition rate. In this work, the RF power was varied from 1.67 to 5 $W.cm^{-2}$.

From the observation, at lower RF power densities, the film thickness was significantly less, and the growth rate was low (~20 $nm.min^{-1}$). While increasing the power density, the film thickness and deposition rates increased linearly. This could be due to the increase in Ar ion flux proportional to the RF power density. The increase of Ar ions flux can increase the sputter rate and generate more species. Therefore, the deposition

rate or film thickness increases with RF power density. Higher deposition rates at high RF power densities (4.17 and 5 $W.cm^{-2}$) may not ensure the proper density of films, grain size, and stoichiometry. Besides, we found metallic Hf and Zr traces at these high-power densities. At higher powers, the bombarding ions will have higher kinetic energy, due to momentum transfer, the target atoms will be sputtered out. Sputtering yield is higher (atoms/ions) and thereby the ejected specie from the target will be more and result in a higher deposition rate. Keeping on increasing the power to get higher and higher deposition rates, will also result in electron bombardment, which can have deleterious effects on the growing film. The target gets heated up and necessitate effective cooling. We speculate that the latter is the reason behind the metallic Hf and Zr found at 500 and 600 W.

At low sputtering pressures of 8×10^{-4} mbar, the deposition rate was found to be relatively low (9.8 $nm.min^{-1}$) due to the fact that there is a low density of sputtering gases, less bombardment, and hence lower sputtering yield. At pressures around 2 to 4.5×10^{-3} mbar, there is a lot of energetic bombardment due to the high sputter gas density and hence an enhanced deposition rate as described in theory. At high pressures 8 to 10×10^{-3} mbar, although there is a high density of sputter gas, scattering phenomenon becomes predominant and the deposition rate decreases. Lowering the sputtering pressure increases the deposition rates [198]. Due to the low working gas pressure, the sputtered particles traverse the discharge space without collisions, which results in high deposition rate. The increment in the deposition rate with the increment of pressure up to can be explained by the relationship of the mean free path with the molecular diameter of the sputtering gas.

The relationship between deposition rate and deposition pressure of HZO thin film is shown in **Figure 95**. It can be observed that deposition rate increases with increasing pressure from 8×10^{-4} to 4.5×10^{-3} mbar, and after this point the deposition rates fall as the pressure increases up to 1×10^{-2} mbar. According to the gas dynamics, for a given gas, the pressure and free path of molecules of that gas can be expressed as:

$$\lambda_g = \frac{kT}{\sqrt{2}\pi P d^2}$$

As pressure increases, it can be observed that when d (molecule diameter) and T (temperature) are fixed, λ_g would drop, increasing the likelihood of collisions between sprayed atoms and gas molecules. This causes the cathode sheath's thickness to decrease,

which in return causes the ion current density to rise. More details are reported by Ameen et al. [210].

As a result, at lower pressures (around 8×10^{-4} mbar), the ion current density rises with pressure. The quantity of gas molecules increases with pressure (from 4.5 to 10 $\times10^{-3}$ mbar), increasing the likelihood of an interaction between sputtered atoms and gas molecules. This lowers the sputtered atoms' energy, which will result in fewer atoms depositing on the substrates and a slower rate of deposition. In contrast, as pressure rises, the average free route of gas molecules shortens. Because of the increased likelihood of sputtered atoms being backscattered and being scattered by gas molecules, sputtered atoms may be redirected away from the deposition location, which lowers deposition rates [211].

The gradual decrease in sputtering rate, as shown in **Figure 83**, with increase in oxygen partial pressure (up to 20 % PO_2) might be occurred due to the fact that sputtering efficiency of oxygen is less than that of argon. Though, the large decrease in sputtering rate with onset of oxygen ambient cannot be solely due to the lower sputtering efficiency with oxygen. This can be attributed to reaction on the target surface leading to oxygen-rich compound formation that would result in sputtering of oxygen-rich HZO, the (Hf+Zr)/O ratio is very low, compared to desired stoichiometric HZO films. Drastic reduction in sputtering rate due to chemical reaction on target surface and compound formation is a typical characteristic of reactive sputtering [212].

Density shows a decreasing trend with increase in PO_2. This deceasing trend for the density of HZO films deposited, with increasing oxygen partial pressure, has been reflected from XRR measurements, shown in **Figure 83**. It can be seen that for both the deposition rate, and density of the films deposited without oxygen partial pressure are high, which might be due to the right stoichiometric composition, in the films compared to reactive sputtering. Densities become lower for films deposited with PO_2 or more which indicate realization of relatively over-stoichiometric films.

The XRD patterns of HZO films at different PO_2 values are shown in Figure 94. After annealing, the dominant peak was obtained at about 30.4°. It is attributed to diffraction from (111) planes of HZO orthorhombic phase. The other less-dominant peaks are attributed to the monoclinic phase of HZO. No diffraction peaks from tetragonal phase were obtained. After annealing, XRD patterns reveal that as the PO_2 increases from 0 to 5 %, the dominant o-peak disappears. The average crystallite size was estimated from the Scherrer's formula.

The XPS measurements revealed the impact of sputtering parameters on the film's composition and the stoichiometry ratios. As seen in the XPS data, the O 1s peak is asymmetric for all the films. This asymmetry indicates the presence of different oxygen species on the surface of the films, The O 1s peak at approximately 531 eV is assigned to O^{2-} ions in the vicinity of V_O, and its relative area can provide a measure of the V_O concentration.

The plot, in Figure 86, shows an increase in the oxygen vacancies with the increasing PO_2. The increase of V_O was unexpected, as the availability of oxygen in the gas might result in its incorporation in the deposited film when the oxygen partial pressure of the sputtering gas was increased. We speculate that the oxygen reacts more, and it led to more Vo as the PO_2 increased. The increase of Vo as function of PO_2 is not linear. It varied nonlinearly especially at low PO_2 values. The best Vo was found at 0% PO_2 and we investigated the impact of sputtering power. Unexpected relationship between the Vo and Power target was revealed. The Vo decreased with power increase from 200 to 400 W, then increased slightly. The best Vo was found at 400 W. we speculate that it is related to the increase of etching rate of HZO species was unbalanced.

It is well known that the electronic and transport properties of dielectrics, in our case HZO, are primarily determined by Vo [213], [214]. The Vo in HZO act as traps for charge carriers and they affect the ferroelectric properties, such as the stabilization of the orthorhombic phase [204] and the polarization switching voltage [215]. The atomic and electronic structure of HZO, with oxygen vacancies, are not understood yet and rarely studied. Another method to determine the electronic structure of oxygen vacancies is quantum-chemical calculations using the density functional theory (DFT) and the latter is out of the scope of this work.

Single doublets can accurately approximate the optimized HZO sample's Hf 4f and Zr 3d XPS spectra (Figure 104). The Hf^{4+} state is associated with the position of the Hf $4f_{7/2}$ maximum at 16.35 eV, which also happens to be the energy position of the same maximum in HfO_2 [216]. For the optimized sample, the difference in binding energies between the O1s and Hf 4f levels is around 513.65 eV, which is also the same as the corresponding HfO_2 value. Similar to this, the peak of Zr $3d_{5/2}$ at 181.3 eV corresponds to the Zr^{4+} state and matches the values for stoichiometric ZrO_2 that have been reported [217]. It appears that Hf and Zr are primarily present as HfO_2 or ZrO_2, respectively, in the optimized sample. Since the atomic and electronic structures of HfO_2 and ZrO_2 are so similar, we cannot conclusively say that the samples are a mixture of the two oxides.

The full width at half height (FWHM) of the Hf 4f peak and the Zr 3d peak in the HZO sample, respectively, are 1.16 eV and 1.22 eV, respectively.

Additional peaks for samples with high sputtering power values, with energies of 17.8 eV and 181.7 eV, respectively, were discovered when the Hf 4f and Zr 3d lines were deconvolved into their individual components. these peaks are typical for Hf and Zr. The creation of a significant amount of oxygen vacancies in the films naturally explains the occurrence of Hf and Zr states with lower oxidation degrees than in HfO_2 and ZrO_2. Maximum energies for the two peaks in the O1s XPS deconvolution to two individual components are 529.8 eV and 531.8 eV (Figure 104). The lattice oxygen in HfO_2 and ZrO_2 is clearly identified as the source of the first peak. On the sample surface, the second one is typical of oxygen vacancies as detailed above.

The bandgap value E_g can be calculated using the O 1s XPS, which represents the photoelectron energy loss spectrum on the electron excitation from the valence band to the conduction band. The linear interpolation of the spectral edge to the background level yields the result. The E_g value was calculated to be 5.32 eV which is confirmed by the computed E_g value of 5.37 eV for $Hf_{0.5}Zr_{0.5}O_2$ derived from transmission spectra and the value of 5.3 eV discovered from photoelectron spectra [218]–[220].

For the optimized conditions, the Zr/Hf ratio is 1.08 which is different from what is expected for HZO target. This might be explained by the fact that Zr and Hf are screened differently by adsorbates, that the free path lengths of the Hf 4f and Zr 4f photoelectrons are different, and that the atomic sensitivity coefficient values might be inaccurate. The reconstructed XPS profile from the ARXPS data confirmed the uniformity of the composition of HZO.

Below 100 nm thickness, the as-deposited films are amorphous of different thicknesses are amorphous and satisfy the crystallinity condition to favour the orthorhombic phase induction during the annealing. The exception of 110 nm thick sample is crystallized into monoclinic phase can be explained by the increasing temperature inside the chamber as function of the deposition time as the film is thicker. This result reveal that several layers of a thickness thinner than 100 nm can be compiled to reach thicker films than 100 nm.

The Ar flow does not change a thing except slight change in density while the deposition time confirms the steadiness of deposition rate with the optimized parameters. The importance scale of sputtering parameters is presented in.

4.2.5 Conclusion

In summary, HZO films were deposited using the RF magnetron sputtering at various deposition conditions. It is noticed that film thickness linearly increases with RF power and deposition time whereas the impact of argon flow rate is almost insignificant. The most impacting factors are the oxygen partial pressure and the deposition pressure. HZO thickness increased from 9.8 to 54 $nm.min^{-1}$ with the deposition power. Films thinner than 100 nm are amorphous as deposited. At high RF sputtering power densities, metallic Hf and Zr appeared (4.17 and 5 $W.cm^{-2}$). XPS measurements confirm the film composition and stoichiometry ratios close to the target's. XPS confirms the existence and increase of oxygen vacancies with the deposition conditions. The high deposition rate plays an important role as an advantage of single target sputtering of HZO.

4.3 Thermal annealing

The sputtering of amorphous HZO films, with good stoichiometric ratios, is not enough to explore the dielectric and ferroelectric properties of HZO films. A post-deposition processing step is required, which is the rapid thermal annealing (RTA). Its importance equals the importance of the film's deposition step. It has been widely reported besides to the impact of its parameters [185], [221]–[223]. Three main parameters characterize influence RTA on the annealed films: annealing temperature, annealing time, and annealing atmosphere or gas. Secondary steps, RTA-related, like heating ramp or cooling ramp can also influence the properties of the annealed films.

RTA can extend the annealing time of several milliseconds applicable to several seconds and minutes using conventional furnace, flash lamps or laser annealing. In this work, we used a conventional rapid annealing furnace, which is the most used nowadays. Besides, we performed an in-situ XRD thermal annealing of HZO amorphous films.

In addition, the potential to induce the orthorhombic phase, in the films grown at RT on Si substrates, makes RTA potentially motivating technology for the fabrication of new devices based on the ferroelectric properties of HZO.

In this part, RTA, and in-situ XRD annealing of sputter-deposited HZO films, stacked between TiN electrodes, on Si substrates were performed and the dependence of the

structural properties on the annealing time, annealing temperature, annealing gas, and film thickness was investigated.

4.3.1 Rapid thermal annealing

RTA of HZO films leads to formation of the metastable non-centrosymmetric orthorhombic phase ($Pca2_1$). This phase is believed to the origin and characteristic of ferroelectric properties in HZO films. Up to date, the existence of orthorhombic phase in XRD patterns is elusive and electrical measurements are required to confirm the ferroelectric behaviour.

Here, we report XRD patterns of the different samples annealed under various conditions. The XRD results represent a hint of the ferroelectric properties of HZO films via the apparition of the orthorhombic phase peak.

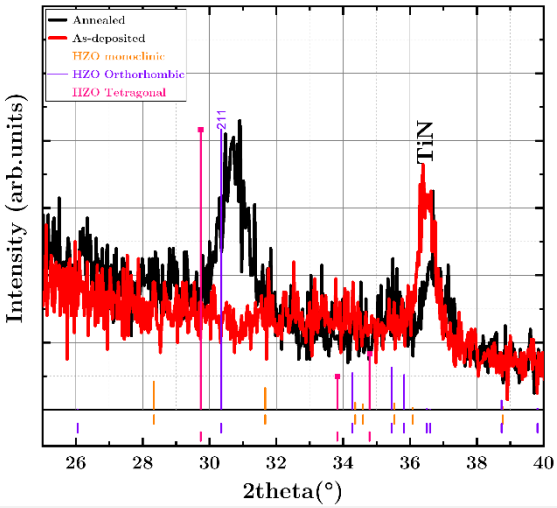

Figure 110 GIXRD patterns of TiN/HZO/TiN stack before and after RTA

In **Figure 110,** GIXRD patterns, of the TiN/HZO/TiN stack before and after annealing, show the apparition of orthorhombic peak around 30.5°, just after annealing. This first result led to us to investigate the effect of RTA and its parameters, before conducting electrical measurements.

Our attention is focused on the formation of orthorhombic phase and avoiding monoclinic phase, which is reported to prevent the ferroelectricity in hafnia. The orthorhombic phase appears between the tetragonal and monoclinic phases, which makes any peak, in this range, a complex mix of the three phases.

Before XRD measurements, we characterized the thickness, roughness, and density of HZO stack before and after annealing by XRR. The results are plotted in **Figure 111**.

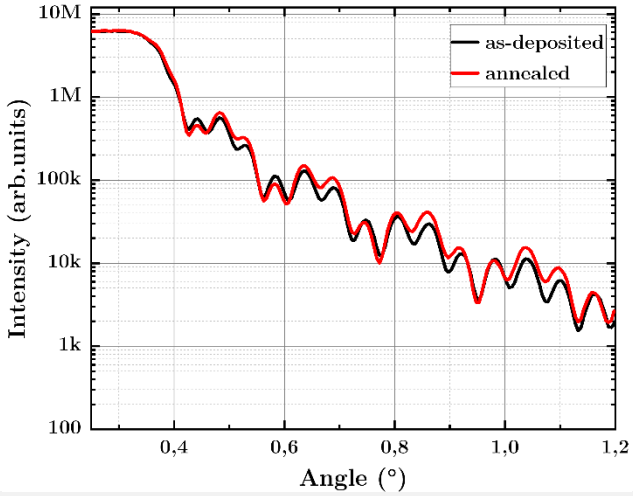

Figure 111 X-ray reflectivity patterns of TiN/HZO/TiN before and after annealing

Figure 111 indicates the X-ray reflectivity patterns of TiN/HZO/TiN stack before (as deposited in black) and after annealing (in red). No noticeable change in the thickness is observed. Very insignificant change in density is observed. Only the roughness increased after annealing.

For the investigation, we chose to study each parameter separately than the design experiment method.

4.3.1.1 Annealing atmosphere

The first parameter studied was the annealing atmosphere effect on HZO-based MIM structure. In the used furnace, we had two gases: N_2 and O_2. The constant gas flow was set at 2 l.min^{-1}. The annealing temperature was at 650 °C for 1 min. The impact of atmosphere on the structural properties was investigated by XRD and the oxygen vacancies parameters was studied by XPS. The film thickness was fixed at 15 nm-HZO in stack of 50 nm TiN electrodes.

We compared the structural and oxygen vacancies' dependence on the annealing atmosphere (N_2 and O_2). The XRD results this comparison for annealed HZO-based are plotted in **Figure 112**.

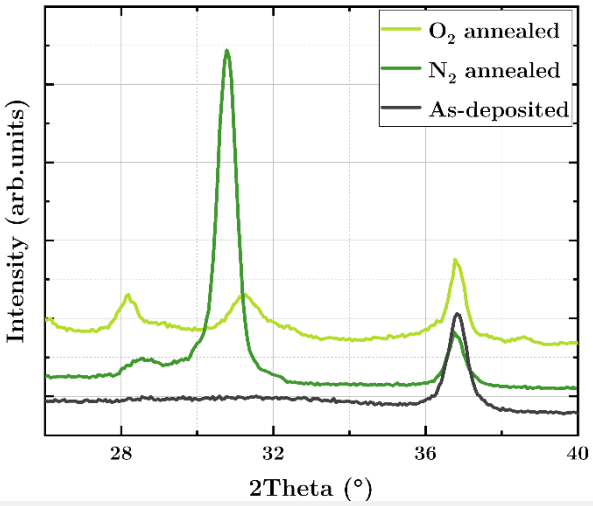

Figure 112 XRD patterns of HZO before and after annealing under N_2 and O_2.

Three stacks based on 15 nm HZO were measured by XRD (**Figure 112**). The as-deposited HZO sample is amorphous while the two other samples crystallized, during RTA, at N_2 and O_2 separately. The TiN cubic phase is the common peak between the three samples around 36.8°. The O_2 annealed sample crystallized in two monoclinic and orthorhombic/tetragonal phases, at 28.4° and 30.7° respectively, with close peak intensities. The N_2 annealed stack shows a very intense orthorhombic/tetragonal phase, at 30.3°, with a very low intensity peak corresponding to the monoclinic phase that can be negligeable. Hence, for the O_2 annealed sample, the monoclinic phase appeared besides o/t peak but shifted. We assume that the same o/t peak, as N_2 annealed, is shifted. The shift indicates a lower in-plane compression stress, which can also refer to the crystallization in a different phases' ratio (o/t).

This result helped us choosing the suitable annealing atmosphere for the sputtered HZO films. The annealing atmosphere can influence the leakage current within the films. Generally, O_2-based atmospheres in RTA decrease (O_2 or H_2/O_2) the concentration of oxygen vacancies (Vo), therefore either increasing the number of electron holes or decreasing the number of electrons. Hypothetically, investigating the conductivity of the annealed films allows to determine the most of electronic carrier type.

We conducted XPS measurement on the three samples: as-deposited, N_2 annealed, and O_2 annealed, to observe the variation of oxygen vacancies as function of the annealing atmosphere. This analysis gives us a hint about the leakage current of each sample.

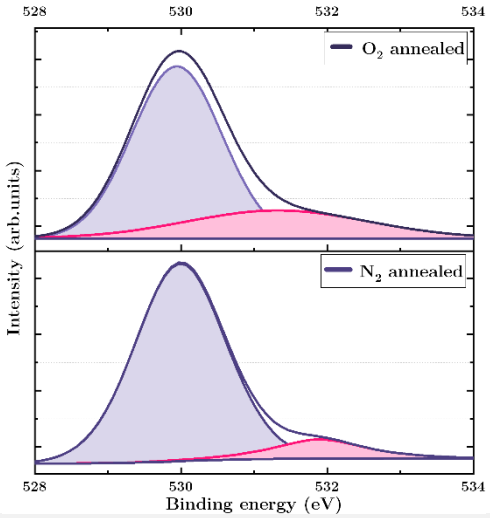

Figure 113 XPS spectra of O 1s region of samples annealed at different RTA atmosphere

Here, we compare the O 1s region of the two samples with a special focus on V_O. The XPS core level of O 1s peaks is shown in **Figure 113** (the as-deposited sample is reported in the previous section). For the two samples, it consists of two very close peaks; the Hf–O and Zr–O bonds and the O–Hf–O and O–Zr–O bonds overlapped at 529–530 eV. For the N_2 annealed sample, the oxygen vacancies (V_O) peak is observed at 532 eV, which corresponds to the oxygen deficiency related to Hf and Zr sub-oxides. The V_O was found 9.2%, which represents an increase compared the as-deposited sample. While the O_2 annealed samples has a higher V_O percentage of 20%. The bonded oxygen peak shifted to lower binding energies, for both samples, compared to the as-deposited sample.

As a result, the N_2 atmosphere led to a lower V_O percentage, higher intensity of o/t peak, and lower intensity of the monoclinic phase peak. Consequently, we used the N_2 as annealing atmosphere for the next studies.

4.3.1.2 Annealing temperature

As a second parameter, the annealing temperature was varied from 400 to 650 °C, in two steps: the first one, at 400 and 650°C, and the second one, from 500 to 650 °C. the upper limit of annealing temperature was set at 650°C as higher reported temperatures led to high leakage currents within films based on HfO_2 or ZrO_2. At the same time, the 400°C was the lower limit below the lowest annealing temperature reported, at the time of conducting annealing. The impact of temperature on the structural properties was investigated. The annealing time and film thickness was fixed at 1 min under N_2 and 15 nm-HZO in stack, respectively.

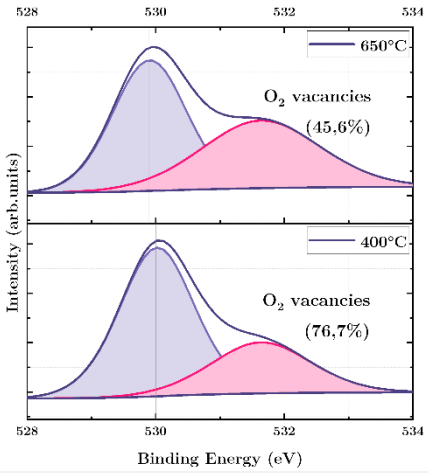

Figure 114 core-level XPS spectra and peak-fitting analysis of O1s

Figure 114 shows the core-level XPS spectra and peak-fitting analysis of O1s.

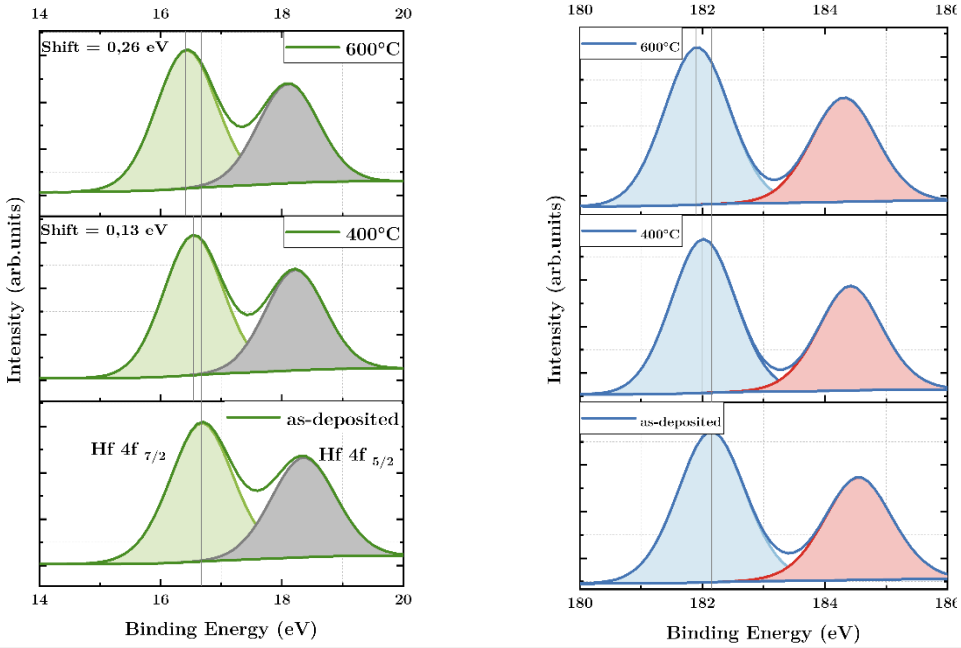

Figure 115 core-level XPS spectra and peak-fitting analysis of (left)Hf 4f and (right) Zr 3d

Figure 115 illustrates core-level XPS spectra and peak-fitting analysis of (left)Hf 4f and (right) Zr 3d

It is worth to note that the constant position of the first O1s XPS peak (530.88 eV) in hafnium oxide after annealing at 950 °C correlates with the constant position of the main Hf 4f doublets after this annealing. It means that short ordering of Hf–O bonds in the hafnium oxide varies a little upon the crystallization of this phase during annealing.

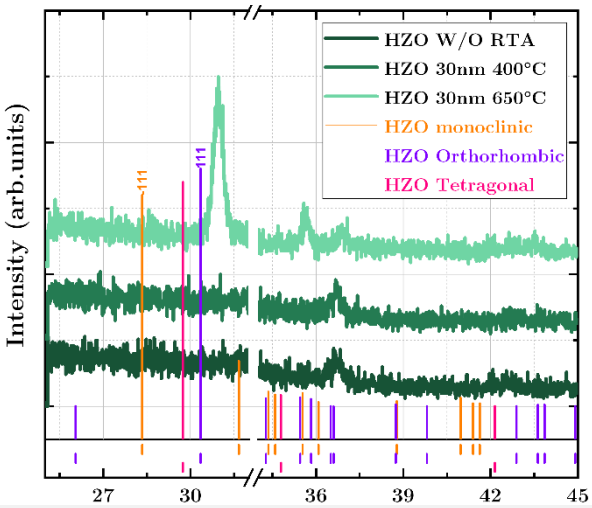

Figure 116 XRD pattern of HZO stack annealed at 400 and 650°C

Three stacks based on 15 nm HZO were measured by XRD, as the patterns are illustrated in **Figure 116**. The as-deposited HZO sample is amorphous. The 400 °C sample shows no peak except the TiN peak at 30.8° while the 650°C crystallized into the o/t phase as the peak appeared at 30.5°, no other peaks appeared corresponding to the absence of the monoclinic phase. This result is in good agreement with the previous section. The XRD pattern indicate the crystallization of HZO films appeared at a temperature of 650 °C, since the fundamental peak of o-(111)/t-(101) became intense. We can speculate that the non-apparition of the latter, at 400°C is due to the annealing time, i.e., the thermal budget is not enough. The 650 °C is only a starting point, at which the o/t peak appeared, the in-situ XRD thermal annealing in the next section will investigate the minimal annealing temperature for a longer annealing time.

As the orthorhombic phase is metastable, it might be highly sensitive to the annealing temperature. So, we investigated the annealing temperatures lower than 650°C, with steps of 50°C. the 2theta range was extended to 25-55° to observe all the appeared phases after annealing. We performed the previous annealing process at 500, 550, 600 and 650 °C. For technical issues, we were in the obligation of using Jibelec furnace instead of the Unitemp furnace used in the previous annealing process.

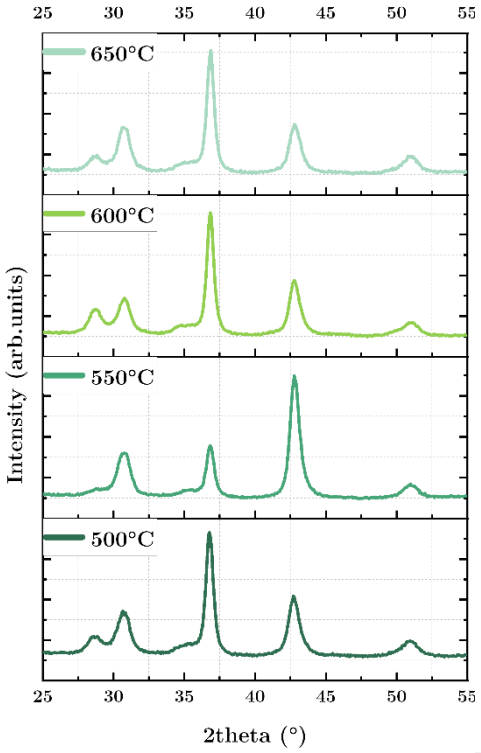

Figure 117 XRD patterns of annealed HZO stacks at different temperatures, from 500 to 650°C

For the four samples, **Figure 117** shows the XRD patterns for the thermally processed 15 nm thick HZO stacks at different temperatures. The four samples have a common intense peaks of TiN electrodes at 36.8° and 42.1°. Our attention is focused on the 27-31° and 50-52° ranges. The first one includes the monoclinic and the o/t phases' peaks while the second includes only the o/t phase. The as-deposited film is amorphous, which represents the ideal starting point toward inducing ferroelectricity following the subsequent rapid thermal annealing [8]. Moreover, the occurrence of three diffraction peaks upon thermal annealing is revealed, indicating progressive HZO film crystallization. Indeed, the XRD patterns show a major contribution from the orthorhombic/tetragonal phases with a predominant broad diffraction peak around 2θ= 30.5°, corresponding to the (111) and (101) reflections of the $Pbc2_1$ orthorhombic and $P4_2nmc$ tetragonal phases, respectively. A diffraction peak with a smaller intensity also occurs around 2θ = 51°, corresponding to the (220) reflection of the $Pbc2_1$ orthorhombic phase. The third diffraction peak observed at 2θ = 28.6° is attributed the $P2_1c$ monoclinic phase through the
(-111) reflection. The most intense monoclinic peak was found at 600°C, then the 500 °C, 650°C, and the 550°C. All three diffraction peaks appear at 500 °C, then increase steadily in intensity up to 600 °C, and starts to slightly decrease at 650 °C.

These results show that the orthorhombic/tetragonal phases can be readily obtained by the crystallization of an amorphous as-deposited HZO film. Although the monoclinic

phase is also formed, the orthorhombic/tetragonal. The formation of the monoclinic in these samples can be explained by the different annealing profile applied in the second furnace as it the heat ramp increases in form of steps (15 seconds at 250°C and 15 seconds 450°C) to not exceed the desired annealing temperature because the heat ramp was not controlled. Despite that, the effect of the orthorhombic phase inducing is well observed as the same as the first furnace. This result led us to investigate the heat ramp rate in the next section.

As a result, o/t-phases are expected to be predominant along the investigated range of annealing temperature. The phase distribution is, however, dependent upon the annealing temperature. Finally, after annealing all the samples crystallized into monoclinic and o/t phases with difference between them but the higher orthorhombic/monoclinic ratio was found at 650 °C. In the next section, we investigate the impact of annealing temperature at 650°C.

4.3.1.3 Annealing time

The same samples as the previous sections were investigated in this section. RTA was performed under N_2 atmosphere with a fixed heating rate of 120 °C.s^{-1} and constant annealing temperature of T = 650 °C while the annealing time t_a was varied between 10 s and 120 s. For the sake of precision, the as-deposited sample was deposited with each study' samples to assure the reproducibility of the depositions and its amorphous nature. It allowed us to detect any anomaly during the deposition.

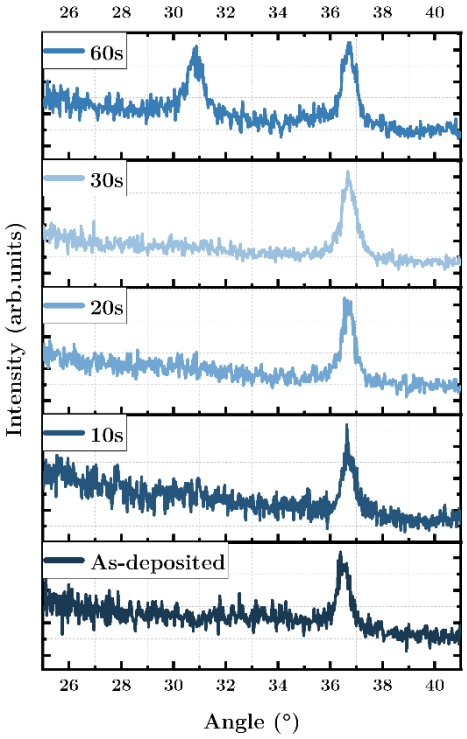

Figure 118 XRD patterns of annealed HZO stacks at different annealing times

The structural properties of the samples were investigated by XRD, as illustrated in **Figure 118**. The diffraction patterns show amorphous films for the as-deposited film and the 10-, 20-, and 30-seconds samples. The five samples show a common intense peaks of TiN electrodes at 36.8°.

After an annealing time of 60-s, the (111)/ (101) peak appeared, and it is dominant. No monoclinic peak appeared for the five samples. The origin of apparition o/t peak apparition after 1 min annealing is unclear. Longer annealing times did not lead to the increase of o/t peak's intensity or the apparition of additional peaks (in shown here). This is indication for the optimum annealing time for 1 min at 650 °C under N_2.

4.3.1.4 Other parameters:

After the investigation of the three RTA parameters (temperature, time, and atmosphere), the change of furnace led us to the investigation of the possible effect of heat ramp rate on the structural properties of annealed HZO. As we concluded that the annealing steps leads to the formation of the monoclinic phase. In this this section we investigate an RTA-related parameter and an HZO-related one: heat ramp rate and TiN electrodes thickness.

4.3.1.4.1 Heat ramp rate

We have performed RTA under N_2 at 650 °C for 1min on three HZO-based MIM stacks with the same thicknesses. The annealing of the three samples was performed with three heat ramp rates: 5, 50, and 150 °C.sec^{-1}. Many studies reported a significant influence of the heat ramp and cooling ramp rates on the structural and morphological properties of the annealed films. In this part, the impact of the heat ramp rate could be controlled and studied but the colling ramp rate was not controlled (fixed at -20 °C.sec^{-1}, from 1000 to 400°C, and -5 °C.sec^{-1} from 400 to 100°C). unfortunately, only XRD measurements were performed on the samples. So, we only focused on the appeared phases as a hint on the ferroelectric properties to choose the optimal heat ramp rate for the annealing step int this work.

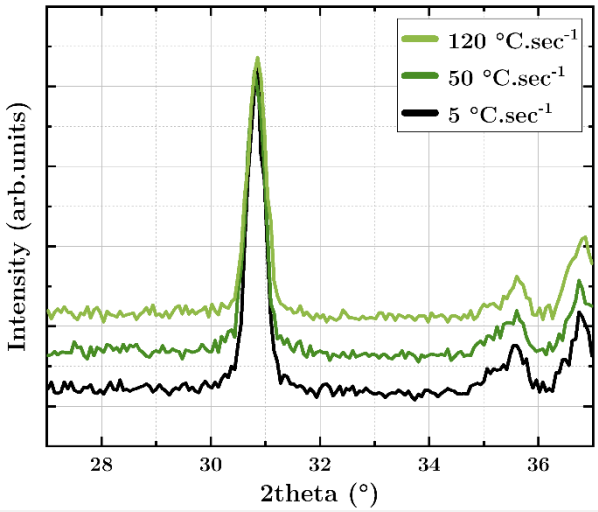

Figure 119 XRD patterns of annealed samples at different heat ramps

No noticeable change was observed in the XRD patterns for the three samples annealed at 5, 50 and 120°C.sec^{-1} heat ramps. For the three samples, the same intensity peak corresponding to the orthorhombic phase appeared, at 30.6°, after annealing at 650°C for 1 min under N_2. Also, no monoclinic phase appeared for the three samples. The XRD results, illustrated in **Figure 119**, confirmed that the orthorhombic phase is the dominant with a high crystalline quality.

4.3.1.4.2 TiN electrodes' thicknesses

In addition to the RTA parameters, we studied another parameter, related to the HZO stacks, suspected to impact the crystallization of HZO films during RTA processing, the thickness of TiN electrodes. As a start, we performed RTA on TiN/HZO/TiN stack with 50 nm thick TiN. The choice of 50 nm was based on bibliographical study and reported studies. We obtained the ferroelectric structural signature through the apparition of the orthorhombic phase. We looked to vary the TiN thickness and study the possibility of optimizing the crystallization quality of HZO. We studied the following thicknesses in annealed HZO stacks: 10, 25, 50, 100 and 200 nm. The same thickness was used for top and bottom electrodes. The five samples were annealed at 650 °C for 1 min under N_2 with 120 °C.sec^{-1}. The XRD patterns of the samples, after annealing, are plotted in **Figure 120**.

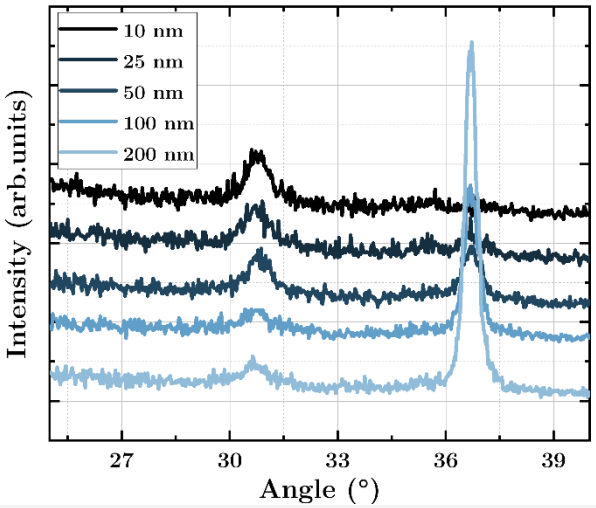

Figure 120 XRD patterns of annealed HZO stacks with different TiN thicknesses

It is noteworthy that all the samples were amorphous before annealing. The five samples have a common intense peaks of TiN electrodes at 36.8°. the TiN electrodes were amorphous for 10 and 25 nm thick electrodes. After annealing, the HZO films crystallized into the o/t peak. The peak's intensity decreased, from 200 to 50 nm, then it became stable, from 50 to 10 nm. No monoclinic peak appeared around the o/t peak.

As a result, we can say that the crystallinity of TiN electrodes does not affect the apparition of the orthorhombic phase or the monoclinic one. Unexpectedly, even at 10 nm thickness, the orthorhombic phase is induced. The reduction of TiN thickness can be an economic and sustainable benefit. Besides, this unexpected result, at 10 nm, triggered our attention to investigate the annealing of top electrode-free HZO stacks after annealing later.

4.3.1.4.3 Thickness dependence

Another HZO stack-related parameter is investigated in this section: the thickness of HZO layer. We wondered if the RTA parameters have the same effect on HZO stacks with different thicknesses of HZO. The aim behind that was to have thicker films of HZO with orthorhombic phase only. The thickness-limit of HZO orthorhombic phase was reported to be around 25 nm. We varied HZO thickness from 8 to 66 nm stacked between 50 nm TiN electrodes. The samples were annealed at 650°C for 1 min under N_2. We only investigated the effect on the structural properties using XRD. The results of annealing are presented in XRD patterns in **Figure 121**.

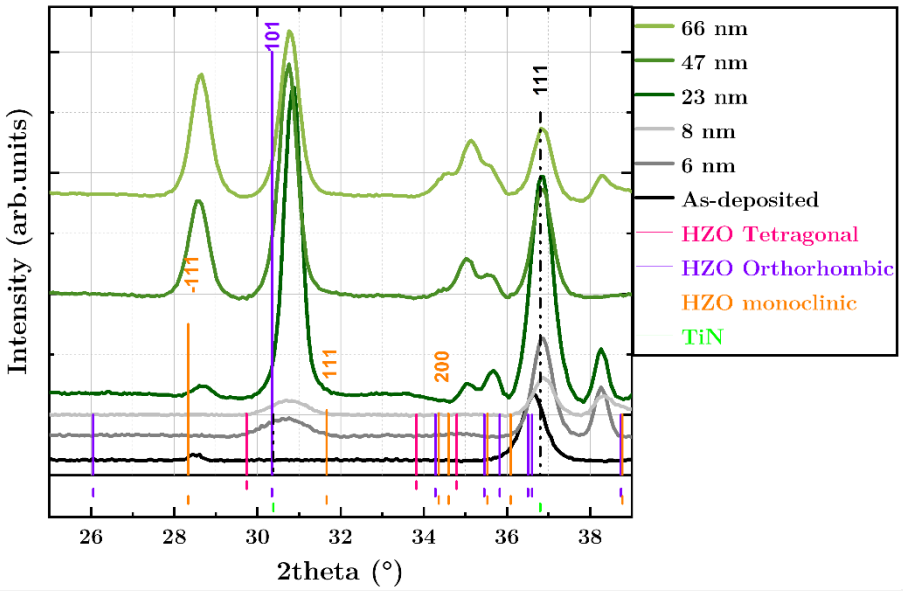

Figure 121 XRD patterns of annealed HZO stacks of different HZO thicknesses

Since the optimal thermal budget, to induce the orthorhombic phase, is unknown, comparing the influence of RTA on HZO films with different thicknesses was challenging. Additionally, similar thermal energy densities of the annealing will, so probably, not correspond to similar annealing temperatures, because the amount of absorbed energy is highly thickness dependent. Therefore, the following comparison of the different thicknesses confirms or not the dependence of HZO thickness on the thermal budget.

The diffraction angle range was set to 25-40°. Clear diffraction peaks are visible in the diffraction pattern of the annealed HZO films with a thickness of 23 nm and in addition to the (111)/ (101) o/t peak as well as (-111) monoclinic peaks.

By taking the 23 nm sample as a reference, the intensity of the o/t peak is decreasing with decreasing thickness, from 23 to 6 nm. For the 6 and 8 nm thicknesses, only the (111)/ (101) peak appeared with a total absence of the monoclinic phase. The monoclinic peak appeared with a low intensity for the 23 nm sample while its intensity increased with the increasing thickness. The monoclinic phase is more present in the thicker films. In addition, two small peaks appeared at 35.5° corresponding to orthorhombic phase.

The ratio of the intensities of the orthorhombic/monoclinic phases peaks decreased with the increasing thickness suggesting that the RTA is thickness dependent. This result is in good accordance with literature results. For a further analysis of the grain growth, TEM studies would be necessary.

4.3.2 In-situ thermal annealing

The previous results strongly suggest the formation of the HZO orthorhombic phase following rapid thermal annealing. However, the corresponding diffraction peak observed around 2θ = 30.4° might also refer to the tetragonal phase contribution. To properly identify the respective contributions of the orthorhombic and tetragonal phases to this diffraction peak, we used a second technique of thermal annealing coupled with XRD equipment; in-situ XRD thermal annealing. The processing time of XRD measurement at different temperature prevents the rapid effect of thermal annealing. This measurement was performed at the LMGP Lab platforms by H.Roussel.

The aim of this kind of measurements is to conduct XRD measurement, in a chosen range, while increasing the annealing measurement. It is considered as a thermal annealing with heat ramp steps. The XRD measurement was conducted in the 30-33° in order to focus on the induction of the orthorhombic phase. Besides, this range includes a monoclinic signature too. The shortness of the range implies quick XRD measurements and smaller impact on the heat ramp. The annealing temperature was set from 30 to 900 °C with XRD measurement, from 50°C, every 25°C. In this way, the diffraction angle-temperature map was designed.

We performed this measurement on TiN/HZO/TiN stack with 22 and 50 nm thicknesses of HZO and TiN electrodes, respectively. The HZO film was amorphous as deposited.

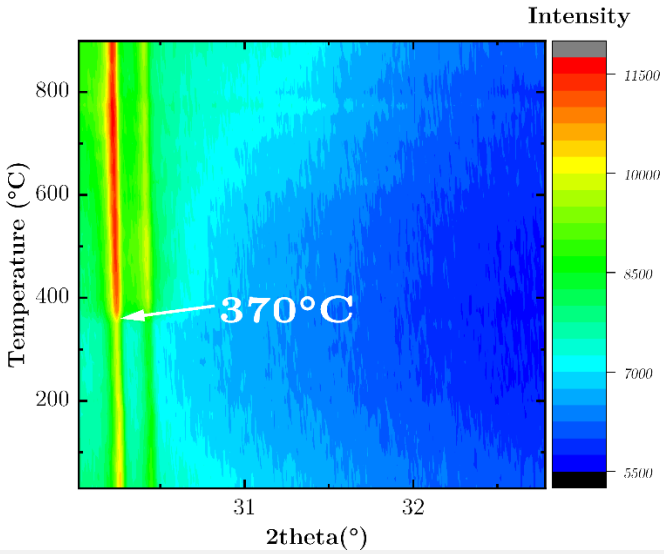

Figure 122 XRD patterns of the TiN/HZO/TiN stack at different *in situ* thermal annealing temperatures in the range of 30–900 °C under N_2 atmosphere during heating.

Figure 122 presents the XRD patterns plotted within a 2theta-annealing temperature map for the annealed stack. The amorphous HZO films starts to crystallize at around 370 °C. Moreover, the occurrence of two distinct diffraction peaks upon thermal

annealing is revealed and is likely related to the $Pbc2_1$ orthorhombic phase (111) and the $P4_2nmc$ tetragonal phase (111), respectively.

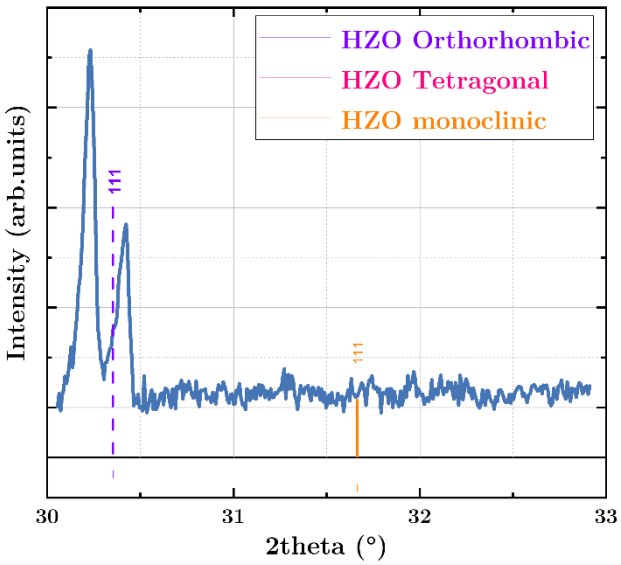

Figure 123 XRD pattern extracted from the in-situ thermal annealing results.

More precisely, **Figure 123** presents an XRD pattern extracted from **Figure 122** at an annealing temperature of 650 °C. It is shown that two well identified diffraction peaks occur at 30.25° and 30.5°, which are attributed to the orthorhombic and tetragonal phases, respectively. As strong evidence of the existence of the orthorhombic phase in HZO film, this result allows us to access the monoclinic and orthorhombic/tetragonal phase co-existence that is reported as being crucial for inducing ferroelectricity in HfO_2 thin films [224], [225]. This result further suggests that the diffraction peak reported in **Figure 123** around 30.4° is the combination of two distinct peaks with a major contribution of the orthorhombic phase as compared to the tetragonal phase, which is a prerequisite to the occurrence of ferroelectricity in HZO films [226]. The existence of the non-ferroelectric tetragonal phase is not detrimental since the ferroelectric behavior was evidenced in HZO films, where the tetragonal and orthorhombic phases co-existed [227]. **Figure 122** also shows that both the diffraction peaks related to the orthorhombic and tetragonal phases pop up at 370°C, which likely represents the start of film crystallization.

At this temperature, the HZO crystallite formation process with the metastable orthorhombic/tetragonal phases begins. However, the Curie temperature of ferroelectric HfO_2 is believed to be in the range of 400–500 °C [228]. It will be investigated in the next chapter. The onset of the crystallization of the orthorhombic phase at lower temperature might be explained by the presence of Zr since ZrO_2 has a lower Curie temperature [35].

As the annealing temperature increases beyond 370 °C, the intensity of both peaks remains stable up to 900 °C, suggesting that no transition to the monoclinic phase occurs.

Figure 124 shows the evolution of the XRD pattern during cooling down of the same stack from 900 °C to room temperature. It can be seen that the two diffraction peaks related to the orthorhombic and tetragonal phases persist down to room temperature with only a small decrease in intensity. This stability suggests that the orthorhombic phase does not disappear during cooling down and that no phase transition to the monoclinic phase is observed.

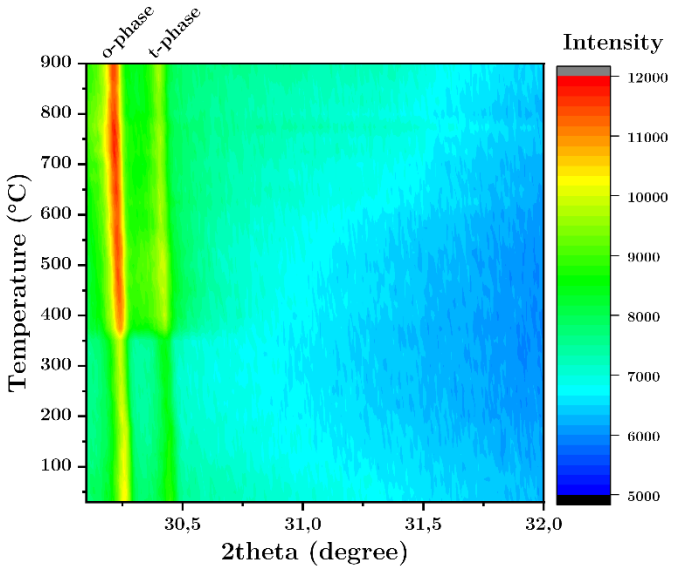

Figure 124 XRD patterns of the TiN/ HZO/TiN stack at different in situ thermal annealing temperatures in the range of 30–900 °C under N_2 atmosphere during cooling down.

In summary, the *in situ* XRD analysis of the crystallization process of the 22 nm thick HZO film upon thermal annealing under a nitrogen atmosphere exhibits three interesting results. First, the amorphous HZO film starts to crystallize in the orthorhombic/tetragonal phases at a low annealing temperature of 370 °C. The intensities of the corresponding diffraction peaks do not show any noticeable increase up to 900 °C. Second, the orthorhombic related diffraction peak persists during the cooling down to room temperature. Third, the crystallization of HZO films in the orthorhombic phase can be achieved through a standard thermal annealing process, whereas most of the results reported on the crystallization of HfO_2-based materials show that rapid thermal annealing [221], [230], [231] must be used in order to stabilize the orthorhombic phase.

4.3.2.1 Thermal annealing of top-electrode free HZO stacks

In the section, the orthorhombic phase appeared at different thicknesses of electrodes, from 10 to 200 nm. This result triggered our attention to study the case of top electrode-free HZO stacks in both RTA and in situ thermal annealing. We fabricated the same stack as the previous section with one exception: top electrode removal. The sample was annealed at 650°C for 1 min under N_2 and the structural properties were characterized by XRD. The HZO thickness was 15 nm.

The top electrode-free HZO stack shows unexpected result, as illustrated in Figure 125. The amorphous sample was amorphous before conduction RTA processing. No monoclinic peak is observed after annealing. The orthorhombic phase is present after annealing. The orthorhombic peak is broad which means lower crystallization quality compared to the HZO stack with top electrode.

This result implies that the inducing of the orthorhombic phase is not dependent on the existence of a top electrode, but the latter helps enhancing the crystallization quality of HZO films during annealing.

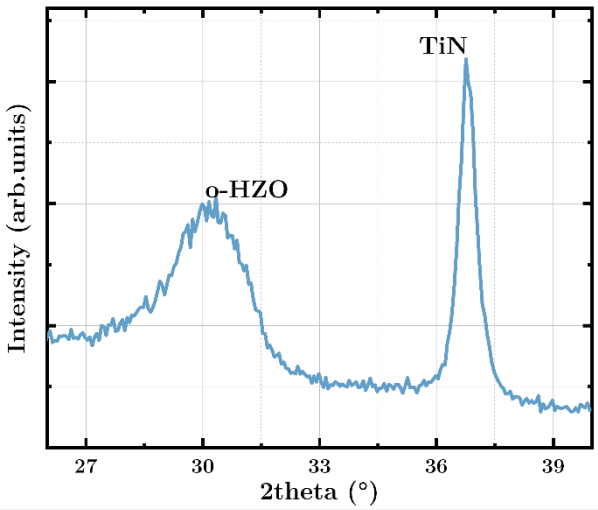

Figure 125 XRD patterns of HZO stacks annealed with different TiN thicknesses

To have more insights about this result, we conducted an in-situ XRD thermal annealing on a 44 nm HZO stack without a top electrode. The same conditions as the previous in situ thermal annealing were applied. The results are plotted in **Figure 126**.

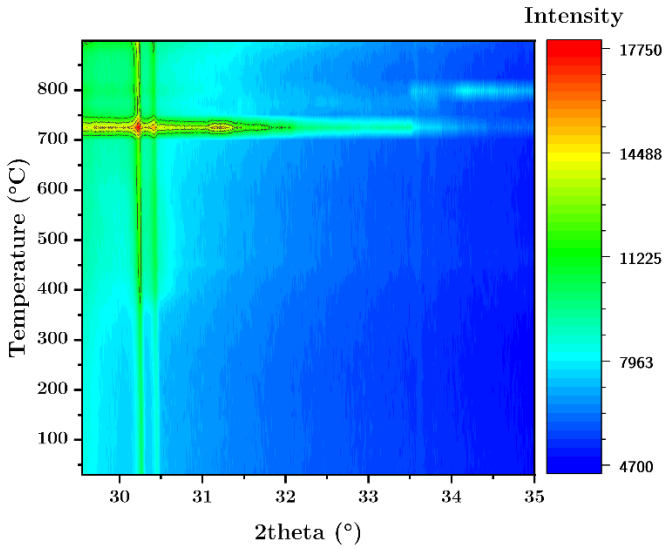

Figure 126 XRD patterns of the TiN/ HZO stack at different in situ thermal annealing temperatures in the range of 30–900 °C under N_2 atmosphere during heating up

The heat map shows a weak intensity peak of the orthorhombic phase appeared around 400°C. the same peak reached it maximum at 725°C then its intensity decreased at higher temperatures.

The heat map, during the cooling phase, is plotted in **Figure 127**. It shows a stable intensity of the orthorhombic phase around 30.4°. this implies that the induced orthorhombic phase without a top electrode is stable as the temperature decreased naturally.

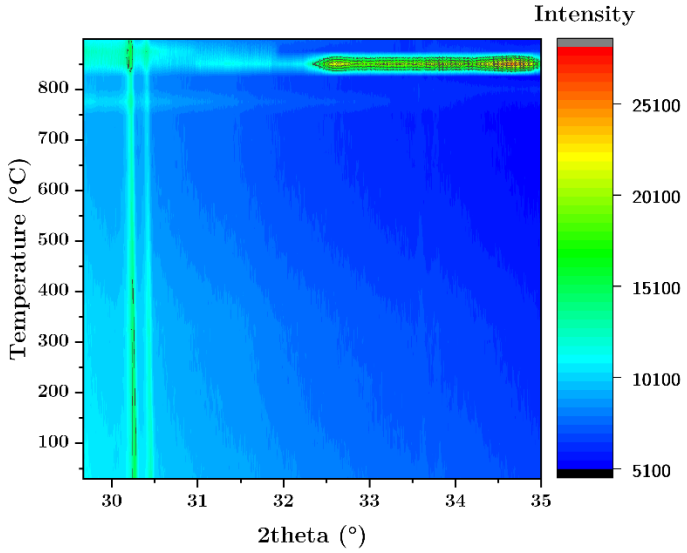

Figure 127 XRD patterns of the TiN/ HZO stack at different in situ thermal annealing temperatures in the range of 900–30 °C under N_2 atmosphere during cooling down

As a result of comparing this result with the full HZO stack, we can deduce that the apparition of the orthorhombic phase is top electrode-independent despite the low intensity o-peak in the top electrode-free stack. The electrode parameters such as the material, the thickness or the texture can optimize the orthorhombic phase. This result can be a trigger for deeper investigations of the effect of RTA conditions on top electrode-free stacks.

4.3.3 Discussion

Before investigating the structural changes during the rapid annealing processing, the thickness, density, and roughness were measured before and after annealing for one stack. No noticeable variations were recorded for thickness and density except for the roughness, which changed slightly as it is related to the surface.

The XRD data of HZO films deposited at various annealing temperatures are presented in **Figure 116**. After annealing at below 500 °C for one minute, no obvious diffraction peaks were detected, which indicates that at a relatively low temperature, the annealed film is still in an amorphous state. This is consistent with the reported values in literature [12], [232]. As the temperature increased at 650 °C, obvious diffraction peaks appeared, and all peaks corresponded to the orthorhombic phase of HZO compared with the reference PDF. The phase transition of the film occurred at 650 °C for the 30 nm thick HZO film. Thinner film of 15 nm was annealed in another furnace at lower temperatures than 650 °C, as presented in Figure 117. The diffraction peaks at 500 °C corresponded to the monoclinic and orthorhombic phases of HZO. The XRD analysis shows that with the increase in temperature, the diffraction peak position of the sample obviously moves to a small angle, revealing the existence of compression stress inside the sample. The crystallite size was calculated using the Scherrer formula and found at around 8 nm. The apparition of the monoclinic phase is related to the step-annealing behaviour in the furnace.

Here, it is noteworthy that the heating ramp variation revealed that it has an insignificant impact on the induction of the o-phase whereas the annealing in steps tends to favour the crystallization into the monoclinic phase, as shown in Figure 119. The effect of cooling rate was not studied here. Further studies might reveal its influence. B.Ku et al. reported that a dramatic increase in the polarization was found in the case of rapid quenching in controlled cooling for ferroelectric Al-doped HfO_2 [233].

The XPS data showed that the oxygen annealing atmosphere induces more oxygen vacancies compared to the N_2 annealing atmosphere at the same temperature as shown in Figure 113. Besides, the XRD data, plotted in Figure 112, revealed that the N_2 atmosphere favoured the dominance of the o-phase over the monoclinic phase compared to the O_2 atmosphere in which equal fractions of o- and m-phases are induced. We recall that for ALD-deposited hafnia ferroelectrics, the oxygen annealing atmosphere

Another important finding is the apparition of the o-phase even without capping layer during the annealing or we can call it "the post-deposition annealing". The rapid thermal annealing was performed under N_2 atmosphere at 650°C for 1 min. The in-situ thermal annealing confirmed the RTA result for HZO sample annealed to 900°C and cooled down to room temperature. The intensity of the o-phase was weaker compared to the post-metallization annealing sample. This finding confirms the role of capping layer to improve the crystallization into the o-phase. Different results between post-deposition and post-metallization annealing have been reported before for Si-doped HfO_2 [234]. The difference occurs due to ted to either the incorporation or removal of oxygen from the capacitor stack during the annealing step, depending on whether a top electrode was present. Before the discovery of ferroelectricity in HZO, Triyoso et al. that the capping of HZO increases the dielectric constant significantly regardless of the film composition [90]. This is consistent with our structural results as the films without the capping layer are less crystallized compared to the capped ones. We speculate that future studies on the annealing pressure can replace the capping effect during annealing.

Increasing the TiN top electrode thickness led to the same result about the crystallization of HZO film into o-phase, which means that the thickness of the top electrode or its crystalline nature have insignificant over the structural signature of ferroelectricity. The electrical properties are to be checked in future studies.

4.3.4 Conclusion

In this work, the chemical composition, and structural properties of HZO single target sputtered thin films were studied to investigate their ferroelectric behaviour. The influence of the annealing time, annealing temperature, and annealing atmosphere on the structural properties of HZO thin films deposited on TiN during RTA was studied. A complex interplay between the roughness, oxygen vacancies as well as variations in the

thicknesses of electrodes and HZO layer were found and their impact on the induction of the orthorhombic phases was discussed.

The following conclusions can be drawn: First, the rapid annealing does not change the thickness or the density of the stack except for the roughness that increased during RTA. The orthorhombic phase induction occurs at about 500 °C for an annealing time of at least 60 s and a film thickness of 15 nm.

Second, a film thickness of less than 25 nm seems to be the optimum thickness for the formation of the orthorhombic phase with a dominance over the monoclinic phase. Thicker films result in an important formation of the monoclinic phase.

Third, the required annealing conditions to achieve a high fraction of the orthorhombic phase is related to other parameters than the three RTA parameters such as the heat ramp and top electrode thickness. Additional parameters, such as the cooling rate and annealing pressure might have more influence.

Finally, the structural signature of ferroelectric HZO, i.e., the orthorhombic phase, was evidenced by GIXRD on HZO films exposed to rapid thermal annealing and, more interestingly, also on HZO films exposed to slow and dynamic thermal annealing at temperatures ramped from 370 to 900°C under an N_2 atmosphere. Indeed, *in situ* XRD analysis performed during the increase in temperature showed the apparition of the HZO orthorhombic phase at 370 °C that persisted up to 900 °C and also during cooling down to room temperature.

4.4 TEM-ASTAR: Crystallographic phase and orientation mapping of ferroelectric HZO

4.4.1 Introduction

To solve the confusion between orthorhombic and tetragonal phase, we used automated crystal phase and orientation mapping with precession (ASTAR) technique in TEM. This technique was rarely reported to be used for ferroelectric HfO_2 except one paper and two conference posters with a similar technique, [240]–[242], due to the complexity of the technique. No HZO paper has been reported using this technique.

It is believed that the ferroelectricity in HZO originates from the o-phase which is a metastable phase. It can coexist with different phases such as monoclinic and tetragonal phases. This coexistence can be impacted by dopants, deposition parameters and post-deposition annealing parameters. The monoclinic and tetragonal phases have an inversion center which prevents ferroelectricity. However, the local orientation of the HZO grains as well as their crystallographic phase is of high importance to confirm, with precision, the ferroelectric behavior as well as its associated piezoelectric and pyroelectric properties.

In this part, the morphological and structural properties of HZO stack were carefully investigated by TEM as well as GIXRD measurements. A special emphasis was made to reveal and map the different phases of HZO at the nanoscale by using high-resolution TEM (HRTEM). The primary purpose of this approach is to reveal and map the crystalline phases and their local orientations in HZO films.

We took XRD reference patterns of the three phases of HZO: monoclinic $P2_1/c$, tetragonal $P4_2/nmc$, and orthorhombic $Pca2_1$, and cubic Fm3m TiN reference. The reference patterns are presented in **Table 12.**

Table 12 XRD reference patterns of TiN, HZO, and Pt phases

Material	Phase	PDF reference
TiN	**Cubic**	**00-038-1420**
HZO	**Monoclinic**	**00-034-0104**
	Tetragonal	**04-002-2773**
	Orthorhombic	**01-083-0808**
Pt	**Cubic**	**00-004-0802**

We investigated three samples of 15 nm sputtered HZO films. The electrodes thicknesses were varied from 25, 50, to 100 nm. After TiN top electrode deposition, the samples were annealed at 650°C for 1 min under N_2 using a rapid thermal annealing process.

Before the sample preparation for TEM, we conducted GIXRD to have a first idea about the existent phases. For the GIXRD scan, a X'Pert Pro Panalytical XRD system was used, collecting patterns in a range between 25 and 40 at a fixed incident angle of 1. The three samples showed the same orthorhombic phase and no apparition of the monoclinic phase. **Figure 128** shows the GIXRD pattern for the 25 nm sample (the two others are not presented here).

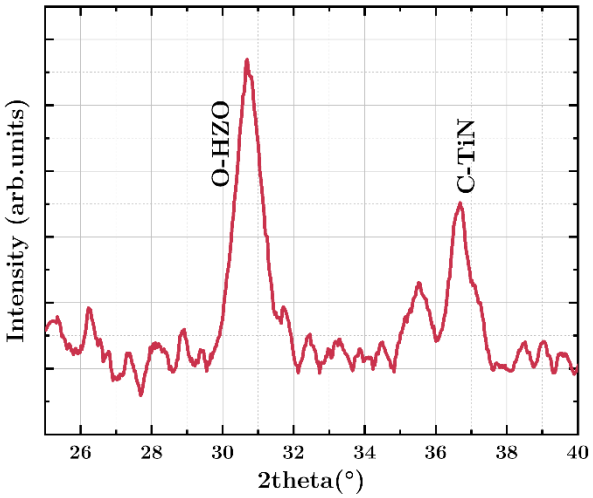

Figure 128 GIXRD pattern of TiN/HZO/TiN stack used for the ASTAR characterization, after annealing at 650 °C under N_2

No monoclinic phase appeared after annealing, as presented in **Figure 128**. Only the orthorhombic peak of HZO and the cubic peak of TiN appeared at 30.5° and 36.8°, respectively. A small peak appeared around 35.4° corresponding to the orthorhombic phase too.

A first information about HZO crystallization is the existence of the orthorhombic phase dominantly. The other phases did not appear and might appear with minor fractions if longer XRD scan would be conducted.

To check this information thoroughly, we conducted the ASTAR measurements on the TiN/HZO/TiN stack, with 25/15/25 nm thicknesses at LMGP lab by V. Consonni and L. Rapenne.

TEM specimens were prepared in cross-section by tripod polishing followed by argon milling by G. Levefre at LTM Lab. TEM and HRTEM images were recorded with a Jeol 2010 microscope operating at 200 kV with a 0.19 nm point-to-point resolution. The Jeol 2100F FEG microscope was further equipped with ASTAR that is a TEM-based experiment allowing crystalline phase and orientation mapping through automated precessed electron diffraction pattern indexing. The precession angle used in the experiments was 1.16°. The diffraction patterns were acquired at a rate of 100 frames per second with a step size of 1 nm, leading to a total acquisition time of 25 min per map.

Figure 129 Cross sectional TEM image of TiN/HZO/TiN stack with 100/15/100 nm

After specimens' preparation, the first cross sectional TEM images revealed that the 100 nm TiN sample contained an adhesion problem between HZO and TiN top electrode. This led to the debonding of TiN top electrode from the HZO layer as can be seen in **Figure 129**. This sample was an exception.

The TEM and HR-TEM images of the 25 nm sample revealed that the sample electrodes and HZO layer are well adhered and crystallized. The cross-sectional images are presented in **Figure 130**.

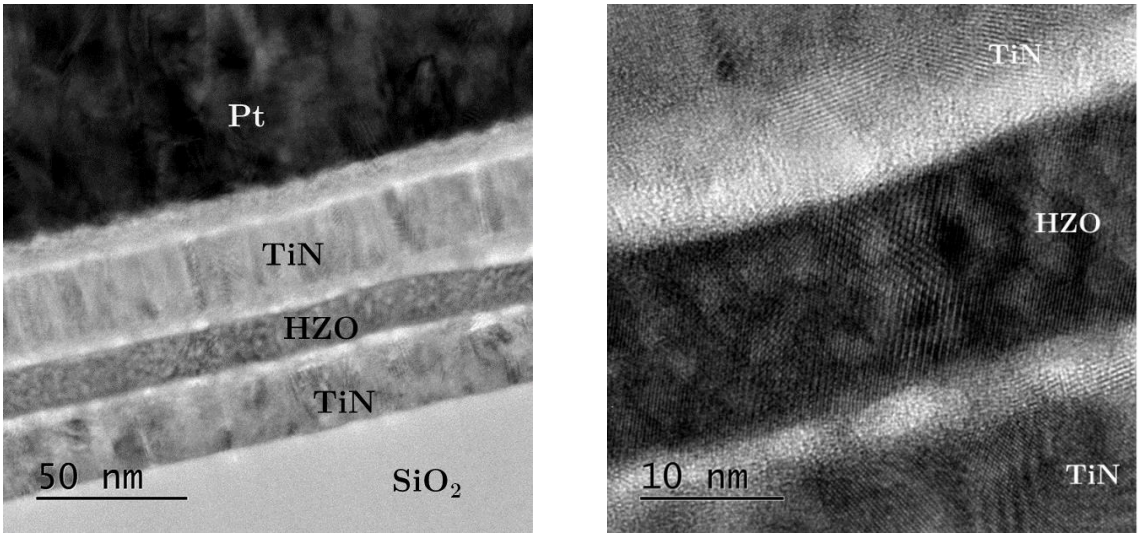

Figure 130 (left) cross sectional TEM and (right) HRTEM images of TiN/HZO/TiN stack with 25/15/25 nm thicknesses.

The TEM image allowed to confirm the thicknesses of the deposited electrodes and HZO layer. Besides, we can see that the layers were uniformly deposited. In good agreement with XRD results, the three layers are crystallized as can be observed in HRTEM image.

For the specimen of 25 nm sample, we conducted ASTAR measurements on three different zones of crystallized HZO in order to correlate with XRD results and confirm the mapping and the dominance of the orthorhombic phase. We started by the FFT diffraction patterns of TEM images in the three zones as the following figures show. The FFT allows to know the d-spacing from the diffraction pattern. The FFT is the first demonstration of the crystallographic phases. The three HZO phases, targeted here, monoclinic, orthorhombic, and tetragonal, have different d-spacing values.

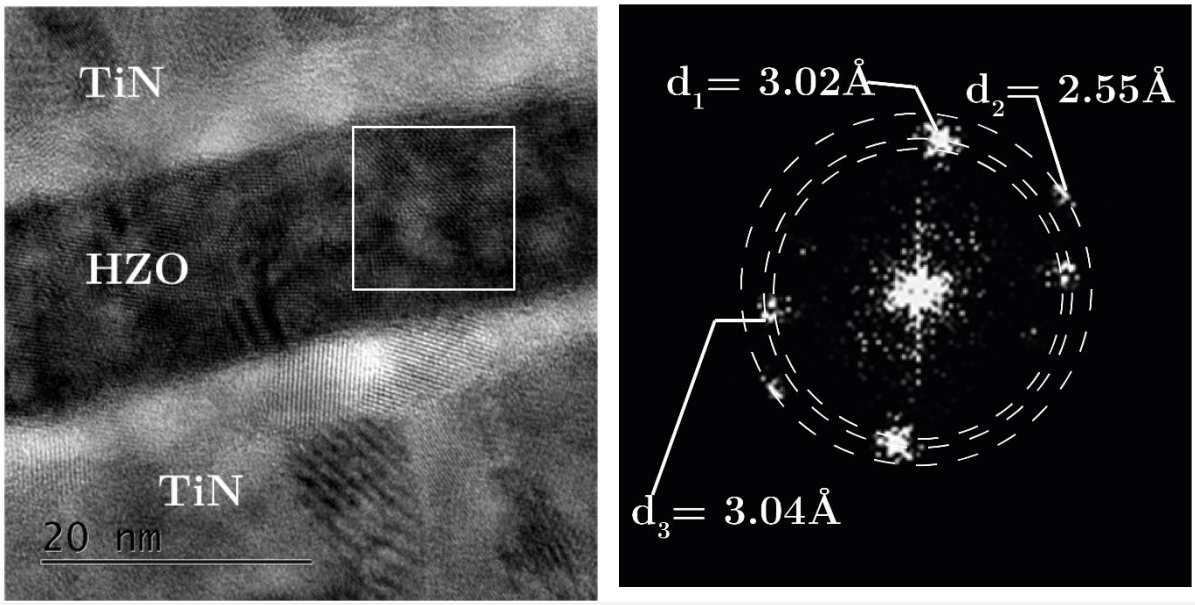

Figure 131 (left) Cross sectional TEM image of the first zone of investigation, in the white square (right) The Fast Fourier Transform (FFT) of the stack TEM image. the growth of the planes (111) along the direction of HZO is indicated.

For the first zone, in Figure 131, the cross-sectional TEM image and FFT patterns reveal the planar d-spacing of two distinct phases: the monoclinic phase around 2.6 Å and the orthorhombic phase around 3 Å. These values were contributed by checking in the PDF XRD reference and literature [243], [244]. Here, three planar d-spacing values are observed d_1, d_2, and d_3. The values of d_1 and d_3 are very close. They correspond to intense orthorhombic phase while the intensity of the monoclinic phase is weak as can been seen in the figure with d_2 value around 2.55 Å.

This result is in good agreement with the diffraction results, depicting significant peak of orthorhombic phase while the monoclinic phase did not appear due to the very low intensity of the peak.

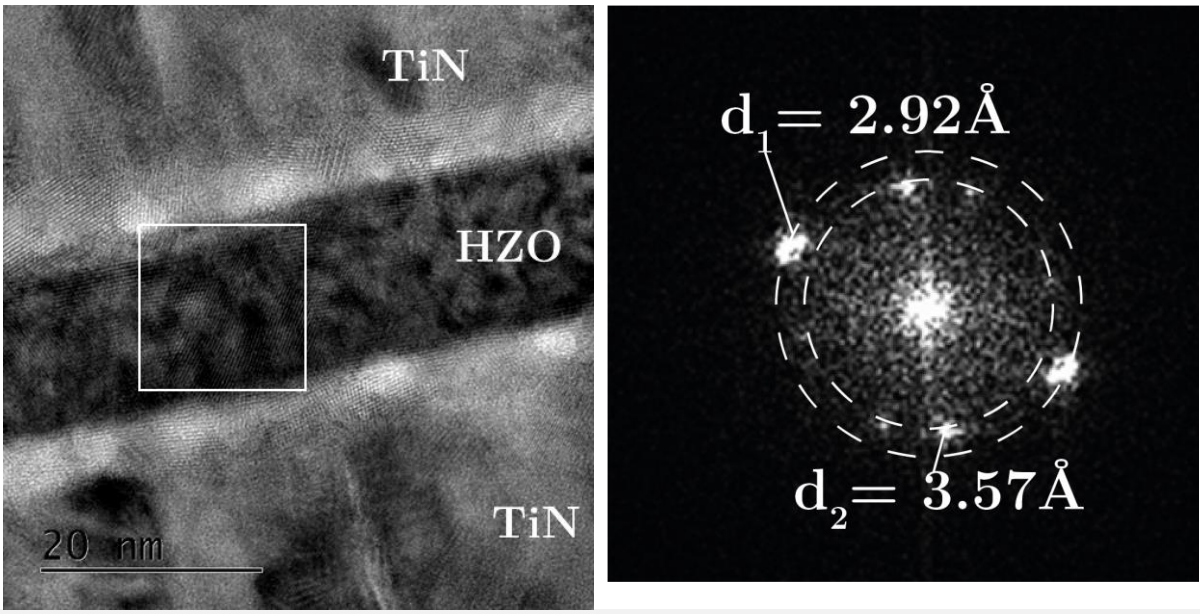

Figure 132 (left) Cross sectional TEM image of the second zone of investigation, in the white square (right) The Fast Fourier Transform (FFT) of the stack TEM image. the growth of the planes (111) along the direction of HZO is indicated.

For the second investigated zone, as can been seen in the white square in **Figure 132**, two d-spacing values are found in FFT: d_1 and d_2. Both correspond to the orthorhombic phase and no monoclinic phase is detected in this zone.

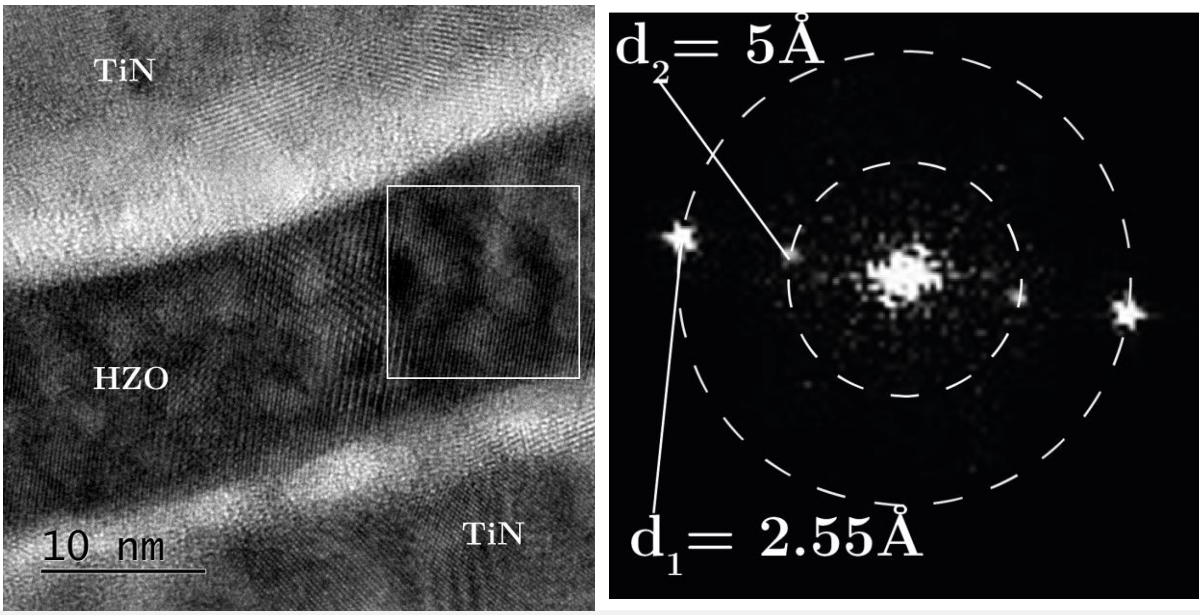

Figure 133 (left) Cross sectional TEM image of the first zone of investigation, in the white square (right) The Fast Fourier Transform (FFT) of the stack TEM image. The growth of the planes (111) along the direction of HZO is indicated.

For the third zone, a low intense diffraction is seen, which corresponds to d_2 around 5 Å and a more intense d_1 around 2.55 Å. The latter corresponds to the monoclinic phase while d_2 corresponds to the orthorhombic phase (100) [245].

For the three zones, we can see that the orthorhombic phase is dominant in the three different zones. This result confirms the information obtained by XRD but with more precision and certainty. The monoclinic phase appeared in two zones with very low intensity of FFT patterns suggesting that longer time in XRD measurement might reveal the low intensity peak of the monoclinic phase. At this stage, no sign of the tetragonal phase was observed.

4.4.2 ASTAR phase mapping

A significant disadvantage to statistically examining the structural characteristics of the HZO is the intrinsic spatial localization of HRTEM imaging at the nanometer scale. To address that issue, the maps of the crystalline phase and orientations of HZO phases are presented in the following figures, in three different zones, from ASTAR measurements.

This method involves precessed and simultaneous scanning of the target area with a few nanometer-sized incident electron beam. A recorded electron diffraction pattern is compared with the entire collection of predicted diffraction patterns at each point. These so-called templates are calculated for all conceivable orientations as well as for all anticipated crystalline phases. Crystalline phase and orientation can be determined by identifying the experimental electron diffraction patterns and templates that match them the best. Precession often reduces the effects of dynamics while improving the indexing quality.

As a reminder, our focus in this study is the crystalline phases of HZO despite that the results include TiN and Pt. For all the three zones, the Pt is green, and some zones are brighter indicating high crystallinity. Additional hints about TiN are obtained. The TiN electrode are shown in red which is in good accordance with the template of cubic phase of TiN. No other phase is detected. The result confirms the XRD results reported in the previous chapter. Uncolored locations are rare corresponding to phases not matching with the templates.

For HZO layer, we used two templates for the monoclinic, and orthorhombic phases with the yellow and blue colors, respectively. In the first zone, the dominant color is the blue corresponding to the dominance of the orthorhombic phase. A typical electron diffraction pattern of HZO recorded on the corresponding map, is shown in **Figure 134**.

The first zone

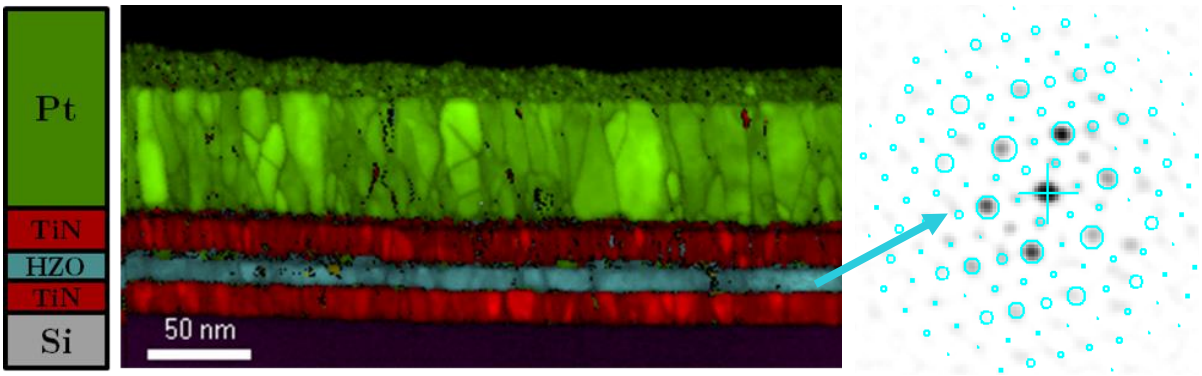

Figure 134 ASTAR map representing the crystalline phases of a HZO and TiN. The colors of TiN, HZO and Pt are shown in Table 2. The inset is a typical electron diffraction pattern of HZO recorded on the corresponding map, as indicated by the blue arrow. The templates that correspond to the most probable solution (i.e., the best match) are represented by blue open circles.

The presence of the monoclinic phase is very weak, as can be seen in the yellow color in the map. Some black void locations can be attributed to the tetragonal phase. By having different colors with varying brightness, this map shows the polycrystalline nature of HZO after annealing. The TiN electrodes are crystallized too.

Table 13 the color code for the mapping

Material	Color
Orthorhombic HZO	Blue
monoclinic HZO	Yellow
Cubic TiN	Red
Pt	Green
Amorphous	Purple

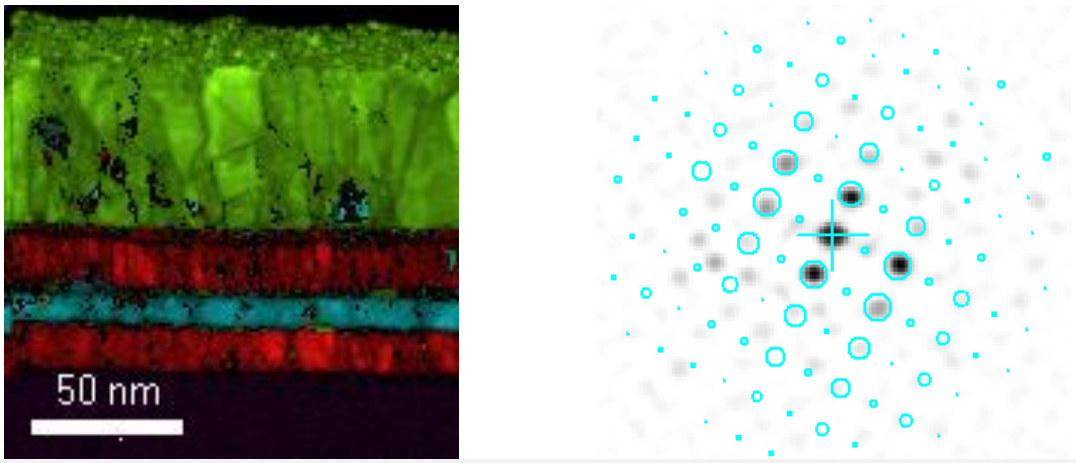

Figure 135 ASTAR map representing the crystalline phases of a HZO and TN. The colors of TiN, HZO and Pt are shown in Table 2. The inset is a typical electron diffraction pattern of HZO recorded on the corresponding map, as indicated by the blue arrow. The templates that correspond to the most probable solution (i.e., the best match) are represented by blue open circles

Compared to the first zone, no noticeable changes can be observed for the second zone, as indicated in **Figure 135**. The orthorhombic phase is dominant in the HZO layer with a monoclinic phase minority. The uncolored locations are more existent in the interfaces. Further studies can be dedicated to the interfaces to have better insights about their role.

Despite the polycrystalline nature of HZO, the grain size is small compared to TiN grain size as can be seen. This observation is confirmed by the grain size calculations by Scherrer's formula, reported in **Chapter 4**, found at around 8 nm.

The grayscale map overlaid on the colored scale map in **Figure 135** shows the degree of reliability, with the brighter parts corresponding to the better matches. **Figure 135** provides instances of how the chosen templates and the diffraction patterns typically match. In HZO films, the orthorhombic crystalline phase existence is therefore unmistakably demonstrated by ASTAR. Furthermore, the orientation map of the HZO phases is presented in **Figure 137**.

4.4.3 Orientation maps:

The first zone:

By plotting the value of the correlation index for the succession of the electron diffraction patterns at each point, the gray scale map shown in **Figure 136** was reconstructed [246].

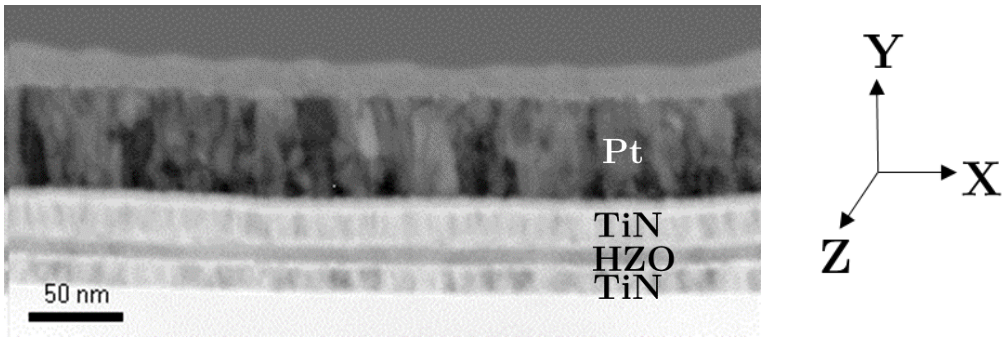

Figure 136 Reconstructed correlation index map

The orientation maps along the X, Y, and Z orientations, for the first zone, are shown in **Figure 137**. Starting by the TiN layers, we can see that the (100) orientation is the dominant one for the bottom electrode while the orientations within the top electrode are more distributed.

Here, we report the orientation map of the HZO and TiN layers. For the three zones, the same triangular color code, presented in **Figure 138**, is used, for both orthorhombic HZO and cubic TiN cases.

For the HZO layer, no color is dominating which indicates that no orientation is dominant. We can see the HZO layer divided into 4 major color representing close locations with the same orientations according to the YZ plan. This diversity is due to the large width of the scan. Focusing on narrow zones can lead to finding dominating orientations in some locations.

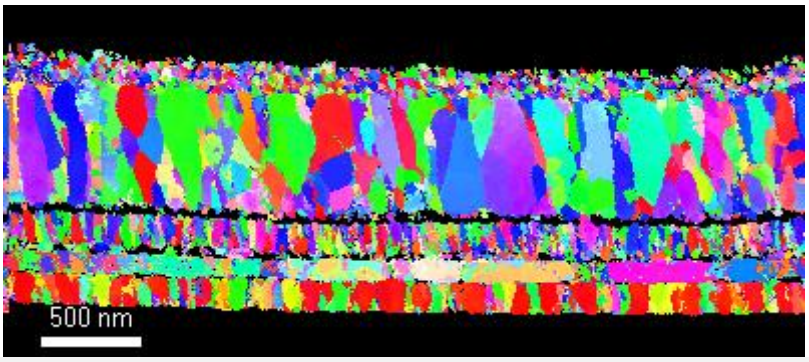

Figure 137 ASTAR crystallographic orientation phase maps of TiN/HZO/TiN/Pt along the three different orientations (a) X orientation

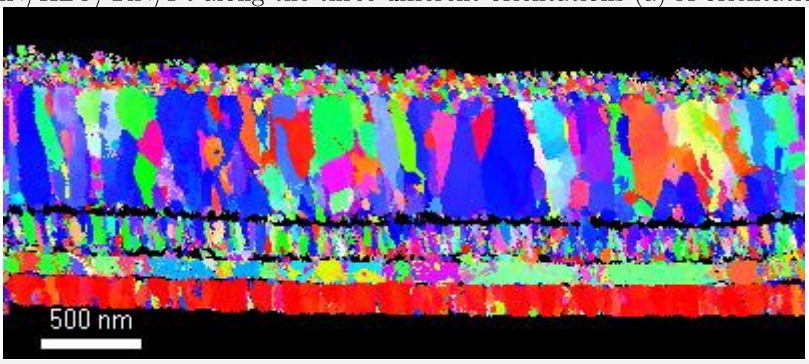

(b) Y Orientation

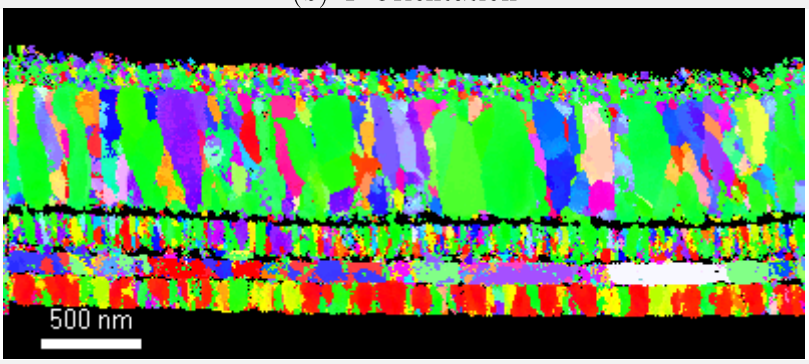

(c) Z Orientation

The (001) TiN is the dominant for the bottom electrode, and it is more orientated compared of the YZ plan. The XZ plan indicates more (100) orientation for the HZO layer. For the XY plan, The HZO layer is composed of some regions with the same orientation. the dominant orientations appeared in the HZO layer in the XY plan are (001) and (010).

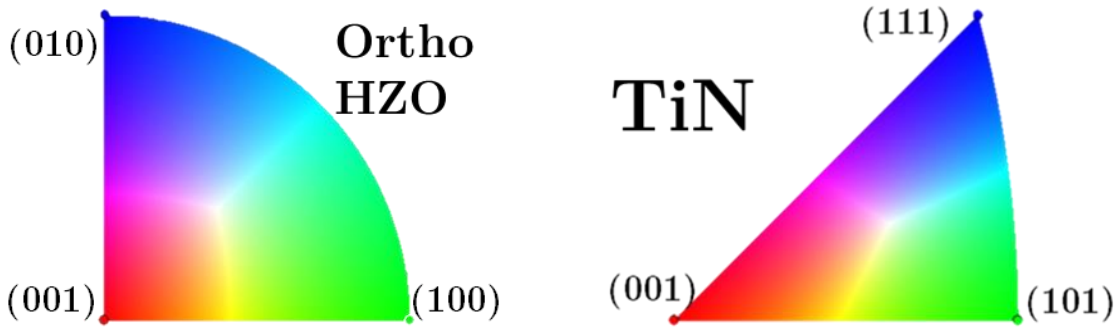

Figure 138 The triangular color code depicts the crystalline directions exhibited for the corresponding plane for both HZO and TiN. The color codes for HZO and TiN.

The second zone:

The orientation maps recorded for the second zone are illustrated in **Figure 139**. The orientation maps of the TiN bottom electrode, in the three planes xy, yz, and xz, indicate the dominance of the (100) orientation. Despite the same thickness of the top and bottom electrodes of TiN, the texture is different as the BE TiN was grown on Si and the TE TiN on HZO. The BE is more homogenous compared to the TE for the three planes.

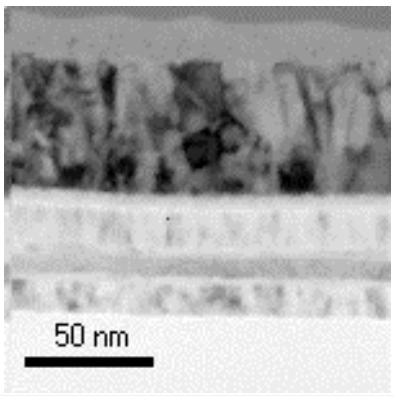

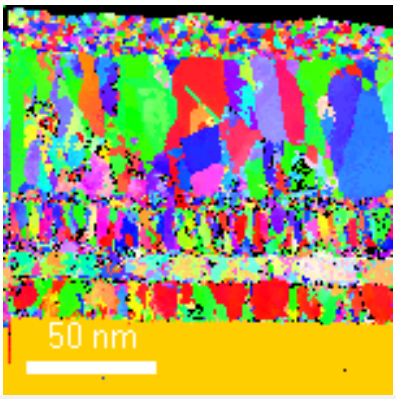

Figure 139 Virtual BF image, Reconstructed correlation index map

Crystallographic orientation phase maps of TiN/HZO/TiN for three different orientations (a) X orientation

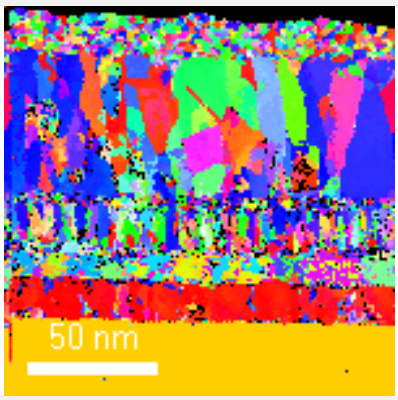

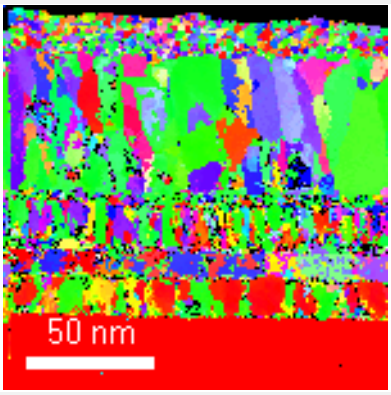

(b) Y Orientation (c) Z Orientation

Moreover, the random orientation of HZO grains is an indication of the lack of any texture for the three planes.

The third zone:

The orientations maps of the third investigated zone are shown in **Figure 140**.

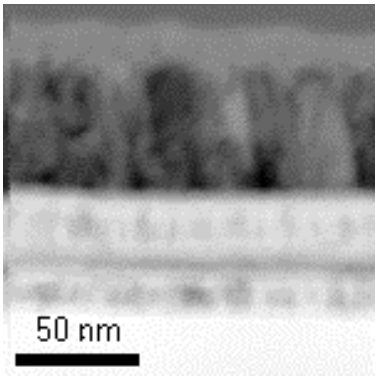

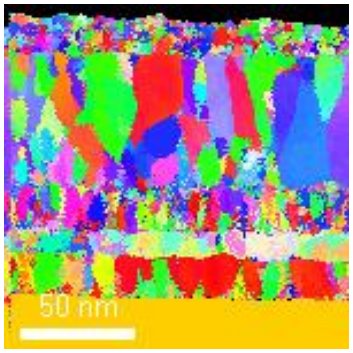

Figure 140 Virtual BF image, Reconstructed correlation index map

Crystallographic orientation phase maps of TiN/HZO/TiN for three different orientations (a) X orientation

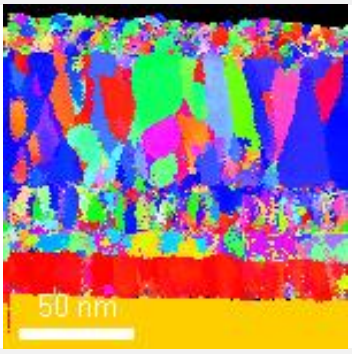

(b) Y Orientation

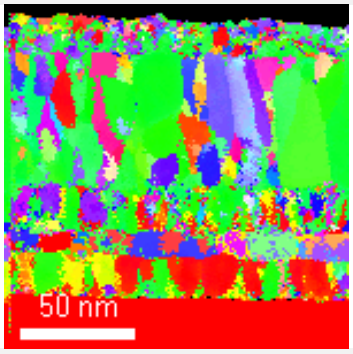

(c) Z Orientation

The three zones confirm the dominance of the orthorhombic phase overall the HZO layer. The small grain size is in good agreement with the XRD results.

4.4.4 Discussion

Through the obtained results, the ASTAR technique confirms, locally and with accuracy, the dominance of the orthorhombic phase within HZO layer in three different zones. The ASTAR results are complementary to the XRD, TEM, and FFT results. Insights about TiN electrodes are found also.

The 25nm-TiN/15nm-HZO/TiN sample indicates the role of RTA in HZO crystallization. First, the latter is observed XRD patterns where the o-phase appeared as dominant in the scan range. Second, the high crystallinity is well appeared in HRTEM cross-sectional images of three zones, and FFT patterns revealing d-spacing values corresponding to a major contribution of the o-phase with a minor contribution of the monoclinic phase.

The tetragonal phase was not present in the HZO film despite its polycrystalline nature. This is a first proof of the lack of confusion between the tetragonal and orthorhombic phase. Further simulations can be launched to support this result. The XRD and TEM results indicate the crystallization of TiN electrodes into dominant cubic phase.

Three zones were investigated, using TEM, to have confirmed result along the sample. For all of them, the o-phase was dominant, and, unlike the XRD, the monoclinic phase appeared with weak intensity. The d-spacing values represent an indicator of the o-phase too.

The phase mapping, in different zones, reveal the dominance of the o-phase for HZO, as can be seen in the blue color. The varied brightness reflects the different degrees of crystallinity in each zone. Despite having one dominant phase, HZO layer is not bright as the highly crystalline TiN. This can be explained by the small size of HZO crystallites. The monoclinic phase presence, in yellow, is very low, which is in full agreement with XRD and FFT results. The absence of tetragonal phase, even in phase maps, confirm the previous revelations. No major difference can be observed in the three zones for the phase maps. This is an indicator of the accuracy of the ASTAR technique and the same crystallization of HZO along the sample width. A visual observation of the phase maps allows the observation of majority small-size grains, in total agreement with the values obtained from XRD patterns using Scherrer's formula. The small-size grains prevent the formation of the monoclinic phase as reported by HJ. Kim et al.[111], it is in good agreement with the predictions reported by density functional theory (DFT) calculations of surface energy thermodynamical model for HZO films [247].

One can speculate that studying the impact of sputtering parameters on the grain size can lead to important discoveries of ferroelectricity in sputtered HZO films. The obtained grain size, around 8 nm, are lower than the reported values in literature, which are between 10 and 30 nm [111], [240], [248]. This can explain the low polarization value obtained in P-E measurements suggesting that a range of grain size is favorable to obtain high polarization. This was studied theoretically by Materlik et al.[247]. MH.Park et al. proposed a kinetic model for the emergence of o-phase in HZO films [249], in which they proposed that the transition to the m-phase was kinetically improved at high RTA temperatures (>700 °C), however the stability of the m-phase decreased thermodynamically at high temperatures. We recall that the ASTAR sample was annealed at 650 °C, which is considered as high temperature. The ASTAR phase mapping of the annealed HZO sample, at 650 °C, indicates that no transition to the monoclinic phase occurred at this RTA temperature, which is in partial agreement with the decrease of monoclinic phase stability at high RTA temperatures. The disagreement with the

suggested kinetic model might be due to the difference in HZO layer and electrodes thickness, suggesting that their model is thickness dependent.

The ASTAR measurement are supported by previous structural results and electrical characterizations in the following parts. Yet, the ASTAR has the advantage of local and accurate precision of the phase distribution. Using image processing of the ASTAR maps, we found the HZO layer is consisted of 97 % of o-phase, 0.9% monoclinic phase, and 2.1% unidentified phase.

The XZ plane represents the HZO layer's out-of-plane directions. It has no distinct texture, as the same as the XY and YZ planes. As a result, most grains are randomly orientated with no out-of-plane or in-plane texutre. One can speculate that the 25 nm thickness of electrodes is not enough to apply stress on HZO layer during deposition or annealing. This lack of in-plane texture can be an explanation of the relatively weak polarization obtained in P-E measurements compared to in-plane textured HfO_2-based ferroelectrics [240]. Because the [001] axis is like the polarization axis, it would be closely aligned with the in-plane direction, the sample would have a low remanent polarization due to the randomly oriented grains. We recall that this sample is in the pristine state. The wake-up might enhance the polarization as reported [250].

The TiN texture is another important factor of ferroelectricity for HZO as reported by Athle et al.[172] where (111) TiN sample had very large polarization compared to the (200) textured sample. In our case, it has a strong out-of-plane texture, and most grains are orientated with the [001] axis pointing out-of plane. Some regions have also in-plane texture for the xy and yz planes. This texture occurred due to the stress applied on the bottom electrode during deposition and RTA.

These results are very well correlated with the reported results in the previous chapter such as XPS for Hf: Zr ratio and XRD for crystallization. The dominance of the o-phase is confirmed in the following parts by electrical measurements.

4.4.5 Conclusion

In conclusion, the ASTAR technique has been used for the first time on TiN/HZO/TiN in the aim of quantifying the appearing phases after annealing. Besides, the results can be confirming the first insights about ferroelectricity by other techniques.

It has been shown that the ASTAR approach makes it possible to determine the phase fraction of HZO with great precision and accuracy. Additionally, we can examine the texture of the HZO layer thanks to the determination of the crystallographic orientation of individual grains. The ferroelectric orthorhombic phase is observed to exist across the

complete range of grain sizes, but the monoclinic phase is only present in a tiny percentage of grains (0.9%) in a HZO thin film. This is consistent with hypotheses based on HZO thermodynamic and kinetic properties. The polycrystalline film also exhibited no out-of-plane texture while the TiN bottom electrode is textured in [001] direction while the top electrode has no texture.

Further studies and calculations can quantify the orthorhombic phase compared to the other phases, and also the phases orientation. This result is a reference for the future studies to enhance the ferroelectricity within HZO films deposited by sputtering.

5 Chapter V Electrical characterizations of HZO-based MIM capacitors.

5.1 Copper impurities in HZO sputtering 195
5.1.1 Introduction 195
5.1.2 Discussion 196
5.1.3 Conclusion 197

5.2 Electrical characterizations of HZO-based MIM capacitors 198
5.2.1 Introduction 198
5.2.2 With capping layer during RTA 199
5.2.3 Without capping layer during RTA 203
5.2.4 Conclusion 208

5.3 Temperature-dependent dielectric properties of HZO in top electrode-free annealing configuration 208
5.3.1 Introduction 208
5.3.2 Discussion 216
5.3.3 Conclusion 217

5.1 Copper impurities in HZO sputtering

5.1.1 Introduction

After the optimization of HZO sputtering, structural hints of ferroelectricity were observed in XRD patterns via the apparition of the orthorhombic phase in the annealed films. Unexpectedly, electrical measurements of the HZO-based MIM stacks showed a high leakage current in most of the capacitors. The aim of this part is to illustrate the reason behind the lossy capacitors found in electrical measurements, which resulted in many unfinished studies for their electrical part.

We conducted XPS measurements on some of the samples with lossy capacitors and we found an unexpected result. XPS results indicated the apparition of copper (Cu) in some samples. First, we suspected the metallic support of the substrate holder and we removed it. Despite that, the copper apparition persisted. Finally, we found that a part of the target's backing plate was exposed to plasma during deposition. The backing plate is made of oxygen-free copper due to its good electrical and thermal properties. The incorporation of copper in HZO films caused a leaky behavior of the capacitors. The exposition of the copper backing plate occurred due to the bad installation of the HZO target.

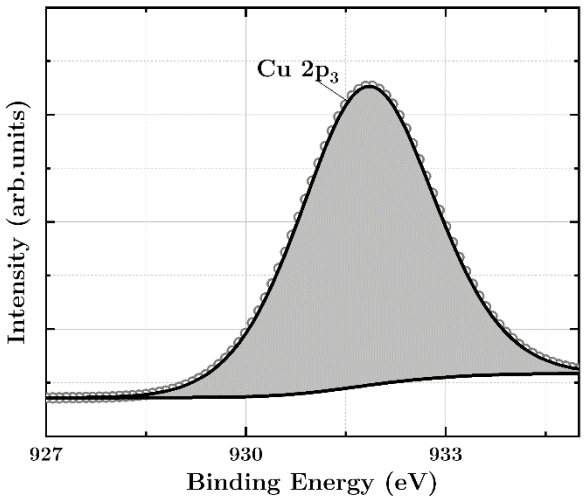

Figure 141 XPS of copper in HZO sputtered films

The Cu peak that appeared in XPS, as illustrated in **Figure 141**, has a low intensity compared to the other expected elements (Hf, Zr, O, and C). in the case of reactive sputtering of HZO, copper oxide is formed within the films because of the oxidation of the copper with the oxygen.

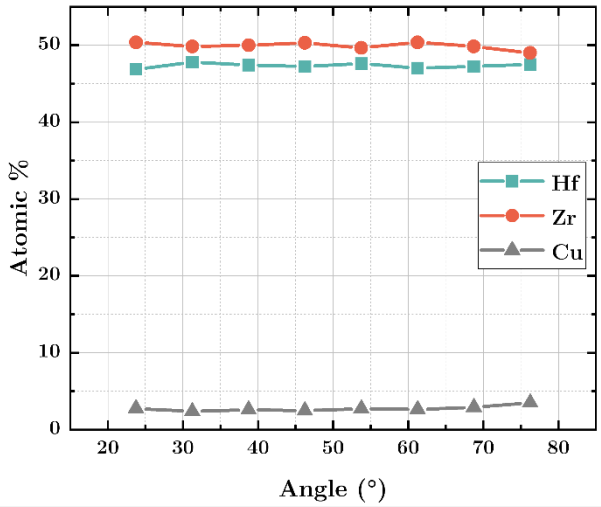

Figure 142 XPS depth profile of Hf, Zr, and Cu in HZO sputtered films.

Despite the low concentration of copper, it impacted the electrical properties of HZO. No copper-doped HZO films have been previously reported but we can find in literature copped-doped zirconium oxide [235]–[238]. Hafnium oxide has been reported as a barrier against copper diffusion [239]. The copper concentration, in angular resolution, is shown in **Figure 142** next to Hf and Zr. The atomic percentage of copper within HZO films is about 2 %.

5.1.2 Discussion

Copper impurities are undesirable inside the sputtering chamber. There was no obvious origin of these impurities.

We suspected Cu impurities left in the chamber from a previous deposition of copper inside the chamber. This possibility was eliminated due to: First, the fact that the pumping system is working very well, and no other elements deposited before having been detected in XPS survey. Second, no copper has been deposited in the same chamber before HZO deposition.

The second possibility was the metallic support of the substrate holder. We eliminated this possibility by removing the metallic support and the problem persisted.

Finally, we suspected the backing plate as it is the only part made of copper inside the chamber. We found an exposed part of the backing plate impacted by the plasma, as can be seen in **Figure 143**. The erosion zone is very close to the edges and possibly, during the deposition, the plasma impacted the backing plate. Contrary to the other targets, the backing plate's color is different for one edge compared to the other edges, for the HZO target. As shown in **Figure 143**, the upper edge of the backing plate is the origin

of the copper impurities, as it is more exposed than the lower edge. Covering the backing plate edges led the elimination of the copper impurities and the electrical measurements confirmed that.

EDX and TEM measurements showed no copper impurities. Only the XPS could detect the low concentration of copper. Copper-doped zirconium oxide can be crystallized into monoclinic phase. The monoclinic peak in XRD patterns is different from those of HZO, so, no confusion for HZO XRD peaks, can occur due to the copper impurities.

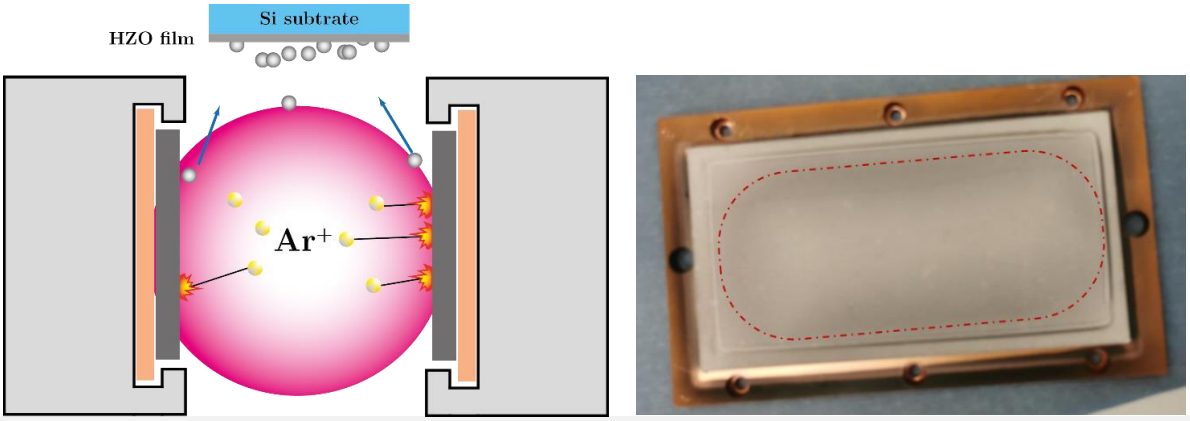

Figure 143 (left) Schematic cross section of facing target sputtering system used for HZO sputtering (right) picture of HZO sputtering.

Despite that the Ar ions attacked the center of the target's surface more than the edges, the lower concentration of copper influenced the electrical properties of HZO, especially after annealing. As **Figure 142** illustrates, the low concentration of copper can impact the properties of HZO. For Cu-dopped ZrO_2 films, Cu doping was studied from 0 to 8% by N.Yao et al.[237]. It was reported that increasing the Cu doping improved the conductivity of the films.

5.1.3 Conclusion

Experimental investigation of sputtering parameters can be often misled by unconventional factors. In our case, we struggled with two main factors:

- The very short time of chamber availability for HZO deposition due to the technical issues.
- The copper impurities.

The copper impurities can be a solid motif to use circular targets instead of rectangular targets. This phenomenon of copper incorporation within HZO films can be interesting as a study of HZO doping. The high conductivity of Cu-HZO films suggests that it can

be a candidate for transparent electrodes. In the next parts, the investigated HZO films are copper-free.

5.2 Electrical characterizations of HZO-based MIM capacitors

5.2.1 Introduction

The electrical characterization represents the second side of this thesis. It has been used to check the successful fabrication process of MIM capacitors, including the etching step, via the dielectric properties of the capacitors and to confirm if the sputtered HZO films are indeed ferroelectric. This confirmation is correlated with the structural hints, and signatures of the ferroelectric orthorhombic phase.

Before measuring the polarization via P-E, we conducted impedance, leakage current and capacitance measurements to have insights about the dielectric properties of HZO.

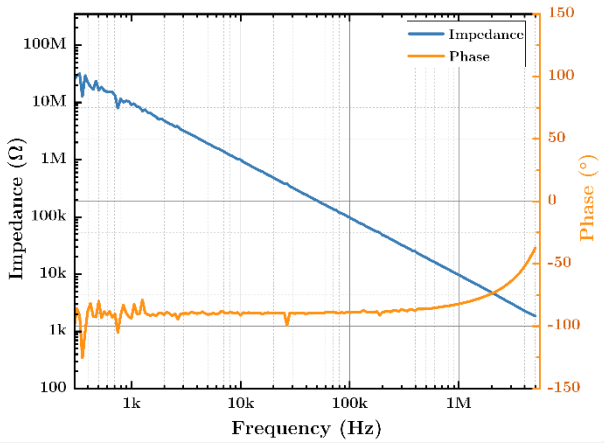

Figure 144 Impedance and phase angle versus frequency of TiN/HZO/TiN stack performed with Hioki IM3570

The analysis of the results for the TiN/HZO/TiN shown in **Figure 144** exhibited a negative slope of the impedance as the frequency increased. In addition, a constant phase angle, determined by the voltage to current phase, at -90° was obtained in the 10-100 kHz frequency range. This behaviour of the impedance characteristic corresponds to a capacitive behavior of the device under test.

In the studied device, corresponding to **Figure 144**, a similar behavior was observed, which is repeated for all HZO samples. The presented impedance characteristic in **Figure 144** can be obtained with the equivalent circuit given in **Figure 145**. In the proposed electrical circuit, a dielectric is assumed to be a perfect insulator and so only has a capacitance C_p. However, in dielectrics, there is always some limited conductivity, which necessitates the addition of a resistance R_p in parallel with the capacitance. Furthermore,

additional resistance in series to this RC element is frequently encountered in practice. Non-ideal electrodes, electrode interfaces, or non-compensated (contact) resistances in the circuit are the reason behind R_S, which is typically several orders of magnitude lower than R_p.

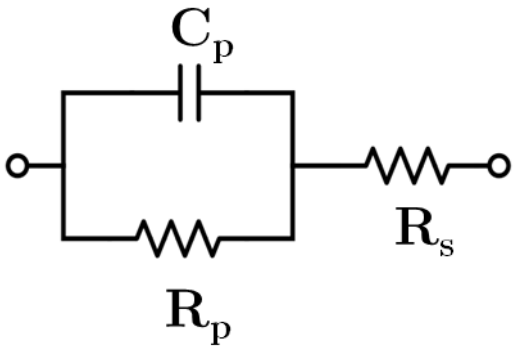

Figure 145 The equivalent circuit of TiN/HZO/TiN

The equivalent circuit is very basic. Further studies are needed to determine the complex equivalent circuit accurately, in accordance with TEM images.

The electrical measurements have been conducted on two kinds of samples, to check the necessity of top electrode during annealing: TiN/HZO/TiN stacks annealed after TiN TE deposition and before TE deposition. For XRD results, both kinds show an o-phase presence after annealing, with higher intensity with TE presence during annealing.

5.2.2 With capping layer during RTA

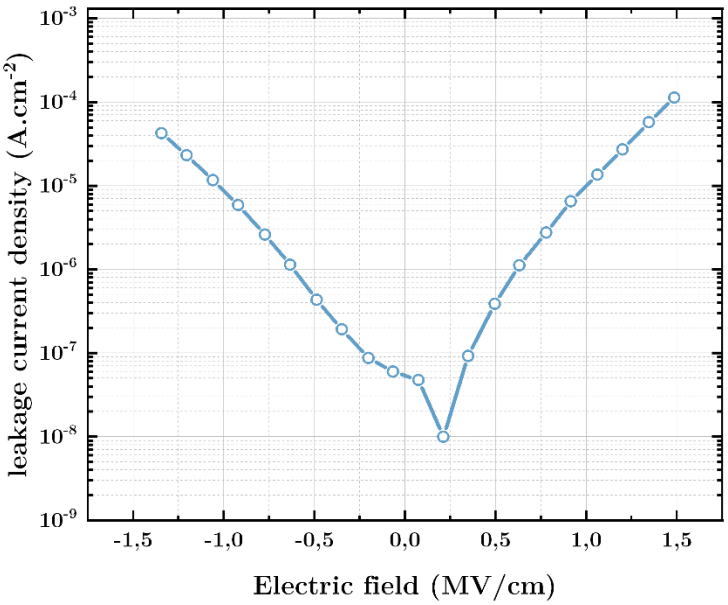

Figure 146 Leakage current density versus electric field for 15 nm HZO

First, we conducted leakage measurements on 15 nm HZO stack annealed at 650 °C for 1 min.

Leakage current measurements indicate current densities in the order of 10^{-4} A.cm^{-2} at 1.5 MV.cm^{-1}, falling within the range of values typically reported in literature for sputtered ferroelectric HZO [124], [232]. Though, it should be highlighted that samples, with few copper impurities, exhibit very high leakage. The leakage measurements were affirmative of the dielectric nature of HZO films. The leakage current density of the 15 nm HZO sample is plotted in **Figure 146**.

The I–V characteristics were determined on the TiN/HZO/TiN stacks to ensure the absence of important leakage current that might hinder the observation of HZO film ferroelectric behavior. Indeed, high leakage current can prevent the buildup of electric field across the stack, resulting in very poor dielectric polarization of the HZO layer. In addition, it was shown that the leakage current density across HZO layers is strongly influenced by the process conditions [251].

We believe that these superior electrical results are due to the enhanced density of the HZO films, thanks to the high power applied to the HZO target (400 W) during film deposition [252]. An additional annealing of HZO films under an high pressure atmosphere could reduce the leakage current by reducing the number of defects within the films [253].

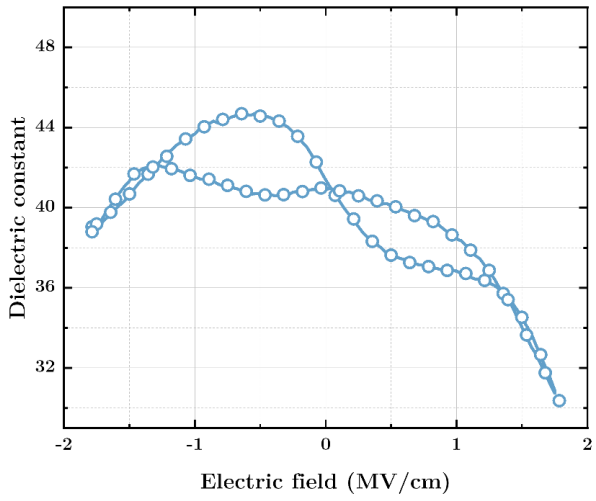

Figure 147 Dielectric constant versus electric field of HZO 15 nm

Separate C-E curves were acquired on the same equipment used for I-V measurements, TF 3000 analayzer, and the relative permittivity was determined from those results. **Figure 147** presents the curve of the dielectric constant versus electric field for the

HZO-based capacitors. At zero field, the dielectric constant is 41, which represents a reference value with the capacitance variation. The C-E, or k-E, has a butterfly shape. This butterfly shape in C-V measurements is an electrical signature of the ferroelectric nature of the material. A butterfly-shaped C–V plot usually attributed to the ferroelectric polarization is obtained at positive and negative polarization once the coercive field is reached. The shape of the curve is a little bit asymmetric because the dielectric constant has different values at the opposite extremities: +1.9 and -1.9 MV.cm^{-1}. This obvious ferroelectric behavior implies that the previously observed XRD diffraction peak was mostly driven by the ferroelectric orthorhombic phase of HZO.

Given that the o-phase of HZO has a lower permittivity than the tetragonal phase and the ASTAR results indicated the absence of the tetragonal phase. We can confirm the o-phase by its dielectric constant.

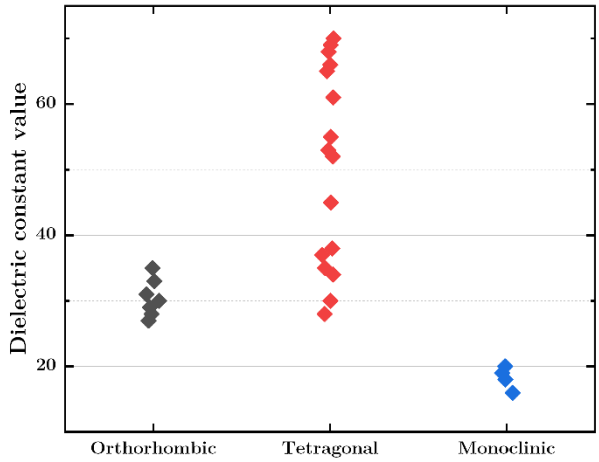

Figure 148 Dielectric constant of HZO phases reported in literature [13], [247], [254]–[259]

The C–V characteristics which showed an orthorhombic HZO phase signature in order to confirm the ferroelectric behavior of the HZO layer. Indeed, besides the well-known polarization–electric field hysteresis (P–E) plot, the so-called butterfly-shaped C–V plot is also used to evidence the ferroelectric behavior [13], [121], [260]. This result is consistent with the structural analysis obtained in the previous sections.

Indeed, the butterfly shape variation, around the 41 value of dielectric constant, is correlated with the contributions of the orthorhombic/tetragonal and monoclinic phases after the annealing of the stack. The values of the dielectric constant, in the range of 30–45, agree with the published data for HZO layers obtained by ALD or sputtering, as presented in **Figure 148**. However, it is noteworthy that the obtained dielectric constants of the single-target sputtered HZO are somewhat higher than those reported for co-sputtering HZO layers. This can be related to the difference in the fraction of tetragonal and orthorhombic phases. Indeed, the dielectric constant of the HZO

tetragonal phase is 40-70, whereas that of the orthorhombic phase is 40. The ASTAR results confirmed the lack of the tetragonal phase contribution, so the dielectric constant is mainly the contribution of the o-phase.

A triangle signal with a frequency of 1 kHz and an amplitude of 4.5 V was used to conduct P-E on the capacitors (2.4 $MV.cm^{-1}$). All devices in this experiment required a wake-up to produce the optimal hysteretic polarization reversal, which is this case 1000 cycles at 2 $MV.cm^{-1}$. Several ferroelectric HZO ferroelectric films have shown this wake-up effect [83], [261], [262] while wake-up free ferroelectric HZO was reported too [263], [264].

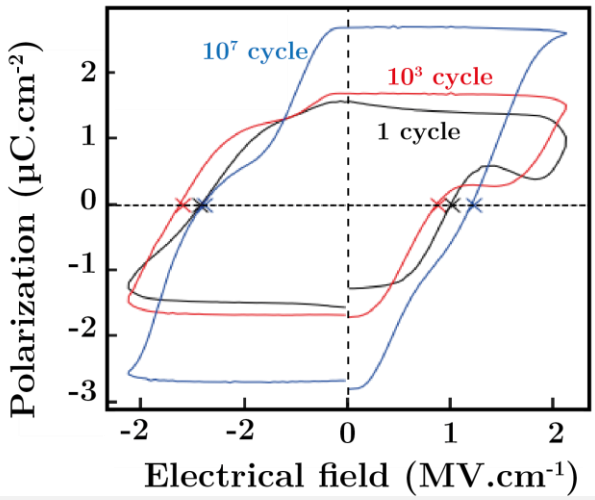

Figure 149 Polarization versus electric field hysteresis loop of the 15 nm HZO after different number of cycles.

As illustrated in **Figure 149**, the P-E hysteresis loop of the 15 nm HZO sample is present. On this DUT (device under test), the wake-up technique was applied. The shape of the first hysteresis loop, in black, is deformed at the extremities, and it has a $2P_r$ value of 3 $\mu C.cm^{-2}$.

After 1000 cycles, the shape of the hysteresis shape, in red, was improved and the $2P_r$ value increased to 3.5 $\mu C.cm^{-2}$. The best shape of the hysteresis loop was recorded after 10^7 cycles, in blue, and $2P_r$ reached it maximum of 5.6 $\mu C.cm^{-2}$, which 2.5 times higher than the first hysteresis loop. The capacitor broke down after 10^7 cycles.

Thicker films of 22 nm HZO stack was electrically characterized to check the thickness dependence of ferroelectric properties of the HZO films. The I-V and C-V results are plotted in **Figure 150**.

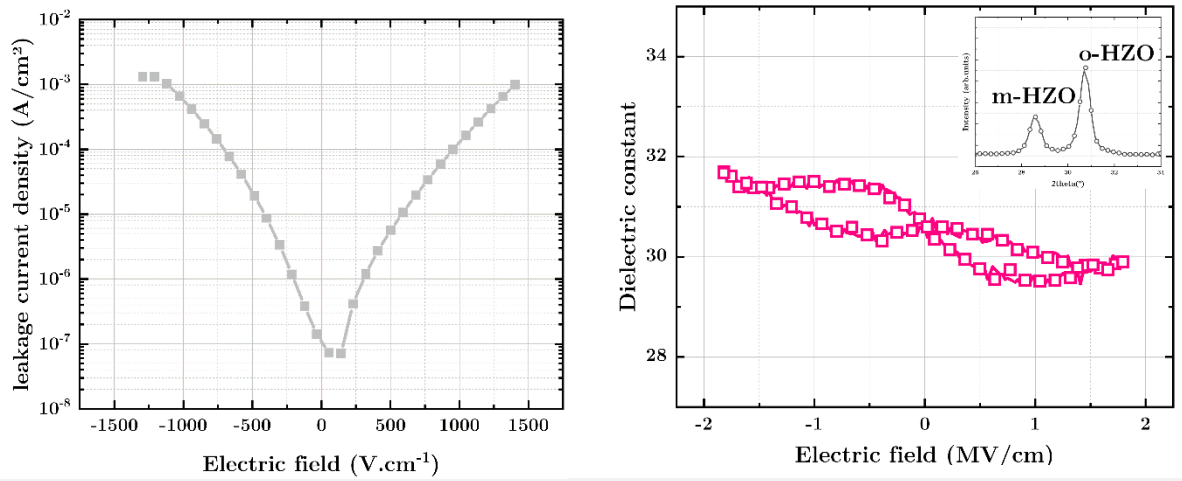

Figure 150 (left) Leakage current density versus electric field (right) Dielectric constant versus electric field of HZO 22 nm. The inset: XRD pattern of the sample.

Compared to the thinner film, the leakage current density is higher; around 10^{-3} A.cm^{-2} at 1.5 MV.cm^{-1}, confirming the dielectric nature of the films with comparable leakage values. The XRD pattern shows high fraction of the m-phase compared to the 15 nm film. Still, the o-phase is the dominant phase. This result is a confirmation of the 25 nm limit of ferroelectricity in HZO.

As the m-phase fraction is higher, its contribution is more noticeable in the C-V curve. The variation of the dielectric constant versus electric field took a butterfly shape. The latter is in total agreement with the o-phase dominance and the thickness limit for ferroelectric HZO. Despite that, the dielectric constant is lower than the thinner films reflecting more important m-phase contribution as its dielectric constant is around 20 as reported above. The dielectric constant is around 31. The C-V shape is more symmetric compared to the thinner film.

5.2.3 Without capping layer during RTA

The second kind of stacks did not have TiN capping layer during annealing. The structural characterization showed a humble presence of the orthorhombic phase after annealing without capping layer at different layers of HZO, as illustrated in **Figure 151**.

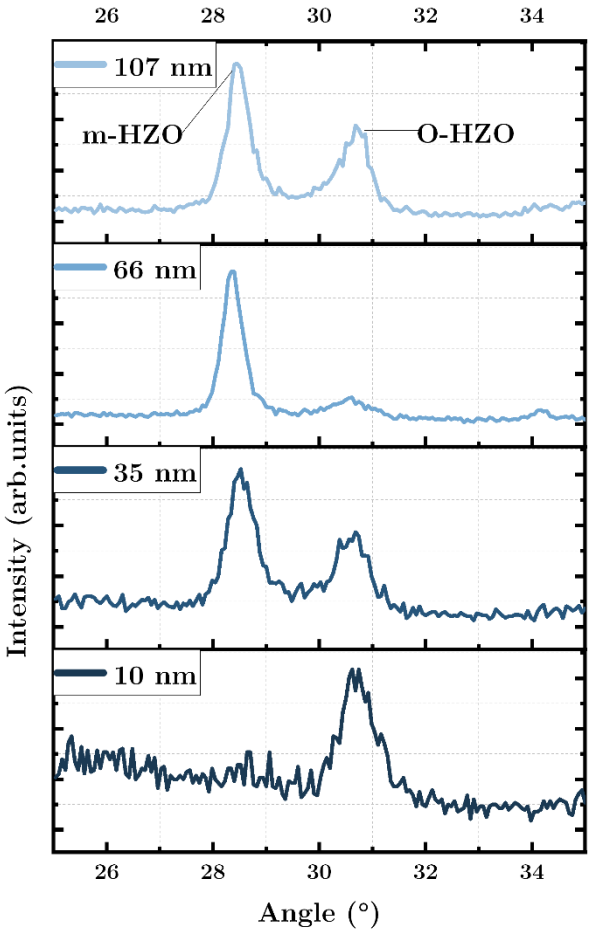

Figure 151 GIXRD patterns of HZO stacks of different thicknesses annealed at 650°C.

The HZO thickness varies from 10, 35, 66, and 107 nm. Unlike the stack with capping layer during RTA, these samples showed a dominant apparition of the monoclinic phase for the 35, 66, and 107 nm samples. The o-phase apparition was very low compared to the monoclinic phase except for the 10 nm sample, in which the o-phase as dominant. This agrees with the hypothesis, reported before, of 25 nm limit for ferroelectricity in HZO films, indirectly the o-phase [265]. The 66 nm sample showed the lowest o/m fraction compared to the others.

For one hand, this finding confirms that the m-phase tends to be more stabilized for thicker HZO films, especially at high annealing temperature (650 °C). This observation is in good agreement with model results reported by MH. Park [249]. In other hand, the presence of capping layer is not necessary for the HZO films thinner than 25 nm while it is important for thicker films to prevent the growth of the monoclinic phase. X.Liu et al. reported 13 nm Al: HfO_2 to be ferroelectric without TE. They suggest that the Al doping mimics the TE role [266].

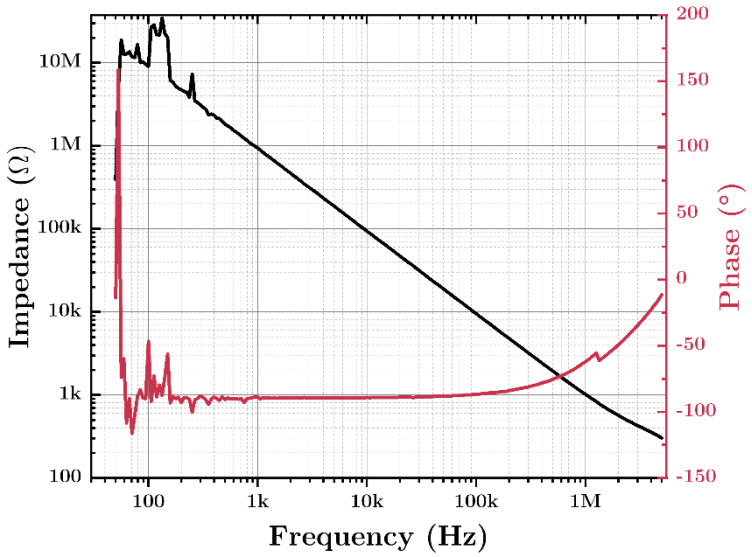

Figure 152 The impedance and phase versus frequency of HZO

After structural characterization, electrical measurements were conducted following the same steps as the previous measurements. The impedance and phase angle analysis against frequency are plotted in **Figure 152**. The same behavior, as the previously reported impedance analysis, is observed. This analysis helps us pick the measurement frequency for the other measurements.

The equivalent circuit is the same basic one mentioned above. No major difference is observed except some non-linearities at low frequencies.

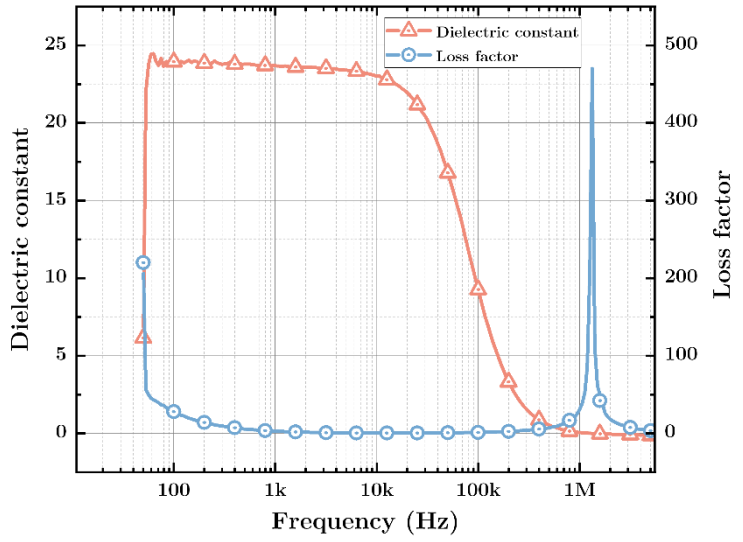

Figure 153 The capacitance and loss factor versus frequency of HZO stack without capping layer during RTA

The dielectric constant stated to decrease at lower frequencies, around 25 kHz, compared to the stack with capping layer during annealing. The dielectric constant does not change

along the 100 Hz – 25 kHz. The next measurements are conducted at 1 kHz. The loss factor resonance occurred at lower frequency ~ 1.5 MHz, inside the measurement range contrary to the stack with capping layer which was out of the range (> 5MHz).

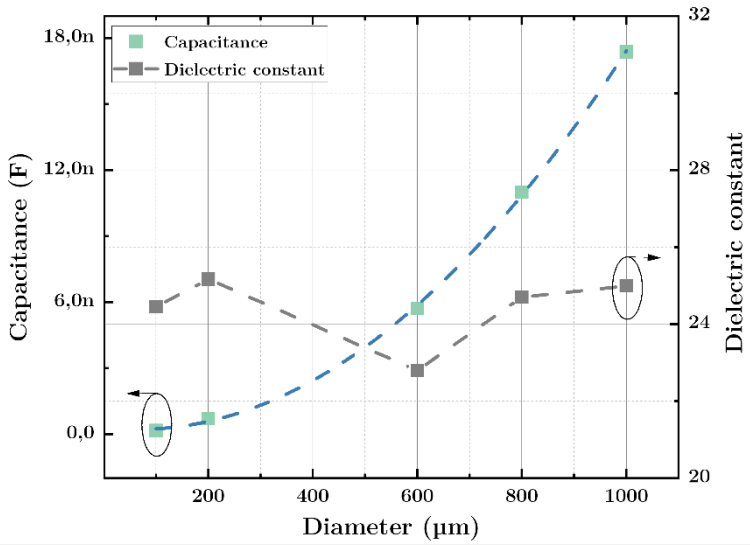

Figure 154 The capacitance and dielectric constant versus pad's diameter

The HZO stack has capacitors with different areas, as shown in Chapter 3. The capacitance and dielectric constant for the HZO stack without capping layer are plotted as function of the pad's diameter. The capacitance increased as expected as the diameter increases while the dielectric constant was calculated for each diameter. The dielectric constant is mostly constant. It slightly decreased from 25 to 23 for 600 µm diameter, then increased again to 25. This constancy reflects the homogeneity of the films overall the substrate surface.

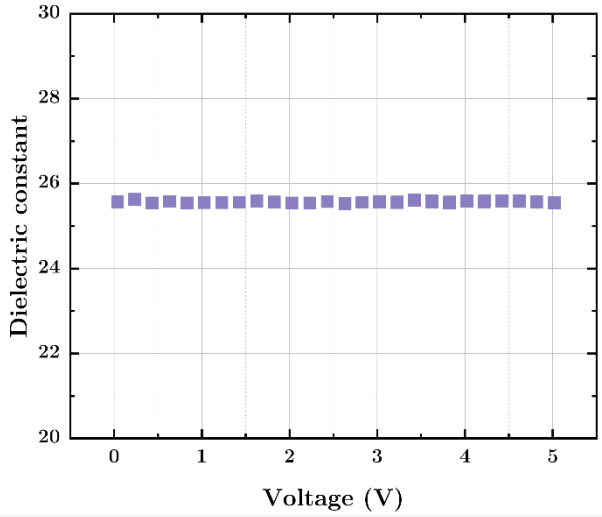

Figure 155 The capacitance-voltage curve for HZO stack without capping layer during RTA.

For each pad, C-V measurements were conducted in the -5 V to 5 V range. The dielectric constant versus the voltage, plotted in **Figure 155**, was calculated from C-V data. The dielectric constant did show not any variations or non-linearities. This reflects that the measured HZO film is not ferroelectric, as the butterfly shape did not appear, but only dielectric. The dielectric nature is direct implication of the dominance of the nonpolar m-phase as shown in XRD patterns. Even for the 10 nm, the dominance of the o-phase is not reflected in C-V results. It indicates the role of the capping layer for the electrical measurements as it acts as a tensile stressor on the HZO layer to stabilize the appeared o-phase in XRD patterns [175].

The I-V measurements shown the leakage behavior of the stack. They indicate better leakage values compared to the capping layer stack. The results are illustrated in **Figure 156**.

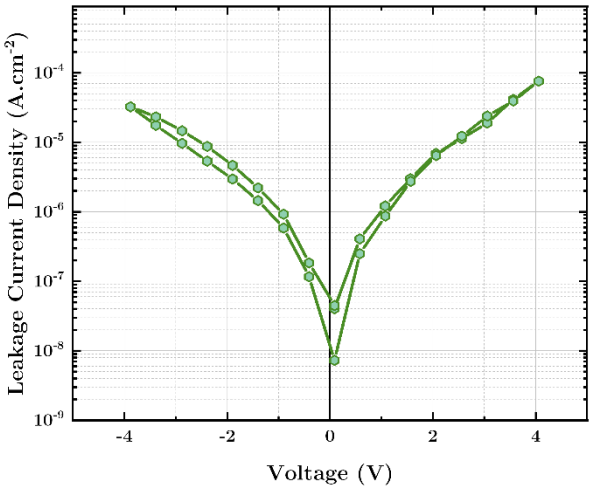

Figure 156 The I-V of HZO stack W/O capping

At 4 V, the leakage current density is 10^{-4} A.cm^{-2}. This result reflects the dominance of the m-phase and the finding of the C-V results.

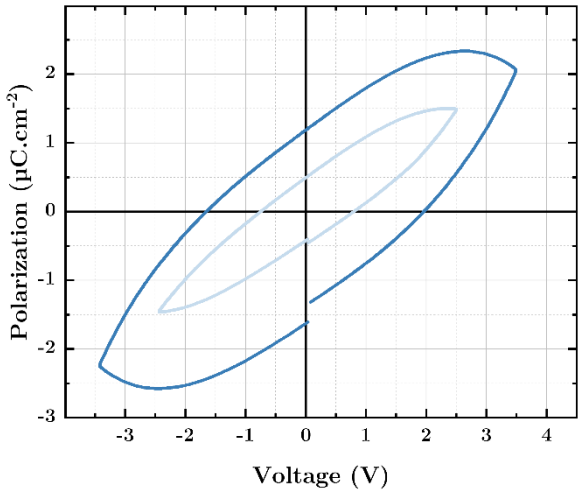

Figure 157 P-E loops of HZO stack W/O capping

The XRD and C-V results indicated no signature of ferroelectricity in the HZO stacks without capping layer during RTA. The P-V measurements were conducted to confirm the correlation with these techniques' findings. At 2.5 V, we found a lossy capacitor behavior and the loop has no hysteretic shape. As the voltage increases, the loop became larger reflecting lossier capacitor behavior. No ferroelectric hysteresis loops appeared for both measurements and for the four samples. This agrees with the previous findings suggesting that the existence of the top electrode is mandatory to correlate the structural and electrical signatures. It implies the capping effect of the TiN TE playing the tensile stressor as mentioned above.

5.2.4 Conclusion

In this part, we confirmed by electrical measurement the ferroelectric nature of sputtered HZO film. This indicates the exactness of the structural characterizations and the relationship between the o—phase dominance and the hysteretic loop of polarization measurements. The role of capping layer during RTA was investigated also. Despite the apparition of the o-phase in structural results, the capping layer is required to obtain electrical signatures of ferroelectricity within HZO films.

5.3 Temperature-dependent dielectric properties of HZO capacitors without capping during the thermal annealing

5.3.1 Introduction

In this part, the aim was to experimentally determine the ferroelectric-paraelectric phase transition temperature of HZO films and investigate the temperature-dependence

of its dielectric properties. To our knowledge, no paper reported the curie temperature of HZO films.

We performed the temperature measurements on two samples with 35 and 66 nm thicknesses of HZO film from room temperature to 550°C. HZO films were sputtered on TiN bottom electrodes. Then, the stack was annealed at 650 °C for 1 min under N_2. The measurement was conducted in G2E Lab, using an impedance analyzer with Linkam temperature control system. The 10 nm sample was tested using Aixacct TF 3000 analyzer with temperature limit of 350°C.

Among the electrical measurement of the previous part, we used only impedance and C-V measurements only. through C-V results, we can observe the evolution of the dielectric constant as function of temperature and the other parameters. This evolution leads to the determination of the ferroelectric-paraelectric phase transition order.

The temperature dependence of the dielectric constants for different HZO samples is established by measuring the device capacitance during heating and cooling phases.

We have tested three samples of different thicknesses: 11, 35, and 66 nm. The difference in thickness gives insight about the thickness-dependence of the transition temperature.

The first sample, of 11 nm, was tested in TF 3000 Aixacct analyzer. The heat of the equipment has a limit temperature of 350°C and the cooling is natural. As we had no idea about the transition temperature. The first step was to conduct the measurement in the range from room temperature to 350°C. We measured the capacitance at 11 values of temperature in the [25, 350°C].

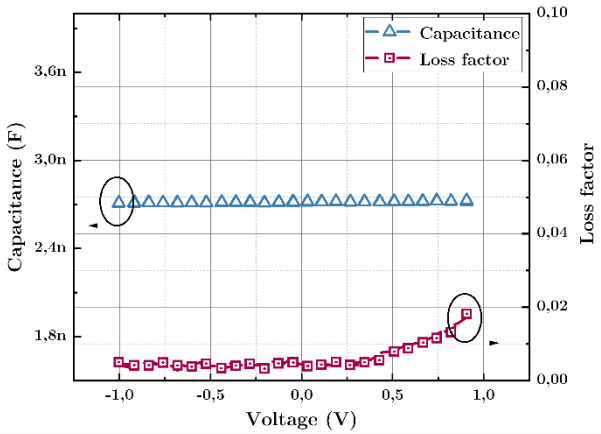

Figure 158 The C-V and loss factor versus voltage at room temperature

Before launching the heating phase, we measured the capacitance and loss factor variations versus voltage, as illustrated in **Figure 158**. The capacitance is constant

between -1V and 1V. this plot is a reference to re-measure the capacitance after cooling. For each measurement temperature, we varied the voltage between -1 and 1V. As expected, the capacitance, dielectric constant, are steady until 100 °C. Then, it increased as the temperature reached 350 °C. at 350 °C, the dielectric constant increased to 29. As no decrease of dielectric constant occurred, one can speculate that the transition temperature is higher than 350 °C. This is a first information about HZO phase transition temperature.

The loss factor has the same tendency of increasing with temperature. It reached 25 % at 350 °C. Both dielectric constant and loss factor are plotted in **Figure 159**.

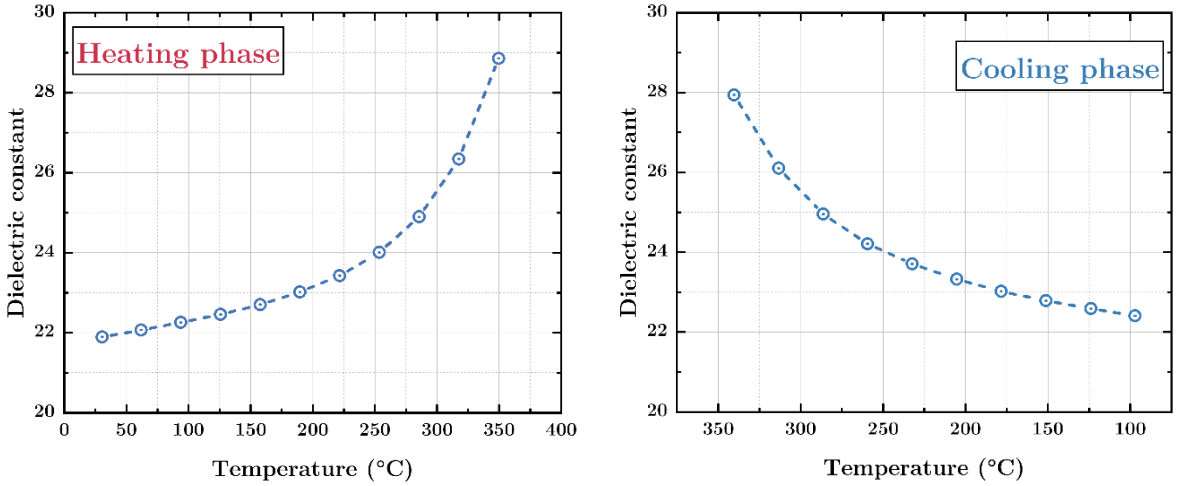

Figure 159 Dielectric constant versus temperature – heating and cooling phases

The second phase of the measurement consisted of remeasuring the dielectric constant variation as the temperature cools down. The cooling was not controlled. The measurement is launched once the temperature is reached. The variation of dielectric constant versus temperature is plotted in **Figure 160**.

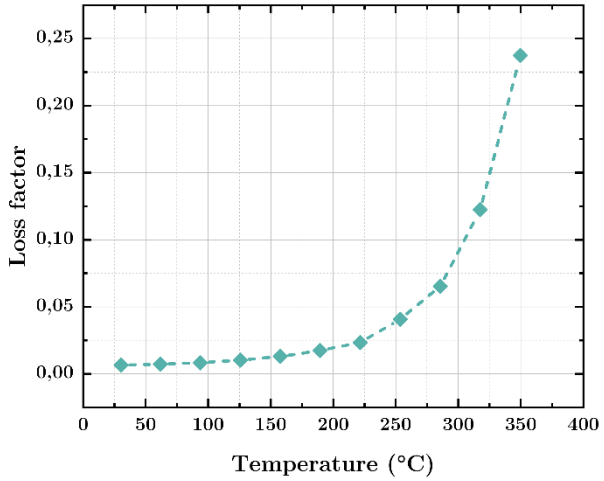

Figure 160 Loss factor versus temperature - cooling

As expected, the temperature-dependence of dielectric constant is confirmed as the dielectric constant decreased exponentially. The dielectric constant value after cooling down, is the same as the reference. The dielectric constant evolutions versus temperature in the two phases are gathered in **Figure 161**.

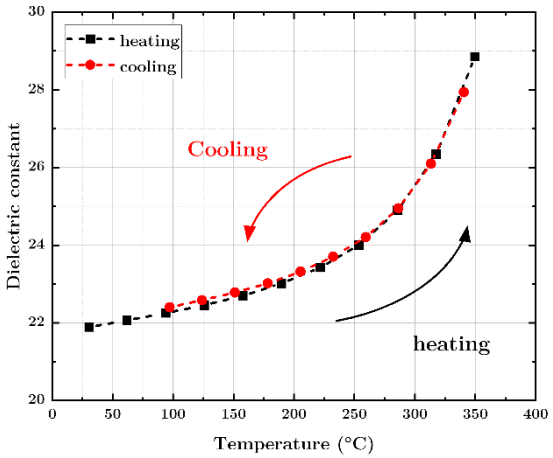

Figure 161 Variation of dielectric constant – heating and cooling

Another parameter was measured to observe the tendency of polarization. It was measured at 250°C and 350°C during heating. Both curves, illustrated in **Figure 162**, show a difference in the shape of P-V loop. As the temperature increases, the P-V loop became larger and P_r value increased to 0.8 µC.cm^{-2}. During the cooling, the same P-V shape was recovered.

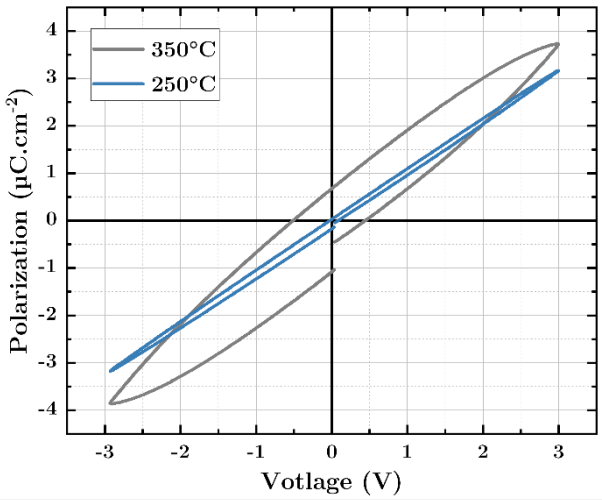

Figure 162 Hysteresis loop at 250 and 350°C

At 350°C, we performed the cycling to check any polarization improvement. The polarization increased as function of the number of cycles, as shown in **Figure 163**, from

0.8 to 1.2 µC.cm^{-2} after 10^6 cycles suggesting the possible existence of wake up phemenon to increase the polarization of HZO films.

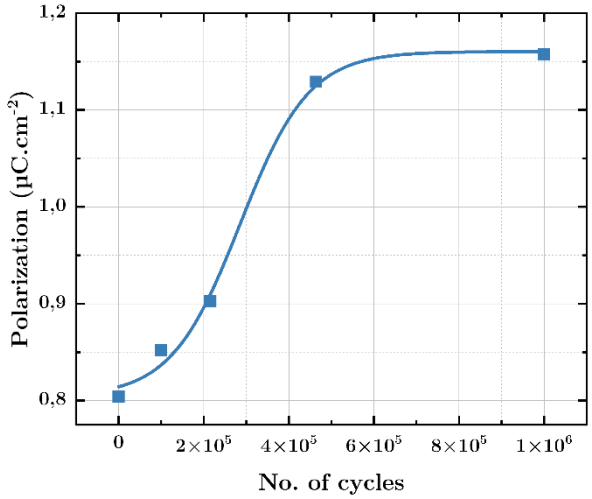

Figure 163 Cycling of the device at 350°C

Higher range of temperature was required to determine the phase transition temperature accurately. We used another equipment, at G2E Lab, with a temperature limit of 550°C.

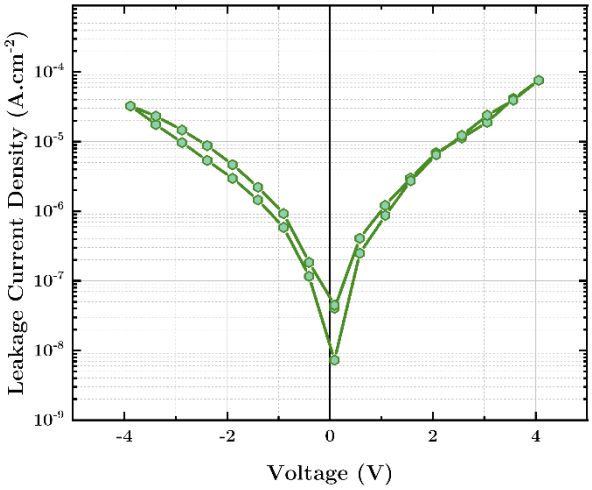

Figure 164 J-V measurement of the 35 nm device

Thicker film was investigated of 35 nm thickness. The leakage current before the temperature measurements indicated a density of 10^{-4} A.cm^{-2} at 4V. The I-V characteristics were measured by applying controlled linear sweep voltage on the TE electrode from 0 V → +4 V → -4 V → 0 V, while the BE was grounded. This non-Ohmic I-V characteristic loop and switching under the 0.1 mA compliance current confirm the device's non-leaky characteristics. Under high voltage, these I-V scans may show a

complex interplay of contributions from defects, ion migration, ferroelectricity, and possibly even interface effects.

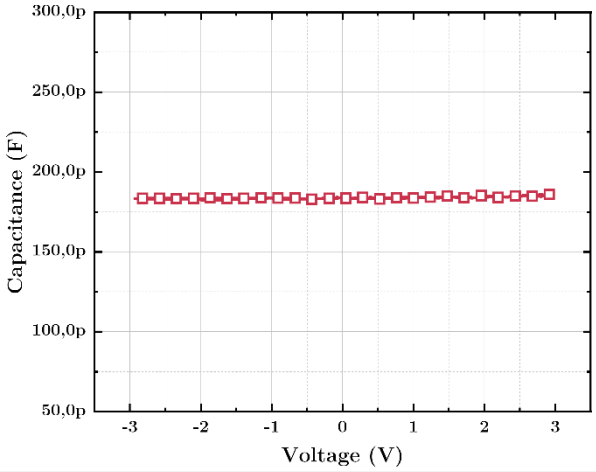

Figure 165 Capacitance versus voltage measured at room temperature

First, we measured the capacitance in the voltage range of -3 to +3V. The capacitance is constant along the voltage range suggesting that the material is mainly dielectric in good agreement with XRD results where the monoclinic phase is the dominant.

Before launching the temperature measurements, we measured the dielectric constant in the frequency range of 0.1-10^6 Hz. The dielectric constant is almost constant until 100 kHz when it decreased abruptly. We conducted the measurement at 1 kHz. In the same range, the loss factor was constant before increasing exponentially around 100 kHz. The dielectric constant and loss factor variations versus frequency are plotted in **Figure 166**.

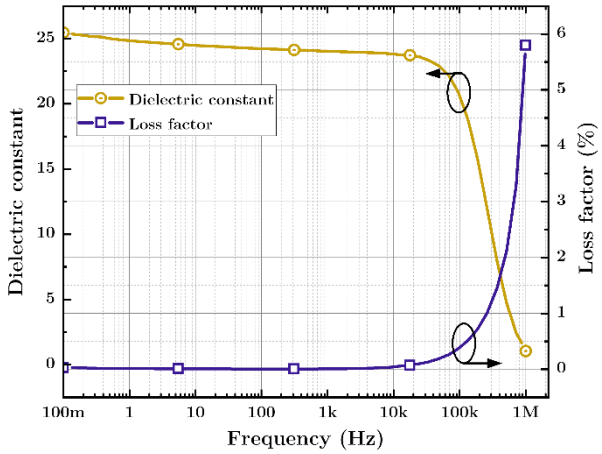

Figure 166 Dielectric constant and loss factor versus frequency

The impedance and phase versus frequency are illustrated in **Figure 167.** The slope of impedance confirms the capacitive nature of the films. No anomalies have been observed. We studied the variation of dielectric constant, loss factor, conductance, and impedance as function of temperature.

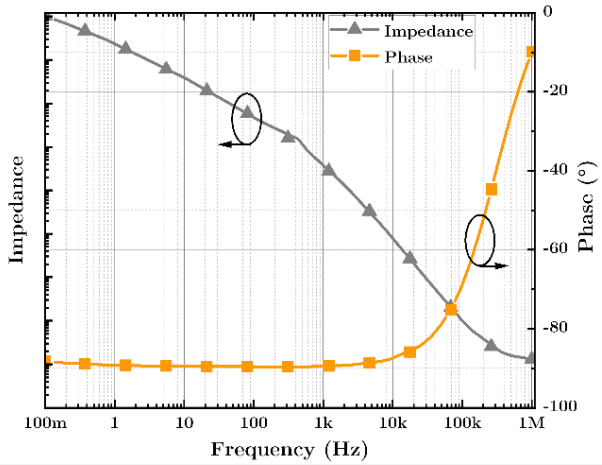

Figure 167 Impedance versus frequency

As the same as the 10 nm sample, the loss factor, presented in **Figure 154**, shows the same tendency until 350 °C. Above this temperature, the loss factor reached its maximum at 460°C, then it started to decrease despite the increase of temperature. The dielectric constant increased until 350 °C before starting to decrease to its minimum at 440 °C. and it started to decrease. This variation was not expected.

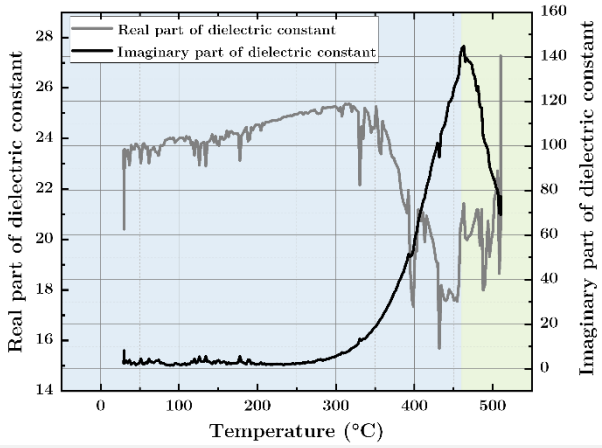

Figure 168 Dielectric constant and loss factor versus temperature

We checked the variation of the other parameters versus temperature: conductance and impedance. Both parameters are peaking at 460 °C, as shown in **Figure 169**. This switching is a characteristic of the ferroelectric-paraelectric phase transition, in total

agreement with the 10 nm findings, in which the phase transition temperature is higher than 350 °C.

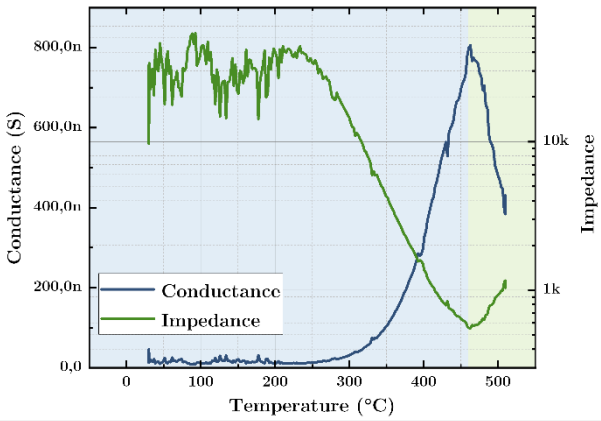

Figure 169 Conductance and impedance versus temperature

A third sample of 66 nm thickness was characterized in order to check the tendency. In **Figure 170**, the expected variation of dielectric constant versus temperature is found. The results are clearer compared to the previous sample, suggesting that the latter's findings are due to experimental setup. The dielectric constant peaking is shifted to 440 °C compared to the other parameters peak, which occurred at 480 °C. During the cooling phase, the dielectric constant decreased as expected with small peaks only.

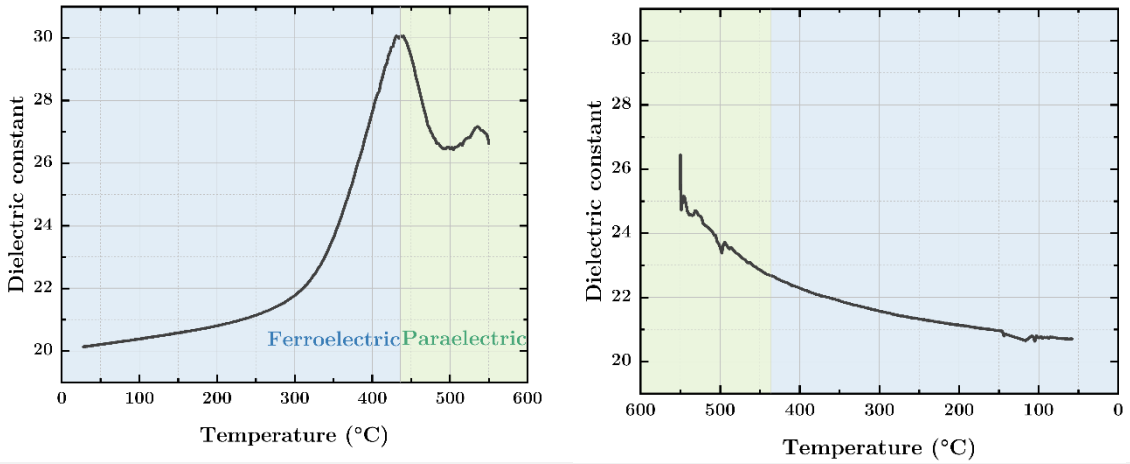

Figure 170 Dielectric constant and loss factor versus temperature

The shift in the phase transition temperature can be explained by the different fractions of the monoclinic and orthorhombic phases for the two samples. Further studies are required to investigate the impact of the phases' contribution to the phase transition temperature. The range of the phase transition temperature is between 440 and 480 °C. The phase transition temperature is thickness dependent.

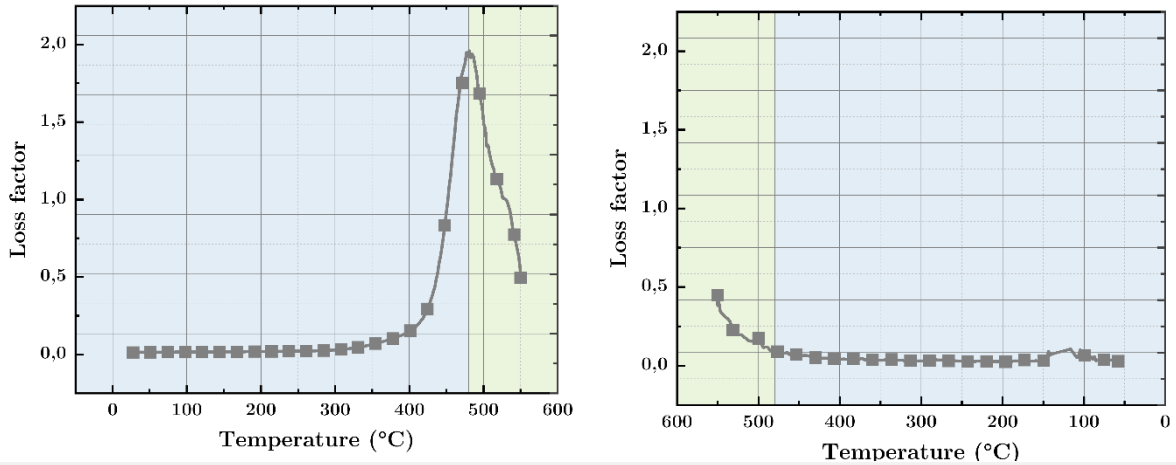

Figure 171 Loss factor variation versus temperature

The evolution of the loss factor indicates the same tendency but peaking at 480 °C. The loss factor is invariant until 300 °C before increasing to its maximum at 480 °C then started to decrease until 550 °C. At the cooling phase, the same tendency is found with small peaks as the temperature decreased. This finding confirms the previous conclusions.

5.3.2 Discussion

The scan of capacitance variation in a voltage range shows a constant linear value as the voltage varies between positive and negative values. For the three samples, the capacitance is constant along the voltage range. This capacitive behavior is correlated with the dominant monoclinic phase in XRD patterns for the 35 and 66 nm samples. Despite that the o-phase is dominant for the 10 nm sample, the capacitance is constant. We recall that the three samples were annealed without capping layer. The C-V measurements were performed over capacitors with different areas and the same behavior was revealed. This capacitance reveals the correlation with the structural results and the importance of the top electrode during annealing despite the apparition of the orthorhombic phase as a dominant phase. It is related to the stress and surface energy required to obtain ferroelectricity.

Below 25 nm, the o-phase is preferred, above 25 nm, the monoclinic phase is less dominant. This is quite confirmed by literature and structural hints reported in the previous chapter. The dielectric constant was almost the same for the different samples. It is around 20 corresponding to the monoclinic phase dominant contribution.

The investigation of the capacitance versus frequency, in larger range, confirmed the frequency-dependence of HZO capacitors. The larger range cancelled the anomalies recorded before. The capacitance is almost constant in the 0.1 to 100 kHz range. For the

three samples, we picked the 1 kHz value for the measurements. Above 100 kHz, the capacitance and loss factor started to decrease and increase, respectively.

Conducting the C-V measurements, as the temperature increased up to 350 °C, revealed that the Curie temperature is higher than 350 °C as the dielectric constant increased without any noticeable decrease as expected. The same values of the dielectric constant were found during the cooling phase from 350 °C to 70 °C. the other parameters shown the same tendency versus the temperature increase. These parameters can also be an indicator of the phase transition temperature.

Extending the temperature range to 550°C indicated that phase transition temperature is around 460 °C as can be seen in the variations of loss factor and conductance except the dielectric constant which presents an unexpected behavior. It increased then decreased abruptly before increasing again to its maximum. One can speculate that this anomaly occurred inside the experimental setup. One can say that the 460°C is the transition temperature as can be shown by the loss factor and conductance. This anomaly of dielectric constant, for the 35 nm sample, was eliminated as the phase transition temperature was confirmed by the 66 nm sample.

This phase transition temperature range is consistent with reported values for HfO_2, ZrO_2 and Y-doped HfO_2 [228], [267]. The shape of dielectric constant-temperature plot revealed that the phase transition is 2^{nd} second order phase transition. This finding illustrates the confusion in the literature about the phase order phase transition for HZO ferroelectrics [268], [269]. The phase transition temperature is thickness independent.

We remind that the polarization measurement was conducted on the 10 nm sample only. The cycling shows that the polarization can be improved by cycling. The measured samples were all in pristine state.

5.3.3 Conclusion

The Curie temperature is an also important ferroelectric nature from both scientific and industrial viewpoints. To further confirm this phase transition, we performed temperature-dependent dielectric constant measurement on our samples. The measurement was performed at frequency of 1 kHz. The dielectric constant measurement shows a sudden increase around the expected Curie Temperature of ~450℃, which is consistent with the results reported for HfO_2 and ZrO_2. This result suggests the existence of phase transition around the temperature regime. Such sharp increase of dielectric constant is a main signature of ferroelectric phase transition, which thus further affirms our previous findings. This study reveals that the HZO films are promising for various

ferroelectric applications because of their comparable ferroelectric properties including polarization and Curie temperature to conventional ferroelectric materials.

Further studies are required to study the possible affecting factors such as cooling and heating rates, the contribution of different phases, the thickness of HZO, on shifting the phase transition temperature.

Dissertation conclusion

This thesis consists of **two** main complementary pillars. The first main goal was a sustainable assessment of the choice of dielectric and electrodes materials in addition to the deposition techniques to understand the context of sustainability in microelectronics. The second one was to study the structural properties of HZO thin films obtained by single target sputtering and all the related parameters. Based on this understanding, advanced structural characterizations have been employed to reveal the structural origin of ferroelectricity within HZO thin films.

It was demonstrated that single-target sputtering (PVD) can be used in order to meet CMOS BEOL fabrication requirements for production of HZO ferroelectric thin films with conventional TiN electrodes. The fabrication process referred to deeper investigation of the thermal processing step to meet the CMOS requirements. Confirmed by similar findings reported in literature later, first hints of the apparition of the orthorhombic phase were revealed below 500 °C. By extending the thermal processing time, it was possible to obtain stable orthorhombic phase at 370 °C, that remained stable during the cooling to room temperature. This result suggested more options for the sputtered HZO compared to ALD-deposited HZO films.

Due to the lack in literature, this thesis represents a first step paving the way for deeper investigations, and it would be interesting to extend the studies to other parameters related to the sputtering, target's composition, or sputtering-annealing cycles. It would make the sputtering gain more competitiveness compared to ALD.

Whether deposited by ALD or PVD, the choice of HZO remains sustainable and more preferred over PZT for the future in terms of sustainability, adequation with CMOS process, and the fabrication nodes. More and more integrations are being published based on HZO films that promising as sustainable material for the microelectronics industry meeting the environment requirements at both fabrication and end consuming levels. Forecasts of hafnium and zirconium markets indicate that higher production is expected which means that both are not critical.

Sharing the same deposition technique for both dielectric layer and electrodes can be a reason to have excellent ferroelectric properties without vacuum breaking between the three steps.

The optimization of sputtering parameters revealed unbalanced impact of the sputtering. The most important parameters are the deposition pressure, the oxygen partial pressure, and the sputtering power. Their effects on the interfaces are still needed to be studied in order to improve interface quality, which has a critical impact on ferroelectric properties. In this regard, an encouraging path to optimize and realize the TiN-HZO-TiN structure without vacuum breaking is targeted to obtain excellent ferroelectric properties.

The findings within this thesis will help moving forward the understanding of the sputtering of HZO films, TiN electrodes, and their structural and electrical properties after the rapid thermal processing on the one hand. On the other hand, these findings will pave the way for deeper investigations to improve the ferroelectric properties of HZO for thicker films and wider range of applications.

After the dense structural characterizations and the confirmed ferroelectric behavior, the obtained results of the HZO films deposited by single target sputtering are comparable with the state-of-the-art, sputtered hafnia-based ferroelectrics, in terms of polarization and the observed wake up effect. Despite that the ALD-deposited hafnia ferroelectrics present higher polarization values, the sputtered HZO has a great potential to reach the same level of performance and might exceed the state-of-the-art if a successful in-situ fabrication of TiN/HZO/TiN stacks is realized. The sputtering technique paves the way for thicker integrated HZO films for pyroelectric and piezoelectric applications.

With the few references and precedents about HZO single target sputtering, at the beginning of this work, we could optimize the main parameters of HZO sputtering and yet there are more secondary parameters that can make HZO more flawless compared to ALD-deposited films.

While ferroelectric HZO films deposited by different techniques is an open challenge, there is also a parallel challenge in ferroelectric characterizations at the nanoscale for HZO films. One of the challenges is the characterization of the ferroelectric switching by PFM, which is a hot topic within the ferroelectric community. Another challenge is the identification of the orthorhombic phase separately from the tetragonal phase. On this, we could be completely sure about having only the orthorhombic phase without any tetragonal phase traces. Despite having 100 % orthorhombic phase, other parameters such as the oxygen vacancies or the interfacial quality can downgrade the quality of HZO films.

The ferroelectric properties of are dominating on the research interest about HZO films Meanwhile, the dielectric properties can attract more interest and lead to the integration of HZO for its high-k similar properties.

A surprising apparition of copper within HZO films might have a great interest if it is well studied for from an electrical point of view.

In outlook, HZO-based ferroelectrics show an unavoidable potential for further enhancement of future IoT sustainable devices. Ferroelectric films of small thicknesses by different techniques have been reported and this work suggests that there is more space to investigate the sputtering of HZO ferroelectrics to scale up accordingly with piezoelectric applications. It is strongly believed that the techniques and approaches addressed in this work will contribute to the exploration of these fascinating properties in the aim of establishing new era of sustainable and powerful ferroelectric, pyroelectric, and piezoelectric devices.

Perspectives

HZO has a very high potential to meet all the beyond-Moore era requirements. The perspectives of this work can be extended due the ferroelectric properties, that keep attracting the main research and industrial players in the world. Various applications are being made possible due to these promising properties of HZO.

Additional deposition techniques such as the high impulse sputtering can reduce the inconvenient of HZO sputtering and realize a breakthrough for 100 nm thick HZO piezoelectric films. Also, spatial ALD is a good compromise between sputtering and ALD combining the advantages of both.

TEM-ASTAR, EBSD, PFM characterizations of sputtered HZO films can reveal more about the switching properties of ferroelectric ultrathin films.

HZO is rarely investigated as a dielectric. It is worthy to be studied thoroughly besides the doping of HZO. Copper doping of HZO is worthy to be studied for electrodes' role besides the copper doping does not change the optical properties in the visible range, being a possible transparent conductor material. Also, Y-HZO was reported to be ferroelectric also. Quaternary target sputtering can be more challenging and interesting at the same time.

For thicker films, deposition-annealing cycles, and intermittent sputtering might be worthy for thicker ferroelectric and piezoelectric HZO films for sensing and actuating applications. Magnetic properties of HZO are investigation-worthy allowing HZO to be ferroic. Additionally, investigating the annealing pressure can be a key factor to meet the CMOS requirements for all dopants of HfO_2. We suspect that in-situ realization of HZO-based stacks might lead to increasing the thickness limit for ferroelectricity within HZO, besides, It might allow other electrode' materials to be functional with HZO.

The study was focused on MIM structure, other structures such as MFIS can be beneficial for negative capacitance applications

Future integrations of HZO into microelectronics devices shall confirm its superiority over PZT in both sustainable and performance sides. Especially, deeper investigation of the phase transition temperature is so important for pyroelectric and CMOS applications.

Bibliography

[1] Statista Research Department, « Internet of Things (IoT) connected devices installed base worldwide from 2015 to 2025 », 2021. [En ligne]. Disponible sur: https://www.statista.com/statistics/471264/iot-number-of-connected-devices-worldwide/

[2] C. Freitag, K. Widdicks, B. Knowles, et G. Blair, « The climate impact of ICT: A review of estimates, trends and regulations », p. 87.

[3] E. Williams, « Environmental effects of information and communications technologies », *Nature*, vol. 479, n° 7373, p. 354-358, nov. 2011, doi: 10.1038/nature10682.

[4] P. A. Wäger, R. Hischier, et R. Widmer, « The Material Basis of ICT », in *ICT Innovations for Sustainability*, vol. 310, L. M. Hilty et B. Aebischer, Éd. Cham: Springer International Publishing, 2015, p. 209-221. doi: 10.1007/978-3-319-09228-7_12.

[5] J. Malmodin et V. Coroama, « Assessing ICT's enabling effect through case study extrapolation — The example of smart metering », in *2016 Electronics Goes Green 2016+ (EGG)*, Berlin, sept. 2016, p. 1-9. doi: 10.1109/EGG.2016.7829814.

[6] C. Håkansson et G. Finnveden, « Indirect rebound and reverse rebound effects in the ICT-sector and emissions of CO2 »:, présenté à EnviroInfo and ICT for Sustainability 2015, Copenhagen, Denmark, 2015. doi: 10.2991/ict4s-env-15.2015.8.

[7] *Directive 2002/95/EC of the European Parliament and of the Council of 27 January 2003 on the restriction of the use of certain hazardous substances in electrical and electronic equipment*, vol. OJ L 37, 13.2.2003,. p. 19-23. [En ligne]. Disponible sur: https://eur-lex.europa.eu/legal-content/EN/TXT/?uri=celex%3A32002L0095

[8] T. S. Böscke, J. Müller, D. Bräuhaus, U. Schröder, et U. Böttger, « Ferroelectricity in hafnium oxide thin films », *Applied Physics Letters*, vol. 99, n° 10, p. 102903, sept. 2011, doi: 10.1063/1.3634052.

[9] F. Ye *et al.*, « Emergent properties at oxide interfaces controlled by ferroelectric polarization », *npj Comput Mater*, vol. 7, n° 1, p. 130, déc. 2021, doi: 10.1038/s41524-021-00601-w.

[10] W. Gao, Y. Zhu, Y. Wang, G. Yuan, et J.-M. Liu, « A review of flexible perovskite oxide ferroelectric films and their application », *Journal of Materiomics*, vol. 6, n° 1, p. 1-16, mars 2020, doi: 10.1016/j.jmat.2019.11.001.

[11] P. Kumari, ;Ashutosh Tiwari, R. Rai, S. Sharma, M. Shandilya, et and Ashutosh Tiwari, « State-of-the-art Of Lead Free Ferroelectrics: A Critical Review », *Adv. Mater. Lett.*, vol. 6, n° 6, p. 453-484, juin 2015, doi: 10.5185/amlett.2015.4086.

[12] Y. H. Lee *et al.*, « Preparation and characterization of ferroelectric $Hf_{0.5}Zr_{0.5}O_2$ thin films grown by reactive sputtering », *Nanotechnology*, vol. 28, n° 30, p. 305703, juill. 2017, doi: 10.1088/1361-6528/aa7624.

[13] T.-H. Ryu, D.-H. Min, et S.-M. Yoon, « Comparative studies on ferroelectric switching kinetics of sputtered $Hf_{0.5}Zr_{0.5}O_2$ thin films with variations in film thickness and crystallinity », *Journal of Applied Physics*, vol. 128, n° 7, p. 074102, août 2020, doi: 10.1063/5.0013487.

[14] J. Bouaziz, P. Rojo Romeo, N. Baboux, et B. Vilquin, « Imprint issue during retention tests for HfO_2-based FRAM: An industrial challenge? », *Appl. Phys. Lett.*, vol. 118, n° 8, p. 082901, févr. 2021, doi: 10.1063/5.0035687.

[15] U. Secretary-General et W. C. on E. and Development, « Report of the World Commission on Environment and Development »:, août 1987, 2021. [En ligne]. Disponible sur: https://digitallibrary.un.org/record/139811
[16] « The concept of sustainability. A birth from the forest. », *zeroCO2*. https://zeroco2.eco/en/2021/09/14/birth-sustainability-concept/.
[17] « United Nations Population Division | Department of Economic and Social Affairs ». https://www.un.org/en/development/desa/population/migration/generalassembly/sessions/index.asp?A60.
[18] « Dimensions of Sustainability - Prakati India ». https://www.prakati.in/dimensions-of-sustainability/.
[19] « THE 17 GOALS | Sustainable Development ». https://sdgs.un.org/goals.
[20] « Sustainable Development - an overview | ScienceDirect Topics ». https://www.sciencedirect.com/topics/engineering/sustainable-development
[21] « Turning to sustainable global business: 5 things to know about the circular economy », *UN News*, 13 juin 2021. https://news.un.org/en/story/2021/06/1093802.
[22] « 2021_Sustainability report (2020 performance) », p. 96.
[23] « Volkswagen Group Sustainability Report ». https://www.volkswagenag.com/en/sustainability/reporting.html
[24] « Environment », *Apple*. https://www.apple.com/environment/
[25] « TSMC Becomes the World's First Semiconductor Company to Join RE100, Committed to 100% Renewable Energy Usage ». https://esg.tsmc.com/en/update/greenManufacturing/caseStudy/37/index.html.
[26] « Supplier Program to Accelerate Responsibility & Commitment (SPARC) », *Intel*. https://www.intel.com/content/www/us/en/supplier/social/sparc.html.
[27] « ST Approach to Sustainability - STMicroelectronics ». https://www.st.com/content/st_com/en/about/st_approach_to_sustainability/st_approach_to_sustainability.html.
[28] « Does sustainability sell? The impact of sustainability claims on the success of national brands' new product introductions - ScienceDirect ». https://www.sciencedirect.com/science/article/pii/S0148296321005889.
[29] A. King, *Critical materials*. Cambridge: Elsevier, 2020.
[30] « EUR-Lex - 52020DC0474 - EN - EUR-Lex ». https://eur-lex.europa.eu/legal-content/EN/TXT/?uri=CELEX%3A52020DC0474.
[31] T. Web, *The Periodic Table of Elements*. 2021. [En ligne]. Disponible sur: https://github.com/tamalweb/periodic-table
[32] « The Most Abundant Elements In The Earth's Crust », *WorldAtlas*, 5 novembre 2020. https://www.worldatlas.com/articles/the-most-abundant-elements-in-the-earth-s-crust.html.
[33] R. Adams, « Review of zirconium », *Mining Engineering*, 2012.
[34] R. Towner, « International Strategic Minerals Inventory Summary Report–zirconium. US Government Printing Office », Circular, 1992.
[35] J. J. Moore, « W. J. KROLL: "A METALLURGIST OF THE UNUSUAL: THE AMPHIBIOUS AND RECALCITRANT LONE WOLF RESEARCHER" », p. 17.
[36] D. Coster et G. Hevesy, « On the Missing Element of Atomic Number 72 », *Nature*, vol. 111, n° 2777, p. 79-79, janv. 1923, doi: 10.1038/111079a0.

[37] R. P. Cox et G. H. Beyer, « SEPARATION OF HAFNIUM FROM ZIRCONIUM USING TRIBUTYL PHOSPHATE », ISC-682, 4366895, oct. 1956. doi: 10.2172/4366895.
[38] « Critical raw materials ». https://ec.europa.eu/growth/sectors/raw-materials/areas-specific-interest/critical-raw-materials_en.
[39] ILUKA, « Mineral Sands Products: Attributes and Applications », 2011.
[40] A. Manhique, « Optimisation of alkali-fusion process for zircon sands: A kinetic study of the process », University of Pretoria, 2003.
[41] N. T. Nassar, T. E. Graedel, et E. M. Harper, « By-product metals are technologically essential but have problematic supply », *Sci Adv*, vol. 1, n° 3, p. e1400180, avr. 2015, doi: 10.1126/sciadv.1400180.
[42] « Dubbo Project », *ASM*. https://asm-au.com/projects/dubbo-project/.
[43] M. Aoyagi, « The impact of the Fukushima accident on nuclear power policy in Japan », *Nat Energy*, vol. 6, n° 4, p. 326-328, avr. 2021, doi: 10.1038/s41560-021-00818-5.
[44] R. and Markets, « Global Zirconium and Hafnium Market Review 2014/2015 with Market Volume Predictions and Prices Trends to 2019 ». https://www.prnewswire.com/news-releases/global-zirconium-and-hafnium-market-review-20142015-with-market-volume-predictions-and-prices-trends-to-2019-300067720.html.
[45] « Mineral Commodity Summaries », 2021.
[46] « How COVID-19 will affect semiconductor demand in 2021 | McKinsey ». https://www.mckinsey.com/industries/advanced-electronics/our-insights/how-the-semiconductor-industry-can-emerge-stronger-after-the-covid-19-crisis.
[47] G. Jones, « Mineral Sands: An Overview of the Industry », *ILUKA*, 2009.
[48] « (PDF) Review of High Temperature Ceramics for Aerospace Applications ». https://www.researchgate.net/publication/287972274_Review_of_High_Temperature_Ceramics_for_Aerospace_Applications.
[49] « Appraising the potential of Zr-based biomedical alloys to reduce magnetic resonance imaging artifacts | Scientific Reports ». https://www.nature.com/articles/s41598-020-59247-1.
[50] Ş. Sadik, F. Durak, M. Paul, N. F. Zulkipli, A. Altuncu, et S. Harun, « Gain-clamping in L-band zirconium–erbium co-doped fiber amplifier with FBG based lasing control », *Microwave and Optical Technology Letters*, oct. 2021, doi: 10.1002/mop.33067.
[51] « Zirconium's essential role in nuclear engineering | Zircon Industry Association ». https://www.zircon-association.org/zirconium%E2%80%99s-essential-role-in-nuclear-engineering.html.
[52] « Electrochemical Analysis of Hydrogen Membrane Fuel Cells with Amorphous Zirconium Phosphate Thin Film Electrolyte ». https://www.jstage.jst.go.jp/article/electrochemistry/82/10/82_14-E00046/_article/-char/ja/.
[53] Staff, « A pinch of hafnium could extend life of turbine blades », *Machine Design*, mai 2005. https://www.machinedesign.com/news/article/21812200/a-pinch-of-hafnium-could-extend-life-of-turbine-blades.

[54] « Hafnium Alloys: Part Two :: Total Materia Article ». https://www.totalmateria.com/page.aspx?ID=CheckArticle&site=ktn&LN=NO&NM=297.

[55] R. Froese, P. Hustad, R. Kuhlman, et T. Wenzel, « Mechanism of Activation of a Hafnium Pyridyl−Amide Olefin Polymerization Catalyst: Ligand Modification by Monomer », *Journal of the American Chemical Society*, vol. 129, p. 7831-40, juill. 2007, doi: 10.1021/ja070718f.

[56] A. Huang, Z. Yang, et P. Chu, « Hafnium-Based High-k Gate Dielectrics », in *Advances in Solid State Circuits Technologie*, 2010. doi: 10.5772/8631.

[57] M. Panzer *et al.*, « Thermal Properties of Ultrathin Hafnium Oxide Gate Dielectric Films », *Electron Device Letters, IEEE*, vol. 30, p. 1269-1271, janv. 2010, doi: 10.1109/LED.2009.2032937.

[58] « Phys. Rev. 92, 1527 (1953) - Neutron Absorption and Scattering by Hafnium ». https://journals.aps.org/pr/abstract/10.1103/PhysRev.92.1527.

[59] « Physical and Electrical Properties of Hafnium–Zirconium–Oxide Films Grown by Atomic Layer Deposition - IOPscience ». https://iopscience.iop.org/article/10.1149/1.2945908.

[60] K. Ukoba, A. Eloka-Eboka, et F. Inambao, « Review of nanostructured NiO thin film deposition using the spray pyrolysis technique », *Renewable and Sustainable Energy Reviews*, vol. 82, nov. 2017, doi: 10.1016/j.rser.2017.10.041.

[61] « REACH Legislation - ECHA ». https://echa.europa.eu/regulations/reach/legislation.

[62] F. Klocke, N. Kramer, R. Grüter, B. Döbbeler, H. M. Binder, et D. Lung, « Ecological Evaluation of PVD and CVD Coating Systems in Metal Cutting Processes », Universitätsverl. d. TU, RWTH-CONV-203831, 2013.. [En ligne]. Disponible sur: https://publications.rwth-aachen.de/record/226357

[63] M. Quirk et J. Serda, *Semiconductor manufacturing technology*. Upper Saddle River, NJ: Prentice Hall, 2001.

[64] « Sputtering Materials for VLSI and Thin Film Devices - 1st Edition ». https://www.elsevier.com/books/sputtering-materials-for-vlsi-and-thin-film-devices/sarkar/978-0-8155-1593-7.

[65] R. and Markets, « Insights on the Sputtering Targets and Sputtered Films Global Market to 2026 - Key Drivers and Restraints ». https://www.prnewswire.com/news-releases/insights-on-the-sputtering-targets-and-sputtered-films-global-market-to-2026---key-drivers-and-restraints-301387047.html.

[66] R. Kishore et S. J. Priya, « A Review on Low-Grade Thermal Energy Harvesting: Materials, Methods and Devices », *Materials*, vol. 11, p. 1433, août 2018, doi: 10.3390/ma11081433.

[67] « Introduction to Solid State Physics, 8th Edition | Wiley », *Wiley.com*. https://www.wiley.com/en-us/Introduction+to+Solid+State+Physics%2C+8th+Edition-p-9780471415268.

[68] « Thermodynamics of Ferroelectricity | SpringerLink ». https://link.springer.com/chapter/10.1007/978-0-387-76540-2_1.

[69] M. H. Park, Y. H. Lee, T. Mikolajick, U. Schroeder, et C. S. Hwang, « Thermodynamic and Kinetic Origins of Ferroelectricity in Fluorite Structure Oxides », *Advanced Electronic Materials*, vol. 5, n° 3, p. 1800522, 2019, doi: 10.1002/aelm.201800522.

[70] P. Chandra et P. B. Littlewood, « A Landau Primer for Ferroelectrics », in *Physics of Ferroelectrics: A Modern Perspective*, Berlin, Heidelberg: Springer, 2007, p. 69-116. doi: 10.1007/978-3-540-34591-6_3.

[71] A. P. Levanyuk, I. Burc Misirlioglu, et M. Baris Okatan, « Landau, Ginzburg, Devonshire and others », *Ferroelectrics*, vol. 569, n° 1, p. 310-323, déc. 2020, doi: 10.1080/00150193.2020.1822684.

[72] A. F. Devonshire, « Theory of ferroelectrics », *Advances in Physics*, vol. 3, n° 10, p. 85-130, avr. 1954, doi: 10.1080/00018735400101173.

[73] J. Vidal, *Thermodynamics: applications in chemical engineering and the petroleum industry*. Paris: Editions Technip, 2003.

[74] P.-W. Martelli, « Modélisation et simulations numériques de la formation de domaines ferroélectriques dans des nanostructures 3D », These de doctorat, Université de Lorraine, 2016. [En ligne]. Disponible sur: http://www.theses.fr/2016LORR0119

[75] D. R. Tilley et B. Žekš, « Landau theory of phase transitions in thick films », *Solid State Communications*, vol. 49, n° 8, p. 823-828, févr. 1984, doi: 10.1016/0038-1098(84)90089-9.

[76] Y. Ishibashi, H. Orihara, et D. R. Tilley, « Thickness Transitions of Ferroelectricity in Thin Films », *J. Phys. Soc. Jpn.*, vol. 67, n° 9, p. 3292-3297, sept. 1998, doi: 10.1143/JPSJ.67.3292.

[77] Y. Ishibashi, H. Orihara, et D. R. Tilley, « Thickness Transitions of Ferroelectricity in Thin Films: II », *J. Phys. Soc. Jpn.*, vol. 71, n° 6, p. 1471-1474, juin 2002, doi: 10.1143/JPSJ.71.1471.

[78] J. E. Brewer et M. Gill, « Nonvolatile Memory Technologies With Emphasis on Flash : A Comprehensive Guide to Understanding and Using NVM Devices », p. 788.

[79] S. S. Fields *et al.*, « Wake-up and fatigue mechanisms in ferroelectric $Hf_{0.5}Zr_{0.5}O_2$ films with symmetric RuO_2 electrodes », *Journal of Applied Physics*, vol. 130, n° 13, p. 134101, oct. 2021, doi: 10.1063/5.0064145.

[80] F. Mehmood, T. Mikolajick, et U. Schroeder, « Wake-up Mechanisms in Ferroelectric Lanthanum Doped $Hf_{0.5}Zr_{0.5}O_2$ Thin Films », *Phys. Status Solidi A*, p. pssa.202000281, sept. 2020, doi: 10.1002/pssa.202000281.

[81] S. Hong, Éd., *Nanoscale Phenomena in Ferroelectric Thin Films*. Boston, MA: Springer US, 2004. doi: 10.1007/978-1-4419-9044-0.

[82] J. Lyu, I. Fina, et F. Sánchez, « Fatigue and retention in the growth window of ferroelectric $Hf_{0.5}Zr_{0.5}O_2$ thin films », *Appl. Phys. Lett.*, vol. 117, n° 7, p. 072901, août 2020, doi: 10.1063/5.0017738.

[83] S. S. Fields *et al.*, « Phase-Exchange-Driven Wake-Up and Fatigue in Ferroelectric Hafnium Zirconium Oxide Films », *ACS Appl. Mater. Interfaces*, p. acsami.0c03570, mai 2020, doi: 10.1021/acsami.0c03570.

[84] F. Huang *et al.*, « Fatigue mechanism of yttrium-doped hafnium oxide ferroelectric thin films fabricated by pulsed laser deposition. », 2017, doi: 10.1039/c6cp07501k.

[85] H. Z. Jin et J. Zhu, « Size effect and fatigue mechanism in ferroelectric thin films », *Journal of Applied Physics*, vol. 92, n° 8, p. 4594-4598, oct. 2002, doi: 10.1063/1.1506193.

[86] A. V. Ievlev *et al.*, « Non-conventional mechanism of ferroelectric fatigue via cation migration », *Nat Commun*, vol. 10, n° 1, p. 3064, juill. 2019, doi: 10.1038/s41467-019-11089-w.

[87] D. C. Lupascu, *Fatigue in Ferroelectric Ceramics and Related Issues*, vol. 61. Berlin, Heidelberg: Springer Berlin Heidelberg, 2004. doi: 10.1007/978-3-662-07189-2.

[88] « Mechanisms of imprint effect on ferroelectric thin films: Journal of Applied Physics: Vol 98, No 2 ». https://aip.scitation.org/doi/10.1063/1.1984075.

[89] R. I. Hegde *et al.*, « Microstructure modified HfO/sub 2/ using Zr addition with Ta/sub x/ C/sub y/ gate for improved device performance and reliability », in *IEEE InternationalElectron Devices Meeting, 2005. IEDM Technical Digest.*, Tempe, Arizon, USA, 2005, p. 35-38. doi: 10.1109/IEDM.2005.1609259.

[90] D. H. Triyoso *et al.*, « Impact of Zr addition on properties of atomic layer deposited HfO2 », *Appl. Phys. Lett.*, vol. 88, n° 22, p. 222901, mai 2006, doi: 10.1063/1.2208558.

[91] R. I. Hegde *et al.*, « Optimization of Hafnium Zirconate (HfZrOx) Gate Dielectric for Device Performance and Reliability », présenté à 2006 International Conference on Solid State Devices and Materials, PACIFICO Yokohama, Yokohama, Japan, 2006. doi: 10.7567/SSDM.2006.J-7-1.

[92] Y. Kuo *et al.*, « Sub 2 nm Thick Zirconium Doped Hafnium Oxide High-K Gate Dielectrics », *ECS Trans.*, vol. 1, n° 5, p. 447-454, déc. 2019, doi: 10.1149/1.2209294.

[93] D. H. Triyoso, R. I. Hegde, R. Gregory, G. Spencer, J. K. Schaeffer, et M. Raymond, « Factors impacting stabilization of tetragonal phase in HfxZr1−xO2 high-k dielectrics », in *2009 IEEE International Conference on IC Design and Technology*, Austin, TX, USA, mai 2009, p. 89-92. doi: 10.1109/ICICDT.2009.5166272.

[94] D. H. Triyoso, « Factors Influencing Characteristics of Hafnium Based High-K Dielectrics », *ECS Trans.*, vol. 3, n° 3, p. 463-477, déc. 2019, doi: 10.1149/1.2355735.

[95] M. Muller *et al.*, « Highly Manufacturable and Cost-effective Single TaxC / HfxZr(1-x)O2 Gate CMOS Bulk Platform for LP Applications at the 45nm Node and Beyond », présenté à 2007 International Conference on Solid State Devices and Materials, Tsukuba International Congress Center (EPOCHAL TSUKUBA), Ibaraki, Japan, 2007. doi: 10.7567/SSDM.2007.A-8-4.

[96] R. I. Hegde, D. H. Triyoso, S. B. Samavedam, et B. E. White, « Hafnium zirconate gate dielectric for advanced gate stack applications », *Journal of Applied Physics*, vol. 101, n° 7, p. 074113, avr. 2007, doi: 10.1063/1.2716399.

[97] A. Birge, C.-H. Lin, et Y. Kuo, « Memory Functions of Nanocrystalline Indium Tin Oxide Embedded Zirconium-Doped Hafnium Oxide MOS Capacitors », *J. Electrochem. Soc.*, vol. 154, n° 10, p. H887, 2007, doi: 10.1149/1.2768291.

[98] C.-H. Lin et Y. Kuo, « Nonvolatile Memories with Dual-Layer Nanocrystalline ZnO Embedded Zr-Doped HfO2 High-k Dielectric », p. 5.

[99] Y. Kuo, X. Liu, C.-H. Yang, et C.-C. Lin, « Nonvolatile Memory Characteristics of Nanocrystalline Molybdenum Oxide Embedded High- k Film - Device Performance and Light Wavelength Effects », *MRS Proc.*, vol. 1430, p. mrss12-1430-e01-10, 2012, doi: 10.1557/opl.2012.1018.

[100] C.-H. Lin et Y. Kuo, « Embedding of Nanocrystalline Ruthenium in ZrHfO High-k Film for Nonvolatile Memories », *ECS Trans.*, vol. 13, n° 1, p. 465-470, déc. 2019, doi: 10.1149/1.2911531.

[101] C.-H. Lin et Y. Kuo, « Mechanism of Charge Storage in nc-RuO Embedded ZrHfO High-k Films », *ECS Trans.*, vol. 16, n° 5, p. 309-316, déc. 2019, doi: 10.1149/1.2981612.

[102] Y. Kuo et C.-C. Lin, « Electroluminescence from Metal Oxide Thin Films », *ECS Solid State Letters*, vol. 2, n° 8, p. Q59-Q61, mai 2013, doi: 10.1149/2.002308ssl.

[103] Y. Kuo et C.-C. Lin, « A light emitting device made from thin zirconium-doped hafnium oxide high- k dielectric film with or without an embedded nanocrystal layer », *Appl. Phys. Lett.*, vol. 102, n° 3, p. 031117, janv. 2013, doi: 10.1063/1.4789531.

[104] Y. Kuo et S. Zhang, « Communication—Co-Planar Structured Nano-Resistor Devices », *ECS J. Solid State Sci. Technol.*, vol. 8, n° 12, p. Q223-Q225, 2019, doi: 10.1149/2.0071912jss.

[105] S. Zhang et Y. Kuo, « Electrical properties of nano-resistors made from the Zr-doped HfO_2 high- k dielectric film », *J. Phys. D: Appl. Phys.*, vol. 51, n° 9, p. 09LT02, mars 2018, doi: 10.1088/1361-6463/aaa9d3.

[106] C.-C. Lin et Y. Kuo, « White-Light Emission from Amorphous ZrHfO Thin Film Dielectrics with and without Embedded Nanocrystalline CdSe Dots », *ECS Transactions*, vol. 61, n° 5, p. 55-60, mars 2014, doi: 10.1149/06105.0055ecst.

[107] S. Zhang et Y. Kuo, « Solid State Incandescent Light Emitting Device Made of WOx Embedded Zr-Doped HfO2 High-k Stack on Si », *ECS Transactions*, vol. 66, n° 4, p. 223-228, mai 2015, doi: 10.1149/06604.0223ecst.

[108] K. Kalam *et al.*, « Electric and Magnetic Properties of Atomic Layer Deposited ZrO_2-HfO_2 Thin Films », *ECS J. Solid State Sci. Technol.*, vol. 7, n° 9, p. N117-N122, 2018, doi: 10.1149/2.0041809jss.

[109] M. Park *et al.*, « Surface and grain boundary energy as the key enabler of ferroelectricity in nanoscale hafnia-zirconia: a comparison of model and experiment. », 2017, doi: 10.1039/c7nr02121f.

[110] J. Müller *et al.*, « Ferroelectric Zr0.5Hf0.5O2 thin films for nonvolatile memory applications », 2011, doi: 10.1063/1.3636417.

[111] H. Kim *et al.*, « Grain size engineering for ferroelectric Hf0.5Zr0.5O2 films by an insertion of Al2O3 interlayer », 2014, doi: 10.1063/1.4902072.

[112] S. S. Cheema *et al.*, « Enhanced ferroelectricity in ultrathin films grown directly on silicon », *Nature*, vol. 580, n° 7804, p. 478-482, avr. 2020, doi: 10.1038/s41586-020-2208-x.

[113] A. Chouprik *et al.*, « Electron transport across ultrathin ferroelectric Hf0.5Zr0.5O2 films on Si », *Microelectronic Engineering*, vol. 178, p. 250-253, juin 2017, doi: 10.1016/j.mee.2017.05.028.

[114] R. Shimura *et al.*, « Preparation of 1 µm thick Y-doped HfO_2 ferroelectric films on (111)Pt/TiO_x/SiO_2/(001)Si substrates by a sputtering method and their ferroelectric and piezoelectric properties », *Jpn. J. Appl. Phys.*, vol. 60, n° 3, p. 031009, mars 2021, doi: 10.35848/1347-4065/abe72e.

[115] T. Schenk *et al.*, « Toward Thick Piezoelectric HfO_2-Based Films », *Phys. Status Solidi RRL*, vol. 14, n° 3, p. 1900626, mars 2020, doi: 10.1002/pssr.201900626.

[116] J. Woo *et al.*, « Improved Ferroelectric Switching in Sputtered $HfZrO_x$ Device Enabled by High Pressure Annealing », *IEEE Electron Device Lett.*, vol. 41, n° 2, p. 232-235, févr. 2020, doi: 10.1109/LED.2019.2959802.

[117] A. Shekhawat *et al.*, « Effect of Forming Gas Furnace Annealing on the Ferroelectricity and Wake-Up Effect of $Hf_{0.5}Zr_{0.5}O_2$ Thin Films », *ECS J. Solid State Sci. Technol.*, vol. 9, n° 2, p. 024011, janv. 2020, doi: 10.1149/2162-8777/ab6b13.

[118] L. Bégon-Lours *et al.*, « Stabilization of phase-pure rhombohedral HfZr O 4 in pulsed laser deposited thin films », *Phys. Rev. Materials*, vol. 4, n° 4, p. 043401, avr. 2020, doi: 10.1103/PhysRevMaterials.4.043401.

[119] Y.-H. Chen, C.-J. Su, T.-H. Yang, C. Hu, et T.-L. Wu, « Improved TDDB Reliability and Interface States in 5-nm Hf $_{0.5}$ Zr $_{0.5}$ O $_{2}$ Ferroelectric Technologies Using NH $_{3}$ Plasma and Microwave Annealing », *IEEE Trans. Electron Devices*, vol. 67, n° 4, p. 1581-1585, avr. 2020, doi: 10.1109/TED.2020.2973652.

[120] M. H. Park *et al.*, « Effect of Annealing Ferroelectric HfO $_{2}$ Thin Films: In Situ, High Temperature X-Ray Diffraction », *Adv. Electron. Mater.*, vol. 4, n° 7, p. 1800091, juill. 2018, doi: 10.1002/aelm.201800091.

[121] M. B. Hachemi *et al.*, « Study of structural and electrical properties of ferroelectric HZO films obtained by single-target sputtering », *AIP Advances*, vol. 11, n° 8, p. 085004, août 2021, doi: 10.1063/5.0058656.

[122] A. E. O. Persson *et al.*, « Reduced annealing temperature for ferroelectric HZO on InAs with enhanced polarization », *Appl. Phys. Lett.*, vol. 116, n° 6, p. 062902, févr. 2020, doi: 10.1063/1.5141403.

[123] S. J. Kim *et al.*, « Low-thermal-budget (300 °C) ferroelectric TiN/Hf0.5Zr0.5O2/TiN capacitors realized using high-pressure annealing », *Applied Physics Letters*, vol. 119, n° 24, p. 242901, déc. 2021, doi: 10.1063/5.0075466.

[124] Y. H. Lee *et al.*, « Preparation and characterization of ferroelectric Hf $_{0.5}$ Zr $_{0.5}$ O $_{2}$ thin films grown by reactive sputtering », *Nanotechnology*, vol. 28, n° 30, p. 305703, juill. 2017, doi: 10.1088/1361-6528/aa7624.

[125] J. Wang *et al.*, « Effect of annealing protection atmosphere on the ferroelectric yttrium doped hafnium oxide thin films », *Ceramics International*, vol. 46, n° 14, p. 22550-22556, oct. 2020, doi: 10.1016/j.ceramint.2020.06.015.

[126] R. Cao *et al.*, « Effects of Capping Electrode on Ferroelectric Properties of Hf $_{0.5}$ Zr $_{0.5}$ O $_{2}$ Thin Films », *IEEE Electron Device Lett.*, vol. 39, n° 8, p. 1207-1210, août 2018, doi: 10.1109/LED.2018.2846570.

[127] L. Xu, T. Nishimura, S. Shibayama, T. Yajima, S. Migita, et A. Toriumi, « Kinetic pathway of the ferroelectric phase formation in doped HfO $_{2}$ films », *Journal of Applied Physics*, vol. 122, n° 12, p. 124104, sept. 2017, doi: 10.1063/1.5003918.

[128] Z. Fan *et al.*, « Ferroelectricity and ferroelectric resistive switching in sputtered Hf $_{0.5}$ Zr $_{0.5}$ O $_{2}$ thin films », *Appl. Phys. Lett.*, vol. 108, n° 23, p. 232905, juin 2016, doi: 10.1063/1.4953461.

[129] Y. H. Lee *et al.*, « Preparation and characterization of ferroelectric Hf $_{0.5}$ Zr $_{0.5}$ O $_{2}$ thin films grown by reactive sputtering », *Nanotechnology*, vol. 28, n° 30, p. 305703, juill. 2017, doi: 10.1088/1361-6528/aa7624.

[130] T. Mittmann *et al.*, « Origin of Ferroelectric Phase in Undoped HfO $_{2}$ Films Deposited by Sputtering », *Adv. Mater. Interfaces*, p. 1900042, avr. 2019, doi: 10.1002/admi.201900042.

[131] D.-H. Min, T.-H. Ryu, S.-J. Yoon, S.-E. Moon, et S.-M. Yoon, « Improvements in the synaptic operations of ferroelectric field-effect transistors using Hf $_{0.5}$ Zr $_{0.5}$ O $_{2}$ thin films controlled by oxygen partial pressures during the sputtering deposition process », *Journal of Materials Chemistry C*, 2020, doi: 10.1039/D0TC01105C.

[132] M. Hoffmann *et al.*, « Unveiling the double-well energy landscape in a ferroelectric layer », *Nature*, vol. 565, n° 7740, p. 464-467, janv. 2019, doi: 10.1038/s41586-018-0854-z.

[133] M. Hoffmann, B. Max, T. Mittmann, U. Schroeder, S. Slesazeck, et T. Mikolajick, « Demonstration of High-speed Hysteresis-free Negative Capacitance in Ferroelectric Hf0.5Zr0.5O2 », in *2018 IEEE International Electron Devices Meeting (IEDM)*, San Francisco, CA, déc. 2018, p. 31.6.1-31.6.4. doi: 10.1109/IEDM.2018.8614677.

[134] S. Salahuddin et S. Datta, « Use of Negative Capacitance to Provide Voltage Amplification for Low Power Nanoscale Devices », *Nano Lett.*, vol. 8, n° 2, p. 405-410, févr. 2008, doi: 10.1021/nl071804g.

[135] S. Salahuddin, « Review of negative capacitance transistors », in *2016 International Symposium on VLSI Technology, Systems and Application (VLSI-TSA)*, Hsinchu, Taiwan, avr. 2016, p. 1-1. doi: 10.1109/VLSI-TSA.2016.7480491.

[136] J. Acharya, R. Goul, J. Wilt, et J. Wu, « Switching On/Off Negative Capacitance in Ultrathin Ferroelectric/Dielectric Capacitors », *ACS Appl. Mater. Interfaces*, vol. 12, n° 8, p. 9902-9908, févr. 2020, doi: 10.1021/acsami.9b19789.

[137] P. Chang, G. Du, et X. Liu, « Design space for stabilized negative capacitance in HfO2 ferroelectric-dielectric stacks based on phase field simulation », *Sci. China Inf. Sci.*, vol. 64, n° 2, p. 122402, févr. 2021, doi: 10.1007/s11432-020-3005-8.

[138] R. R. Shaik et K. P. Pradhan, « Impact of HZO and HSO thin film ferroelectric on FDSOI NCFET », in *2021 IEEE 21st International Conference on Nanotechnology (NANO)*, Montreal, QC, Canada, juill. 2021, p. 126-129. doi: 10.1109/NANO51122.2021.9514307.

[139] S. Semwal et A. Kranti, « Ferroelectric Thickness Dependent Characteristics of Negative Capacitance Transistors », in *2021 IEEE International Symposium on Applications of Ferroelectrics (ISAF)*, Sydney, Australia, mai 2021, p. 1-4. doi: 10.1109/ISAF51943.2021.9477365.

[140] C. Wang, J. Wu, H. Yu, G. Han, X. Miao, et X. Wang, « Effects of Temperature on the Performance of $Hf_{0.5}Zr_{0.5}O_2$-Based Negative Capacitance FETs », *IEEE Electron Device Lett.*, vol. 41, n° 11, p. 1625-1628, nov. 2020, doi: 10.1109/LED.2020.3022384.

[141] T. Francois *et al.*, « Demonstration of BEOL-compatible ferroelectric $Hf_{0.5}Zr_{0.5}O_2$ scaled FeRAM co-integrated with 130nm CMOS for embedded NVM applications », in *2019 IEEE International Electron Devices Meeting (IEDM)*, San Francisco, CA, USA, déc. 2019, p. 15.7.1-15.7.4. doi: 10.1109/IEDM19573.2019.8993485.

[142] M. Ghatge, G. Walters, T. Nishida, et R. Tabrizian, « An ultrathin integrated nanoelectromechanical transducer based on hafnium zirconium oxide », *Nat Electron*, vol. 2, n° 11, p. 506-512, nov. 2019, doi: 10.1038/s41928-019-0305-3.

[143] C. Mart, W. Weinreich, M. Czernohorsky, S. Riedel, S. Zybell, et K. Kuhnel, « CMOS Compatible Pyroelectric Applications Enabled by Doped HfO2 Films on Deep-Trench Structures », in *2018 48th European Solid-State Device Research Conference (ESSDERC)*, Dresden, sept. 2018, p. 130-133. doi: 10.1109/ESSDERC.2018.8486864.

[144] L. Chen *et al.*, « Ultra-low power $Hf_{0.5}Zr_{0.5}O_2$ based ferroelectric tunnel junction synapses for hardware neural network applications », *Nanoscale*, vol. 10, n° 33, p. 15826-15833, 2018, doi: 10.1039/C8NR04734K.

[145] Y. Goh, J. Hwang, Y. Lee, M. Kim, et S. Jeon, « Ultra-thin $Hf_{0.5}Zr_{0.5}O_2$ thin-film-based ferroelectric tunnel junction via stress induced crystallization », *Appl. Phys. Lett.*, vol. 117, nº 24, p. 242901, déc. 2020, doi: 10.1063/5.0029516.

[146] W. Shim et S. Yu, « Ferroelectric Field-Effect Transistor-Based 3-D NAND Architecture for Energy-Efficient on-Chip Training Accelerator », *IEEE J. Explor. Solid-State Comput. Devices Circuits*, vol. 7, nº 1, p. 1-9, juin 2021, doi: 10.1109/JXCDC.2021.3057856.

[147] T. Yu *et al.*, « Hf0.5Zr0.5O2-based ferroelectric memristor with multilevel storage potential and artificial synaptic plasticity », *Sci. China Mater.*, sept. 2020, doi: 10.1007/s40843-020-1444-1.

[148] H. Ryu, H. Wu, F. Rao, et W. Zhu, « Ferroelectric Tunneling Junctions Based on Aluminum Oxide/ Zirconium-Doped Hafnium Oxide for Neuromorphic Computing », *Sci Rep*, vol. 9, nº 1, p. 20383, déc. 2019, doi: 10.1038/s41598-019-56816-x.

[149] J. Bouaziz, P. Rojo Romeo, N. Baboux, R. Negrea, L. Pintilie, et B. Vilquin, « Dramatic impact of pressure and annealing temperature on the properties of sputtered ferroelectric HZO layers », *APL Materials*, vol. 7, nº 8, p. 081109, août 2019, doi: 10.1063/1.5110894.

[150] Y. Qi, X. Xu, I. Krylov, et M. Eizenberg, « Ferroelectricity of as-deposited HZO fabricated by plasma-enhanced atomic layer deposition at 300 °C by inserting TiO_2 interlayers », *Appl. Phys. Lett.*, vol. 118, nº 3, p. 032906, janv. 2021, doi: 10.1063/5.0037887.

[151] K. Ahadi et K. Cadien, « $Hf_{1-x}Zr_xO_2$ and HfO_2 /ZrO_2 gate dielectrics with extremely low density of interfacial defects using low temperature atomic layer deposition on GaN and InP », *Journal of Vacuum Science & Technology A*, vol. 39, nº 3, p. 032407, mai 2021, doi: 10.1116/6.0000914.

[152] H. Ryu, H. Wu, F. Rao, et W. Zhu, « Ferroelectric Tunneling Junctions Based on Aluminum Oxide/ Zirconium-Doped Hafnium Oxide for Neuromorphic Computing », *Sci Rep*, vol. 9, nº 1, p. 20383, déc. 2019, doi: 10.1038/s41598-019-56816-x.

[153] C. Abe *et al.*, « Crystal structure and dielectric/ferroelectric properties of CSD-derived HfO 2 -ZrO 2 solid solution films », *Ceramics International*, vol. 43, p. S501-S505, août 2017, doi: 10.1016/j.ceramint.2017.05.253.

[154] Y. Lee *et al.*, « Unexpectedly large remanent polarization of $Hf_{0.5}Zr_{0.5}O_2$ metal–ferroelectric–metal capacitor fabricated without breaking vacuum », *Appl. Phys. Lett.*, vol. 118, nº 1, p. 012903, janv. 2021, doi: 10.1063/5.0029532.

[155] S. Kar, Éd., *High Permittivity Gate Dielectric Materials*, vol. 43. Berlin, Heidelberg: Springer Berlin Heidelberg, 2013. doi: 10.1007/978-3-642-36535-5.

[156] W. Steckelmacher, « Sputtering by particle bombardment III: Characteristics of sputtered particles, technical applications », *Vacuum*, vol. 43, nº 8, p. 857, août 1992, doi: 10.1016/0042-207X(92)90152-M.

[157] K. Wasa, M. Kitabatake, et H. Adachi, *Thin film materials technology: sputtering of compound materials*. Norwich, NY : Heidelberg: William Andrew Pub. ; Springer, 2004.

[158] T. Ali *et al.*, « Silicon doped hafnium oxide (HSO) and hafnium zirconium oxide (HZO) based FeFET: A material relation to device physics », *Applied Physics Letters*, vol. 112, nº 22, p. 222903, mai 2018, doi: 10.1063/1.5029324.

[159] « Untersuchungen zur Totalreflexion von Röntgenstrahlen - Kiessig - 1931 - Annalen der Physik - Wiley Online Library ». https://onlinelibrary.wiley.com/doi/10.1002/andp.19314020607.
[160] « X-ray thin-film measurement techniques V. X-ray reflectivity measurement | Rigaku Global Website ». https://www.rigaku.com/journal/summer-2010-volume-26-no-2/01-09.
[161] « XPS Interpretation of Carbon ». https://www.jp.xpssimplified.com/elements/carbon.php.
[162] « Système de traitement de données Avantage ». https://www.thermofisher.com/order/catalog/product/IQLAADGACKFAKRMAVI.
[163] « Copyright © 2005 Casa Software Ltd ». http://www.casaxps.com/.
[164] « Transmission Electron Microscopy and Diffractometry of Materials | SpringerLink ». https://link.springer.com/book/10.1007/978-3-642-29761-8.
[165] M. Halter *et al.*, « XRD and PFM evidence for the stabilization of ultra-thin ferroelectric HfxZr1-xO2 by millisecond flash lamp annealing », p. 1 p., 2019, doi: 10.3929/ETHZ-B-000382712.
[166] C.-H. Wu, A. Useinov, T.-L. Wu, et C.-J. Su, « Ferroelectric Characterization in Ultrathin Hf0.5Zr0.5O2 MFIS Capacitors by Piezoresponse Force Microscopy (PFM) in Vacuum », in *2021 International Symposium on VLSI Technology, Systems and Applications (VLSI-TSA)*, Hsinchu, Taiwan, avr. 2021, p. 1-2. doi: 10.1109/VLSI-TSA51926.2021.9440099.
[167] E. Barsoukov et J. R. Macdonald, Éd., *Impedance spectroscopy: theory, experiment, and applications*, Third edition. Hoboken, NJ: Wiley, 2018.
[168] C. B. Sawyer et C. H. Tower, « Rochelle Salt as a Dielectric », *Phys. Rev.*, vol. 35, n° 3, p. 269-273, févr. 1930, doi: 10.1103/PhysRev.35.269.
[169] « Integration of Ferroelectric and Piezoelectric Thin Films | Wiley Online Books ». https://onlinelibrary.wiley.com/doi/book/10.1002/9781118616635.
[170] « TF 3000 ferroelectric Analyzer - Aixacct », vol. 16, n° 1, p. 8-12.
[171] G. V. Naik, J. L. Schroeder, X. Ni, A. V. Kildishev, T. D. Sands, et A. Boltasseva, « Titanium nitride as a plasmonic material for visible and near-infrared wavelengths », *Opt. Mater. Express*, vol. 2, n° 4, p. 478, avr. 2012, doi: 10.1364/OME.2.000478.
[172] R. Athle, A. E. O. Persson, A. Irish, H. Menon, R. Timm, et M. Borg, « Effects of TiN Top Electrode Texturing on Ferroelectricity in $Hf_{1-x}Zr_xO_2$ », *ACS Appl. Mater. Interfaces*, vol. 13, n° 9, p. 11089-11095, mars 2021, doi: 10.1021/acsami.1c01734.
[173] M. Ghatge, G. Walters, T. Nishida, et R. Tabrizian, « A Nano-Mechanical Resonator with 10nm Hafnium-Zirconium Oxide Ferroelectric Transducer », in *2018 IEEE International Electron Devices Meeting (IEDM)*, San Francisco, CA, déc. 2018, p. 4.6.1-4.6.4. doi: 10.1109/IEDM.2018.8614633.
[174] M. H. Park, Y. H. Lee, T. Mikolajick, U. Schroeder, et C. S. Hwang, « Review and perspective on ferroelectric HfO2-based thin films for memory applications », *MRS Communications*, vol. 8, n° 03, p. 795-808, sept. 2018, doi: 10.1557/mrc.2018.175.
[175] S. J. Kim *et al.*, « A Comprehensive Study on the Effect of TiN Top and Bottom Electrodes on Atomic Layer Deposited Ferroelectric Hf0.5Zr0.5O2 Thin Films », *Materials*, vol. 13, n° 13, p. 2968, juill. 2020, doi: 10.3390/ma13132968.

[176] S. Xiao *et al.*, « Resputtering effect during MgO buffer layer deposition by magnetron sputtering for superconducting coated conductors », *J. Vac. Sci. Technol. A*, vol. 33, n° 4, p. 7, 2015.

[177] B. Bouaouina *et al.*, « Nanocolumnar TiN thin film growth by oblique angle sputter-deposition: Experiments vs. simulations », *Materials & Design*, vol. 160, p. 338-349, déc. 2018, doi: 10.1016/j.matdes.2018.09.023.

[178] R. Mareus, C. Mastail, F. Anğay, N. Brunetière, et G. Abadias, « Study of columnar growth, texture development and wettability of reactively sputter-deposited TiN, ZrN and HfN thin films at glancing angle incidence », *Surface and Coatings Technology*, vol. 399, p. 126130, oct. 2020, doi: 10.1016/j.surfcoat.2020.126130.

[179] P. Scherrer, « Bestimmung der Größe und der inneren Struktur von Kolloidteilchen mittels Röntgenstrahlen », *Nachrichten von der Gesellschaft der Wissenschaften zu Göttingen, Mathematisch-Physikalische Klasse*, vol. 1918, p. 98-100, 1918,. [En ligne]. Disponible sur: https://eudml.org/doc/59018

[180] K. Hansen, M. Cardona, A. Dutta, et C. Yang, « Plasma Enhanced Atomic Layer Deposition of Plasmonic TiN Ultrathin Films Using TDMATi and NH3 », *Materials (Basel)*, vol. 13, n° 5, p. 1058, févr. 2020, doi: 10.3390/ma13051058.

[181] None Available, « Materials Data on TiN by Materials Project ». LBNL Materials Project; Lawrence Berkeley National Laboratory (LBNL), Berkeley, CA (United States), 2020. doi: 10.17188/1208488.

[182] I. Milošev, H.-H. Strehblow, B. Navinšek, et P. Panjan, « Titanium Nitride by XPS », *Surface Science Spectra*, vol. 5, n° 2, p. 145-151, avr. 1998, doi: 10.1116/1.1247863.

[183] E. Galvanetto, F. P. Galliano, F. Borgioli, U. Bardi, et A. Lavacchi, « XRD and XPS study on reactive plasma sprayed titanium–titanium nitride coatings », *Thin Solid Films*, vol. 384, n° 2, p. 223-229, mars 2001, doi: 10.1016/S0040-6090(00)01871-X.

[184] M. J. Buiting et A. H. Reader, « Influence of Impurities and Microstructure on the Resistivity of LPCVD Titanium Nitride Films », *MRS Proc.*, vol. 168, p. 199, 1989, doi: 10.1557/PROC-168-199.

[185] N. K. Ponon *et al.*, « Effect of deposition conditions and post deposition anneal on reactively sputtered titanium nitride thin films », *Thin Solid Films*, vol. 578, p. 31-37, mars 2015, doi: 10.1016/j.tsf.2015.02.009.

[186] D. Güttler, B. Abendroth, R. Grötzschel, W. Möller, et D. Depla, « Mechanisms of target poisoning during magnetron sputtering as investigated by real-time *in situ* analysis and collisional computer simulation », *Appl. Phys. Lett.*, vol. 85, n° 25, p. 6134-6136, déc. 2004, doi: 10.1063/1.1835002.

[187] S. Grosso, L. Latu-Romain, G. Berthomé, G. Renou, T. Le Coz, et M. Mantel, « Titanium and titanium nitride thin films grown by dc reactive magnetron sputtering Physical Vapor Deposition in a continuous mode on stainless steel wires: Chemical, morphological and structural investigations », *Surface and Coatings Technology*, vol. 324, p. 318-327, sept. 2017, doi: 10.1016/j.surfcoat.2017.05.089.

[188] G. Segantini *et al.*, « Bottom electrodes impact on Hf0.5Zr0.5O2 ferroelectric tunnel junctions », p. 6.

[189] Ph. Roquiny, F. Bodart, et G. Terwagne, « Colour control of titanium nitride coatings produced by reactive magnetron sputtering at temperature less than 100°C », *Surface*

and Coatings Technology, vol. 116-119, p. 278-283, sept. 1999, doi: 10.1016/S0257-8972(99)00076-6.

[190] W. M. Mohammed *et al.*, « Electrical properties of titanium nitride films synthesized by reactive magnetron sputtering », *J. Phys.: Conf. Ser.*, vol. 927, p. 012036, nov. 2017, doi: 10.1088/1742-6596/927/1/012036.

[191] P. Saikia, A. Joseph, R. Rane, B. Saikia, et S. Mukherjee, « Role of substrate and deposition conditions on the texture evolution of titanium nitride thin film on bare and plasma-nitrided high-speed steel », *J Theor Appl Phys*, vol. 7, n° 1, p. 66, 2013, doi: 10.1186/2251-7235-7-66.

[192] G. Abadias, « Stress and preferred orientation in nitride-based PVD coatings », *Surface and Coatings Technology*, vol. 202, n° 11, p. 2223-2235, févr. 2008, doi: 10.1016/j.surfcoat.2007.08.029.

[193] W.-J. Chou, G.-P. Yu, et J.-H. Huang, « Mechanical properties of TiN thin film coatings on 304 stainless steel substrates », *Surface and Coatings Technology*, vol. 149, n° 1, p. 7-13, janv. 2002, doi: 10.1016/S0257-8972(01)01382-2.

[194] I. Petrov, P. B. Barna, L. Hultman, et J. E. Greene, « Microstructural evolution during film growth », *Journal of Vacuum Science & Technology A: Vacuum, Surfaces, and Films*, vol. 21, n° 5, p. S117-S128, sept. 2003, doi: 10.1116/1.1601610.

[195] J. E. Greene, J. -E. Sundgren, L. Hultman, I. Petrov, et D. B. Bergstrom, « Development of preferred orientation in polycrystalline TiN layers grown by ultrahigh vacuum reactive magnetron sputtering », *Appl. Phys. Lett.*, vol. 67, n° 20, p. 2928-2930, nov. 1995, doi: 10.1063/1.114845.

[196] S. Datta, M. Das, V. K. Balla, S. Bodhak, et V. K. Murugesan, « Mechanical, wear, corrosion and biological properties of arc deposited titanium nitride coatings », *Surface and Coatings Technology*, vol. 344, p. 214-222, juin 2018, doi: 10.1016/j.surfcoat.2018.03.019.

[197] « Vacuum Magnetron Sputtering Machine manufacturer », *Alliance Concept English*. https://www.alliance-concept.com/en/dp-range-vacuum-magnetron-sputtering.html.

[198] K. Wasa, I. Kanno, et H. Kotera, Éd., *Handbook of sputter deposition technology: fundamentals and applications for functional thin films, nanomaterials and MEMS*, 2nd ed. Waltham, MA: William Andrew, 2012.

[199] R. Singh, M. Gupta, D. M. Phase, et S. K. Mukherjee, « Phase growth analysis of sputtered TiO $_2$ thin films at low oxygen partial pressures using XANES and XRR », *Mater. Res. Express*, vol. 6, n° 11, p. 116449, oct. 2019, doi: 10.1088/2053-1591/ab4e3f.

[200] G. Panomsuwan et N. Saito, « Effect of Oxygen Partial Pressure on Crystal Structure, Oxygen Vacancy, and Surface Morphology of Epitaxial SrTiO3 Thin Films Grown by Ion Beam Sputter Deposition », *Oxygen*, vol. 1, n° 1, p. 62-72, sept. 2021, doi: 10.3390/oxygen1010007.

[201] S. Jena *et al.*, « Influence of oxygen partial pressure on microstructure, optical properties, residual stress and laser induced damage threshold of amorphous HfO2 thin films », *Journal of Alloys and Compounds*, vol. 771, p. 373-381, janv. 2019, doi: 10.1016/j.jallcom.2018.08.327.

[202] Y.-J. Lin *et al.*, « Role of electrode-induced oxygen vacancies in regulating polarization wake-up in ferroelectric capacitors », *Applied Surface Science*, vol. 528, p. 147014, oct. 2020, doi: 10.1016/j.apsusc.2020.147014.

[203] Y. Goh, S. H. Cho, S.-H. K. Park, et S. Jeon, « Oxygen vacancy control as a strategy to achieve highly reliable hafnia ferroelectrics using oxide electrode », *Nanoscale*, vol. 12, nº 16, p. 9024-9031, 2020, doi: 10.1039/D0NR00933D.

[204] T. Mittmann, M. Materano, S.-C. Chang, I. Karpov, T. Mikolajick, et U. Schroeder, « Impact of Oxygen Vacancy Content in Ferroelectric HZO films on the Device Performance », in *2020 IEEE International Electron Devices Meeting (IEDM)*, San Francisco, CA, USA, déc. 2020, p. 18.4.1-18.4.4. doi: 10.1109/IEDM13553.2020.9372097.

[205] S. U. Sharath *et al.*, « Towards forming-free resistive switching in oxygen engineered HfO_{2-x} », *Appl. Phys. Lett.*, vol. 104, nº 6, p. 063502, févr. 2014, doi: 10.1063/1.4864653.

[206] D. Sotiropoulou et S. Ladas, « An XPS and XAES study of the Ni/ZrO2 interface », *Surface Science*, vol. 408, nº 1-3, p. 182-189, juin 1998, doi: 10.1016/S0039-6028(98)00219-2.

[207] « NIST XPS Database ». https://srdata.nist.gov/xps/elm_Spectra_query.aspx?Elm1=Hf&LD1=4f7%2f2&Elm2=&LD2=&Elm3=&LD3=&Elm4=&LD4=&sType=PE.

[208] Md. Akhtaruzzaman *et al.*, « Impact of Ar Flow Rates on Micro-Structural Properties of WS2 Thin Film by RF Magnetron Sputtering », *Nanomaterials*, vol. 11, nº 7, p. 1635, juin 2021, doi: 10.3390/nano11071635.

[209] M. Al-Mansoori, S. Al-Shaibani, A. Al-Jaeedi, J. Lee, D. Choi, et F. S. Hasoon, « Effects of gas flow rate on the structure and elemental composition of tin oxide thin films deposited by RF sputtering », *AIP Advances*, vol. 7, nº 12, p. 125105, déc. 2017, doi: 10.1063/1.5001883.

[210] S. Ameen, M. S. Akhtar, H.-K. Seo, M. K. Nazeeruddin, et H.-S. Shin, « Exclusion of metal oxide by an RF sputtered Ti layer in flexible perovskite solar cells: energetic interface between a Ti layer and an organic charge transporting layer », *Dalton Trans.*, vol. 44, nº 14, p. 6439-6448, 2015, doi: 10.1039/C4DT03920C.

[211] M. Ohring, « The Materials Science of Thin Films », p. 742.

[212] W. D. Sproul, D. J. Christie, et D. C. Carter, « Control of reactive sputtering processes », *Thin Solid Films*, vol. 491, nº 1-2, p. 1-17, nov. 2005, doi: 10.1016/j.tsf.2005.05.022.

[213] X. Li, Z. Sun, Y. Zhang, D. Huang, et J. Hu, « Effects of Oxygen Vacancies on Dielectric Properties and Relaxor Behavior of Ba(Zr$\less$sub$\greater$x$\less$/sub$\greater$Ti$\less$sub$\greater$1-x$\less$/sub$\greater$)O$\less$sub$\greater$3$\less$/sub$\greater$ Ceramics », *J. Phys.: Conf. Ser.*, vol. 2101, nº 1, p. 012050, nov. 2021, doi: 10.1088/1742-6596/2101/1/012050.

[214] J. Robertson, K. Xiong, et K. Tse, « Importance of Oxygen Vacancies in High K Gate Dielectrics », in *2007 IEEE International Conference on Integrated Circuit Design and Technology*, mai 2007, p. 1-4. doi: 10.1109/ICICDT.2007.4299548.

[215] « Controlling Resistance Switching Performances of Hf0.5Zr0.5O2 Films by Substrate Stress and Potential in Neuromorphic Computing - Xiao - - Advanced Intelligent Systems - Wiley Online Library ». https://onlinelibrary.wiley.com/doi/full/10.1002/aisy.202100244.

[216] D. Barreca, A. Milanov, R. A. Fischer, A. Devi, et E. Tondello, « Hafnium oxide thin film grown by ALD: An XPS study », *Surface Science Spectra*, vol. 14, n° 1, p. 34-40, déc. 2007, doi: 10.1116/11.20080401.

[217] R. Brenier, J. Mugnier, et E. Mirica, « XPS study of amorphous zirconium oxide films prepared by sol–gel », *Applied Surface Science*, vol. 143, n° 1-4, p. 85-91, avr. 1999, doi: 10.1016/S0169-4332(98)00901-5.

[218] T. V. Perevalov *et al.*, « The atomic and electronic structure of Hf0.5Zr0.5O2 and Hf0.5Zr0.5O2:La films », *Journal of Science: Advanced Materials and Devices*, p. S2468217921000642, août 2021, doi: 10.1016/j.jsamd.2021.08.001.

[219] T. V. Perevalov, D. R. Islamov, V. A. Gritsenko, et I. P. Prosvirin, « Electronic structure of stoichiometric and oxygen-deficient ferroelectric Hf$\less$sub$\greater$0.5$\less$/sub$\greater$Zr$\less$sub$\greater$0.5$\less$/sub$\greater$O$\less$sub$\greater$2$\less$/sub$\greater$ », *Nanotechnology*, vol. 29, n° 19, p. 194001, mars 2018, doi: 10.1088/1361-6528/aaacb1.

[220] F. Ambriz-Vargas *et al.*, « Tunneling electroresistance effect in a Pt/Hf0.5Zr0.5O2/Pt structure », *Appl. Phys. Lett.*, vol. 110, n° 9, p. 093106, févr. 2017, doi: 10.1063/1.4977028.

[221] T. Kim, J. Park, B.-H. Cheong, et S. Jeon, « Effects of high pressure nitrogen annealing on ferroelectric Hf0.5Zr0.5O2 films », 2018, doi: 10.1063/1.5003369.

[222] J. Bouaziz, P. Rojo Romeo, N. Baboux, R. Negrea, L. Pintilie, et B. Vilquin, « Dramatic impact of pressure and annealing temperature on the properties of sputtered ferroelectric HZO layers », *APL Materials*, vol. 7, n° 8, p. 081109, août 2019, doi: 10.1063/1.5110894.

[223] J. Hwang, Y. Goh, et S. Jeon, « Effect of Forming Gas High-Pressure Annealing on Metal-Ferroelectric-Semiconductor Hafnia Ferroelectric Tunnel Junction », *IEEE Electron Device Lett.*, vol. 41, n° 8, p. 1193-1196, août 2020, doi: 10.1109/LED.2020.3001639.

[224] M. Dogan, N. Gong, T.-P. Ma, et S. Ismail-Beigi, « Causes of ferroelectricity in HfO$_{2}$-based thin films: An $\textit{ab initio}$ perspective », *Phys. Chem. Chem. Phys.*, vol. 21, n° 23, p. 12150-12162, 2019, doi: 10.1039/C9CP01880H.

[225] R. Materlik, C. Künneth, et A. Kersch, « The origin of ferroelectricity in $Hf_{1-x}Zr_xO_2$: A computational investigation and a surface energy model », *Journal of Applied Physics*, vol. 117, n° 13, p. 134109, avr. 2015, doi: 10.1063/1.4916707.

[226] M. Hyuk Park, H. Joon Kim, Y. Jin Kim, W. Lee, T. Moon, et C. Seong Hwang, « Evolution of phases and ferroelectric properties of thin $Hf_{0.5}Zr_{0.5}O_2$ films according to the thickness and annealing temperature », *Applied Physics Letters*, vol. 102, n° 24, p. 242905, juin 2013, doi: 10.1063/1.4811483.

[227] D. H. Triyoso *et al.*, « Material Innovation in the Era of Artificial Intelligence - A Case Study of Hf-Zr Systems », in *2020 4th IEEE Electron Devices Technology & Manufacturing Conference (EDTM)*, Penang, Malaysia, avr. 2020, p. 1-4. doi: 10.1109/EDTM47692.2020.9117861.

[228] T. Shimizu *et al.*, « The demonstration of significant ferroelectricity in epitaxial Y-doped HfO2 film », *Scientific Reports*, vol. 6, n° 1, déc. 2016, doi: 10.1038/srep32931.

[229] J. Müller *et al.*, « Ferroelectricity in Simple Binary ZrO2 and HfO2. », 2012, doi: 10.1021/nl302049k.

[230] Y. H. Lee *et al.*, « Preparation and characterization of ferroelectric Hf0.5Zr0.5O2 thin films grown by reactive sputtering. », 2017, doi: 10.1088/1361-6528/aa7624.

[231] J. Bouaziz, P. Rojo Romeo, N. Baboux, R. Negrea, L. Pintilie, et B. Vilquin, « Dramatic impact of pressure and annealing temperature on the properties of sputtered ferroelectric HZO layers », *APL Materials*, vol. 7, n° 8, p. 081109, août 2019, doi: 10.1063/1.5110894.

[232] J. Bouaziz, P. Rojo Romeo, N. Baboux, et B. Vilquin, « Characterization of ferroelectric hafnium/zirconium oxide solid solutions deposited by reactive magnetron sputtering », *Journal of Vacuum Science & Technology B*, vol. 37, n° 2, p. 021203, mars 2019, doi: 10.1116/1.5060643.

[233] B. Ku, Y.-R. Jeon, M. Choi, C. Chung, et C. Choi, « Effects of post cooling on the remnant polarization and coercive field characteristics of atomic layer deposited Al-doped HfO2 thin films », *Applied Surface Science*, vol. 601, p. 154039, nov. 2022, doi: 10.1016/j.apsusc.2022.154039.

[234] T. S. Böscke, « Crystalline Hafnia and Zirconia based Dielectrics for Memory Applications », . *INTRODUCTION*, p. 14.

[235] N. F. Habubi, O. M. Abdulmunem, Z. M. Shaban, I. R. Agool, M. O. Dawood, et S. S. Chiad, « Effect of Cu doping ZrO $_2$ Thin films on physical properties grown by spray pyrolysis deposition », *IOP Conf. Ser.: Earth Environ. Sci.*, vol. 790, n° 1, p. 012078, juin 2021, doi: 10.1088/1755-1315/790/1/012078.

[236] N. B. Hassan, G. H. Mohamad, et M. M. Abd-Alkadum, « Influence of Annealing Temperature on Morphology and Electrical Properties of ZrO2:CuO Thin Films Prepared by Pulse Laser Deposition », p. 6.

[237] N.-Q. Yao, Z.-C. Liu, G.-R. Gu, et B.-J. Wu, « Structural, optical, and electrical properties of Cu-doped ZrO $_2$ films prepared by magnetron co-sputtering », *Chinese Phys. B*, vol. 26, n° 10, p. 106801, sept. 2017, doi: 10.1088/1674-1056/26/10/106801.

[238] A. Figini Albisetti, C. Biffi, et A. Tuissi, « Synthesis and Structural Analysis of Copper-Zirconium Oxide », *Metals*, vol. 6, n° 9, p. 195, août 2016, doi: 10.3390/met6090195.

[239] M. Kotilainen *et al.*, « Hafnium oxide thin films as a barrier against copper diffusion in solar absorbers », *Solar Energy Materials and Solar Cells*, vol. 166, p. 140-146, juill. 2017, doi: 10.1016/j.solmat.2017.02.033.

[240] M. Lederer *et al.*, « Local crystallographic phase detection and texture mapping in ferroelectric Zr doped HfO $_2$ films by transmission-EBSD », *Appl. Phys. Lett.*, vol. 115, n° 22, p. 222902, nov. 2019, doi: 10.1063/1.5129318.

[241] M. Lederer, T. Kämpfe, C. Mart, T. Ali, L. Roy, et K. Seidel, « Crystallographic phase and orientation mapping of ferroelectric HfO2 thin films by transmission Kikuchi diffraction », p. 2.

[242] T. Kämpfe *et al.*, « Phase and orientation mapping of ferroelectric HfO2 grains in 22nm FDSOI FeFETs », p. 1.

[243] Y. Wei *et al.*, « A rhombohedral ferroelectric phase in epitaxially strained Hf0.5Zr0.5O2 thin films », *Nature Materials*, vol. 17, n° 12, p. 1095-1100, déc. 2018, doi: 10.1038/s41563-018-0196-0.

[244] H. W. Cho *et al.*, « Direct growth of orthorhombic Hf0.5Zr0.5O2 thin films for hysteresis-free MoS2 negative capacitance field-effect transistors », *npj 2D Mater Appl*, vol. 5, n° 1, p. 46, déc. 2021, doi: 10.1038/s41699-021-00229-w.

[245] Q. Luo *et al.*, « A highly CMOS compatible hafnia-based ferroelectric diode », *Nat Commun*, vol. 11, n° 1, p. 1391, déc. 2020, doi: 10.1038/s41467-020-15159-2.

[246] E. F. Rauch, J. Portillo, S. Nicolopoulos, D. Bultreys, S. Rouvimov, et P. Moeck, « Automated nanocrystal orientation and phase mapping in the transmission electron microscope on the basis of precession electron diffraction », *Zeitschrift für Kristallographie*, vol. 225, n° 2-3, p. 103-109, mars 2010, doi: 10.1524/zkri.2010.1205.

[247] R. Materlik, C. Künneth, et A. Kersch, « The origin of ferroelectricity in $Hf_{1-x}Zr_xO_2$: A computational investigation and a surface energy model », *Journal of Applied Physics*, vol. 117, n° 13, p. 134109, avr. 2015, doi: 10.1063/1.4916707.

[248] Q. Chen, Y. Zhang, W. Liu, J. Jiang, Q. Yang, et L. Jiang, « Ferroelectric switching behavior of nanoscale Hf0.5Zr0.5O2 grains », *International Journal of Mechanical Sciences*, vol. 212, p. 106828, déc. 2021, doi: 10.1016/j.ijmecsci.2021.106828.

[249] M. H. Park *et al.*, « Understanding the formation of the metastable ferroelectric phase in hafnia–zirconia solid solution thin films », *Nanoscale*, vol. 10, n° 2, p. 716-725, 2018, doi: 10.1039/C7NR06342C.

[250] J. W. Adkins, I. Fina, F. Sánchez, S. R. Bakaul, et J. T. Abiade, « Thermal evolution of ferroelectric behavior in epitaxial $Hf_{0.5}Zr_{0.5}O_2$ », *Appl. Phys. Lett.*, vol. 117, n° 14, p. 142902, oct. 2020, doi: 10.1063/5.0015547.

[251] « 33rd International Conference on the Physics of Semiconductors », *J. Phys.: Conf. Ser.*, vol. 864, p. 011001, juin 2017, doi: 10.1088/1742-6596/864/1/011001.

[252] Y. Kouzuma, K. Teii, K. Uchino, et K. Muraoka, « Diamond nucleation density as a function of ion-bombardment energy in electron cyclotron resonance plasma », *Phys. Rev. B*, vol. 68, n° 6, p. 064104, août 2003, doi: 10.1103/PhysRevB.68.064104.

[253] D. Das, B. Buyantogtokh, V. Gaddam, et S. Jeon, « Influence of High-Pressure Annealing Conditions on Ferroelectric and Interfacial Properties of Zr-Rich $Hf_xZr_{1-x}O_2$Capacitors », *IEEE Trans. Electron Devices*, vol. 68, n° 4, p. 1996-2002, avr. 2021, doi: 10.1109/TED.2021.3061963.

[254] J. Müller *et al.*, « Ferroelectricity in Simple Binary ZrO_2 and HfO_2 », *Nano Letters*, vol. 12, n° 8, p. 4318-4323, août 2012, doi: 10.1021/nl302049k.

[255] R. Alcala *et al.*, « Influence of oxygen source on the ferroelectric properties of ALD grown $Hf_{1-x}Zr_xO_2$ films », *J. Phys. D: Appl. Phys.*, vol. 54, n° 3, p. 035102, janv. 2021, doi: 10.1088/1361-6463/abbc98.

[256] T. Kim, M. An, et S. Jeon, « Evolution of crystallographic structure and ferroelectricity of $Hf_{0.5}Zr_{0.5}O_2$ films with different deposition rate », *AIP Advances*, vol. 10, n° 1, p. 015104, janv. 2020, doi: 10.1063/1.5121454.

[257] S. Lun, « Ferroelectricity in nanocrystalline Hf0.5Zr0.5O2 thin films », p. 52.

[258] Min Hung Lee *et al.*, « Ferroelectricity of $HfZrO_2$ in Energy Landscape With Surface Potential Gain for Low-Power Steep-Slope Transistors », *IEEE Journal of the Electron Devices Society*, vol. 3, n° 4, p. 377-381, juill. 2015, doi: 10.1109/JEDS.2015.2435492.

[259] A. Kashir et H. Hwang, « Ferroelectric and Dielectric Properties of $Hf_{0.5}Zr_{0.5}O_2$ Thin Film Near Morphotropic Phase Boundary », *Phys. Status Solidi A*, p. 2000819, févr. 2021, doi: 10.1002/pssa.202000819.

[260] T. Mittmann, M. Materano, S.-C. Chang, I. Karpov, T. Mikolajick, et U. Schroeder, « Impact of Oxygen Vacancy Content in Ferroelectric HZO films on the Device

Performance », in *2020 IEEE International Electron Devices Meeting (IEDM)*, San Francisco, CA, USA, déc. 2020, p. 18.4.1-18.4.4. doi: 10.1109/IEDM13553.2020.9372097.

[261] M. Kozodaev *et al.*, « Mitigating wakeup effect and improving endurance of ferroelectric HfO2-ZrO2 thin films by careful La-doping », *Journal of Applied Physics*, 2019, doi: 10.1063/1.5050700.

[262] F. Mehmood, T. Mikolajick, et U. Schroeder, « Wake-Up Mechanisms in Ferroelectric Lanthanum-Doped Hf $_{0.5}$ Zr $_{0.5}$ O $_{2}$ Thin Films », *Phys. Status Solidi A*, vol. 217, n° 22, p. 2000281, nov. 2020, doi: 10.1002/pssa.202000281.

[263] M.-C. Nguyen, S. Kim, K. Lee, J.-Y. Yim, R. Choi, et D. Kwon, « Wakeup-free and Endurance-robust Ferroelectric Field-Effect Transistor Memory Using High Pressure Annealing », *IEEE Electron Device Lett.*, p. 1-1, 2021, doi: 10.1109/LED.2021.3096248.

[264] « JFS1-4 Excellent Reliability of Ferroelectric HfZrOx Free from Wake-Up and Fatigue Effects by NH3 Plasma Treatment », p. 2.

[265] M. H. Park *et al.*, « Surface and grain boundary energy as the key enabler of ferroelectricity in nanoscale hafnia-zirconia: a comparison of model and experiment », *Nanoscale*, vol. 9, n° 28, p. 9973-9986, 2017, doi: 10.1039/C7NR02121F.

[266] X. Liu, L. Yao, Y. Cheng, B. Xiao, M. Liu, et W. Wang, « Observing large ferroelectric polarization in top-electrode-free Al:HfO2 thin films with Al-rich strip structures », *Applied Physics Letters*, 2019, doi: 10.1063/1.5110668.

[267] M. H. Park *et al.*, « Origin of Temperature-Dependent Ferroelectricity in Si-Doped HfO $_{2}$ », *Advanced Electronic Materials*, vol. 4, n° 4, p. 1700489, avr. 2018, doi: 10.1002/aelm.201700489.

[268] T. S. Böscke *et al.*, « Phase transitions in ferroelectric silicon doped hafnium oxide », *Appl. Phys. Lett.*, vol. 99, n° 11, p. 112904, sept. 2011, doi: 10.1063/1.3636434.

[269] U. Schroeder *et al.*, « Temperature-Dependent Phase Transitions in Hf $_{x}$ Zr $_{1-x}$ O $_{2}$ Mixed Oxides: Indications of a Proper Ferroelectric Material », *Adv Elect Materials*, p. 2200265, mai 2022, doi: 10.1002/aelm.202200265.

Abstract

The discovery of ferroelectricity in doped hafnium oxide thin films has turned it into one of the leading CMOS-compatible lead-free materials. Ferroelectric hafnium oxide can open the way to the design of new devices in multiple fields like ferroelectric memories, negative capacitance field effect transistors (FET), pyroelectric sensors or microsystems. For such applications, the typical material is PZT, currently used in daily-used devices. For environmental reasons, PZT is being prohibited in industry. HZO appears among other hafnia-based ferroelectrics as a promising alternative, which can take the devices' performance to a higher level and expand the properties at smaller thickness, allowing the industry to move to new fabrication nodes with more easiness as hafnia ferroelectrics are more CMOS compatible than PZT. HfO_2 and ZrO_2 were already, as high-k dielectrics, in industry. When the ferroelectricity was discovered within HfO_2 thin films in 2011. Both materials were already employed in the CMOS process. The research community started by understanding the origins and mechanisms of inducing the ferroelectricity in hafnia films, then optimizing the fabrication process steps to improve the polarization and endurance. In this thesis, hafnium zirconium oxide thin films have been deposited by single target sputtering, unlike most published reports using ALD. In addition, different deposition conditions have been investigated (e.g. oxygen partial pressure, RF power, deposition pressure) as well as various post-deposition annealing (temperature, time, and atmosphere). This thesis contributes to the sustainable CMOS-compatible fabrication of ferroelectric HZO films deposited by single target sputtering and the structural characterization of the orthorhombic phase. The majority of HZO films grown by single target sputtering were amorphous, a condition to induce the o-phase. The films have the desired stoichiometry, and they need high thermal budget during the thermal annealing step to become ferroelectric. In this work, we performed in-situ XRD annealing to follow the evolution of the o-phase. The sputtered films are partially crystallized at only low annealing temperatures. Besides the optimization of the deposition and annealing steps, detailed characterization of the o-phase was performed by XRD and ASTAR-TEM techniques. The latter allowed to identify accurately the o-phase from the tetragonal phase, which is a current issue in the state-of-the-art. Ferroelectricity in uncapped HZO is explored, giving insight into phase evolution during the annealing. Not reported in literature, a study on HZO films demonstrated the phase transition temperature of HZO films from the ferroelectric to paraelectric phase. Comparing HZO films of different thickness, a partial crystallization was noted at thicker films.

Résumé

La découverte de la ferroélectricité dans les couches minces d'oxyde d'hafnium dopé en a fait l'un des principaux matériaux sans plomb, compatibles avec le CMOS processus. HfO_2 ferroélectrique peut ouvrir la voie à la conception de nouveaux dispositifs dans de multiples domaines comme les mémoires ferroélectriques, les transistors à effet de champ à capacité négative (FET), les capteurs pyroélectriques ou les microsystèmes. Pour de telles applications, le matériau typique est le PZT, actuellement utilisé dans les appareils utilisés quotidiennement. Pour des raisons environnementales, le PZT est interdit dans l'industrie. HZO apparaît parmi d'autres ferroélectriques à base d'hafnia comme une alternative prometteuse, qui peut porter les performances des dispositifs à un niveau supérieur et étendre les propriétés à une épaisseur plus petite, permettant à l'industrie de passer à de nouveaux nœuds de fabrication avec plus de facilité car les ferroélectriques hafnia sont plus compatibles avec le CMOS processus que PZT. HfO_2 et ZrO_2 étaient déjà connues et utilisées, en tant que diélectriques high-k, dans l'industrie. Lorsque la ferroélectricité a été découverte dans les couches minces de HfO_2 en 2011. Les deux matériaux étaient déjà utilisés dans le procédé CMOS. La communauté de recherche a commencé par comprendre les origines et les mécanismes d'induction de la ferroélectricité dans les films d'hafnia, puis a optimisé les étapes du processus de fabrication pour améliorer la polarisation et l'endurance. Dans cette thèse, des couches minces d'oxyde de zirconium et d'hafnium ont été déposées par pulvérisation monocible, contrairement à la plupart des rapports publiés utilisant l'ALD. De plus, différentes conditions de dépôt ont été étudiées (par exemple, la pression partielle d'oxygène, la puissance RF, la pression de dépôt) ainsi que divers paramètres de recuit post-dépôt (température, durée et atmosphère). Cette thèse contribue à la fabrication durable compatible CMOS des couches ferroélectriques HZO déposés par pulvérisation monocible et à la caractérisation structurale de la phase orthorhombique. La majorité des films HZO développés par pulvérisation cathodique à cible unique étaient amorphes, une condition pour induire la phase orthorhombique. Les films ont la stœchiométrie souhaitée, et ils ont besoin d'un budget thermique élevé lors de l'étape de recuit thermique pour devenir ferroélectriques. Dans ce travail, nous avons effectué un recuit DRX in-situ pour suivre l'évolution de la phase orthorhombique. Les films déposés par pulvérisation sont partiellement cristallisés uniquement à de basses températures de recuit. Outre l'optimisation des étapes de dépôt et de recuit, la caractérisation détaillée de la phase orthorhombique par les techniques XRD et ASTAR-TEM a été effectuée. Cette dernière a permis d'identifier avec précision la phase orthorhombique de la phase tétragonale, ce qui est un problème courant dans l'état de l'art. La ferroélectricité dans le HZO sans top electrode est explorée, donnant un aperçu de l'évolution de la phase pendant le recuit. Non rapportée dans la littérature, une étude sur des films HZO a démontré la température de transition de phase des films HZO de la phase ferroélectrique à la phase paraélectrique. En comparant les films HZO d'épaisseur différente, une cristallisation partielle a été observée au niveau des films plus épais.